UAB
Universitat Autònoma de Barcelona

Hybrid Cu-HTS Coating for CERN's Future Circular Collider Beam Screen

Guilherme Theophilo TELLES

ADVERTIMENT. L'accés als continguts d'aquesta tesi queda condicionat a l'acceptació de les condicions d'ús establertes per la següent llicència Creative Commons: https://creativecommons.org/licenses/?lang=ca

ADVERTENCIA. El acceso a los contenidos de esta tesis queda condicionado a la aceptación de las condiciones de uso establecidas por la siguiente licencia Creative Commons: https://creativecommons.org/licenses/?lang=es

WARNING. The access to the contents of this doctoral thesis it is limited to the acceptance of the use conditions set by the following Creative Commons license: https://creativecommons.org/licenses/?lang=en

UNIVERSITAT AUTÒNOMA DE BARCELONA

DOCTORAL THESIS

Hybrid Cu-HTS Coating for CERN's Future Circular Collider Beam Screen

Author:
Guilherme Theophilo TELLES

Supervisors:
Dr. Joffre GUTIERREZ,
Dr. Xavier GRANADOS

A dissertation submitted in fulfillment of the requirements
for the degree of Doctor of Philosophy

in the

Superconducting Materials and Large Scale Nanostructures Department (SUMAN)
Institut de Ciència de Materials de Barcelona (ICMAB-CSIC)

Tutor: Dr. Nuria del Valle Benedi

Doctorat en Física
Departament de Física - Facultat de Ciències
Universitat Autònoma de Barcelona

June 3, 2024

Guilherme Theophilo Telles
ICMAB-CSIC
Campus de la UAB, Bellaterra, Barcelona
gtelles@icmab.es

June 2024



This work is published under Creative Commons, CC BY-NC-ND 4.0
The material can be copied and reproduced, providing appropriate credit to the author. You may not use the whole or part of the material for any commercial purposes. No derivatives of the material are allowed under this license. The distribution of modified material requires the authors permission.

ICMAB
INSTITUT DE CIÈNCIA DE MATERIALS DE BARCELONA
EXCELENCIA SEVERO OCHOA
CSIC
CONSEJO SUPERIOR DE INVESTIGACIONES CIENTÍFICAS

UAB
Universitat Autònoma de Barcelona
Facultat de Ciències
Departament de Física

Memòria que porta per títol **"Hybrid Cu-HTS Coating for CERN's Future Circular Collider Beam Screen"** i presentada per aspirar al Grau de Doctor en Física per **Guilherme Theophilo Telles**

Autor:
Guilherme Theophilo Telles, M. Sc.

amb el vist i plau de: **Dr. Joffre Guttiérez Royo**, Científic Titular del Institut de Ciències de Materials de Barcelona (ICMAB-CSIC), **Dr. Xavier Granados Garcia**, Científic Titular Ad Honorem del Institut de Ciències de Materials de Barcelona (ICMAB-CSIC); i **Dr. Nuria del Valle Benedi**, Professora Agregada del Departament de Física de la Universitat Autònoma de Barcelona (UAB).

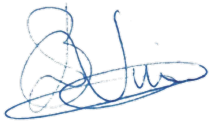
I per a que així consti, signen el present certificat.



Director:
Dr. Joffre Guttiérez Royo



Director:
Dr. Xavier Granados Garcia



Tutor:
Dr. Nuria del Valle Benedi

Bellaterra, Juny de 2024

UNIVERSITAT AUTÒNOMA DE BARCELONA

Abstract

Department of Physics

Institut de Ciència de Materials de Barcelona (ICMAB-CSIC)

Doctor of Philosophy

Hybrid Cu-HTS Coating for CERN's Future Circular Collider Beam Screen

by Guilherme Theophilo TELLES

The Future Circular Collider (FCC) is the next generation particle collider proposed by the European Organization for Nuclear Research (CERN) as the successor of the current world's most powerful accelerator, the Large Hadron Colider (LHC). The FCC Feasibility Study counts with more than 150 entities worldwide to evaluate the suitability of this new machine, aiming for collision energies of 100 TeV, more than seven times those currently reachable at the LHC. Researchers hope that the data generated in such collisions sheds some light onto mysteries of the universe such as the matter-antimatter asymmetry, dark matter and dark energy, and the hyerarchy problem.

In high-energy circular colliders such as the FCC, a series of powerful superconducting magnets is responsible for maintaining the particle beam in a stable orbit. To protect these magnets from the synchrotron radiation emitted by the beam, a stainless steel structure is interposed between the beam and the magnets to absorb the radiation, the so-called beam screen. However, to ensure that the beam orbit is not disturbed, it must present a low surface impedance without affecting the surrounding magnetic field above acceptable levels. For this reason, in the LHC, the stainless steel beam screen is coated with a copper layer. On the other hand, the higher operation temperatures of the FCC beam screen, between 40 and 60 K, might result in an exceeding surface resistance coming from the copper coating.

To mitigate this, the Superconducting Materials and Large Scales Nanostructures (SUMAN) group at the Institute of Materials Science of Barcelona (ICMAB - CSIC) has been studying since 2017, in a collaboration with CERN, the viability of adopting Rare Earth-$Ba_2Cu_3O_{7-\delta}$ (REBCO) High Temperature Superconductors (HTS) as an alternative coating for the FCC beam screen. More specifically, a hybrid REBCO-Cu coating is proposed as a means to decrease the overall surface resistance of the beam screen while preserving high magnetic field quality inside the vacuum chamber of the FCC.

In this thesis, we investigate the behavior of the hybrid-coated beam screen under the operating conditions of the FCC. Finite Elements Method (FEM) numerical analysis is employed to evaluate its electromagnetic and thermomechanical response to the magnetic fields of up to 16 T of the bending and focusing magnets as well as the AC magnetic field generated by the beam itself. The extreme scenario of a dipole magnet quench and its repercussions in the beam screen is also considered. Coating techniques based on REBCO Coated Conductors (CC) have been developed and laboratory scale samples of the hybrid coating have been produced, as well as an early prototype for the coated beam screen.

Acknowledgements

Although the quest for the doctoral degree is only an early stage on the scientific career, it has been quite a journey to get to this point, and there are many people without whose contributions this accomplishment would not have been possible. These pages are a meager attempt to show them my gratitude.

First and foremost, I would like to thank my thesis supervisors, Dr. Joffre Gutierrez and Dr. Xavier Granados. Your guidance has been invaluable throughout these years and I was fortunate to work under people who not only motivate and inspire their students on a professional level, but who also always care for their well-being. Thank you for all the lengthy explanations, lessons and discussions, but also for the just as important light-hearted conversations, for listening to all my problems, and for easing many of my concerns. Even though I am so far away from home, you made me feel at home here as well, and for that I will always be grateful.

When I first came to Spain, being someone who had never before travelled abroad, I was quite scared of how day-to-day life would be. Luckily, my worries were unfounded as I was welcomed by an amazing work environment at ICMAB. To those with whom I had the privilege to work more closely, thank you for all your support and companionship, professionally or otherwise. I would like to thank SUMAN Group Leader, Prof. Teresa Puig, for steering me in the right direction while still allowing me the freedom to do things in my own way. I constantly felt that my efforts were recognized and I appreciate the trust you had in me and in my work in so many occasions. To my PhD colleagues Dr. Artur Romanov, Neil Lamas, Irfan Ahmed and Luca Benedetti, it was a pleasure to be part of your team. Whether we were characterizing coated conductors, coating RF cavities or debugging simulations, it was always a productive time, but really fun too. I specially appreciate Dr Artur Romanov's tips for the writing of the thesis. I also extend my thanks to Dr. Bernat Bozzo and Dr. Ana Esther Carrillo for the PPMS and SEM/EDX measurements, respectively. The results obtained with your help were an important part of this thesis. In addition, I thank Mariona de Palau for the tremendous task of making sure everything was in order in all our laboratories.

The interdisciplinarity provided by the combined efforts of our project consortium were fundamental for many of the discussions and analyses made throughout this thesis, and allowed for the expansion of my own point of view regarding several subjects. To Julia Mundet, Rafael Garcia and Pau Llanes, thank you for all the effort to automate our coating procedures, making our lives much easier. To Prof. Joan O'callaghan, Dr. Montse Pont, Dr. Patrick Krkotić, Nikki Tagdulang and Oriol Traver, thank you for all the clarification regarding synchrotron radiation and the realm of radio-frequency, as well as the manufacturing of the dielectric resonator system used in this thesis. I must express my gratitude in particular to Dr. Patrick Krkotić for being one of the most welcoming people I have ever met, and for making sure from day one that I never felt out of place.

It is no wonder that, in such a complex subject as the FCC, there were many instances in which I had to inquire of the experts at CERN about the inner workings of particle accelerators and beam screens. To Dr. Sergio Calatroni, thank you for all the answers you had for my many, many questions regarding accelerators, material properties, magnets and so on. Whenever you did not have the answers yourself, you were quick to point me towards where to find them, and that was an incredible help. I would also like to thank Dr. Massimo Giovannozzi for the fruitful discussions regarding the magnetic field requirements of the FCC beam screen.

Although we did not have the opportunity to work on the same projects, many are the names of other colleagues who shared a little bit of their time with me as well, be it in the labs, in conferences or even in purely social events: Aiswarya Kethamkuzhi, Aleix Barrera, Dr. Alejandro Fernández, Carla Torres, Dr. Cornelia Pop, Darla Mare, Emma Ghiara, Dr. Jordi Alcalà, Dr. Juri Banchewski, Karla Mena, Dr. Mathieu Mirjolet, Dr. Lavinia Saltarelli, Ona Mola, Dr. Pamela Machado, Dr. Pedro Barusco, Dr. Roxana Vlad, Thomas Günkel, Vittorio Bertini, among so many others.

I want to thank Dr. Lavinia Saltarelli in particular for being so patient with me while explaining several repeated times how the thesis submission process works. Special thanks go to Dr. Pedro Barusco, who has been a dear friend and colleague since we met, fourteen years ago. Without your words of encouragement I would have never crossed the sea, and my life would be very different today. Thank you.

None of the scientific work carried out throughout this thesis would have been possible without the great assistance of those who dealt with administrative tasks. Thank you, Pietat Sierra, Pilar López, Yrene Dominguez and Dr. Mar Tristany for sparing me from dealing with all the paperwork. Special thanks are in order to Dr. Mar Tristany for being always available and willing to help, for her unending patience and for always going the extra mile to solve whatever problems with witch I would bother her.

I would like to acknowledge the support and samples provided by Bruker HTS GmbH, Faraday Factory Japan LLC, Fujikura Ltd., Sunam Co., SuperPower Inc. and THEVA Dünnschishttenchnik. In addition, I acknowledge financial support from Spanish Ministry of Science and Innovation through the "Severo Ochoa" Programme for Centres of Excellence in R&D (CEX2019-000917-S and SEV-2015-0496), SUPERENERTECH and SUMATE projects (PID2021-127297OB-C21 and RTI2018-095853-B-C21, co-financed by the European Regional Development Fund, MCIN/AEI/FEDER,UE), SUPERPOWER project (TED2021-130004B-I00, MCIN/AEI/10.13039/501100011033 and EU "NextGenerationEU"/PRTR) and PTI+TransEner CSIC programme (TRE2102002) for Spanish NGEU. I also thank support from CERN funding FCCGOV-CC-0208 (KE4947/ATS), from the European Union for SUPERQUMAP project (Cost Action CA 21144), HI-SCALE (Cost Action CA 19108), NANOCOHYBRI (Cost Action CA 16218) and from the Catalan Government with 2021-SGR-00440, 2017-SGR-1519, and Catalan energy network XRE4S (2018 XARDI 00002).

A mis queridos amigos de la congregación Cerdanyola Norte, les debo mi más profundo agradecimiento. Estoy convencido de que no habría aguantado solo los primeros meses en un nuevo país sin vuestro apoyo incondicional. Fuisteis amigos y familiares cuando más los necesité y por eso os estaré eternamente agradecido. Aunque cada uno de vosotros ha jugado un papel importante de una forma u otra, me siento obligado a agradecer específicamente a Juan y Esther; Ismael y Diana; Joaquín y Katy; Gerard, Priscila y Leire; y Claudio, Victoria, Antonio y Cristián. Gracias por hacerme sentir que pertenezco.

Embora as seguintes pessoas não tenham sido influências diretas ao longo do curso de doutorado, foram fundamentais para que eu alcançasse esse estágio, como mentores do ensino médio e da universidade, que me inspiraram a perseguir o sonho da ciência e me motivaram a seguir minhas aspirações. Obrigado à Profa. Sonia Abi Daud, Prof. Fausto Lima e Prof. Rubens de Andrade por despertarem em mim essa chama eterna e me encorajarem nos momentos de dúvida.

Poucos são aqueles afortunados que podem contar com tantos amigos como eu. E de fato são tantos nomes que uma outra tese inteira seria necessária para agradecer a todos. Ao Grupo Perfeito, obrigado por serem exatamente isso. Cada um de vocês tem um lugar especial no meu coração. A Hannah e Luiz André, obrigado por estarem ao meu lado nos bons e maus momentos. Às meninas, ou seja, Hanna, Nathalia, Katarina e Thamires, eu ainda sinto saudade da Taquara, e certamente não é por causa da boa gastronomia. Toda sexta-feira aqui, além-mar, grita um pedido inatendido por board games e filmes na sua companhia. Espero ansiosamente a próxima vez em que estaremos todos juntos. A Thais e Débora, obrigado pelo companheirismo em tempos de necessidade. As portas da minha casa sempre estarão abertas pra vocês. A todos os meus amigos que me ajudam a salvar o mundo, Azeroth, a Super Terra, os Ancients ou o Traveler, obrigado por preservar minha sanidade. Vocês são a equipe que eu gostaria de ter ao meu lado em qualquer apocalipse. A Pedro, Rubio, Renan, Betinho, Tus, Sharingan, Lynik e Miojo, thanks for carrying. Aos meus amigos de outros carnavais, Fernando e Vinicius, mesmo passando um ano sem nos falar, sempre que nos

reencontramos parece que foram apenas alguns dias. Voces não são menos importantes por conta da distância ou do tempo, e sempre me visitam em pensamentos. A meus irmãos da vida, Bruno e Luiz Felipe, nem com um roll de carisma 20 eu poderia expressar pra vocês aquilo que vocês já sabem tão bem. Obrigado por tudo.

À minha família, eu devo tudo o que sou a vocês, ao seu carinho e sua dedicação. Por todo o seu apoio nessa fase da minha vida e em todas as outras, eu devo meu eterno agradecimento a meus pais, Andrea e Miguel, a minhas avós, Maria Ângela e Detta, ao meu tio Rodrigo e ao meu avô Fernando, que apesar de não estar mais presente, se mantém vivo no meu pensamento. Obrigado por sempre me fazerem saber que, não importa o que aconteça, sempre há uma solução.

Se felizes são aqueles que podem contar com uma família como a minha, ainda mais são os que têm duas. A meus sogros, Ione e Alexandre, e meus cunhados, Filipe e Xandinho, obrigado por todo o seu apoio, amizade e parceria. Eu sei que sempre posso contar com vocês, assim como vocês podem contar comigo. Obrigado por me acolherem nessa família maluca mas maravilhosa.

Finalmente, mas definitivamente não menos importante, agradeço à minha esposa, Juliana. Sem você, eu não teria nem começado essa empreitada; não teria motivação nem propósito. Obrigado por ser tudo o que eu preciso e muito mais; por me fazer ver o que é realmente importante e por me apoiar em tudo em que eu ponho minha mente. Você é minha Lúthien, minha Sara, meu amor. E por voce eu faria tudo de novo, ou desfaria tudo que fiz. Obrigado.

Contents

Abstract v

Acknowledgements vii

List of Journal Articles xvii

1 Introduction 1
- 1.1 The Future Circular Collider . . . 1
- 1.2 Superconductors: a low surface impedance coating . . . 3
  - 1.2.1 History of Superconductivity . . . 3
  - 1.2.2 The two types of superconductors . . . 4
  - 1.2.3 REBCO Coated Conductors . . . 7
- 1.3 Objectives and Outline . . . 9

2 Theoretical Background 11
- 2.1 Models for HTS . . . 11
  - 2.1.1 The Bean Critical State Model . . . 11
  - 2.1.2 The Anderson-Kim Model . . . 12
  - 2.1.3 Further Considerations for REBCO HTS . . . 14
  - 2.1.4 Overcritical Adaptation of the Power Law . . . 15
- 2.2 High Frequency Behaviour . . . 16
  - 2.2.1 Surface Impedance . . . 16
  - 2.2.2 AC Field Demagnetization . . . 20
- 2.3 A Review of Particle Accelerators . . . 23
  - 2.3.1 Particle Accelerator Optics . . . 23
  - 2.3.2 Beam Interactions . . . 28
  - 2.3.3 The FCC-hh Beam Screen . . . 32
  - 2.3.4 A Hybrid REBCO-Cu Coating for the FCC Beam Screen . . . 33

3 Methods for Production and Quality Evaluation of REBCO Coatings 37
- 3.1 Coating Surfaces with Delaminated Coated Conductors . . . 37
  - 3.1.1 Coated Conductor Preparation . . . 37
  - 3.1.2 Soldering and Delamination . . . 39
- 3.2 Dielectric Resonator Radio Frequency Measurement . . . 41
- 3.3 Combined Microscopy Analysis . . . 44
  - 3.3.1 Optical Microscopy . . . 44
  - 3.3.2 Scanning Electron Microscopy and Energy Dispersive Spectroscopy . . . 45

3.3.3 Scanning Hall Probe Microscopy . . . 47
3.3.4 A Quick Assessment of Coating Quality . . . 48

4 Field Quality of the Coated Beam Screen 51
4.1 The Finite Elements Method . . . 51
4.2 Numerical Analysis Model . . . 53
4.2.1 H-Formulation . . . 53
4.2.2 REBCO Resistivity . . . 55
4.2.3 Geometry Parametrization . . . 57
4.3 Field Quality Simulations . . . 59
4.3.1 Ramping up the Dipole Field . . . 59
4.3.2 AC Demagnetization at High DC Fields . . . 62
4.3.3 High Field Quality Geometries . . . 63
4.3.4 Dipole Cancellation and Proposed Geometry . . . 65
4.4 Magnetization and Surface Resistance Measurements . . . 67
4.5 Chapter Summary and Conclusions . . . 70

5 Quadrupole, Beam Screen Misalignments and Other Field Configurations 73
5.1 Model Adaptations . . . 73
5.2 Field Quality in a Quadrupole Field . . . 76
5.3 Misalignment Effects on the Field Quality . . . 78
5.4 Other Field Configurations . . . 80
5.4.1 Harmonic Relaxation during Injection . . . 81
5.4.2 Hysteresis Effects . . . 82
5.4.3 Combined Magnet-Coating Harmonics . . . 85
5.5 Chapter Summary and Conclusions . . . 86

6 Thermomechanical Behaviour of the Coated Beam Screen 89
6.1 Thermomechanical Model . . . 89
6.2 Beam-Induced Effects in the Beam Screen . . . 91
6.2.1 Numerical Calculation of the Image Current Distribution . . . 91
6.2.2 Resistive Wall Heating . . . 93
6.2.3 Beam-Induced Forces . . . 97
6.3 Thermomechanical Simulations . . . 98
6.4 Chapter Summary and Conclusions . . . 102

7 The Coated Beam Screen during a Dipole Magnet Quench 103
7.1 Model Adaptations . . . 103
7.2 Thermomechanical Simulations during a Magnet Quench . . . 106
7.3 Pull-off Adhesion Testing . . . 112
7.4 Chapter Summary and Conclusions . . . 116

8 Transversal Current Flow in the Hybrid Coating 117
8.1 Electronically Coupled HTS Segments . . . 117
8.2 Numerical Analysis for Transverse Currents Simulation . . . 121
8.3 The Effect of Contact Resistance in Transverse Current Flow . . . 124

8.4 Coupled HTS Segments in a Constant Field . . . 127
8.5 Chapter Summary and Conclusions . . . 131

9 HTS Coated Beam Screen Prototypes and Radio-Frequency Cavities 133
9.1 HTS Coated Beam Screen Prototypes . . . 133
9.2 REBCO-Coated Cavities for Axion Dark Matter Search . . . 136
9.3 REBCO-Coated Disc for RF Testing . . . 138
9.4 Chapter Summary and Conclusions . . . 139

10 General Conclusions 141

A Simulation Details 145
A.1 Parametric Study and other Dipole Simulations . . . 145
A.2 Simulation of AC Field Demagnetization . . . 157
A.3 Quadrupole and Other Field Configurations . . . 158
A.4 Thermomechanical Simulations . . . 159
A.5 Magnet Quench Simulations . . . 161
A.6 Transverse Current Simulations . . . 162

Bibliography 163

List of Abbreviations

a-C	Amorphous Carbon
AC	Alternating Current
BS	Beam Screen
CC	Coated Condcutor
CERN	European Organization for Nuclear Research
DC	Direct Current
DR	Dielectric Resonator
EDX	Energy Dispersive Spectroscopy
EM	Electromagnetic
FC	Field Cooling
FCC-hh	Future Circular Collider hadron-hadron
FEM	Finite Elements Method
HTS	High Temperature Superconductor
HSV	Hue, Saturation and Value
ICMAB - CSIC	Institute of Materials Science of Barcelona
IFAE	Institute of High Energy Physics
LHC	Large Hadron Collider
LN2	Liquid Nitrogen
ODE	Ordinary Differential Equations
OM	Optical Microscopy
PDE	Partial Differential Equations
PGS	Pyrolitic Graphite Sheet
PPMS	Physical Properties Measurement System
RADES	Relic Axion Detector Exploratory Setup
REBCO	Rare Earth-$Ba_2Cu_3O_{7-\delta}$
RF	Radio-Frequency
RMS	Root Mean Square
RRR	Residual Resistivity Ratio
SEM	Scanning Electron Microscopy
SEY	Secondary Electron Yield
SHPM	Scanning Hall Probe Microscopy
SLAC	Stanford Linear Accelerator Center
SS	Stainless Steel
SUMAN	Superconducting Materials and Large Scale Nanostructures group at ICMAB
VNA	Vector Network Analyser
YBCO	$YBa_2Cu_3O_{7-\delta}$

List of Journal Articles

Published journal articles:

1. A. Romanov, P. Krkotić, G. T. Telles, J. O'Callaghan, T. Puig, M. Pont, F. Perez, X. Granados, S. Calatroni, T. Puig & J. Gutierrez. "High frequency response of thick REBCO coated conductors in the framework of the FCC study." *Scientific Reports* 10.1 (2020): 094006. DOI: https://doi.org/10.1038/s41598-020-69004-z

2. P. Krkotić, A. Romanov, N. Tagdulang, G. T. Telles, , T. Puig, J. Gutierrez, X. Granados, S. Calatroni, F. Perez, M. Pont & J. O'Callaghan. "Evaluation of the nonlinear surface resistance of REBCO coated conductors for their use in the FCC-hh beam screen." *Superconductor Science and Technology* 35.2 (2022): 025015. DOI: https://doi.org/10.1088/1361-6668/ac4465

3. J. Golm, S. Arguedas Cuendis, S. Calatroni, C. Cogollos, B. Döbrich, J.D. Gallego, J. M. García Barceló, X. Granados, J. Gutierrez, I. G. Irastorza, T. Koettig, N. Lamas, J. Liberadzka-Porret, C. Malbrunot, W. L. Millar, P. Navarro, C. Pereira Carlos, T. Puig, G. J. Rosaz, M. Siodlaczek, G. T. Telles, W. Wuensch. "Thin Film (High Temperature) Superconducting Radiofrequency Cavities for the Search of Axion Dark Matter." *IEEE Transactions on Applied Superconductivity*, vol. 32, no. 4, pp. 1-5, June 2022, Art no. 1500605, DOI: 10.1109/TASC.2022.3147741.

4. G. T. Telles, A. Romanov, S. Calatroni, X. Granados, T. Puig & J. Gutierrez. "Field quality and surface resistance studies of a superconducting $REBa_2Cu_3O_{7-x}$ - Cu hybrid coating for the FCC beam screen." *Superconductor Science and Technology*, vol. 36, no. 4, February 2023, DOI: 10.1088/1361-6668/ac97c9

To be submitted journal articles:

1. FCC consortium collaboration. "Novel high-temperature superconducting coatings for large scale microwave applications." To be submitted.

2. FCC consortium collaboration. "Electromagnetic simulations of a superconducting $REBa_2Cu_3O_{7-x}$ - Cu hybrid coating for the FCC beam screen." To be submitted.

Chapter 1

Introduction

In particle accelerators, high energy particles such as electrons and protons are brought to velocities close the speed of light and collided against each other, breaking down into their most fundamental constituents. The repeating collisions carried out over the course of years in these colossal machines provide scientists with the data they need to eventually discover new fundamental particles and their properties, filling piece by piece the Standard Model of particle physics [1].

Currently, the world's largest and most powerful particle accelerator is the Large Haldron Collider (LHC), belonging to the Accelerator Complex of the European Organization for Nuclear Research (CERN). In this circular accelerator, 8 cm long particle bunches containing 10^{11} charged particles are submitted to three external influences responsible for preserving their trajectory, all of them produced by superconducting devices: sixteen radio-frequency (RF) cavities accelerate the particles by submitting them to an alternating electromagnetic field that propels them forward; the Lorentz force generated by 1232 dipole magnets steers them in a circular path; and hundreds of focusing magnets converge the particle beams [2, 3]. Two particle beams are accelerated in opposite directions in two adjacent circular paths with periodic cross-over sections where the beams can interact with each other and some of their particles collide. These interaction points are the locations of the LHC detectors, namely ALICE, ATLAS, CMS and LHCb, which track the particles resulting from the collisions and gather the data necessary for analysis.

With a total circumference of around 27 km and operating under a dipole field of up to 8.33 T at top energy, the LHC achieves center-of-mass collision energies of 14 TeV, allowing for discoveries such as, and most remarkably, the Higgs Boson, whose interaction with matter particles is responsible for giving them mass [4–6]. The range of possible particles to be discovered, however, is tightly correlated with the achievable collision energies. Therefore, in order to branch up to new particles and physics, new energy levels must be accomplished. Since the particle collision energy is proportional to the accelerator circumference and the dipole magnetic field, a next generation particle accelerator would have to attain higher values for one or both characteristics [7, 8].

1.1 The Future Circular Collider

The Future Circular Collider (FCC) is CERN's response to this need in the form of a collaboration study counting with more than 150 member entities all over the world. It aims to assess the feasibility of said next generation particle accelerator, which would operate under a 16 T dipole field at top energy and a circumference of 91 km, as depicted in Figure 1.1. This means reaching collision energies of roughly 100 TeV, that is, more than seven times those currently achieved at the LHC, possibly shedding some light into new fundamental particles, as well as today's frontier subjects such as dark matter and dark energy [9].

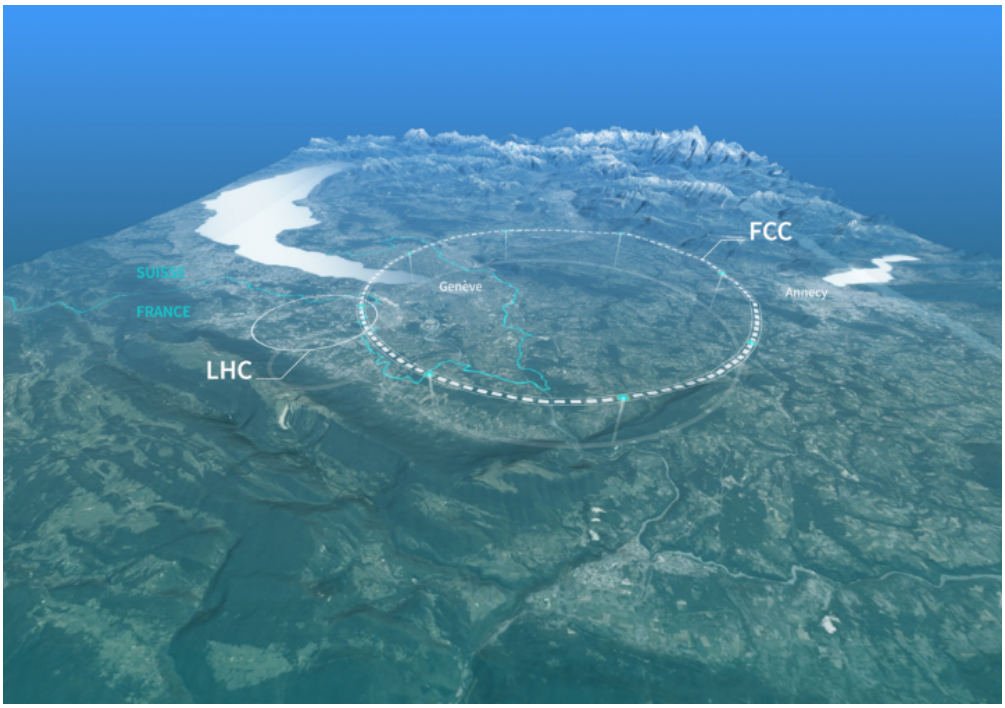


FIGURE 1.1: Schematic map of the planned location for the Future Circular Collider. This image is a courtesy from CERN.

It is no surprise that such improvements in performance introduce several new challenges. Most relevant for this work are the higher magnitudes of synchrotron radiation generated in the FCC. In circular accelerators such as the LHC and the FCC, when the charged particles are steered in a circular path under a perpendicular magnetic field, synchrotron light is emitted tangentially to the beam. In the LHC, the superconducting Nb-Ti magnets on the surrounding regions operate at 1.9 K, and must be shielded from this radiation in order for the temperature to be preserved. The device responsible for this is the beam screen, which consists of a stainless steel pipe surrounding the beam orbit and intercepting and absorbing the heat which would otherwise reach the magnets. The LHC cooling system keeps the beam screen and the vacuum chamber surrounded by it between 5 and 20 K. In the case of the FCC, on the other hand, the synchrotron radiation is so high (160 higher than in the LHC) that the cooling power to maintain such low temperature would be unfeasible [10]. Therefore a new target operating temperature of 50 ± 10 K was set [11].

In both cases, the small radius of the vacuum chamber results in a strong electromagnetic coupling between the beam and the beam screen, in the form of the wake fields and image currents induced by the travelling charged particles. This electromagnetic (EM) interaction, defined by the coupling impedance between the beam and the beam screen, can introduce instabilities to the particles' motion, causing them to lose their orbit and miss collision or even to hit the surrounding structure. To avoid this, it is important that the beam screen's internal surface is coated with a highly conductive material, since the coupling impedance is directly proportional to the surface impedance of the material. In the LHC, the stainless steel beam screen is covered by a 50 µm copper layer. Due to the higher operating temperatures of the FCC, however, the surface impedance of copper may increase above acceptable values. As a means to solve this issue, the usage of high temperature superconductors (HTS) is proposed [12, 13].

1.2 Superconductors: a low surface impedance coating

Superconductors are materials that, under certain critical field and temperature values, can transport high electric current densities with no energy dissipation. Many HTS, in particular, can do so in temperatures higher than the boiling point of liquid nitrogen (LN2), compared to low temperature superconductors (LTS), whose critical temperature often sits in the range of a few K above absolute zero. Additionally, HTS such as Rare Earth-$Ba_2Cu_3O_{7-\delta}$ (REBCO) are capable of preserving superconductivity even at very high magnetic fields of up to more than 100 T. This wide operating ranges of temperature and magnetic field makes them suitable for such highly demanding applications as the FCC.

1.2.1 History of Superconductivity

The first occurrence of superconductivity was reported in 1911 as the researchers of the Leiden Laboratory, in the Netherlands, studied the behaviour of mercury in cryogenic temperatures [14, 15]. The liquefaction of helium, achieved two years prior in the same laboratory, allowed them to reach for the first time temperatures under 4 K, breaching a new frontier in cryogenics, and revealing startling new material properties.

The team, led by the dutch scientist Heike Kamerlingh-Onnes, noticed that once a temperature of around 4.2 K was reached, the electric resistance of the material, which behaved as a standard metal until then, would abruptly drop to zero. To confirm this, they then made current flow through a loop of cooled mercury. Contrary to normal conductors, where the current would quickly vanish due to their electric resistance, the current persisted indefinitely, as long as the material remained below the transition temperature, or critical temperature T_c.

This unexpected discovery earned Onnes the Nobel prize in 1913 [16] and launched the field of superconductivity. Over the span of little more than a century, it developed from the study of a barely know property of a small selection of materials, to complex material engineering with a growing range of industrial and research applications.

Although the results published by Onnes sparked interest from the scientific community, the following couple of decades saw no great advancements concerning superconductivity. A basic theory would remain unformulated for several years despite the many attempts to understand the phenomenon in the first half of the century. It was only in 1933 when some new light was shed onto the subject. Until this point, it was believed that superconductors behaved as perfect conductors. Therefore, when exposed to an external field and then cooled below its critical temperature (Field Cooling - FC), Faraday's law should ensure that, at any subsequent point in time while $T < T_c$, the internal field in the superconductor be equal to the external field at the moment of transition. This was put to the test when Meissner and Ochsenfeld conducted an experiment that revealed that, under these conditions, the superconducting material would instead shield its interior, expelling all magnetic field [17, 18]. In other words, it behaved as a perfect diamagnet, with zero permeability.

In the following year, Gortor and Casimir proposed the two-fluid model, which introduces a combination of electron-like quasiparticles and a superfluid condensate of electrons instead of normal electrons as the charge carriers inside a superconductor [19]. This model can be used in combination with other models to predict the behaviour of superconductors under certain conditions, such as under RF field excitation, as examined in section 2.2. In quick succession, the brothers Heinz and Fritz London formulated what is later known as the London theory, according to which the Ohm's law is replaced by two constitutive relations for superconductors, that relate the superconducting current to the magnetic and electric fields [20, 21]. From this relationship, they were able to explain both Onnes's zero resistance as well as Meissner-Ochsenfeld's perfect diamagnetic effect. The latter is made possible by a current flowing within a

certain depth from the surface of the superconductor in such a way to oppose the external magnetic field. This region of current flow is defined by the London penetration depth λ_L.

In 1950, the combined experiments of E. Maxwell and C. A. Reynolds with mercury isotopes showed that there was a correlation between the critical temperature of a superconductor and the mass of its constituent element [22, 23]. Two months later, this was further explored by H. Frölich, by proposing that superconductivity was created by the interactions between lattice vibrations and electrons [24].

In the same year, V. Ginzburg and L. Landau worked to fill the gaps of the London theory, by accounting for the surface tension between normal and Meissner states as well as the transition out of Meissner state due to an excessive magnetic field or electric current [25]. The Ginzburg-Landau theory introduces the concept of coherence length ξ and the Ginzburg-Landau parameter $\kappa = \lambda_L/\xi$, which relates to the surface energy and is later used to differentiate the two types of superconductor, as discussed in subsection 1.2.2.

It was only in 1957, almost five decades after the discovery of the phenomenon, that a microscopic theory of superconductivity was proposed in the form of the BCS theory, formulated by John Bardeen, Leon Cooper, and John Robert Schrieffer, earning them the Nobel prize in Physics 15 years later [26, 27]. According to the authors, superconductivity is a result of the bonding of pairs of electrons into what is known as Cooper pairs. When one electron moves through the lattice, it attracts the surrounding positive charges, which in turn attract the second electron. This vibration in the lattice is therefore the mediator between the two electrons in a Cooper pair, and the resulting interaction force surpasses the Coulomb repulsive force between the two electrons. Due to the amount of Cooper pairs in a superconductor, they strongly overlap, forming a Bose condensate. This means that any disturbances to individual pairs changes the energy of the whole condensate, which in turn implies that only energy values that are high enough to break the entire condensate can break any of the cooper pairs, allowing them to flow without experiencing resistance. The theory confirms claims that were made in the previous theories, such as the correlation between T_c and the isotopic mass, the lattice vibrations being the cause of superconductivity and the transition from normal to Meissner state being a second order phase transition.

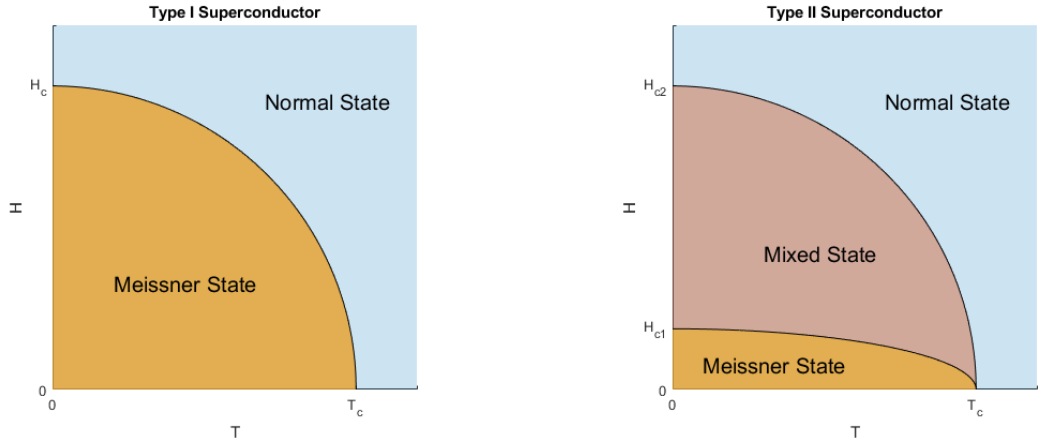
For a while, the BCS theory was considered by many as the final theory to encompass all superconductors, and that the phenomenon was finally and completely explained. The perception on the matter changed completely when, in 1986, Bednorz and Müller discovered lanthanum oxides that exhibited superconducting behaviour occurring in temperatures higher than those believed possible according to the BCS theory [28]. This announcement, met with skepticism by experts in the area, represented the first step in the investitagion of HTS, many of which present T_c above the boiling point of nitrogen (77 K), a much more abundant, cheaper, and easier to use coolant. In particular, the layered, anisotropic REBCO ceramic materials are the main focus of this work, with strong superconducting properties and commercially available in the form of coated conductors.

1.2.2 The two types of superconductors

Superconductors can be classified with regards to the interface between normal and superconducting regions as type I (or conventional or soft) and type II (or unconventional or hard) superconductors. This can be quantified in the Ginzburg-Landau parameter κ, depending on whose value the superconductor will have different behaviours.

In type I superconductors, with $\kappa < 1/\sqrt{2}$, the interface between normal and superconducting regions shows positive surface energy, which means that the minimum energy state corresponds to having a single interface. In other words, The Meissner state encompasses the entirety of the material, locally transitioning to the normal state within the London penetration depth λ_L from the surface of the material. In addition to the limiting critical temperature T_c, superconductivity in only maintained under a magnetic field smaller than H_c, the critical magnetic field intensity.

On the other hand, type II superconductors can often be found in a mixed state, with $\kappa > 1/\sqrt{2}$ and negative interfacial surface energy, meaning that the minimum energy state corresponds to maximizing the interface between superconducting and normal regions [29]. Therefore type II superconductors have two critical fields: H_{c1}, the threshold between Meissner and mixed state; and H_{c2}, marking the transition to normal state. The phase diagram for both types of superconductors is shown in Figure 1.2



(a) (b)

FIGURE 1.2: Phase diagram of the two types of superconductors: (a) Type I, with normal and Meissner states; and (b) Type II, with mixed state as well. Figure adapted from [30].

In practice, this means that, while type I superconductors expel the entirety of the magnetic field applied to them from their interior, type II superconductors in the mixed state have normal-conducting regions in them to maximize the interface, allowing for some of this magnetic field to flow through the material. This magnetic field is produced by circular currents surrounding the normal regions. Each of these so called vortices only allows for a specific amount of magnetic flux to penetrate: the magnetic flux quantum $\Phi_0 = \frac{h}{2e} \approx 2.07 \times 10^{-15}\,\mathrm{Tm}^2$, but the combined contributions of all the vortices summ up to the original field the superconductor was exposed to, minus any decay due to energy dissipation. The behaviour of the two types of superconductors is shown in Figure 1.3.

In homogeneous materials, the Lorentz forces between the superconducting currents $\boldsymbol{J}_{sc}$ and the magnetic fields $\boldsymbol{B}$ of the different vortices, given by

$$\boldsymbol{f}_L = \boldsymbol{J}_{sc} \times \boldsymbol{B}\,, \tag{1.1}$$

cause them to arrange in a hexagonal grid, also known as the Abrikosov vortex lattice [31] with side length a_Δ given by [32]

$$a_\Delta = \sqrt{\frac{2}{\sqrt{3}}\frac{\Phi_0}{\mu_0 H}}\,, \tag{1.2}$$

where $\mu_0 = 4\pi \times 10^{-7}\mathrm{H/m}$ is the magnetic permeability of vacuum.

It is interesting to note that a_Δ decreases as the field H increases, meaning that the vortex density $\eta_v = \frac{\mu_0 H}{\Phi_0}$ increases with the field. A comparison between the superconducting currents and the resulting magnetic field distribution in both mixed and Meissner states is presented in Figure 1.4, with details regarding the Abrikosov vortex lattice.

More often than not, however, superconductors are not perfectly homogeneous, presenting small defects such as impurities in the material, stacking faults or grain or twin boundaries. Since superconductivity is already locally broken within these imperfections, it is energetically favorable for the vortices to envelop these normal zones, which

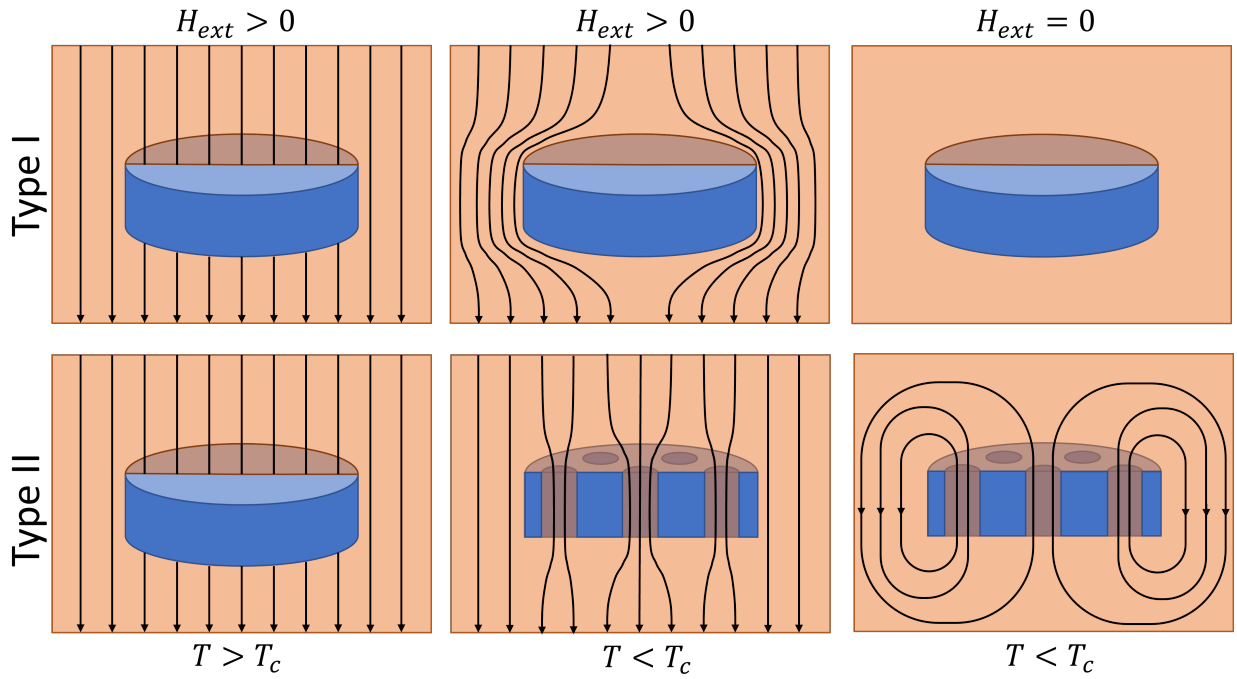


FIGURE 1.3: Behaviour of the two types of superconductors when submitted to field cooling. Type I shields the magnetic field in its interior; Type II maintains the internal field equal to the one it was exposed to during cooling.

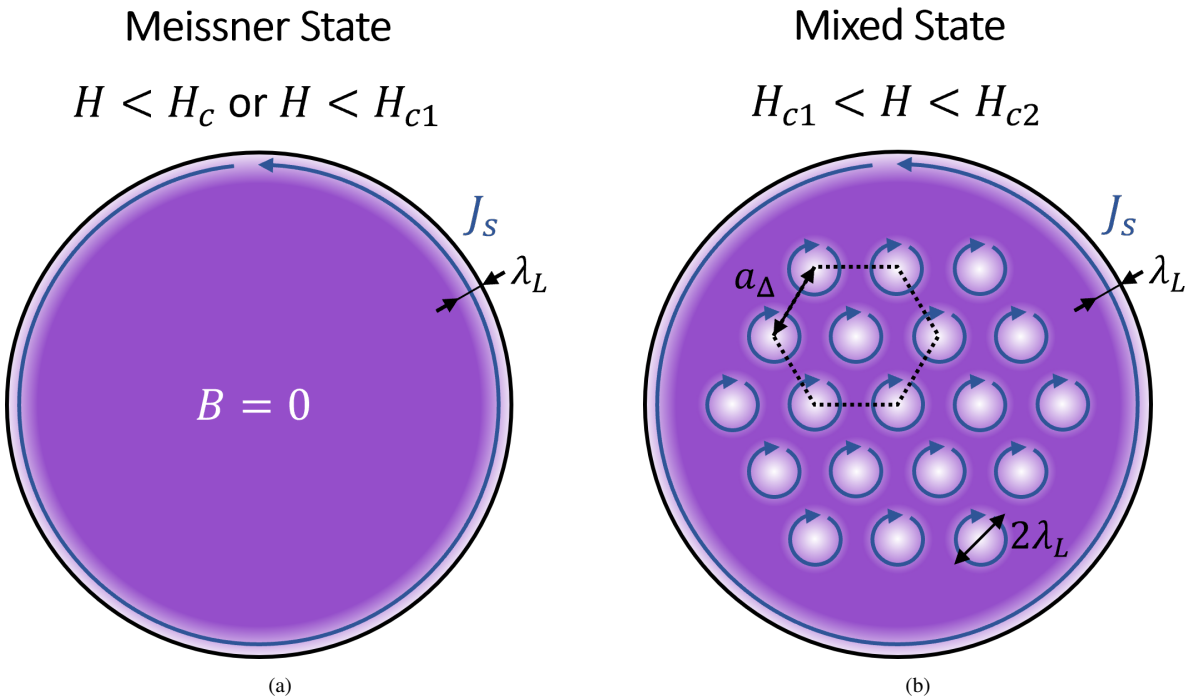


FIGURE 1.4: Magnetic field and current distribution inside a superconductor. (a) Meissner State: superconducting currents flow within λ_L from the edge, shielding the interior from the external magnetic field and minimizing interface; and (b) Mixed State: superconducting currrents also flow in the interior of the material, creating vortices, which arrange according to the Abrikosov vortex lattice.

then act as pinning centers to the vortices, holding them in place with the pinning force,

$$\boldsymbol{f}_p = \boldsymbol{J}_c \times \boldsymbol{B}\,, \tag{1.3}$$

where J_c is the critical current density. If the superconducting currents J_{sc} induced by external influences such as imposition of current or a varying external magnetic field are below J_c, the Lorentz force is smaller than the limiting pinning force, and the vortices are kept in place. On the contrary, if $J_{sc} > J_c$, then the resulting force is larger than zero and the vortices move, creating an electric field and causing energy dissipation inside the material. Therefore, although J_c is not a hard limit to superconductivity, it is associated with a dissipative scenario inside the superconducting state, which is often seen as a practical limit for most applications.

While the mixed state is limited by the two critical fields H_{c1} and H_{c2}, there is a stricter practical limit to be considered. The temperature-dependent irreversibility field or irrevesibility line $H_{irr}(T)$ sets the limit up to which the vortex lattice behaves as a solid [33]. Past this point, thermal energies are enough to melt the lattice, which in turn behaves as a liquid, which can no longer be pinned. The loose interaction between vortices allows for relative movement, causing the material to shift to a dissipative state.

To prevent the movement of vortices, controlled defects are artificially introduced to the material, shifting the irreversibility line and increasing the pinning force and, consequentially, the critical current density [34–36]. This allows for higher currents to flow without losses in the superconductor, increasing the range of applications for which these materials are suited.

1.2.3 REBCO Coated Conductors

Rare Earth-$Ba_2Cu_3O_{7-\delta}$ (REBCO) cuprates are ceramic materials belonging to the type II superconductor family. Among these, $YBa_2Cu_3O_{7-\delta}$ (YBCO) was the first HTS to be discovered with T_c above the boiling point of liquid nitrogen ($T_c > 77\,\mathrm{K}$) [37]. Their complex perovskite crystal structure, shown in Figure 1.5, revolves around a central rare earth atom with stacked layers of CuO_2, BaO and $CuO_{1-\delta}$ above and beneath it [38]. The oxygen content of $CuO_{1-\delta}$ layer, defined by the oxygen deficiency δ, affects the REBCO crystal structure and therefore its material properties [39]. For $0.65 < \delta \leq 1$, the oxygen atoms randomly occupy about half the vacancies in the $CuO_{1-\delta}$ layer, resulting in a tetragonal structure and presenting insulating behaviour. On the other hand, if $0 \leq \delta < 0.65$, the oxygen and copper atoms form chains along the b-axis, resulting in an orthorhombic structure, and enabling superconducting properties [40].

Even when exhibiting the orthorhombic structure, the material properties of REBCO are very sensitive to the oxygen deficiency in the $CuO_{1-\delta}$ planes, since it influences the density of holes in the oxygen sites of the CuO_2, which in turn act as carriers for electric current. Therefore, superconductivity emerges from the combined contributions from both the $CuO_{1-\delta}$ and CuO_2 layers. Furthermore, due to the high anisotropy of REBCO, its properties vary significantly when examined along the plane of the aforementioned layers, the ab-plane, or along the normal direction, the c-axis. For instance, the critical current density along the ab-plane is much larger than its counterpart along the c-axis.

Due to the heavily layered, anisotropic structure of REBCO, it is important not only to optimize its oxygen deficiency δ, but also to ensure a biaxially oriented epitaxial growth in order to maximize its superconducting properties. To achieve this biaxial alignment in the production of long conductors, two methods can be used: Ion-Beam-Assisted Deposition (IBAD) [41] and Rolling Assisted Biaxially Textured Substrate (RABiTS) [42]. The former consists on depositing an oxide layer, usually MgO, onto a polycristalline alloy such as stainless steel or Hastelloy®, while simultaneously inducing a biaxial texture with an ion beam. In the latter, a metallic substrate is rolled so that the desired

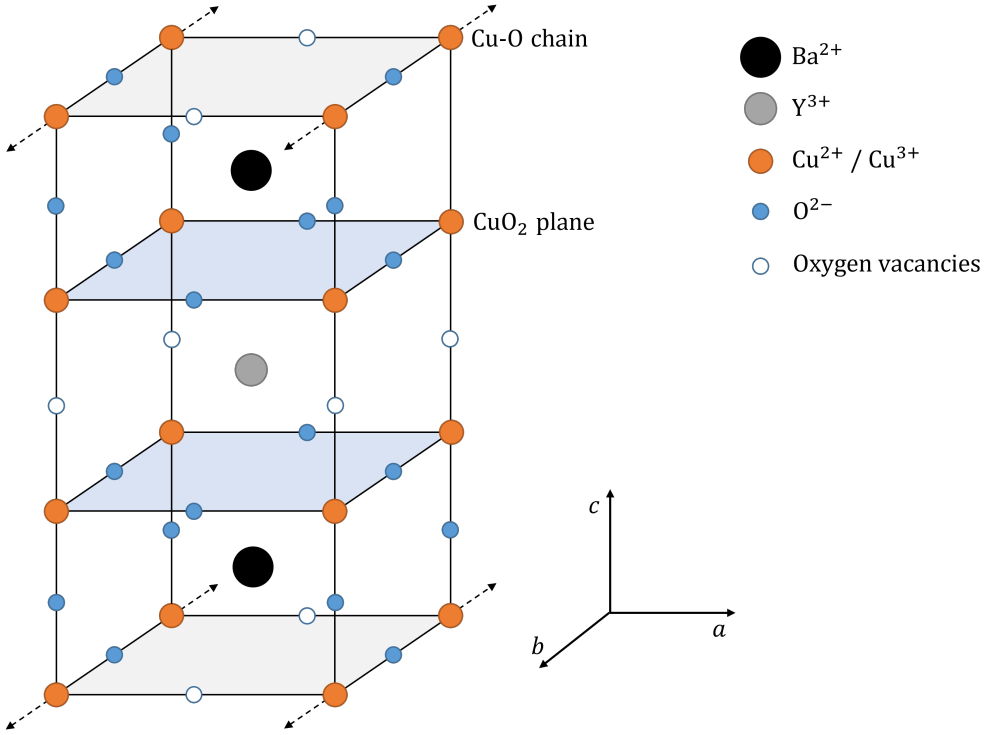


FIGURE 1.5: Crystal structure of Rare Earth-$Ba_2Cu_3O_{7-\delta}$ (REBCO) ceramic superconductors.

biaxial texture is induced directly onto it. In either method, the oxide buffer layers added onto the substrate are responsible to enhance the texture needed for the subsequent growth of REBCO and to avoid chemical cross-contamination between the REBCO layer and the substrate. Finally, the REBCO is grown on top of the buffer layers, which can be accomplished via several techniques, such as Pulsed Layered Deposition (PLD) [43], metal-organic Chemical Vapour Deposition (MOCVD) [44] and Chemical Solution Deposition (CSD) [45], among others. The resulting superconducting films are grown to thicknesses of one micron and beyond and are capable of transporting electric currents of up to hundreds of amperes with no losses.

As a consequence of the automated and reproducible application of these texturing and growth methods, commercially available REBCO films most commonly take the shape of multi-layered structures called second generation HTS tapes or Coated Conductors (CC). These tapes are highly homogeneous over lengths of hundreds of meters [46–48] and are made available by several providers, such as Fujikura Ltd., SuNAM Co. Ltd., Faraday Factory Japan LLC, SuperPower Inc. and THEVA Dünnschichttechnik GmbH, which are collaborators in this project, providing samples for electromagnetic and thermomechanical characterization.

Figure 1.6 shows the multi-layered structure of a coated conductor. Additionally to their purpose with respect to REBCO growth, the metallic substrate (50 to 100 μm) and the stack of oxide buffer layers ($\approx 0.2\,\mu$m) also provide mechanical robustness and chemical stability. Surrounding these layers, a silver ($\approx 2\,\mu$m) and copper ($\approx 20\,\mu$m) envelope protects the REBCO from humidity and other external influences, as well as serving as an electric shunt and thermal dissipator without hindering the electric and thermal contact of the superconducting film.

Althoguh the REBCO layer corresponds to only around 1% of the thickness of the coated conductor, CC's can still achieve very high critical current (I_c) values due to the high J_c of these materials:

$$I_c = \int_{S_{cs}} J_c \, dS, \tag{1.4}$$

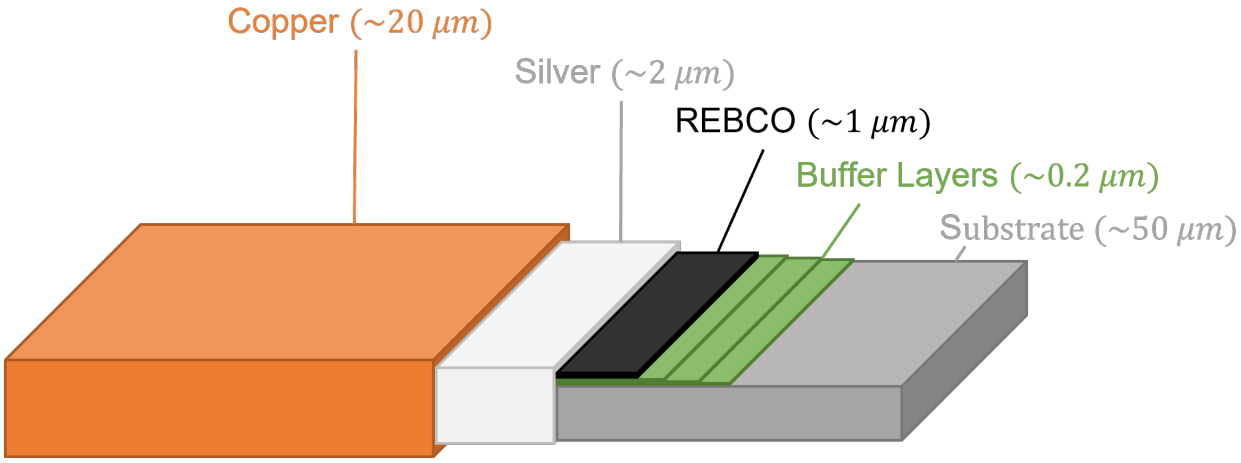


FIGURE 1.6: Multi-layered structure of the coated conductors. The 1 to 3 μm REBCO layer is grown on top of a thick metallic substrate covered by oxide buffer layers, and the whole structure is surrounded by an envelope of silver and copper. Figure adapted from [49]

where S_{cs} is the cross-section area of the REBCO layer. Even so, it is of great interest to increase the engineering critical current density

$$J_e = \frac{I_c}{S_{cc}}, \tag{1.5}$$

where S_{cc} is the cross-section area of the entire coated conductor, either by increasing the critical current density or the thickness of the REBCO film, or by decreasing the total thickness of the coated conductor, resulting in a more commercially attractive electric conductor for many applications.

Coated conductors were extensively characterized in magnetic field, temperature and RF frequency conditions similar to those defined for the FCC [12, 13, 49–55], showing surface resistance values much lower than copper even at high magnetic fields, and surface reactance of the same order of magnitude as copper's. Their high electromagnetic properties, large-scale availability and versatility sets coated conductors as promising candidates for several applications, especially for high field magnets and high energy physics. In this work, coated conductors are a fundamental piece of the hybrid coating solution for the field quality and surface impedance requirements of the FCC-hh's beam screen.

1.3 Objectives and Outline

Having set the context for the hybrid REBCO-Cu coating as a means to reduce the surface impedance of the FCC beam screen, the first goal of this work is to determine the best geometry for the coating that fulfills not only the field quality and surface impedance criteria, but also that is compatible with other requirements such as thermal and mechanical stability. This is done by the means of finite elements numerical analysis which consists of H-formulation of the electromagnetic equations applied to superconductors, coupled with thermal and mechanical physics. The simulation results explore a wide range of geometries and operating scenarios and are corroborated by experimental data that validate the model and the methods.

In addition, this work develops the techniques necessary to realize the attachment of the REBCO segments to the beam screen, as well as the striation process to produce the envisioned hybrid coating. In particular, the method of delamination to peel off the unnecessary layers and reveal the REBCO layer of the coating is discussed. This thesis is organized as follows:

- **Chapter** 2 summarizes the most relevant concepts of superconductivity, and especially how superconductors behave in DC and radiofrequency magnetic fields. Fundamental concepts of particle accelerators and magnetic field optics are also discussed.
- **Chapter** 3 encompasses the experimental methods used for soldering, delaminating and striating coated conductors onto flat and curved surfaces, in order to produce the hybrid REBCO-Cu Coating for the FCC beam screen, among other devices. In addition, the microscopy techniques employed to analyse the resulting coatings are discussed.
- **Chapter** 4 discusses the model and results of numerical simulations of the electromagnetic behaviour of the hybrid coating when submitted to the dipole field of the bending magnets. The numerical results are used to narrow the possible geometries of the coating with regards to field quality. Magnetization and surface resistance measurements of samples that comply with the field quality criterion imposed by CERN are used to validate the model and to show that both field quality and surface resistance criteria can be met simultaneously.
- **Chapter** 5 expands the electromagnetic simulations into other field configurations. The field harmonics produced by the hybrid coating in a quadrupole field are studied and the effects of having a misaligned beam screen are discussed.
- **Chapter** 6 extends the simulation results to consider thermal effects due to beam-induced resistive wall heating and syncrhotron radiation, as well as dipole field-induced joule heating. In addition, the mechanical stresses produced by Lorentz forces are analysed in order to verify if the coating can endure the conditions of the FCC during normal operation.
- **Chapter** 7 addresses the behaviour of the coated beam screen when the superconducting dipole magnets suffer a quench. The very high induced currents and consequent joule heat and Lorentz forces are discussed, evaluating the risk of thermal or mechanical damage to the coating.
- **Chapter** 8 brings to discussion possible consequences of tranverse current flow through the metallic structure of the beam screen. Analytic calculations and numerical analysis are performed in a simplified geometry to evaluate how this effect might impact the field quality in the vacuum chamber.
- **Chapter** 9 develops proof-of-concept devices of the beam screen coating employing the coating techniques described in Chapter 3. In addition, the results of applying our coating technique to other devices are analyzed.
- **Chapter** 10 summarizes the the main results and conclusion of this thesis.

Chapter 2

Theoretical Background

Superconductors are materials that can, under the appropriate conditions, conduct electric current without losses. Their emerging properties, such as low surface impedance under radio-frequency (RF) electromagnetic fields, raise them as promising candidates for a potential coating material for high-energy particle accelerators, in particular the hadron-hadron collider mode of the Future Circular Collider (FCC-hh).

In this chapter, we review the most relevant models for superconductivity, with a particular focus on the electromagnetic properties of superconductors under DC and AC fields. In addition, it is interesting to cover the basic operation of circular accelerators, especially regarding the steering of the particle beam by the external bending and focusing magnets, as well as the beam interaction with the surrounding environment.

2.1 Models for HTS

In this section, we discuss some of the models for HTS. These models describe the behaviour of these materials when under an external continuous magnetic field or applied electric field or current. For this work, we take special interest in how the resistivity of the material changes with the surrounding electromagnetic conditions.

2.1.1 The Bean Critical State Model

Introduced by C. P. Bean in 1962, the Bean Critical State Model gives a macroscopic explanation of the irreversible magnetization behavior of hard Type-II superconductors [56]. It is particularly useful for semi-analytic calculations or a quick assessment of the superconductor's response to external excitation.

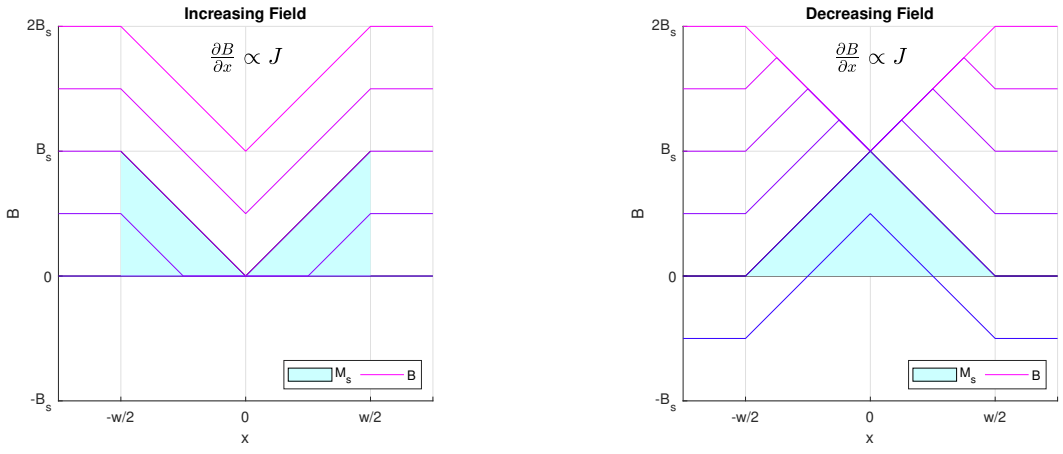
In type II superconductors, as the external magnetic field increases, vortices slowly penetrate the material, flowing from its edges. As more and more vortices penetrate, the lattice is pushed inward, up to the point when the whole material is filled. If the external field keeps increasing past this point, the vortex density will increase until superconductivity is broken.

From a macroscopic standpoint, the individual vortex contributions can be ignored so that we focus instead in the current density that results from the vortex gradient in the material. In this case, a current density will start flowing in the material in such a way as to generate a magnetic field that opposes the external field. As the external field increases, the current will penetrate the superconductor more and more, spreading inward from the edge until the center is reached or until the magnetization at the center equals the external field.

The Bean model states that the current density flowing through the material can only assume two distinct values: zero or J_c. This simplified assumption means that the magnetization of the superconductor changes linearly where

$J = J_c$, and is constant where $J = 0$. Since the magnetization is proportional to the vortex density, the latter shows the same behaviour.

If at some point the external field starts decreasing, a current density will flow in the opposite direction, once again spreading inward from the edge. This results in a magnetization profile that depends on the history of the external magnetic field, which accurately reflects the hysteretic behaviour of type II superconductors. Figure 2.1 summarizes the field response of a superconductor according to the Bean model.



(a) (b)

FIGURE 2.1: Field and magnetization of an infinite superconducting slab with width w according to the Bean model while (a) increasing and (b) decreasing external field. The slope of the B curve is proportional to J, which, in turn, is equal to zero or J_c. B_s corresponds to the maximum field that can be fully shielded by the supercurrents, with maximum magnetization M_s. Figure adapted from [57].

Since the current density can only take pre-defined values, the resistivity of the material can only be defined if the induced or applied electric field is also known. The resistivity would then be described by

$$\rho = \begin{cases} 0, & J = 0 \\ \frac{E}{J_c}, & J = J_c \end{cases}. \tag{2.1}$$

2.1.2 The Anderson-Kim Model

The Anderson-Kim Model was formulated to account for flux creep, the thermally activated motion of bundles of flux lines, aided by the Lorentz force $\boldsymbol{J} \times \boldsymbol{B}$, over free energy barriers coming from the pinning effects of inhomogeneities, strains, dislocations, or other physical defects. This effect, particularly important in HTS, results in energy dissipation inside the superconductor, and is described in the model by a non-linear relationship between current density and electric field [58, 59]. The so called Anderson-Kim's power law is given by

$$\frac{E}{E_c} = \left(\frac{J}{J_c}\right)^N, \tag{2.2}$$

where E_c is the critical electric field, which is a pre-defined value that corresponds to $J = J_c$ and is often defined in literature as $1 \times 10^{-4}\,\mathrm{V/m}$, and N is the transition index, which defines the steepness of the E-J curve. Figure 2.2 shows examples of the power law curve with J and E normalized with regards to J_c and E_c, respectively. From

equation 2.2, we can also deduce the resistivity of the superconductor according to the power law:

$$\rho_{pl} = \frac{E_c}{J_c}\left(\frac{J}{J_c}\right)^{N-1}. \tag{2.3}$$

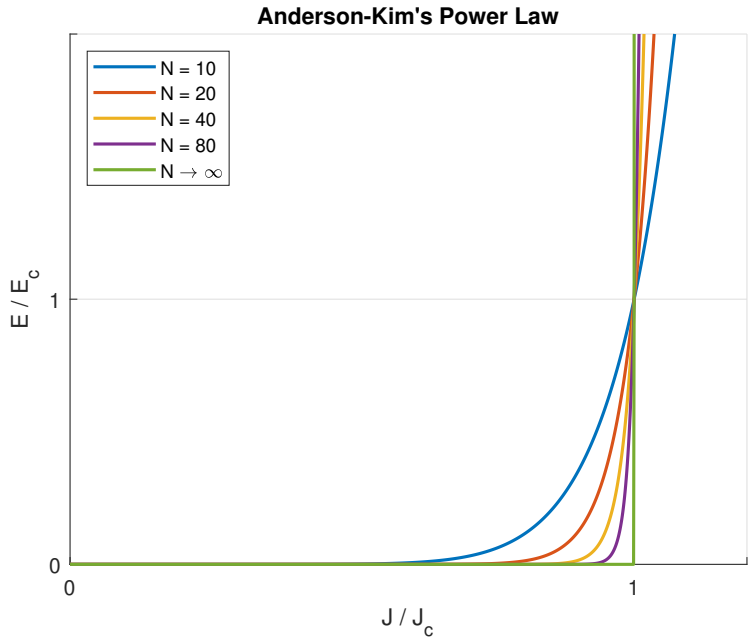


FIGURE 2.2: Anderson-Kim's Power Law for different N values. It describes the E-J relationship in superconductors, given by Equation 2.2.

Careful interpretation of the E-J curve can give us valuable information on how the superconductor works when the current density is under and around its critical value. It is interesting to note that the normalized electric field E/E_c relates to the normalized current density J/J_c through an exponent of power N, whose value depends on the material as well as the electromagnetic and thermomechanical conditions.

For the steep curves described by the power law, a few remarks can be pointed out depending on the current density range of operation. Firstly, for $J << J_c$, any current density will result in a very low electric field, causing virtually zero energy dissipation in the material. This agrees with the fact that the supercurrents should flow unhindered as long as the superconductor is operating within its critical boundaries and below H_{irr}. The higher the N value is, the closer can J get to J_c with no practical dissipation.

As the current density approaches J_c, the material starts resisting the current flow and energy dissipation in the form of Joule-like heating begins. At this point, very slight changes in the current density have a massive impact on the electric field, and therefore also in the collateral heating power. On the other hand, if a change on the electric field is triggered by any external influence, a minute adjustment of the current density will be enough to restore equilibrium.

It is interesting that, mathematically, when taking into account the power law, J_c is not a hard limit that separates superconducting and normal states. It is instead an arbitrary point around which a continuous, although abrupt, transition interval lies. The nonlinear relationship between E and J results in an interesting current behavior when the superconductor is exposed to an external magnetic field.

When it comes to real superconducting tapes, the values of J_c and N in the Anderson-Kim's power law are not constant, but rather change depending on other physical quantities. Most notably, both J_c and N depend on the temperature and the magnetic field applied to the superconductor, but can also be affected by mechanical strain and pressure.

As a rule, as the point of operation gets closer to the boundary of the superconducting region in the $B \times T$ plane, the smaller are both J_c and N. The reasoning behind the drop in the critical current density is quite clear, since the lower J_c results in a higher resistivity as the material approaches normal state. The drop in the transition index N, on the other hand, means that the E-J curve is now less steep, but the consequences of this are not as straightforward.

On the one hand, a smaller N means greater dissipation at $J < J_c$ when compared to higher N and same J_c. On the other, it results in lower dissipation for $J > J_c$. Of course only the combined effect of the change in both J_c and N should be taken into account and the overall consequence is that the resistivity ρ_{pl} increases with both B and T.

2.1.3 Further Considerations for REBCO HTS

For REBCO superconductors, it is important to recall that the magnetic field B has also an impact on the critical current density depending on its angle θ with regards to the surface of the superconductor, and not only its magnitude. Due to their high anisotropy, they are much more sensitive to the component of the field $B_\perp$ normal to the surface of the material than they are to the parallel component $B_\parallel$.

Although there is no consolidated theory that accounts for the field and temperature dependence of J_c, there are many formulations that can accurately describe this dependence within certain regions of the $B \times T$ plane. Among other formulae, the J_c as a function of the field can be fenomenologically represented by [59–61]

$$J_c(B) = J_c^{sf} \left(1 + \frac{B'}{B^*}\right)^{-\alpha} \left(1 - \frac{B'}{B_{irr}}\right)^2, \tag{2.4}$$

where, J_c^{sf} is the self field critical current density at a given temperature, B^* is a crossover point between regions in the $B \times T$ plane dominated by vortex-pinning and vortex-vortex interactions, and B_{irr} is the irreversibility field. This relationship will be useful in Chapter 4 for the modelling of the resistivity of the HTS in a ramping magnetic field. The assimetric dependence of J_c with the normal and parallel components of the field can be introduced by scaling the magnetic field according to [62]

$$B' = B\sqrt{(\cos\theta)^2 + \left(\frac{1}{\zeta}\sin\theta\right)^2}, \tag{2.5}$$

where ζ is the anisotropy of the material, which is usually between 5 and 7 for REBCO, and θ is the angle of the field with respect to the superconductor, with $\theta = 0$ for a purely normal field.

Changes in temperature can also have a drastic effect on J_c sharply decreasing it the as the material approaches the critical temperature T_c. Examples on how J_c is affected by both magnetic field and temperature can be seen in Figure 2.3.

Apart from its dependence with the temperature and magnetic field, the critical current density also varies depending on the direction along which it is evaluated. Due to the anisotropy of REBCO, the J_c on the c-axis (normal to the surface) can be orders of magnitude lower than on the ab-plane (parallel to the surface), leading to a preferential direction of current flow.

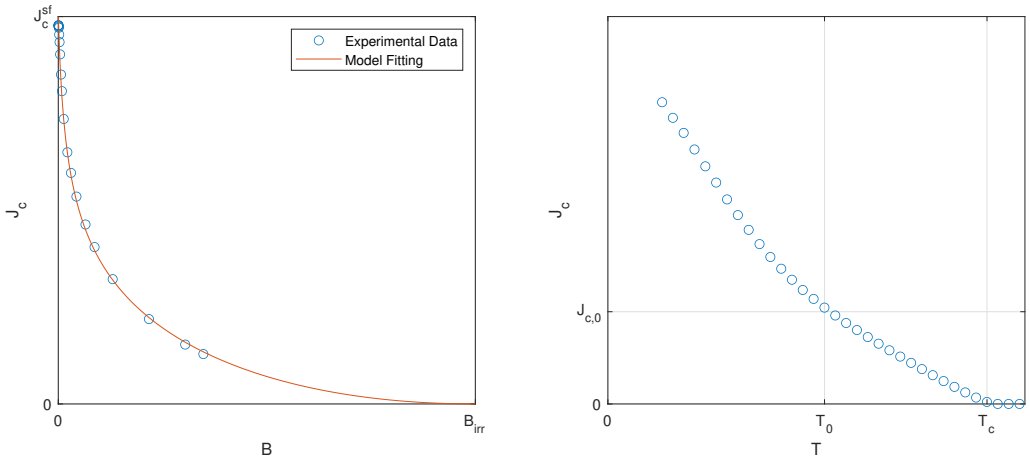


FIGURE 2.3: Examples of J_c dependence with magnetic field and temperature. The model used to fit the data of J_c as a function of the magnetic field is described by Equation 2.4. Data from [63].

Accounting for these relationships, as we get closer to the boundaries of the superconducting state, the resistivity will increase, both due to temperature and field. However, as the current density increases past J_c, the normal state resistivity of the material starts to play a role in determining its overall resistivity. For $J >> J_c$, the Anderson-Kim model is no longer appropriate, which makes the adoption of some form of overcritical model necessary.

2.1.4 Overcritical Adaptation of the Power Law

In situations when the current density far exceeds its critical value, be it due to transient electromagnetic effects, the rise of a hot spot or the simple imposition of a high current, models like the Anderson-Kim's power law by themselves may not be enough to accurately describe the resistive behaviour of the material. For this, an overcritical model should be used instead.

There are several such models that can be used to describe the resistivity of a superconductor when above J_c. Among these, the power law can be adapted to account for the gradual transition to the normal state resistivity, whether by introducing a dependence between the index N and J so that N slowly decreases as J increases, eventually reaching $N = 1$ when the normal state is reached [64]; or by simply making the total equivalent resistivity of the material equal to the power law resistivity in parallel with the normal state resistivity [65]:

$$\rho_{eq} = \rho_{pl} \parallel \rho_{ns} = \frac{\rho_{pl} \cdot \rho_{ns}}{\rho_{pl} + \rho_{ns}}, \tag{2.6}$$

where "$\parallel$" denotes being in parallel, ρ_{ns} is the normal state resistivity and the power law resistivity ρ_{pl} is derived from equation 2.2 and given by 2.3. Although not necessarily the most accurate representation of the superconductor behaviour [66], it is a simple way of accounting for the gradual transition between states. Figure 2.4 shows the resulting curve coming from this equivalent resistivity when compared to the resistivity values coming solely from the power law or the normal state. It is clear that the power law by itself would largely overestimate the equivalent resistivity past the intersection point of the two curves, far exceeding the normal state resistivity.

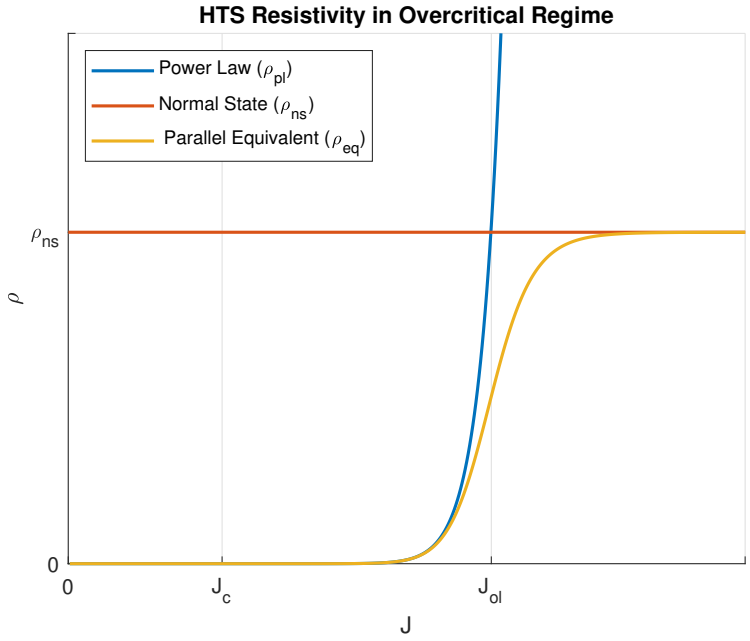


FIGURE 2.4: Comparison between HTS Resistivity curves in overcritical regime according to the Power Law and the equivalent parallel of the Power Law with normal state resistivity.

2.2 High Frequency Behaviour

As we have seen, superconductors can carry direct currents (DC) without losses, provided they are below J_c. On the other hand, they always show non-zero dissipation when carrying alternating currents (AC). This section introduces the concept of surface impedance by analysing the behaviour of superconductors and normal conductors exposed to high frequency electromagnetic fields [38, 49, 67, 68].

2.2.1 Surface Impedance

While the J_c is used as the benchmark to asses the quality of a superconductor under DC conditions, the surface impedance plays that role in the AC regime. Let us consider an oscillating electromagnetic field around the interface of vacuum and a highly conductive material with electric conductivity σ and magnetic permeability μ as sketched in Figure 2.5. The conductor extends infinitely through the $z > 0$ half-space and the electromagnetic field is given by

$$\boldsymbol{E} = E_x e^{i\omega t}\hat{\boldsymbol{x}} \tag{2.7}$$

$$\boldsymbol{H} = H_y e^{i\omega t}\hat{\boldsymbol{y}}\,. \tag{2.8}$$

The alternated fields induce currents at the surface of the material that take the form

$$\boldsymbol{J} = J_x e^{i\omega t}\hat{\boldsymbol{x}}\,, \tag{2.9}$$

which in turn contribute to the decay of both electric and magnetic fields over a small distance from the interface. Solving the Maxwell equations for these conditions results in the following current and field distribution inside the

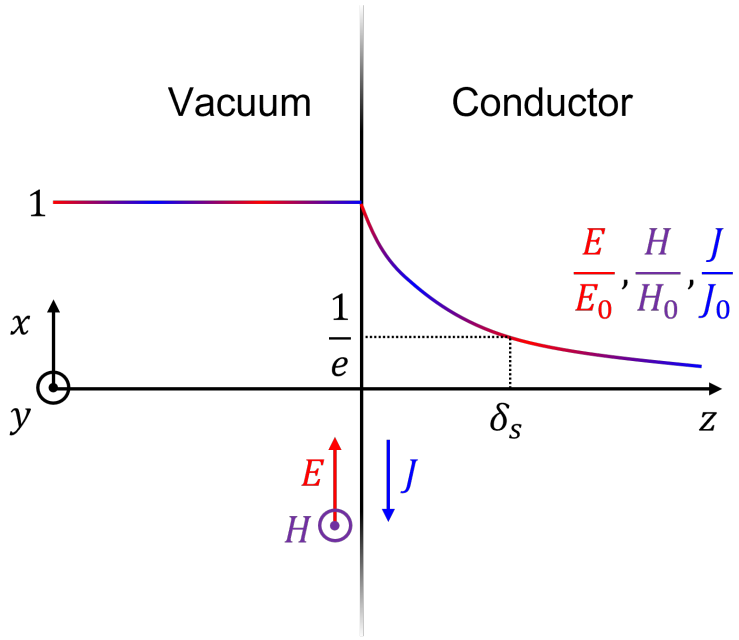


FIGURE 2.5: Electromagnetic field normal to the interface between conductive material and vacuum. Fields (E, H) and induced current (J) decay as they penetrate the material. The skin depth δ_s is defined where the magnitudes decay by e^{-1}. Figure adapted from [67].

material:

$$E_x = E_0 e^{-\gamma z} \tag{2.10}$$

$$J_x = J_0 e^{-\gamma z} \tag{2.11}$$

$$H_y = H_0 e^{-\gamma z}, \tag{2.12}$$

where the 0 indices refer to the magnitudes at the surface of the conductor ($z = 0$) and γ is the complex propagation constant

$$\gamma = \sqrt{i\omega\mu\sigma} = \alpha + i\beta, \qquad (\alpha, \beta) \in \mathbb{R}. \tag{2.13}$$

The purpose of splitting γ into its components α and β becomes clear if, for instance, Equations 2.13 and 2.10 are plugged into Equation 2.7 and rearranged:

$$\boldsymbol{E} = E_0 e^{-\gamma z} e^{i\omega t}\hat{\boldsymbol{x}} = E_0 e^{-(\alpha+i\beta)z} e^{i\omega t}\hat{\boldsymbol{x}} = E_0 e^{-\alpha z} e^{i(\omega t+\beta z)}\hat{\boldsymbol{x}}. \tag{2.14}$$

Here we can see that the magnitude of $\boldsymbol{E}$ (as well as $\boldsymbol{H}$ and $\boldsymbol{J}$) drops by a factor $e^{-\alpha z}$, depending on the distance from the surface of the conductor. On the other hand, the time-dependent behaviour is now $e^{i(\omega t+\beta)}$, which introduces a phase shift when compared to the electric field E_0 at the surface. The two constants are therefore appropriately named attenuation constant and phase constant, respectively. In addition, the skin depth $\delta_s = 1/\alpha$ is defined as the distance z over which the magnitude decreases by a factor e^{-1}.

The magnitudes in Equations 2.10 to 2.12 are related to each other via the conductivity and the complex propagation constant of the material:

$$J_0 = \sigma E_0 \tag{2.15}$$

$$H_0 = \frac{1}{\gamma} J_0 \,. \tag{2.16}$$

We can then use these to calculate the surface impedance of the material. The surface impedance is closely related to the power dissipation caused by the surface currents induced by the alternating electromagnetic field. It is defined as the ratio between the components of $\boldsymbol{E}$ and $\boldsymbol{H}$ parallel to the surface of the conductor, $E_{||}$ and $H_{||}$, which in this case are simply $E_0 e^{i\omega t}$ and $H_0 e^{i\omega t}$. By combining this with Equations 2.15 and 2.16, we have

$$Z_s = \frac{E_{||}}{H_{||}} = \frac{E_0 e^{i\omega t}}{H_0 e^{i\omega t}} = \frac{\gamma}{\sigma} = \sqrt{\frac{i\omega\mu}{\sigma}} = \sqrt{i\omega\mu\rho}\,, \tag{2.17}$$

with $\rho = 1/\sigma$ being the electric resistivity of the material. Much like the complex propagation constant, we can split Z_s into its real and imaginary components, the surface resistance and the surface reactance, respectively:

$$Z_s = R_s + iX_s \tag{2.18}$$

In normal conductors with real ρ and μ, by combining Equations 2.17 and 2.18, the surface resistance and reactance have the same value, given by

$$R_s^{nc} = X_s^{nc} = \sqrt{\frac{\mu\omega\rho}{2}}\,, \tag{2.19}$$

which leads to a frequency dependence scaling with $\sqrt{\omega}$.

Following the same steps in order to obtain the surface impedance for superconductors, we must know the resistivity of the material in the superconducting state and what its frequency dependence is. In this case, however, the resistivity is a complex value, which by itself also depends on the frequency. This results in distinct R_s^{sc} and X_s^{sc} for superconductors, with a frequency response other than $\sqrt{\omega}$.

The Two Fluid Model

One of the first models formulated with the goal of describing superconductivity, the Two Fluid Model proposes that a portion of the electrons within a superconductor behaves as they would in a normal conductor, obeying Ohm's law, while another portion is responsible for the superconducting nature of the material. The crucial aspect of this model is that the ratio between the two types of electrons varies with the temperature, going from entirely superconducting at absolute zero to presenting only normal electrons at T_c. Although this model is an oversimplification, it is the standard working approximation for understanding electric AC losses in superconductors, so that dissipation can be anticipated and minimized in applications such as microwave resonators.

Let us consider a superconductor under no external magnetic field. Mimicking the duality in the behavior of electrons, the current flowing through the material is also split into normal and supercurrents [69]. The normal currents (J_n) are the result of the movement of normal electrons, while supercurrents (J_s) arise from the flow of electron pairs connected by lattice vibrations, or phonons. Each current component depends on the density of each type of charge

carrier according to

$$J_n = n_n e v_n \tag{2.20}$$

$$J_{sc} = n_s e v_s \,, \tag{2.21}$$

where n_n and n_s are the carrier densities of normal electrons and electron pairs and v_n and v_s are their respective velocities.

The electron pairs move unhindered through the material, and therefore the only force acting upon them is the one produced by the electric field that pushes them forward. Their equation of motion is thus given by

$$m\frac{dv_s}{dt} = -eE \,, \tag{2.22}$$

where m refers to the mass of the electron. On the other hand, normal electrons are subject to a drag force due to the collision with atoms:

$$m\frac{dv_n}{dt} = -m\frac{v_n}{\tau} - eE \,, \tag{2.23}$$

where τ is the relaxation time arising from the loss of momentum due to said collisions. Substituting Equations 2.20 and 2.21 into Equations 2.22 and 2.23, and solving for sinusoidal currents and electric fields with frequency ω, we get the normal and superconducting conductivity:

$$\sigma_n = \frac{E}{J_n} = e\left(i\omega\frac{m}{n_n e} + \frac{m}{n_n e\tau}\right)^{-1} \tag{2.24}$$

$$\sigma_s = \frac{E}{J_{sc}} = -i\frac{e^2 n_s}{\omega m} \,. \tag{2.25}$$

The total conductivity from the two fluids model can be then found by adding both contributions:

$$\sigma_{2f} = \sigma_n + \sigma_s = \frac{n_n e^2\tau}{m(1+\omega^2\tau^2)} - i\left(\frac{n_s e^2}{m\omega} + \frac{n_n e^2\omega\tau^2}{m(1+\omega^2\tau^2}\right) = \sigma_1 - i\sigma_2 \,, \qquad (\sigma_1,\sigma_2)\in\mathbb{R},. \tag{2.26}$$

Having obtained the conductivity of the superconductor under zero magnetic field, we can calculate the surface impedance in the same conditions by substituting Equation 2.26 in Equation 2.17:

$$Z_s = R_s + iX_s = \sqrt{\frac{i\omega\mu_0}{\sigma_1 - i\sigma_2}} = \sqrt{\omega\mu_0\frac{i\sigma_1 - \sigma_2}{\sigma_1^2 - \sigma_2^2}} \,. \tag{2.27}$$

Assuming that the electrical loss in the superconductor is very small, we get $\sigma_2 >> \sigma_1$, and therefore Equation 2.27 can be simplified to

$$Z_s \approx \sqrt{\frac{\omega\mu_0}{\sigma_2}}\sqrt{i\frac{\sigma_1}{\sigma_2} - 1} \approx \sqrt{\frac{\omega\mu_0}{\sigma_2}}\left(i + \frac{\sigma_1}{2\sigma_2}\right) \,, \tag{2.28}$$

which, finally, results in

$$R_s = \sqrt{\frac{\omega\mu_0}{\sigma_2}}\frac{\sigma_1}{2\sigma_2} \tag{2.29}$$

$$X_s = \sqrt{\frac{\omega\mu_0}{\sigma_2}} \,. \tag{2.30}$$

Replacing Equation 2.26 into Equation 2.28, the frequency dependence becomes evident:

$$R_s = \frac{\omega^2 \mu_0^2 \sigma_1 \lambda_L^3}{2} \tag{2.31}$$

$$X_s = \omega \mu \lambda_L \,. \tag{2.32}$$

It is important to note, however, that in the presence of an external DC magnetic field, other contributions to the surface impedance will occur, changing its frequency dependence. It has been shown that the square dependence from Equation 2.31 weakens as the field increases due to vortex motion[70, 71].

2.2.2 AC Field Demagnetization

As discussed previously, practical applications of HTS require them to be below the irreversibility field B_{irr}, above which the vortex-pinning interaction can no longer restrain the motion of the vortices, resulting in a melting of the vortex lattice. However, the irreversibility field can be impacted by other factors such as the presence of an oscillating field, as is the case in RF applications [72–74].

Let us consider a superconducting tape centered at $(\hat{\boldsymbol{x}},\hat{\boldsymbol{y}},\hat{\boldsymbol{z}}) = (0,0,0)$ oriented in such a way that its length extends towards infinity in the $\hat{\boldsymbol{z}}$ axis, with width w in the $\hat{\boldsymbol{x}}$ direction and thickness d in the $\hat{\boldsymbol{y}}$ direction. A normal continuous magnetic field $\boldsymbol{H}_{dc} = H_y\hat{\boldsymbol{y}}$ parallel to the c-axis is applied after field cooling, which induces a current flow in the superconductor in order to partially shield its interior. Using the Bean's model and following the right-hand rule, the current density J will be $-J_c$ for $x < 0$ and J_c for $x > 0$. For a fully saturating field $B_y = \mu_0 H_y >> B_s$ (see Figure 2.1), the HTS will be permeated by vortices.

Suppose then a perpendicular field $\boldsymbol{H}_{ac} = H_x \cos(\omega t)\hat{\boldsymbol{x}}$ oscillating at high frequency is introduced, as shown in Figure 2.6. As they oscillate, the vortices present in the HTS will bend, aligning themselves with the instantaneous magnetic field inside the HTS:

$$\frac{\partial x}{\partial y} = \frac{B_x}{B_y}\,, \tag{2.33}$$

where x and y refer to the position of a given vortex and B_x is the resulting x component of the field inside the tape. If we consider a vertical strip of the tape at a given x and apply the Ampere's law along the x direction,

$$\frac{\partial B_x}{\partial y} = \mu_0 J\,, \tag{2.34}$$

and combine with Equation 2.33 , we get

$$\frac{\partial^2 x}{\partial y^2} = \frac{\mu_0 J}{B_y}\,, \tag{2.35}$$

which defines the shape of the bent vortex by the quadratic relationship $x = ay^2 + by + c$, where the sign of $a = \pm\mu_0 J_c/(2B_y)$ depends on the direction of the current flow. Therefore, at least two quadratic equations with different coefficients are needed to described the shape of the vortex, one where $J = J_c$ and one where $J = -J_c$. At every half cycle, there is only one point where the current changes direction, meaning only two equations are needed.

Before finding the coefficients of these equations, we need to find the point around which the bending happens. To do this, we now consider the sheet current density flowing through the vertical strip of the tape

$$J_s = \int_{-d/2}^{d/2} J(y)dy = J_{s,dc}\,, \tag{2.36}$$

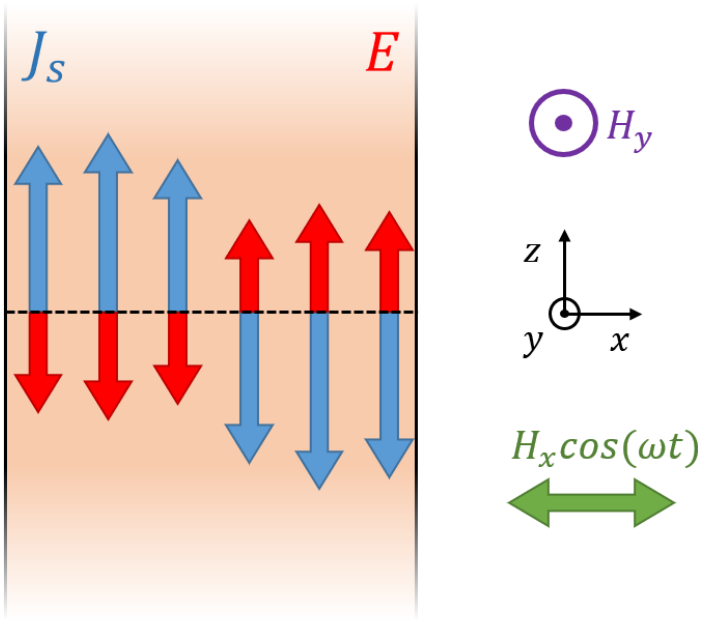


FIGURE 2.6: Demagnetizing effect of a perpendicular oscillating field on a HTS tape under a DC field parallel to the c-axis. Electric fields opposing current flow are induced when a perpendicular AC field is applied. Figure adapted from [74].

where $J_{s,dc}$ is the contribution to the current coming from $\boldsymbol{H}_{dc}$. There is no contribution from the AC counterpart, since whatever current change induced by the oscillating field will have a zero average along the thickness. At every half cycle, the current will be given by

$$J(y) = \begin{cases} \pm J_c, & -\frac{d}{2} < y < y_0 \\ \mp J_c, & y_0 < y < \frac{d}{2} \end{cases}, \tag{2.37}$$

with the sign of J swapping every half cycle. The height y_0 corresponds to the point where the current changes direction. However, since the magnetization of the tape happens from the outside inward, y_0 does not change for an entire half cycle. Therefore, it also corresponds to the swivel height around which the bending of the vortices happen.

Knowing the current density distribution along the strip and the sheet current density of the strip, we can easily find y_0 with

$$J_s = \pm \int_{-d/2}^{y_0(t)} J_c dy \mp \int_{y_0(t)}^{d/2} J_c dy = \pm 2 J_c y_0 = J_{s,dc}\,, \tag{2.38}$$

which results in

$$y_0 = \pm \frac{J_{s,dc}}{2J_c}\,. \tag{2.39}$$

Note that since the sign of y_0 changes every half cycle, the vortices have an average speed $v_{avg} \neq 0$, as seen in Figure 2.7 and therefore move from both edges towards the center of the tape, contributing to its demagnetization.

We can now determine the coefficients of the two quadratic equations $x(y \geq y_0) = ay^2 + b_1 y + c_1$ and $x(y \leq y_0) = -ay^2 + b_2 y + c_2$ by setting some boundary conditions, in addition to Equation 2.35. Firstly, the angle of the vortex at both surfaces ($y = \pm d/2$) is the same as the angle of the superimposition of the DC field, the AC field and the field

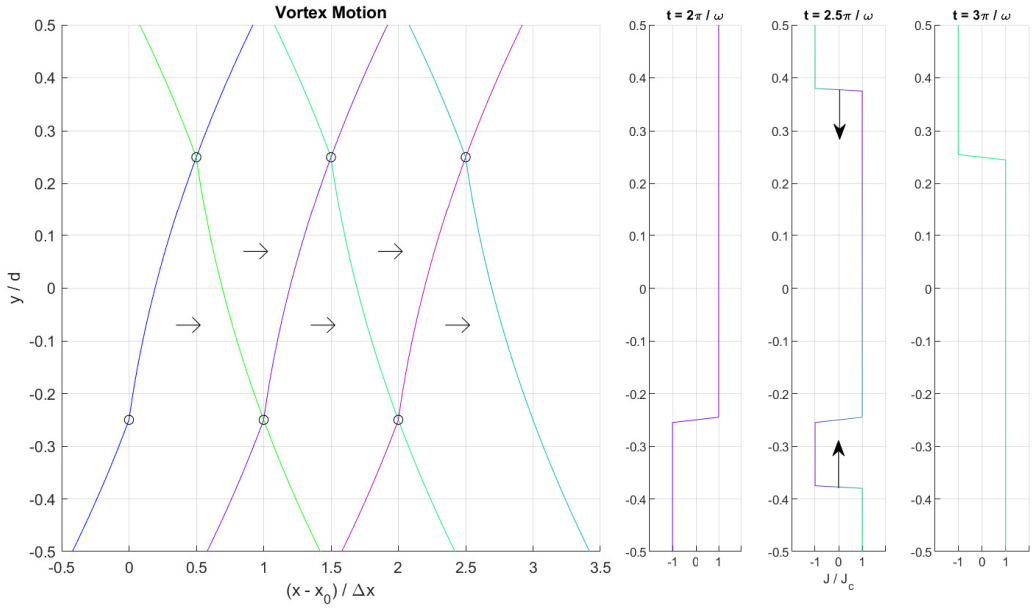


FIGURE 2.7: Demagnetizing effect of a perpendicular oscillating field on a HTS tape under a DC field parallel to the c-axis. On the left, position and shape of a vortex at every half cycle (lines) and swivel points (circles). On the right, current distribution along a vertical strip at every quarter cycle. Figure adapted from [74].

produced by the current in the superconductor $H_I = |J_s|/2$:

$$\left[\frac{\partial x}{\partial y}\right]_{\pm d/2} = \frac{H_x + H_I}{H_y}\,. \tag{2.40}$$

Secondly, the swivel point y_0 sets the limit between the two equations, and therefore both of them should be able to describe this point in particular:

$$[x(y \geq y_0)]_{y_0} = [x(y \leq y_0)]_{y_0}\,. \tag{2.41}$$

By applying these conditions we get

$$b = b_1 = b_2 = \frac{H_x - H_p}{H_y} \tag{2.42}$$

$$c_2 - c_1 = 2ay_0^2\,, \tag{2.43}$$

where $H_p = (dJ_c - |J_s|)/2$ is the parallel field necessary to saturate the tape. Note that b is the same for both equations while only the difference $c_2 - c_1$ can be determined. In fact, c_1 can be arbitrarily chosen depending on the initial position of the vortex.

Now that the shape of the vortex is known, as well as the swivel point around which it bends during a half cycle, we can use this to calculate the displacement Δx of the vortex during a single cycle. At any even half cycle, the vortex behaves in the same manner as in the previous off half cycle, but inverted in the $\hat{y}$ direction and displaced by $\Delta x/2$. In addition, subsequent cycles share the same swivel point. Therefore,

$$ay_0^2 + by_0 + c = a(-y_0)^2 + b(-y_0) + c + \frac{\Delta x}{2} \tag{2.44}$$

$$\Delta x = 4by_0\,. \tag{2.45}$$

Since any motion happens only if $Hx > H_p$, we can finally define the displacement in a cycle by

$$\Delta x = \begin{cases} 2\frac{J_s}{J_c}\frac{H_x - H_p}{H_y} & H_x > H_p \\ 0 & H_x \leq H_p \end{cases}. \tag{2.46}$$

This results in an average speed $v = \Delta x\omega/(2\pi)$ towards the center of the tape. It is interesting to note how the resulting vortex dislocation is dependent on both J_s/J_c and H_x/H_y. In fact, while the first one defines the swivel height y_0, the second one sets the bending angle of the vortex (Equation 2.33). It is clear that a sample with no magnetization in the first place ($J_s(x) = 0$) cannot be demagnetized in this manner, and the same applies for an external field with no AC component.

This vortex motion through the HTS generates an electric field perpendicular to its movement

$$\boldsymbol{E}_v = \boldsymbol{v} \times \boldsymbol{B}_y = \pm\frac{\omega}{2\pi}\Delta x B_y \hat{\boldsymbol{z}} \tag{2.47}$$

in the opposite direction with respect to the DC current flow. It is remarkable that an AC excitation of magnetic field generates a DC electric field in addition to the electric field that was already present at the superconductor due to DC field. From an energy stand point, this additional electric field represents the dissipation due to the vortex motion, and the demagnetization can be understood by a decay in the current due to the emergence of this higher resistivity or by the inward flow of vortices.

2.3 A Review of Particle Accelerators

Particle accelerators set the conditions for the study of particle interaction by colliding particles against each other in speeds close to the speed of light $c \approx 3 \times 10^8\,\mathrm{m/s}$. While the rigorous description of particle dynamics inside an accelerator is a complex topic on its own, the goal of this section is to review the basic operation of particles accelerators with regards to the electromagnetic interaction between the particle beam and its surroundings, as well as the electromagnetic field needed for its acceleration.

2.3.1 Particle Accelerator Optics

In circular colliders, as is the case of the Large Hadron Collider (LHC) and the Future Circular Collider (FCC), the particle beam is organized in bunches of particles that move closely together along a circular orbit contained within the vacuum chamber of the accelerator. Although its cross-section is not a perfect circle, the vacuum chamber can be approximated by a toroid with inner radius $R_m - r_{cs}$ and outer radius $R_m + r_{cs}$, where R_m and r_{cs} are the average radius of the machine and of its cross-section, respectively. For the mathematical developments presented in this section [75, 76], it is useful to consider a few different coordinate systems: a cylindrical system $(\hat{\boldsymbol{R}}, \hat{\boldsymbol{\psi}}, \hat{\boldsymbol{y}})$, concentric with the machine; and a local coordinate system in both rectangular $(\hat{\boldsymbol{x}}, \hat{\boldsymbol{y}}, \hat{\boldsymbol{z}})$ and cylindrical $(\hat{\mathbf{r}}, \hat{\boldsymbol{\phi}}, \hat{\boldsymbol{z}})$ forms concentric with the cross-section of the vacuum chamber (see Figure 2.8).

For a given particle of charge q, mass m and velocity $\boldsymbol{v}$, the resulting force from the interaction between it and an external electromagnetic field $(\boldsymbol{B}, \boldsymbol{E})$ is given by

$$\boldsymbol{F} = q(\boldsymbol{E} + \boldsymbol{v} \times \boldsymbol{B})\,. \tag{2.48}$$

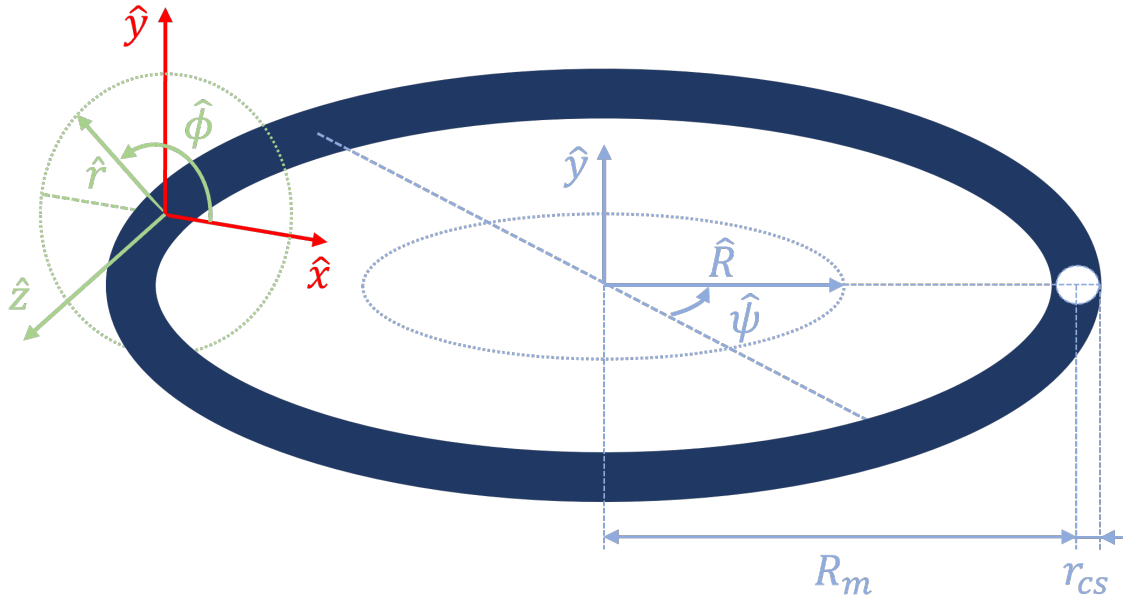


FIGURE 2.8: Global and local coordinate systems used throughout this work. A cylindrical coordinate system $(\hat{\boldsymbol{R}},\hat{\psi},\hat{\boldsymbol{y}})$ is concentric with the machine while the local system in rectangular $(\hat{\boldsymbol{x}},\hat{\boldsymbol{y}},\hat{\boldsymbol{z}})$ and cylindrical $(\hat{\mathbf{r}},\hat{\phi},\hat{z})$ forms is concentric with the vacuum chamber cross section.

The first term is parallel to the electric field $\boldsymbol{E}$, while the second is always perpendicular to both $\boldsymbol{B}$ and $\boldsymbol{v}$. This tells us that in order to accelerate a particle in the same direction of its velocity, a purely parallel electric field can be used, resulting in an acceleration $a_{\parallel} = \frac{q}{m}E$. On the other hand, if the goal is to accelerate the particle perpendicularly to its velocity, magnetic fields should be used instead.

Let us consider an ideal dipole magnetic field in the $-\hat{\boldsymbol{y}}$ direction interacting with a positively charged particle moving towards the positive $\hat{\psi}$. This results in a circular motion where $\boldsymbol{F}$ acts as the centripetal force:

$$F_{\perp} = qvB = \frac{m}{R}v^2 \,. \tag{2.49}$$

Rearranging, we can obtain the bending strength of the dipole magnet

$$\frac{1}{R} = \frac{Bq}{mv} \,. \tag{2.50}$$

It is easy to see that as the velocity of the particles increases, so too must the dipole field to steer them. Therefore, while the particles are being accelerated, the dipole field increases along with their speed in order to keep them confined to the circular trajectory corresponding to the radius of the accelerator. In reality, the accelerator is composed of straight and curved sections, and the dipole magnets are only present in the curved parts, responsible to bend the particle trajectory. Figures 2.9a and 2.9d show the magnetic field and force distribution of the an ideal dipole magnet.

Along with the dipole magnets, there are other magnetic arrangements which are necessary to control the dynamic behaviour of the particle bunches. Among these, the quadrupole field has the purpose of ensuring that the particles do not deviate from their nominal trajectory. For convenience, let us consider the complex coordinate $z = x + iy = re^{i\phi}$ that corresponds to the location of a given particle with regards to the local rectangular coordinate system. In this case,

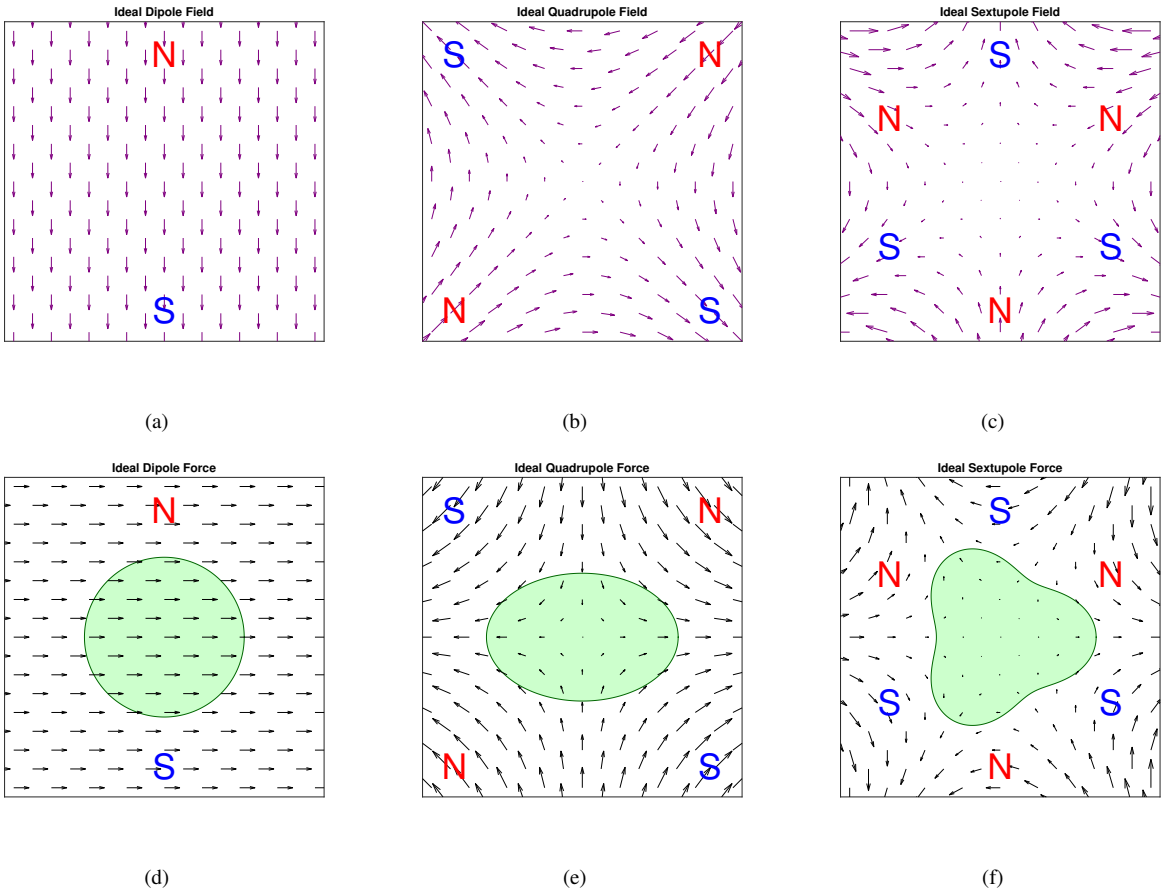


FIGURE 2.9: Magnetic field and force distribution in an ideal dipole (a and d), quadrupole (b and e) and sextupole (c and f) magnets for a positively charged particle bunch contained within the marked area and moving towards the reader. The dipole accelerates the bunches perpendicularly to their velocity and the quadrupole tends to shrink and stretch them in different perpendicular directions, while the sextupole has a coupled effect in both directions.

an ideal $2k$-pole field centered around the origin can be represented as

$$\tilde{B}_k = B_0 \left(\frac{r}{r_0} e^{i\phi} \right)^{k-1} = B_{ref} \left(\frac{r}{r_0} \right)^{k-1} (\cos((k-1)\phi) + i\sin((k-1)\phi)), \tag{2.51}$$

where the real and imaginary parts correspond to the $\hat{\boldsymbol{y}}$ and $\hat{\boldsymbol{x}}$ components, respectively, r_0 is a reference radius and $\tilde{B}_0$ is the field magnitude at r_0. While the dipole field ($k = 1$) is constant and unidirectional with $B_1 = B_0$ everywhere, the quadrupole field ($k = 2$) changes both in angle and intensity depending on its location, taking the form

$$\tilde{B}_2 = B_0 \frac{r}{r_0} e^{i\phi} = g r e^{i\phi} = g r(\cos\phi + i\sin\phi). \tag{2.52}$$

Here, $g = \frac{\partial B}{\partial r} = \frac{B_0}{r_0}$ is the quadrupole field gradient, which is constant and dictates the field optics, acurately named due to the quadrupole field acting as a lens to focus the particle beam. It is interesting to note that, if the particles bunches are moving in the $\hat{\boldsymbol{z}}$ direction, the horizontal and vertical components of the forces generated by this magnetic

configuration are decoupled:

$$F_x = m\ddot{x} = \pm qvgx \tag{2.53}$$

$$F_y = m\ddot{y} = \mp qvgy\,, \tag{2.54}$$

assuming that the changes in direction due to the magnetic force are negligible since $v_z >> v_\perp$. Depending on its polarity and the charge and velocity of the particles, a quadrupole magnet tends to focus and defocus the bunches in the $\hat{x}$ and $\hat{y}$ directions, as shown in Figures 2.9b and 2.9e and according to equations 2.53 and 2.54. Since the force is proportional to the distance, this effect is more intense on particles that deviate more from the center, and the larger the gradient, the stronger is the lensing effect.

The focusing strength k_f of the magnet is given by

$$k_f = \pm\frac{qg}{p} \approx \pm\frac{qg}{mv}\,. \tag{2.55}$$

For a positive k_f, the quadrupole is vertically focusing and horizontally defocusing, and for a negative k_f, the opposite occurs. The sign of equation 2.55 depends on the polarity of the magnet. It is worthwhile to point out that these equations assume a normal quadrupole, that is, with the poles in angles $\phi = pi/4 + n\pi/2$, $n = 1, 2, 3, 4$. If the quadrupole is tilted with respect to this configuration, the horizontal and vertical equations of motions will be coupled.

Since a single quadrupole would concentrate the particles in one direction but disperse them in the other, a combination of alternated focusing and defocusing quadrupoles, the FODO cell, is often used to contain the particle beam within a given $r < r_{lim}$ from its ideal orbit. In this case, the overall tendency of the quadrupole doublet will result in a focusing effect, regardless of the order of the magnets, as sketched in Figure 2.10.

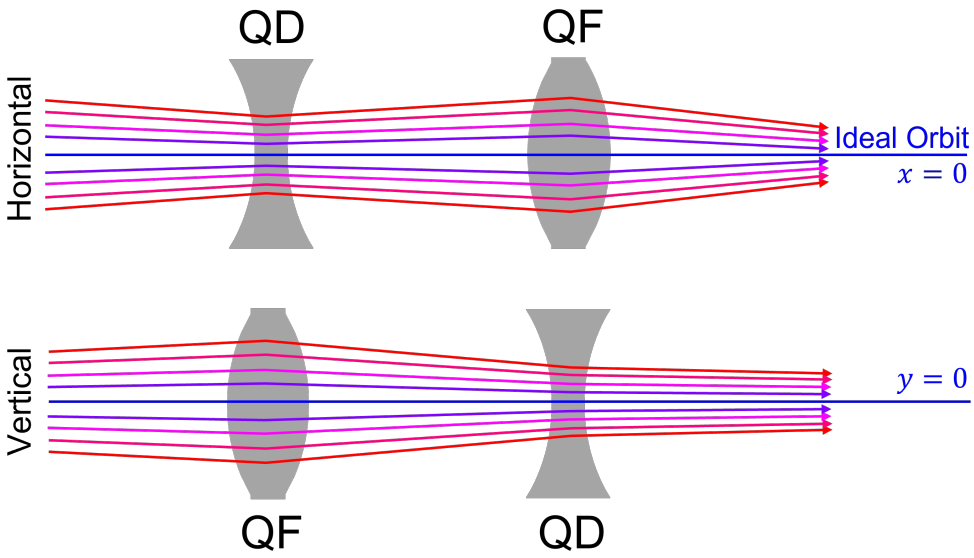


FIGURE 2.10: Magnet system composed of focusing (QF) and defocusing (QD) quadrupoles. Although the individual effect of each magnet is to focus the beam in one direction and defocus in the other, their combined effect is to focus in both.

Now let us consider particles within the bunch that travel at the nominal angular velocity, but with a radius slightly mismatching the ideal orbit. These particles will exhibit a shift in their linear velocity $v = \omega R$ with respect to the ideal orbit, resulting in a focusing strength k_f also deviated from its ideal value. To counteract this effect, a third magnetic

configuration can be used: the sextupole. From equation 2.51, we have the sextupole field

$$\tilde{B}_3 = B_0 \left(\frac{r}{r_0} e^{i\phi} \right)^2 = B_0 \left(\frac{r}{r_0} \right)^2 (\cos(2\phi) + i\sin(2\phi)) . \tag{2.56}$$

The resulting equation of motion in the horizontal plane ($y = 0$) would then be

$$F_x = m\ddot{x} = \frac{1}{2} qvg' x^2 , \tag{2.57}$$

where $g' = \frac{\partial^2 B}{\partial r^2} = \frac{B_0}{r_0^2}$. Note, by comparing with equation 2.53, that this is analogous to a quadrupole with focusing strength proportional to x, but whose sign is independent of x. Consequently, displaced particles will be accelerated towards the same direction whether they are within or without the ideal orbit, but this effect will be more pronounced the further they are from it.

Much like the quadrupoles, the sextupoles should also be used in pairs of focusing and defocusing magnets, which result in a generally focusing system. In a FODO cell, each sextupole is placed next to its quadrupole equivalent. It must be pointed out, however, that, unlike the case of quadrupole magnets, the use of sextupoles introduces coupling between the veritcal and horizontal motions, an issue that can be minimized by utilizing several weaker magnets spread along the machine circumference instead of a smaller number of stronger ones.

In reality, the magnetic field produced by a magnet will never be a perfect $2k$-pole field, but will instead be composed of the nominal field, given by equation 2.51, plus a field error:

$$\tilde{B}_{magnet} = \tilde{B}_k + \Delta\tilde{B} . \tag{2.58}$$

Thanks to the Gauss's law for magnetism, $\nabla \cdot \boldsymbol{B} = 0$, any field $\tilde{B}$ can in turn be decomposed into a sum of virtual contributions with a distinct number of poles, the field harmonics:

$$\Delta\tilde{B} = \Delta B_y + i\Delta B_x = \sum_{n=1}^{\infty} \tilde{c}_n \Delta\tilde{B}_n , \qquad \tilde{c}_k = b_k + ia_k \tag{2.59}$$

or, in cylindrical coordinates,

$$\Delta B_r = \sum_{k=1}^{\infty} b_k \sin(k\phi) + a_k \cos(k\phi) \tag{2.60}$$

$$\Delta B_\phi = \sum_{k=1}^{\infty} b_k \cos(k\phi) - a_k \sin(k\phi) . \tag{2.61}$$

The normal and skew coefficients b_k and a_k can be calculated similarly to a Fourier series expansion, but with respect to space instead of time. For this, it is convenient to define the coefficients in terms of the radial component of the field B_r:

$$a_n = \frac{1}{\pi B_0} \int_0^{2\pi} \Delta B_r(\phi) \cos(k\phi) d\phi \tag{2.62}$$

$$b_n = \frac{1}{\pi B_0} \int_0^{2\pi} \Delta B_r(\phi) \sin(k\phi) d\phi . \tag{2.63}$$

It is clear that if the field harmonics are relatively high with respect to the nominal field, there will occur unwanted

effects in the optics of the accelerator, possibly resulting in the introduction of instabilities to the particle orbit. In order to avoid this, maximum coefficients of a few units in 10^{-4} are desired, as is the case for the Future Circular Collider [9, 77, 78].

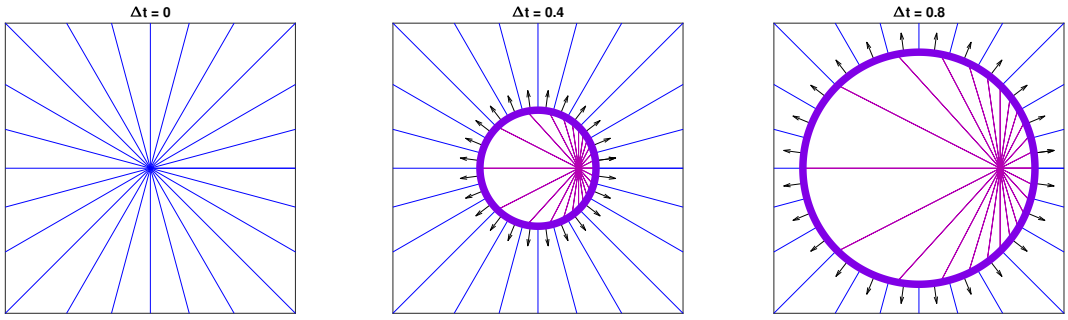
2.3.2 Beam Interactions

While the magnets focus and steer the beam, we also need to ensure that the beam does not scatter due to unwanted collisions. To do this, the beam is stored inside a vacuum chamber, which keeps it at pressures of the order of 10^{-9}mbar, reducing the amount of gas molecules present around the beam orbit. The vacuum chamber is located inside the cold bore of the magnets, and is subjected to their magnetic fields. However, as the beam travels around the accelerator, there are other means by which it can interact with the surrounding structure. Synchrotron radiation, electron cloud build up, gas desorption, and wake fields and image currents can both damage nearby equipment as well as destabilize the beam orbit, and the vacuum chamber and cooling systems must be designed to account for these unwanted side effects.

Synchrotron Radiation

Stationary charged particles generate static electric field lines that extends radially from the particle position s_0. If the particle is then accelerated with respect to the same inertial reference frame, the field lines will now extend from the new particle position s_1. Furthermore, if the new particle velocity $v = \beta c$ is close to the speed of light c, the field lines will contract in the direction of motion due to relativistic effects.

However, since any information travels at the speed of light, the field lines will only assume the new, post-acceleration shape after a time delay $\Delta t = \frac{r_a}{c}$, where r_a is the distance from the position of acceleration. This results in the propagation of an electromagnetic perturbation, as seen in Figure 2.11, which can be interpreted as the emanation of photons in the form of radiation. For non-relativistic scenarios, this is called cyclotron radiation, which does not involve the contraction of the field lines. In relativistic scenarios, such as the case in particle accelerators, it is called synchrotron radiation [50, 79].



(a) (b) (c)

FIGURE 2.11: Propagation of synchrotron radiation from an accelerated charged particle. The electric field lines are changed after a time delay of (a) $\Delta t = 0$, (b) $\Delta t = 0.4$ and (c) $\Delta t = 0.8$ emanating radially from the acceleration point at the speed of light c. Figure adapted from [50].

We can use the Liénard Formula to calculate the power of the radiation:

$$P = \frac{2Kq^2}{3c}\gamma^6 \left| \dot{\beta}^2 - \left(\beta \times \dot{\beta}\right)^2 \right|, \tag{2.64}$$

where $K = (4\pi\varepsilon_0)^{-1}$ is Coulomb's constant, $\gamma = (1-\beta^2)^{-0.5}$ is the universal Lorentz factor and $\dot{\beta} = \frac{a}{c}$ is the derivative of β with respect to time. In the specific cases of linear ($\beta \times \dot{\beta} = 0$) and circular ($|\beta \times \dot{\beta}| = \beta\dot{\beta}$) motion, this is reduced to

$$P_{linear} = \frac{2Kq^2}{3c}\gamma^6\dot{\beta}^2 \tag{2.65}$$

$$P_{circular} = \frac{2Kq^2}{3c}\gamma^4\dot{\beta}^2\,. \tag{2.66}$$

In both cases, the forces exerted on the particle are given by the time derivative of the relativistic momentum $p = mc\gamma\beta$. With some mathematical manipulation, these can be written as

$$F_{linear} = mc\gamma^3\dot{\beta} \tag{2.67}$$

$$F_{circular} = mc\gamma\dot{\beta}\,. \tag{2.68}$$

The discrepancy between the two forces arises from the different directions of the acceleration with respect to the velocity. In the circular motion case, γ is constant, which is not true for linear accelerated motion. This changes the expressions by a factor γ^2 between each other when calculating $\frac{dp}{dt}$.

Substituting Equations 2.67 and 2.68 into Equations 2.65 and 2.66, we find the power as a function of the applied force in both cases:

$$P_{linear} = \frac{2Kq^2}{3m^2c^3}F_{linear}^2 \tag{2.69}$$

$$P_{circular} = \frac{2Kq^2}{3m^2c^3}\gamma^2F_{circular}^2\,. \tag{2.70}$$

Therefore, for a given force $F = F_{linear} = F_{circular}$, the power emitted in the form of synchrotron radiation will be higher by a factor γ^2 in the case of perpendicular acceleration. This means that as β gets closer to one, the power produced in linear acceleration will be negligible when compared to its circular counterpart. In practice, the main contribution to synchrotron radiation in circular accelerators comes from bending and focusing magnets, which use magnetic field to accelerate particles perpendicular to their trajectories.

Since in a circular motion, the acceleration is given by $a = \frac{v^2}{R}$, and therefore $\dot{\beta} = \frac{\beta^2}{cR}$, Equation 2.66 can be rearranged into

$$P = \frac{2Kq^2c}{3}\frac{\gamma^4\beta^4}{R^2}\,. \tag{2.71}$$

Finally, the amount of energy per cycle emitted by the particle beam, assuming a constant bending radius can be found by integrating over the full circumference:

$$U = \int_0^{2\pi} P\frac{ds}{c\beta} = \frac{q^2}{3\varepsilon_0}\frac{\beta^3\gamma^4}{R}\,. \tag{2.72}$$

The unavoidable emission of synchrotron radiation has negative side-effects that must be accounted for when designing particle accelerators. Firstly, the energy lost by the particle via synchrotron radiation affects the particle dynamics and it must be reintroduced by the means of powerful RF systems. Secondly, the radiation emanates tangentially to the beam orbit, impinging on the inner walls of the vacuum chamber and heating the surrounding components, representing a danger especially to the focusing and bending magnets, which are composed of superconducting coils

and operate at 1.9 K in the LHC. Finally, when the radiation hits the walls of the vacuum chamber, they also contribute to gas desorption and electron clouds formation, which further disrupt the beam orbit.

Gas Desorption and Electron Clouds

Although there is significant effort to reduce particle scattering inside the vacuum chamber, it is unavoidable that some of the beam particles or emitted photons eventually impinge on the surrounding structure. When this happens, apart from any heating effects, it may result in the release of gas molecules that were pumped out of the central region of the vacuum chamber and deposited onto its walls. While maintaining low pressure and temperature contributes to decreasing gas desorption, it is often beneficial to shield the vacuum chamber limits, the cold bore, from the beam with a structure that will safely receive the impact of scattered particles.

When hit by scattered particles, the materials close to the beam are also susceptible to releasing electrons into the vacuum chamber. As electrons are released, they are accelerated by the electromagnetic fields, hitting the walls again and, in turn, possibly releasing more electrons [80]. The ratio between emitted and received electrons in a given material is dictated by its secondary electron yield (SEY). For SEY < 1, each electron impinging on the walls will statistically generate less than one electron coming out of it, and therefore, the process ends naturally after a limited amount of bounces. However, if the SEY is larger than one, it may trigger a chain reaction that fills the vacuum chamber with an electron cloud that, due to its electric charge, may exert forces on the beam, negatively impacting its stability. Therefore, it is important that the outermost layer of the objects exposed to the beam have a SEY < 1. Both scenarios are shown in Figure 2.12.

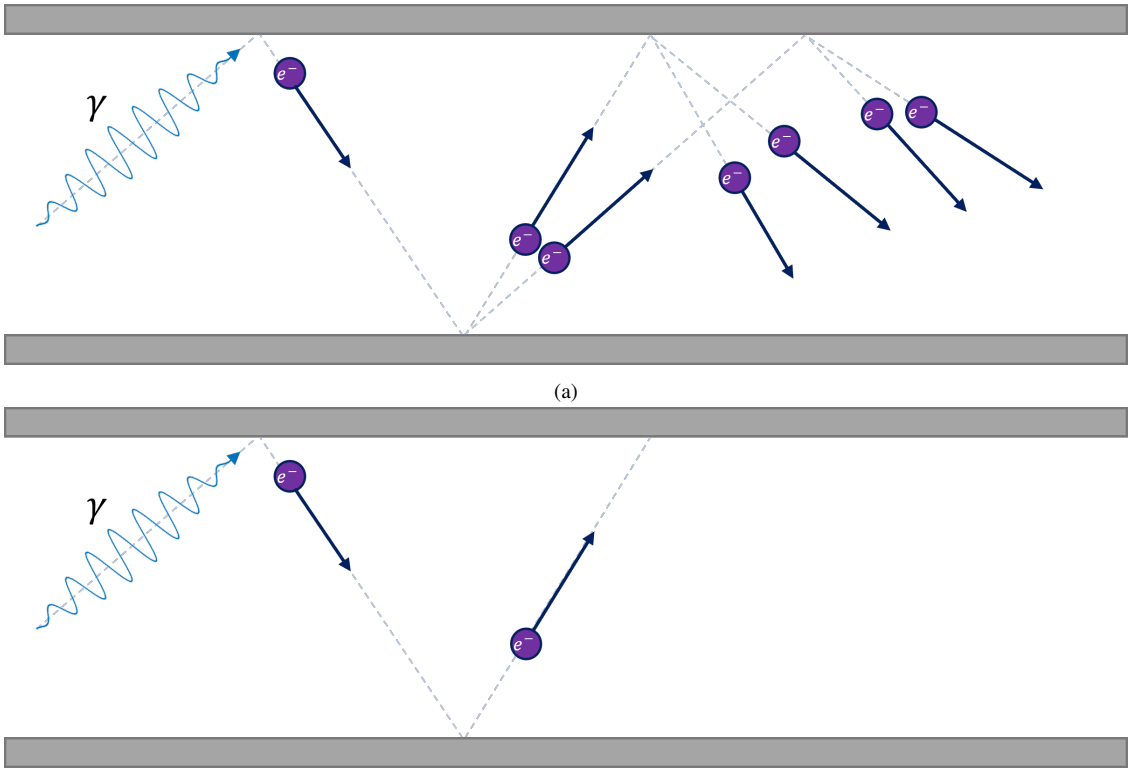


FIGURE 2.12: Emission of electrons (e^-) due to the impingement of photons (γ) or other scattered particles into the vacuum chamber walls. (a) With a SEY> 1, an electron cloud forms, leading to beam disturbances; (b) with a SEY< 1, the process ends after a few bounces.

Wake Fields and Image Currents

The electromagnetic fields produced by charged particles depends not only on the properties of the particle, but also of the environment through which the particle travels. In the case of particle accelerators, the electromagnetic field produced by the beam is influenced by the materials and geometries in the vicinity, and in turn can influence the subsequent particles that will come in contact with this field [81–83].

Let us consider a charged particle travelling through a perfectly cylindrical vacuum chamber contained within perfect electric conductor (PEC) walls. The electric field lines generated by the moving particle have to be normal to the conductor's surface, which is achieved by an induction of image currents onto the inner surface of the walls of the vacuum chamber. However, as long as these are longitudinally symmetric and PEC, the electric field at the particle's frame of reference should be constant at all times.

The situation shifts when one of these two conditions changes. First let us assume that at some point along the particle path there is a sudden change in the radius of the chamber, which is representative of several equipment components that may be present, such as radio-frequency cavities or interconnections, as shown in Figure 2.13. In this case, the new electromagnetic fields will be distorted to maintain the boundary conditions. However, since the charged particles are travelling close to the speed of light ($\beta \approx 1$), the magnetic field perturbations happen only in the wake of the particle, and are therefore called wakefields. In the case of a particle beam with several bunches, each composed of many particles, the wakefields can be significant enough to disrupt the path of the following particles within a bunch or even to affect the bunch as a whole.

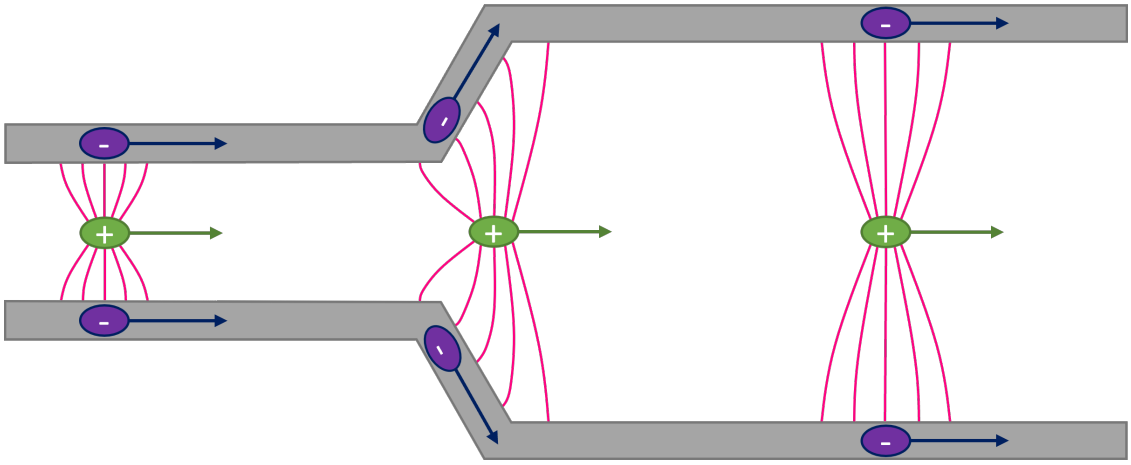


FIGURE 2.13: Electric field and image currents induced by travelling charged particles. The impedance as perceived by the beam depends on the geometry and materials of the nearby structure.

But the wakefields do not arise only from changes in the geometry of the vacuum chamber. In practice, the materials in the vicinity, as good a conductor as they may be, will always present some resistance to the electric currents induced by the particle beam, which in turn incur energy dissipation in the form of Joule heating. These interactions between the beam and the surrounding conductors are summarised by the beam coupling impedance, which is a frequency dependent response to the beam current that takes into account the surrounding environment and must be minimized in order to optimize beam stability.

In particular, the largest contribution to the beam coupling impedance comes from the resistive wall impedance Z^{rw}, which represents the heat generation and wake fields emerging from the finite resistivity of the materials in the vacuum

chamber. In the simplified case of a round pipe with surface impedance $Z_s(\omega) = R_s(\omega) + iX(\omega)$, it is given by

$$Z_{\parallel}^{rw}(\omega) = \frac{L}{2\pi r_{wall}} Z_s(\omega) \tag{2.73}$$

$$Z_{\perp}^{rw}(\omega) = \frac{cL}{\omega r_{wall}^3} Z_s(\omega)\,, \tag{2.74}$$

where r_{wall} refers to the radius of the cylinder, L to its length, and $\omega = 2\pi f$ to the angular frequency of the current component.

On the other hand, the resistive wall heating per unit length produced by the image currents induced in the walls is given by

$$\frac{P_{rw}}{L} = \int_{\omega} Z_{\parallel}^{rw}(\omega) I_b^2(\omega) d\omega\,, \tag{2.75}$$

where $I_b(\omega)$ is the Fourier transform of the beam current.

2.3.3 The FCC-hh Beam Screen

The beam screen is a device that surrounds the beam orbit, with the main purpose of absorbing the synchrotron radiation emitted by the particle beam and thus protect the superconducting magnets from the excessive heat load. In addition, it is responsible for mitigating the electron cloud generation and gas desorption, which are secondary effects of the impingement of synchrotron radiation and scattered particles onto the surrounding infrastructure, as previously mentioned [9, 84].

However, the introduction of conductive material so close to the beam poses its own challenges. As discussed in the previous subsection, the small distance between the beam and the beam screen makes the electromagnetic interaction between them potentially harmful to both. On the one hand, the resistive wall impedance of the beam screen disturbs the bean dynamics, possibly leading to instabilities. On the other, the image currents induced in the beam screen contribute to its heat load. Finally, since the beam screen is located inside the cold bore of the magnets, it must maintain magnetic field quality by not excessively distorting the magnetic field perceived by the beam.

A schematic representation of the FCC-hh beam screen layout is given in Figure 2.14. The beam screen is composed by a primary chamber, two lateral secondary chambers and two vertically placed cooling channels. The primary chamber is limited by the inner walls of the beam screen, while the secondary chambers lie between the inner and outer walls. The entire beam screen is contained within the cold bore, which separates the vaccum chamber from the superfluid helium that cools the magnet coils down to 1.9K.

Starting from the outside, the outer walls are made of 1 mm thick P506 stainless steel (SS) covered by a 75 μm copper layer and are responsible for absorbing the synchrotron radiation, which is emitted tangentially to the beam orbit. The radiation travels horizontally through the primary and secondary chambers, passing through a 7.5 mm gap in the inner walls and finally hitting the outer walls. To maximize the absorption of synchrotron radiation, the central portion of the outer walls has a saw-tooth surface finishing such that the incidence angle is close to 90°. Since the outer walls shield the cold bore from the synchrotron radiation, they also avoid desorption of the gas molecules from the cold bore. However, to allow the gas in the vaccum chamber to be pumped out towards the cold bore, each of the outer wall has two rows of pumping holes located as far as possible from the irradiated area.

The inner walls are made of 1mm P506 SS covered with 0.3 mm of copper and are placed in such a way that most of the secondary chambers and especially the pumping holes are hidden from the beam. This way, the contribution of the

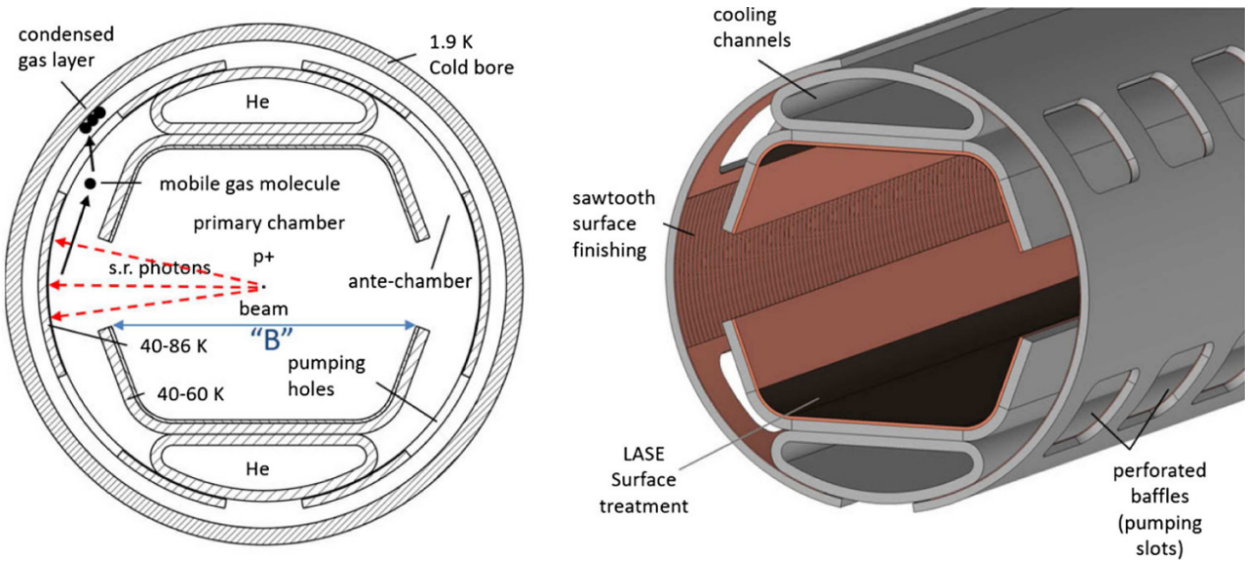


FIGURE 2.14: The FCC-hh Beam Screen. It is composed by a primary and secondary chambers to shield the magnet cold bore from the beam, protecting it from the beam-induced heat load, as well as preventing electron cloud formation. Figure reproduced from [9].

pumping holes to the beam screen impedance is negligible, allowing them to be much larger and, therefore, maintain higher pumping speeds than otherwise.

While the inner walls receive a negligible amount of synchrotron power, the image currents induced by the beam may be enough to generate significant heat due to the beam's proximity. For the same reason, the wakefields impinging onto the inner walls also have a larger impact on the bean dynamics. Both effects are minimized by adopting a coating material with high electric conductivity, and is the main reason why the stainless steel in both the inner and outer walls is covered with a copper layer of at least 100 residual resistivity ratio (RRR).

In order to mitigate the electron cloud accumulation, there are two proposed options to decrease the secondary electron yield (SEY) of the primary chamber: an amorphous carbon (a-C) coating or laser ablation surface engineering (LASE) treatment of some parts of the inner walls. Both can reduce the SEY below one, while preserving low surface resistance valves.

The cooling channels are placed above and below the primary chamber and are the only mechanical connection between the outer and inner walls. The liquid helium flowing through the cooling channels absorbs the heat produced by the synchrothon radiation on the outer walls and by the image currents on the inner walls, keeping the beam screen between 40 and 60 K. The cooling power to maintain the beam screen at such temperatures is much lower than that which would be necessary to achieve the temperatures similar to those of the LHC, 5 to 20 K, especially considering the larger circumference of the FCC. However, at this higher temperature range, the surface impedance of copper, although quite low, may not be low enough to ensure beam stability.

2.3.4 A Hybrid REBCO-Cu Coating for the FCC Beam Screen

Reducing the resistive wall impedance of the beam screen is necessary to decrease the heat load on the cooling channels as well as to diminish the impact of the wakefields on the beam dynamics, and may be a decisive factor in the operational feasibility of the FCC. However, since the dimensions of the beam screen are restricted to being contained inside the cold bore, and therefore are unavoidably close to the beam, the only means to achieve such reduction is to

employ a coating material that shows surface resistance values lower than copper. Coupled with the relatively high operating temperatures of the FCC beam screen, this makes HTS a promising candidate to substitute copper.

However, while improvements can be expected with respect to the radio-frequency behaviour of this coating, it must also be tailored to accommodate other needs of the vacuum chamber. Namely, as discussed, field quality must be maintained and the formation of electron clouds has to be prevented, as well as material degassing in vacuum due to whatever method is used to attach the HTS to the beam screen walls. In addition, the coating technique must be scalable to the the tens of kilometers of the FCC.

Regarding field quality, the trapped field inside a superconductive coating could disrupt the magnetic field in the vicinity of the beam to levels that could threaten the beam stability. On the other hand, it is known that if the same amount of superconductor is split into several segments, then the trapped field will decrease proportionally to the number of segments. This can be shown by considering the Bean model, as depicted in Figure 2.15. Therefore, in order to achieve both low surface resistance and high field quality, a coating geometry must be found such that the amount of HTS and the number of segments into which it is split are maximized, therefore minimizing the surface impedance and the field disturbance. The gaps between the HTS segments have the copper coating already present in the beam screen exposed, so that their contribution to the surface impedance is lower than the otherwise exposed stainless steel wall. The coating must also be longitudinally symmetric, as depicted in Figure 2.16, to avoid an increase in the beam impedance due to discontinuities in the path of the induced image currents. Of course, aiming for small gaps leads to limits to the technical feasibility of the coating, and a balance must be found between field quality and surface resistance, on one hand; and complexity and cost, on the other. Previous studies have shown that such a hybrid geometry can indeed achieve high field quality when compared to a full HTS coating [85], and it is expected that it can also provide low surface impedance, as long as the ratio of HTS is large enough.

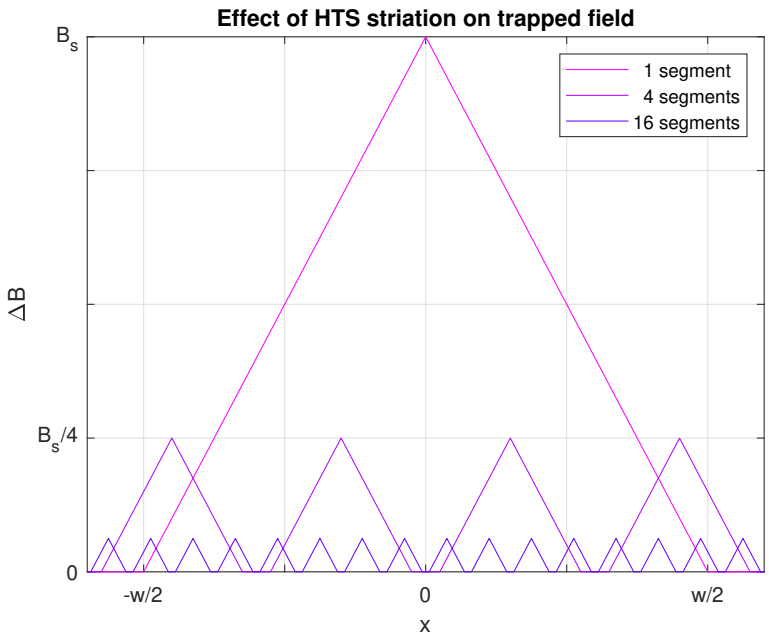


FIGURE 2.15: Trapped field inside a superconductor according to the Bean model. Comparison between a single segment with width w, four segments with width $w/4$ and 16 segments with width $w/16$ separated by copper gaps. The maximum trapped field is inversely proportional to the number of segments into which the HTS tape is split.

The proposed production method for the hybrid coating consists of attaching REBCO coated conductors to the

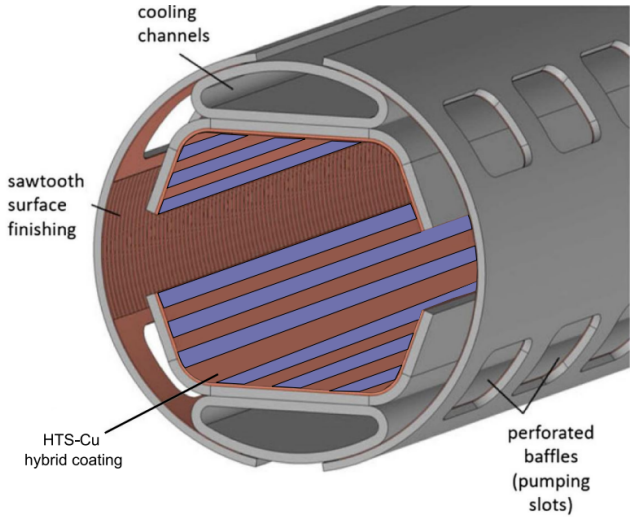


FIGURE 2.16: The FCC beam screen coated with a hybrid REBCO-Cu coating to minimize surface impedance. The coating is composed of longitudinal HTS segments separated by gaps of exposed copper. Figure reproduced from [49]

inner walls of the beam screen with the REBCO layer closest to the wall. Afterwards, the outermost layers, namely the substrate and buffer layers, as well as the copper and silver envelope, are delaminated, exposing the REBCO material. If the desired segments are smaller than the width of the coated conductors, the HTS must then be striated to produce these segments. The resulting coating is then covered with a thin layer of amorphous carbon to reduce the SEY, which has only a minor impact on the surface impedance values of the HTS [12]. The choice of coated conductors arises from the fact that they are commercially available in hundreds of meters lengths with high quality and homogeneous properties, while growing HTS directly on the beam screen walls would prove impossible with the currently available methodology due to their uneven geometry and the highly epitaxial substrate needed for REBCO growth (see Section 3.1).

Chapter 3

Methods for Production and Quality Evaluation of REBCO Coatings

The production process of the REBCO coatings developed in this thesis centers around the usage of delaminated coated conductors as the means to achieve an outermost layer of HTS and avoiding the need to grow the superconducting material directly on top of the surface to be coated. Although coated conductors are fairly sturdy cables, a specific methodology must be employed to ensure that the superconducting properties are preserved throughout the manufacturing process of the coating, especially considering delaminated coated conductors, which are much more sensitive to mechanical stresses and chemical interactions due to the lack of protective layers and the substrate.

In this chapter, the methods for production and analysis of the coatings will be described. The resulting coatings are evaluated in terms of their surface resistance, magnetization and composition and a technique for quickly assessing the quality of the coating is developed.

3.1 Coating Surfaces with Delaminated Coated Conductors

The main goal of HTS coatings is to achieve low surface impedance by exposing the REBCO layer as the outermost layer of the surface to be coated. If done properly, the external radio-frequency electromagnetic fields will interact only with the REBCO layer, ignoring the worst conducting layers beneath, such as copper or steel. The starting point for the coating technique is the adoption of coated conductors, due to their homogeneous properties and large scale availability, as discussed in section 1.2.3, as well as the possibility of coating surfaces with different geometries, including non-flat surfaces.

In summary, the coating technique consists in attaching the coated conductor onto the surface to be coated and then removing all the layers covering the HTS, exposing it to the high-frequency electromagnetic fields to which the coated device will be subject. In this section we will go through the step-by-step production process of the coating, from the preparation of the coated conductors to their delamination. The methods described in this section were developed and optimized in collaboration with the PhD candidate Neil Lamas.

3.1.1 Coated Conductor Preparation

The first step to produce a coated conductor-based HTS coating is to prepare the coated conductors so they are properly attached to the surface to be coated. In this case, the attachment method employed is to solder the coated conductors onto the surface. Therefore, it is necessary to apply a thin layer of soldering alloy to the top surface of the coated

conductor. The alloy used throughout this work is a 60/38/02 Sn-Pb-Cu alloy, due to its widespread availability and relatively low melting point ($T_{mp} \approx 180°C$)[1]. The thickness of the alloy layer is of particular interest and plays a major role on how well attached the coated conductor will be: if the layer is too thin, the coated conductors will detach easily; if it is too thick, the coating may not be perfectly flat or the excess of solder may cover the edges of the CC, hindering its delamination. The target thickness for the coatings produced in this work was around 15 μm, measured both by weighting the samples before and after adding the soldering alloy and via optical microscopy analysis of its cross-section, as shown in Figure 3.1.

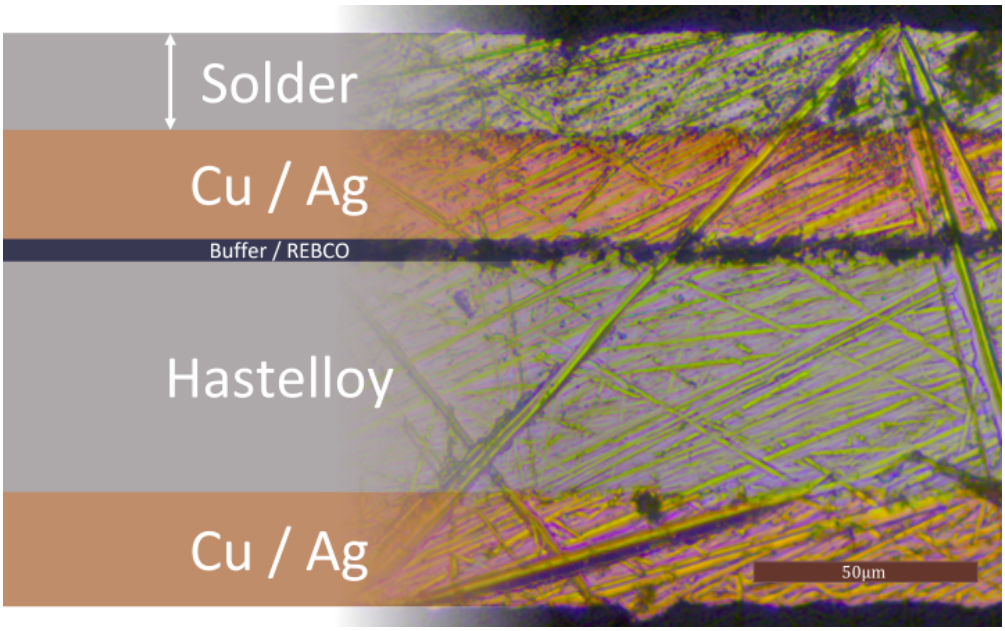


FIGURE 3.1: Cross-section of the coated conductor with an added layer of soldering alloy.

To apply the soldering alloy, the coated conductor is heated locally by a heater, where a wire of the soldering alloy comes in contact with the CC, as shown in Figure 3.2a. As the alloy melts, the CC is pulled at constant speed, so that the alloy is deposited and melts on top of the whole length of the coated conductor. Placed at the end of the heater, a thin blade is pressed against the coated conductor, retaining the excess of solder so that it does not solidify, effectively limiting the thickness of the alloy layer.

Most of the samples produced throughout this work were assembled semi-automatically by using a motor to pull the coated conductor and manually applying the alloy and pressing the blade. Although it is possible to control the thickness of the alloy layer by varying the speed of the coated conductor or the angle and pressure of the blade, we found that, under these conditions, it was more reliable to introduced small grooves in the tip of the blade, as depicted in Figure 3.2b. By changing the size of these grooves, the amount of alloy could be optimized. The downside is that the thickness of the soldering alloy would no longer be homogeneous along the width of the CC. However, this proved not to be an issue due to the melting of the alloy during the soldering process, which homogenizes its thickness.

It is important to note that the temperature of the heater must be controlled in order not to excessively surpass the melting point of the soldering alloy. In CCs, the REBCO may show signs of degradation after being exposed to temperatures as low as 225°C, presenting a decrease of around 5% in J_c after only 10 minutes [86]. If the REBCO is exposed to air, the temperature above which degradation is noticeable is even lower, at approximately 150°C [87]. This

[1] It must be noted, however, that soldering alloys containing Pb are toxic and must be handled with care, and that a in-depth study of the behaviour of this alloy in vacuum is necessary for it to be used in applications that require such low-pressure conditions, like the FCC beam screen.

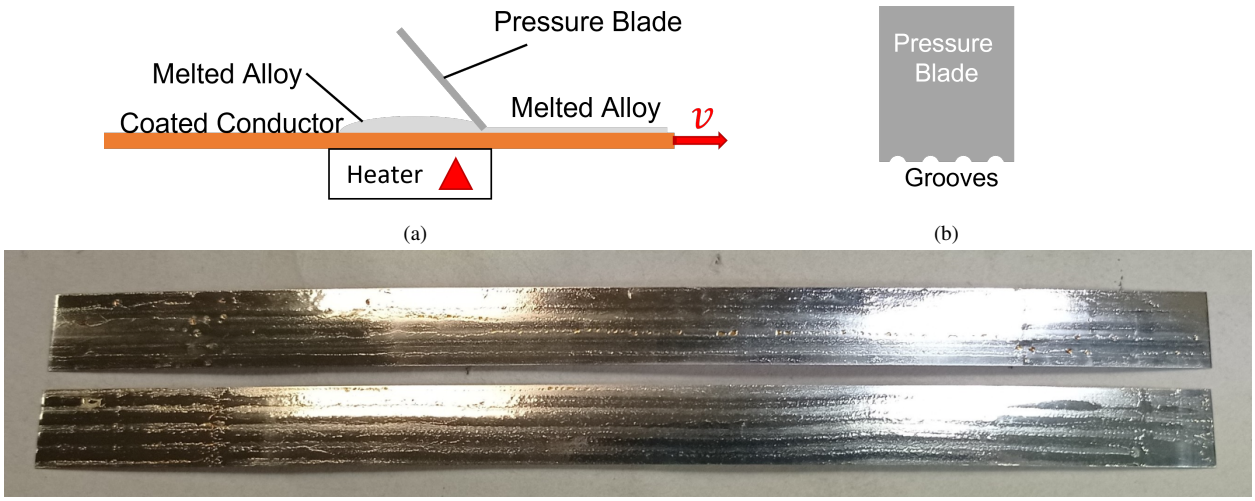


FIGURE 3.2: First step of the production of a coated conductor-based HTS coating. (a) The aplication of a layer of soldering alloy on the top surface of the coated conductor. The CC is moved at constant speed on top of a heater where the alloy melts and is spread along the CC by a thin blade. (b) The grooves in the blade are used to control the thickness of the alloy layer. (c) The resulting coated conductor with the added soldering alloy can be seen, with in-homogeneous thickness due to the grooves of the pressure blade.

is one of the most important limiting factors when choosing a proper soldering alloy. Therefore, for our coatings, the temperature applied was of around 200°C during this step and never surpassed 230°C throughout the entire production process. To improve on this production step and guarantee higher reproducibility, an automated system has been developed in parallel with this work in the Institut de Física d'Altes Energies (IFAE). Figure 3.2c shows an example of coated conductors with the added layer of soldering alloy.

As described in section 1.2.3, the coated conductor is composed of several layers and surrounded by protective layers of silver and copper. The second step of the CC preparation is the removal of the copper and the silver on the sides of the coated conductor, as well as any excess of soldering alloy that may have leaked to the side, as presented in Figure 3.3. The reason for this is to facilitate the subsequent delamination of the coated conductor. If the side envelope is not removed, the mechanical stresses introduced during delamination may damage the edges of the HTS layer, locally destroying superconductivity.



FIGURE 3.3: Second step of the production of a coated conductor-based HTs coating. The copper and silver layers on the side of the coated conductor are removed, as well as any excess of soldering alloy. This is done to prevent damages during delamination.

3.1.2 Soldering and Delamination

Once the coated conductors have been prepared with the added soldering alloy layer and have had the envelope layers removed from the sides, they are ready for the next step of the coating procedure. While there are other ways of

attaching the coated conductor, onto the surface to be coated, soldering presents advantages. In addition to being a simple and fast method, it offers good thermal contact between the superconducting layer and the metallic surface, which may be a benefit in some applications. In the case of the FCC beam screen, a good thermal contact would help dissipate the heat generated by the currents induced in the REBCO layer. On the other hand, the good electric contact associated with such a method induce the flow of transverse currents through the different materials, which in turn might pose an issue with respect to field quality in certain scenarios, as will be discussed in Chapter 8.

To solder the coated conductor, the CC surface with the added soldering alloy layer is pressed against the surface to be coated, as shown in Figure 3.4. A heater and a thermometer are placed on top of the CC and are responsible for the temperature control during soldering. A pressure homogenizer is positioned between the heater and the press. Homogeneous pressure along the entire sample's surface is essential to the soldering process, as it will ensure that the soldering alloy distributes itself homogeneously after its melting and subsequent cooling under pressure.

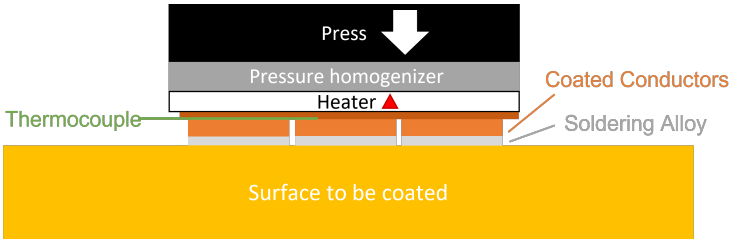


FIGURE 3.4: Cross-section of the assembly required for the third step of the production of a coated conductor-based HTS coating. Coated conductors are soldered onto the surface to be coated by pressing and increasing the temperature above the melting point of the solering alloy.

When all the components are assembled, the temperature is increased beyond the melting point of the soldering alloy and kept there for a few minutes to ensure that the entire alloy layer melts and adheres to both surfaces. At this point, the pressure is increased and the temperature slowly decreased to room temperature. The maximum temperature applied during the soldering of the samples prepared throughout this work was of 230°C for no more than five minutes to minimize damage to the HTS. The profile of applied pressure during the soldering process was the subject of an in-depth study that is part of Neil Lamas's doctoral thesis.

After soldering, the attached coated conductors can then be delaminated. A thin cutter blade is carefully pressed against the side of the soldered coated conductor, in such a way to delaminate it along its weakest interface, ideally between the REBCO and buffer layers, as illustrated in Figure 3.5. The blade is then moved away from the REBCO, peeling off the outermost layers, namely the substrate and buffer layers, as well as the copper and silver layers that were originally beneath the substrate.

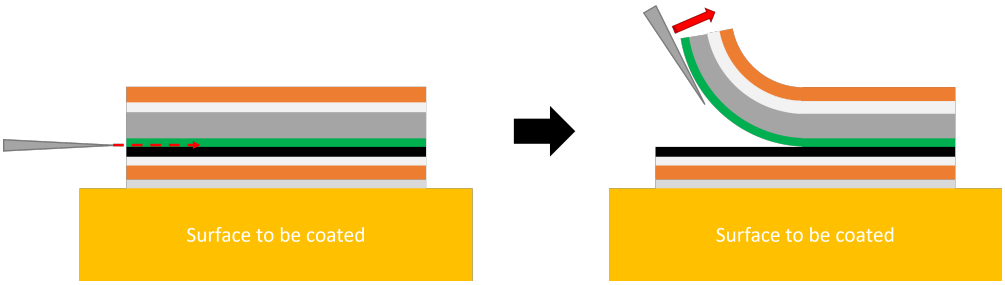
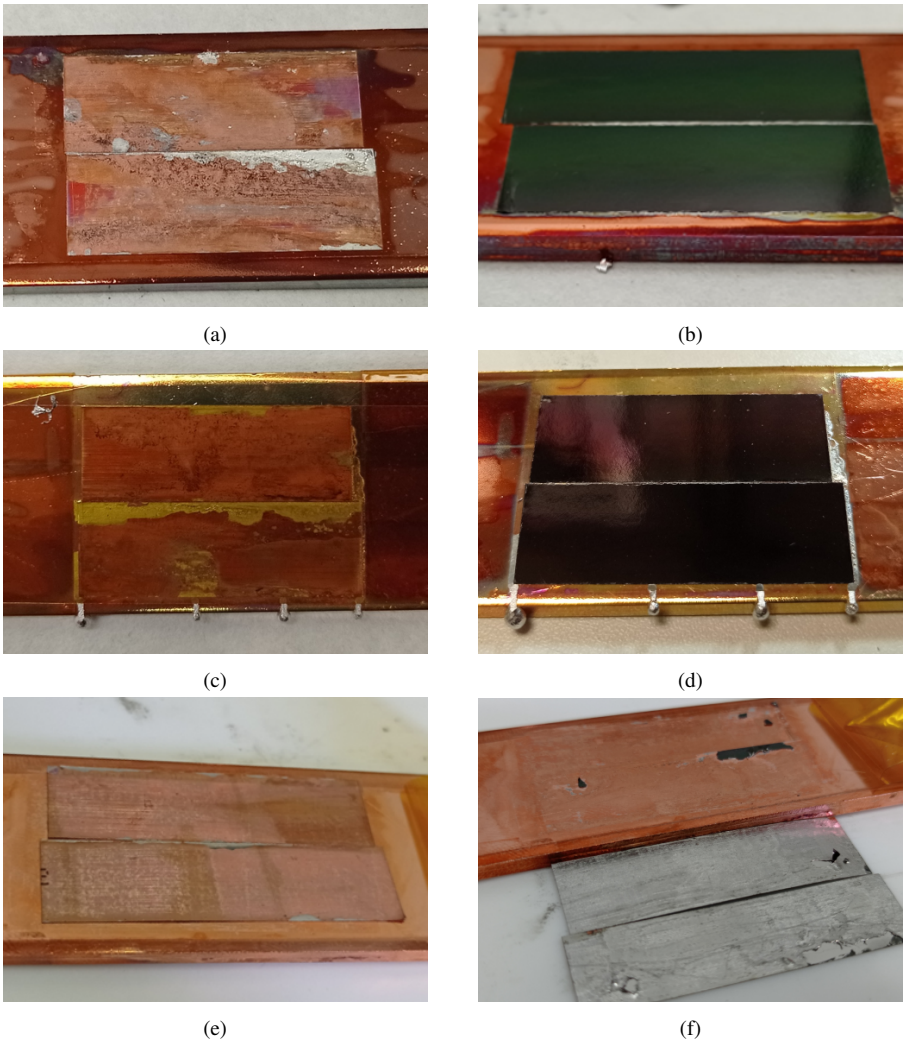


FIGURE 3.5: Fourth step of the production of a coated conductor-based HTs coating. The coated conductor is delaminated, removing the outermost layers and exposing the REBCO layer.

Figure 3.6 shows examples of coating samples after soldering. While at this point it is still early to precisely determine the quality of the coating, there are some early telltale signs that some issues may have arisen. An excess of soldering alloy may become evident by leaks of the melted alloy onto exposed regions of the surface to be coated. On the other hand, if there is not enough pressure or the soldering layer is too thin, it may cause some areas of the CC to be loosely attached, which is revealed by a rugged surface of the exposed REBCO and suggesting the presence of air bubbles in the soldering layer beneath. After delamination, a badly soldered sample may detach partially or completely, and an excess of soldering alloy may lead to damage in the edges of the CC, as well as uneven coating.



(a) (b) (c) (d) (e) (f)

FIGURE 3.6: Examples of coating samples after (a,c,e) soldering and (b,d,f) delamination. (a,b) Sample with no apparent defects; (c,d) sample with excess of soldering alloy and (e,f) sample not properly attached to the surface.

3.2 Dielectric Resonator Radio Frequency Measurement

To measure the surface impedance of both REBCO coatings and regular coated conductors as a function of temperature and with magnetic fields of up to 9 T, a radio-frequency measurement system is used. This experimental setup is composed by a vector network analyser (VNA), a custom built Hakki-Coleman type dielectric resonator (DR) [88, 89] with resonant frequency $f_0(50\,\mathrm{K}) \approx 8\,\mathrm{GHz}$ and a Physical Property Measurement System (Quantum Design PPMS®). A schematic of the devices and their interconnections is shown in Figure 3.7. A brief description of the system will be

given in this section. For a more in-depth description of each component as well how the data is processed, refer to [49].

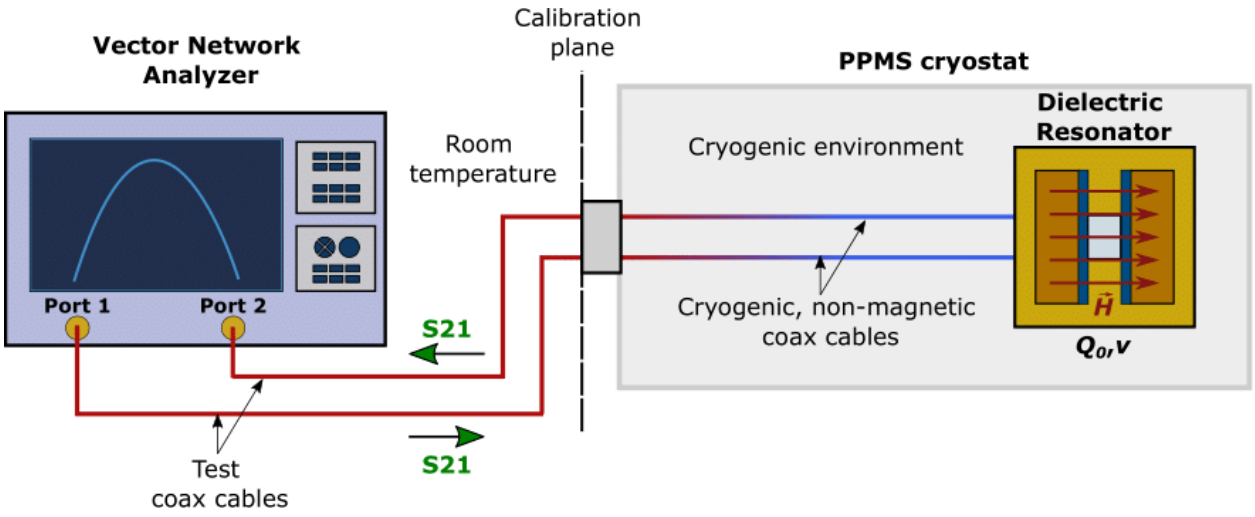


FIGURE 3.7: Layout schematic of the radio-frequency measurement system used to measure the surface impedance of delaminated and regular coated conductors. Figure created by Dr. Artur Romanov [49].

The concept behind this measurement system revolves around the losses that occur when the DR is submitted to an AC electromagnetic excitation, based on which the surface impedance Z_s of the samples under test can be calculated [90]. The VNA is responsible for generating this excitation, which is transmitted to the DR by the means of two coaxial cables. The cables end in two coupling loops located inside the DR, which produce a resonating electromagnetic field in the interior of the DR cavity, inducing electric currents in the surrounding conductors. The DR is a hollow metallic cylinder terminated by the pair of samples under test, as shown in Figure 3.8. The resonating cavity is therefore limited by the brass walls and the superconducting floor and ceiling. Sandwiched between the two coated conductors, a dielectric, in this case a TiO_2 rutile crystal, focuses the RF electromagnetic field so that it is concentrated in the center of the samples. The VNA is set to monitor the TE_{011} mode (see Figure 3.8c), responsible for a purely vertical component to the RF magnetic field in the superconducting samples, since the currents induced in them are circular in the horizontal plane. A Cernox® temperature sensor is placed close to the samples and the temperature and DC magnetic field in the cavity is controlled by the PPMS.

As the cavity resonates, the VNA also captures the system's frequency response to the EM excitation, which is affected by the losses of the currents induced in the metallic walls and the superconducting samples, and of the EM field in the dielectric, as well as the losses in the coaxial cables. The total losses of the system are represented by the loaded quality factor Q_l [91], given by

$$\frac{1}{Q_l} = \frac{1}{Q_0} + \frac{1}{Q_{ex}}, \tag{3.1}$$

where Q_0 is the unloaded quality factor, which considers only the contribution coming from the DR, and Q_{ex} represents the losses coming from external sources, namely the coaxial cables and connections [92]. Knowing beforehand the systematic losses at a given frequency, one can calculate the contribution of the samples to the quality factor, and with it, the surface resistance [93]:

$$R_s(T,B) = \frac{G}{2}\left[\frac{1}{Q_0(T,B)} - \tan\delta(T)\right], \tag{3.2}$$

where G is a geometric coefficient [89] and $\tan\delta = \frac{\varepsilon''}{\varepsilon'}$ is the loss tangent of the dielectric, given by the ratio between the imaginary and real parts of its electric permittivity $\varepsilon = \varepsilon' + i\varepsilon''$ [94].

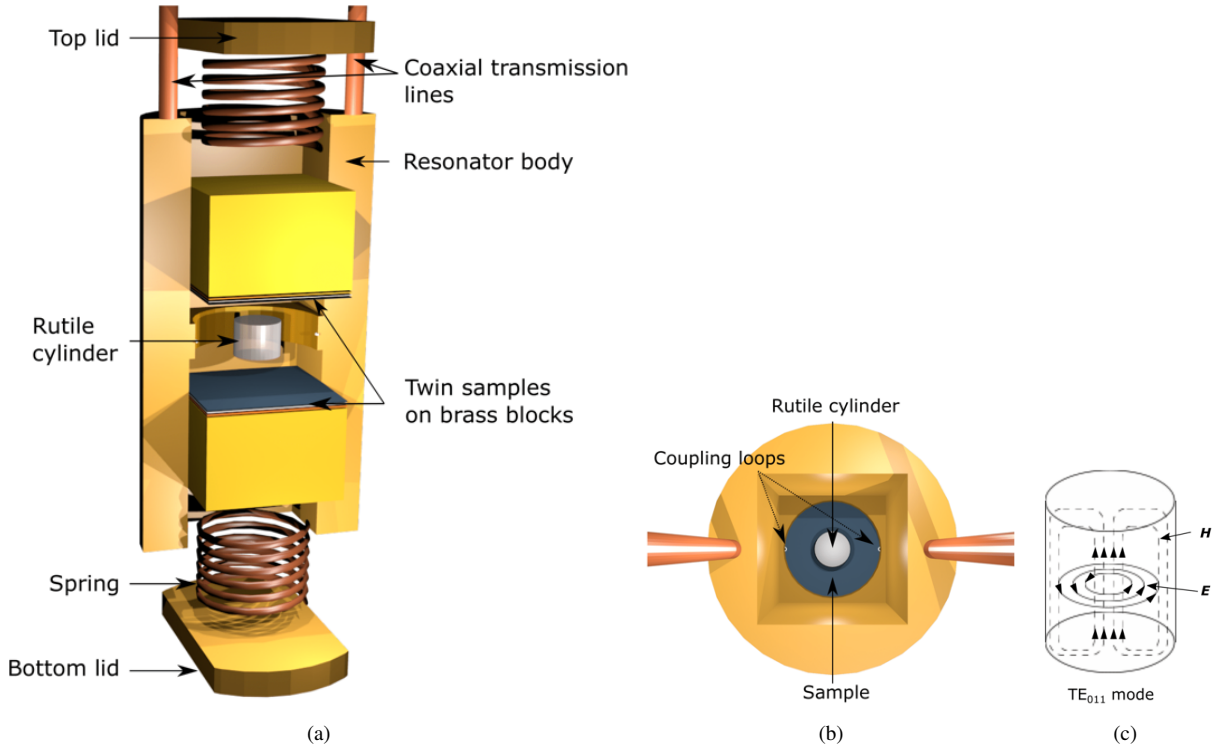


FIGURE 3.8: Schematic of the dielectric resonator (DR) with coated conductor samples under test. (a) Cross section of the dielectric resonator, where the samples combine with the brass walls to create the resonating cavity; (b) Top view of the resonating cavity; and (c) Field distribution of the TE_{011} mode. Figure created by Dr. Artur Romanov [49].

Likewise, the shift in surface reactance over a given temperature or magnetic field range, ΔX_s can be calculated based on the same measurements, but it also depends on the shift in the resonant frequency [93, 95]:

$$\Delta X_s(T,\Delta T,B,\Delta B) = -G\left[\frac{\Delta f_0(\Delta T,\Delta B)}{f_{0,ref}(T,B)} + \frac{1}{2}\frac{\Delta \varepsilon_r'(\Delta T)}{\varepsilon_{r,ref}(T)}\right], \tag{3.3}$$

with Δ corresponding to a variation with respect to the reference values denoted by the index ref, and f_0, ε_r and ε_r' being the resonant frequency and the relative electric permittivity and its real part, respectively.

Two VNAs were used for the measurements presented in this thesis and associated works: a Keysight FieldFox N9918A [96] and a Rohde & Schwarz ZNB 20 [97]. Python scripts are used to automate the measurement process. For the Keysight FieldFox N9918A, a script named DRΩMS was developed in collaboration with Dr. Patrick Krkotić and Dr. Bernat Bozzo [50, 98]. A second script, for measurements with the Rhode & Schwarz ZNB 20, was developped by Dr. Artur Romanov and Dr. Bernat Bozzo [99].

Figure 3.9 shows the surface resistance as a function of magnetic field at $T = 50\,\mathrm{K}$ and $f_0 = 8\,\mathrm{GHz}$ of four samples from the providers SuperPower and Fujikura, two being regular coated conductor without their copper and silver layers and two being delaminated. Properly produced REBCO coatings show slight performance improvements when compared to their CC counterparts. This arises from the fact that, in the REBCO coating, the REBCO surface exposed to the electromagnetic excitation is the one that was originally in contact with the substrate and buffer layers (bottom surface), and therefore presents a higher quality crystallographic structure as compared to the opposite surface of the REBCO layer (top surface), which is the one exposed in the regular coated conductors by etching away the Cu and

Ag layers. The increase in the surface resistance for the delaminated SuperPower sample at $B < 1\,\mathrm{T}$ is associated with the presence of remnant patches of buffer layers on top of the REBCO layer, which give an electromagnetic response. This increase can be neutralized by removing the patches of buffer layers after delamination. An in-depth analysis of the radio-frequency behaviour of delaminated samples and the effect of remaining buffer layers is presented as part of Dr. Artur Romanov's doctoral thesis [49].

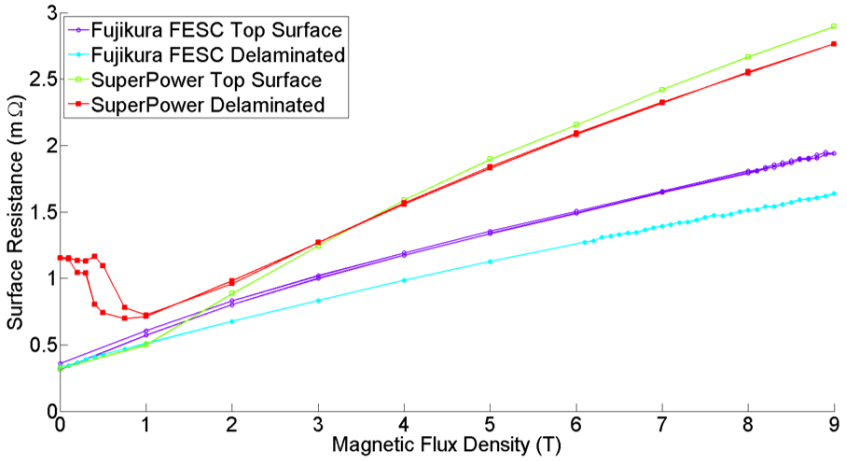


FIGURE 3.9: Surface resistance as a function of the magnetic field at $T = 50\,\mathrm{K}$ and $f_0 = 8\,\mathrm{GHz}$ for REBCO coatings and regular coated conductors from SuperPower and Fujikura. The surface resistance of the coatings, corresponding to the bottom surface of the REBCO layer (closer to the substrate), has lower values than their corresponding top surface coated conductors [49].

3.3 Combined Microscopy Analysis

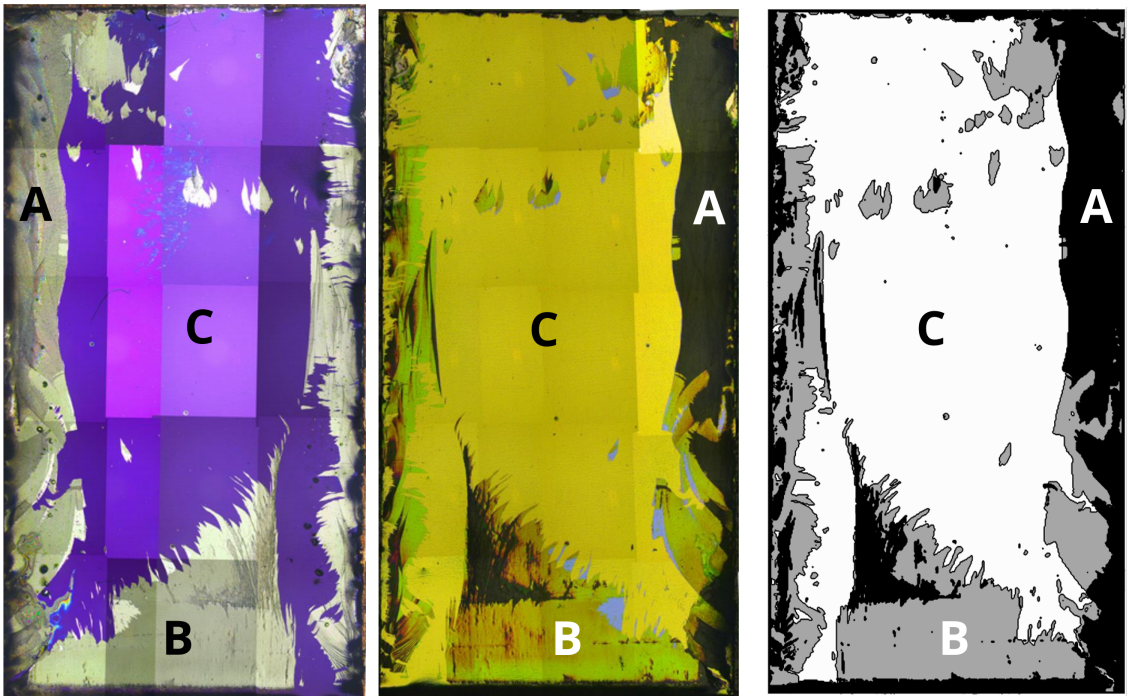
Apart from the radio-frequency behavior of the produced coatings, it is also interesting to know if the electromagnetic properties of the HTS are locally preserved throughout the entirety of the REBCO layer. To analyse this, we employ a combined microscopy analysis, composed of optical microscopy (OM), scanning Hall probe microscopy (SHPM), scanning electron microscopy (SEM) and energy dispersive spectroscopy (EDX). These combined techniques allow for a correlation between damaged areas and potential losses in the electromagnetic properties, and also facilitate the visual evaluation of the quality of the resulting samples.

3.3.1 Optical Microscopy

Although the goal of the coating production process is to expose the REBCO layer of the delaminated coated conductors, there are often imperfections that may arise from inappropriate solder thicknesses or other manufacturing steps. These result in remnants of buffer layer patches that remain attached to the REBCO layer, partially covering it, as well as excavations in the REBCO layer.

By analysing the resulting samples with an optical microscope, it becomes clear that they may present very distinct regions that can be differentiated by their colors. Figure 3.10 shows the optical images of a sample and its delaminated substrate prepared from a 12 mm wide SuperPower coated conductor. Although ideally one would expect that the delamination occurred only between the topmost buffer layer and the REBCO layer, in reality it may happen between different buffer layers, or even splitting the REBCO layer itself, ultimately resulting in distinct exposed layers in the coating. These are revealed by the different regions in Figure 3.10c, which are obtained by filtering the color distribution of the image of the delaminated substrate in terms of hue, saturation and value (HSV) with the Color

Threshold MATLAB® app [100, 101]. The three regions of Figure 3.10c are named Regions A, B and C, corresponding to the black, gray and white regions, respectively. Note that the image of the substrate always corresponds to a mirrored projection of the image of the coating, since the depicted layers from each side were originally in contact with each other.



(a) (b) (c)

FIGURE 3.10: Optical images of delaminated 12 mm wide SuperPower coated conductors. In (a) the resulting coating with the exposed REBCO layer is shown. The substrate side is presented in (b). (c) shows the image of the delaminated substrate filtered in terms of hue, saturation and value, where three distinct regions, black, gray and white are clearly observed.

By itself, the optical microscope analysis can only be used to find these different delamination interfaces and to estimate how much of the sample, in terms of area ratio, is represented by each. The next step would be to determine what these exposed layers are and how the coating's electromagnetic properties are affected by them.

3.3.2 Scanning Electron Microscopy and Energy Dispersive Spectroscopy

The scanning electron microscopy (SEM) consists on bombarding the sample under test with a beam of electrons. The secondary electrons emitted by the sample are then detected, generating images of the sample's topography. When the electrons impinge on the sample, it also releases energy in the form of X-rays, which can be analysed via energy dispersive spectroscopy (EDX), to determine the composition of the sample [102]. The SEM system used is in this work is ICMAB's QUANTA™ FEI 200 FEG-ESEM.

Figure 3.11 shows the images obtained both from optical and scanning electron microscopy of a small area of the sample shown in Figure 3.10. This particular spot was chosen for containing parts of the three regions seen in Figure 3.10c, which are clearly distinguished by their colors in Figure 3.11d and by the different tones of gray in Figure 3.11b. By analysing each of the regions in both the substrate and the coating with EDX, we can determine their compositions and find between which layers the delamination happened.

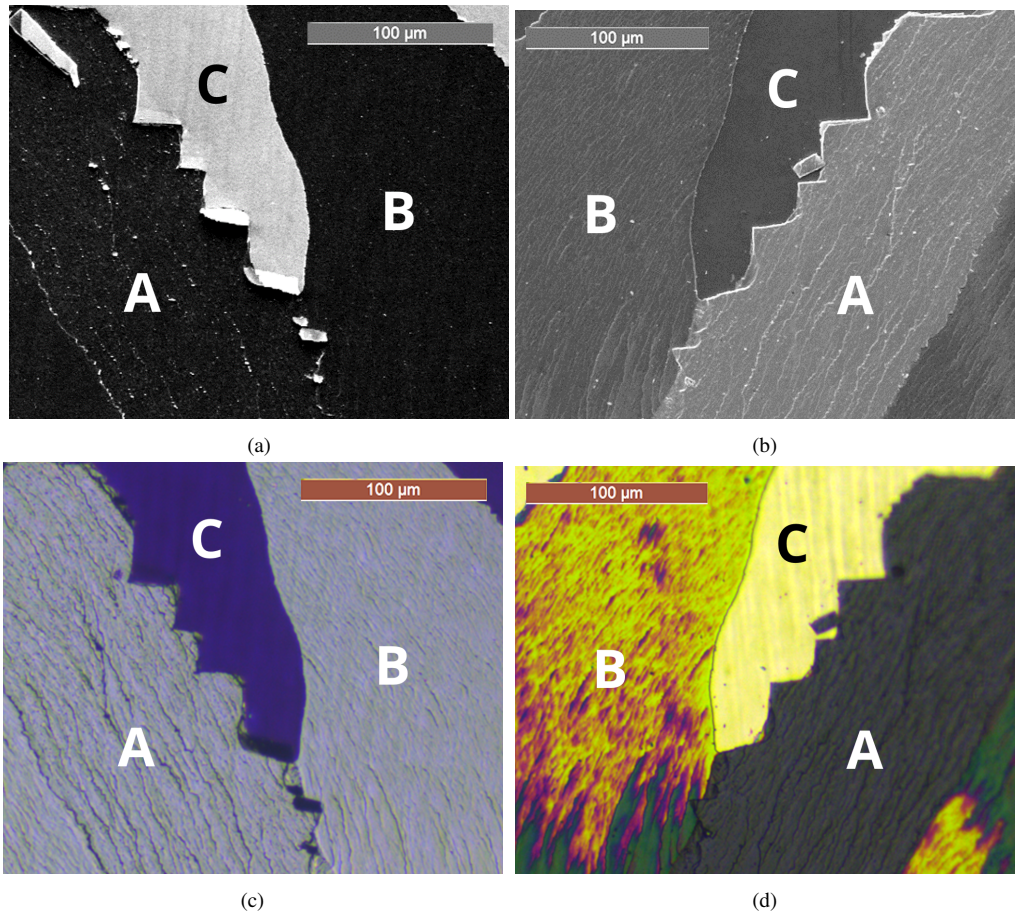


FIGURE 3.11: Optical and SEM images of delaminated 12 mm wide SuperPower coated conductors, magnified by a factor 1000. SEM images of (a) the coating sample and (b) the delaminated substrate and equivalent optical images (c, d). Once again, the three regions evidenced in Figure 3.10 are clearly in the optical and SEM images of the delaminated substrate.

THE EDX results are shown in Table 3.1, where we can see the composition of each region. By comparing the composition in both the substrate and the coating, we can find the delamination interface for each region.

Let us start by evaluating Region A (Black), where EDX reveals a high percentage of the REBCO elements in both the coating and the substrate. This suggests that the delamination happened in such a way that the REBCO layer was split, resulting in an excavation of the REBCO from the coating. The interface is therefore inside the HTS, and the exposed surface in the coating is a somewhat damaged REBCO layer. EDX on Region B (Gray) shows, on the other hand, a high percentage of REBCO elements in the coating, but only a small percentage in the substrate. This means that the delamination happened between the REBCO and the closest buffer layer. The exposed layer in the coating is the REBCO layer. EDX shows that REBCO excavation in this region is an order of magnitude smaller than that in Region A. Finally, EDX on Region C shows a high percentage of REBCO elements in the coating, but no signs of Gd and Ba in the delaminated substrate. In addition, unlike in the other regions, elements belonging to the buffer layers are present only on the coating side, suggesting that the delamination occurred between a buffer layer and the substrate.

Combining the EDX results with the processed image shown in Figure 3.10c, we can infer that 56% of the sample surface is actually covered with remnant buffer layers (Region C - white), while smaller areas correspond to either excavated REBCO (Region A - black) or a mostly intact REBCO layer (Region B - gray), each representing 22% of

TABLE 3.1: Elemental composition obtained via EDX of each region of the coating produced from a delaminated SuperPower coated conductor. Regions A, B and C correspond to black, gray and white regions of Figure 3.10c and the orange, yellow and black regions of Figures 3.10b and 3.11d, respectively. Only the elements that belong exclusively to the buffer or REBCO layers are shown.

			Region A (Black)		Region B (Gray)		Region C (White)	
	Layer	Element	Weight %	Atomic %	Weight %	Atomic %	Weight %	Atomic %
Coating	REBCO	Gd	15.99	7.12	15.06	6.74	11.48	4.03
		Ba	42.18	21.49	42.46	21.75	32.23	12.95
	Buffer	La					9.06	3.60
		Mg					8.74	19.83
		Al						
	Other		41.83	71.39	42.48	71.51	38.49	59.59
Substrate	REBCO	Gd	14.52	6.27	1.14	0.30		
		Ba	35.83	17.72	3.21	0.97		
	Buffer	La	4.97	2.43	8.07	2.43		
		Mg	0.28	0.79	5.31	9.12		
		Al					12.19	19.95
	Other		44.4	72.79	82.27	87.18	87.81	80.05

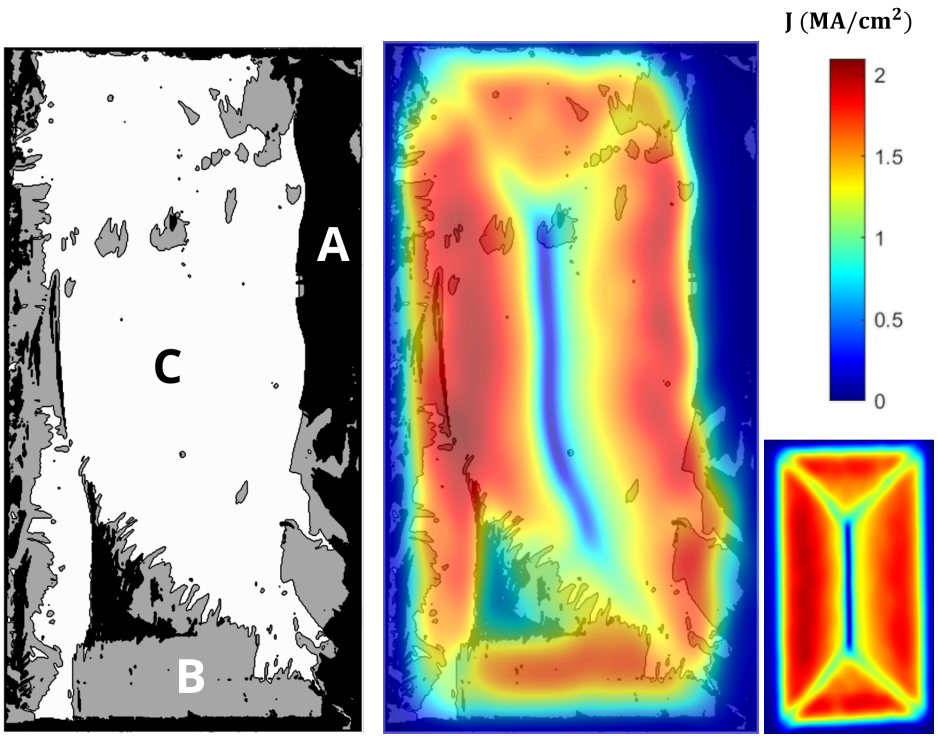
the sample. The final step of the combined microscopy analysis is to determine how each of the exposed layers affects the local electromagnetic properties of the coating.

3.3.3 Scanning Hall Probe Microscopy

The scanning hall probe microscopy (SHPM) is a means to obtain the magnetization profile of superconducting samples. It consists on cooling the sample below its critical temperature under an externally applied magnetic field (field cooling), which is then removed. Afterwards, the trapped magnetic field is measured throughout the entire sample surface with a scanning Hall probe. The trapped field can be used to calculate the current density distribution of the persistent currents in the sample after the removal of the external field [103]. Wherever there is damage to the REBCO layer, it will impact on local J_c, and therefore also in the field distribution.

Our SHPM measurements are in a liquid nitrogen (LN2) bath, at 77 K. The means to produce the external field applied during field cooling is the placement of a Nd-B magnet on top of the sample under test. The magnetic field density of 350 ± 50 mT imposed by the magnet is high enough to fully penetrate the HTS sample, and can be considered homogeneous and normal to the tape. The Hall probe used is a pre-calibrated Toshiba THS118 sensor driven by a 5 mA current and moved by step motors in the plane parallel to the tape and is positioned $400 \pm 100\,\mu$m above the sample's surface. To maintain this constant height, a thin aluminium foil is placed between the sensor casing and the sample, so as to always be in contact with the sensor.

Figure 3.12b shows the resulting current density profile obtained from the SHPM measurements of the sample introduced in Figure 3.10. The current distribution is superimposed with the three regions of Figure 3.10c, so we can easily correlate any decrease in J with the corresponding region. As a reference, Figure 3.12c shows the current distribution in an undamaged, non-delaminated sample. As we can see, the current flow is significantly different between the two samples. While the non-delaminated sample shows a regular, rectangular-shaped current profile, the one from our coating sample is distorted. While the current density still reaches high values for both Regions B and C, it vanishes completely in Region A. This shows that having remnant buffer layers or exposed REBCO show no significant reduction in the critical current density, and therefore the electromagnetic properties of the material are preserved in these areas. However, wherever there is excavation of the REBCO layer, it will cause a sharp drop in J_c, effectively destroying superconductivity in the vicinity.



(a) (b) (c)

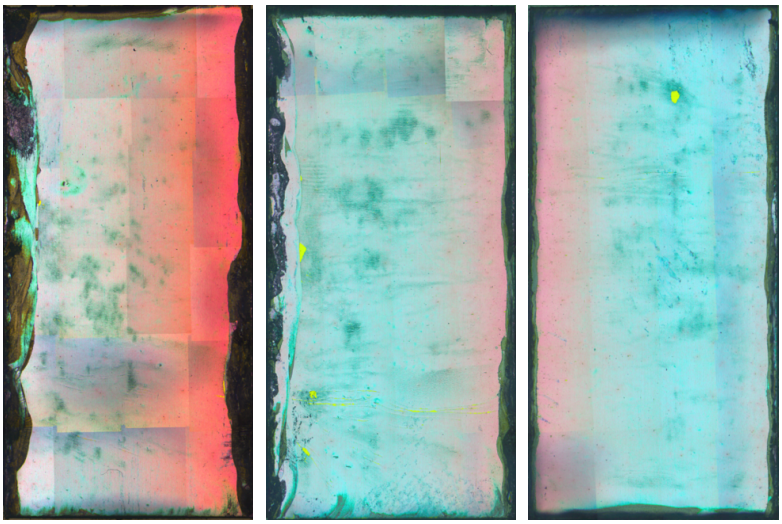
FIGURE 3.12: Current density distribution of delaminated 12 mm wide SuperPower coated conductors, obtained via SHPM. The distinct delamination interfaces (a) and SHPM results for (b) a coating sample superimposed with the three regions of Figure 3.10c and for (c) an undamaged, non-delaminated sample. While the current density flows in an uninterrupted rectangular pattern in the non-delaminated sample, it avoids regions of the coating where the HTS was damaged, particularly in the areas corresponding to Region A, where REBCO was excavated from the coating during delamination.

3.3.4 A Quick Assessment of Coating Quality

Now that we have correlated the three regions with their corresponding composition and potential damage to superconducting properties, the coating samples can be visually evaluated for a quick estimation of the defects introduced during the coating production. While this does not replace magnetization or surface impedance measurements, it serves as a quick assessment of the coating quality and was used throughout this work to improve the manufacturing steps and help in the design of IFAE's automated system, mentioned previously in this chapter. As an example, Figure 3.13 shows delaminated Fujikura coated conductors with different ratios of excavated REBCO. The coating used through this section is an example of a bad coating, since it makes it easier to visualize the different possible outcomes of delamination. Nevertheless, we have fine-tuned the production technique in order to preserve the superconducting properties of our coatings in over 95% of their area, with the damage being concentrated exclusively on the edges, as it can be observed in Figure 3.13.

It is interesting to note that, depending on the provider, the delamination tends to occur in different interfaces. Most notably, the samples prepared from Fujikura coated conductors, shown in Figure 3.13 present a very tiny percentage of buffer layers, identifiable as the yellow spots. On the other extreme, samples produced from Theva coated conductors often present almost the entirety of their surface covered with a remnant buffer layer, as seen in Figure 3.14.

Having remnant buffer layers covering the REBCO layer does not constitute a serious problem in terms of the coating's superconducting properties. From a magnetization perspective, the J_c remains unchanged, as shown in



(a) (b) (c)

FIGURE 3.13: Optical images of the substrates delaminated from 12 mm wide Fujikura coated conductors. The surfaces of the corresponding coatings are mainly consistent of exposed REBCO, with minor remnant buffer patches and (a) 20, (b) 15, and (c) 5% excavated REBCO, mainly concentrated on the edges. The coating manufacturing process was improved in order to minimize excavated REBCO, and therefore also minimize damage to its superconducting properties.

Figure 3.12. From a radio-frequency standpoint, on the other hand, it was shown that most buffer layers have little to no effect on the surface resistance of delaminated coated conductors. However, some buffer layers, such as the $LaMnO_3$ oxide layer present in SuperPower coated conductors, can show mild increases in the surface resistance below 1 T fields (see Figure 3.9) [49]. Remnant buffer layers can even be beneficial as a means to protect the REBCO layer from degradation due to direct contact with ambient humidity and other external influences.



FIGURE 3.14: Optical image of a coating produced from a 12 mm wide Theva coated conductor. Almost the entirety of the sample's surface is covered with a remnant buffer layer, only presenting minor damage close to the edges.

Chapter 4

Field Quality of the Coated Beam Screen

A REBCO CC-based coating is a promising solution to decrease the surface impedance of the beam screen in particle accelerators. However, it is important that not only the coating offers low surface impedance, but also that it does not disrupt the field in such a manner that the beam dynamics are compromised. To balance these two aspects, a proper coating geometry must be found.

In this chapter, we employ FEM numerical analysis of the coated beam screen under the field produced by the bending magnets, a dipole field, which corresponds to a magnetic length of 14.069 m, the largest among the different types of magnet used in the FCC. The numerical model used will be described, as well as the steps taken to study a broad range of coating geometries, and experimental measurements will be shown as a means to validate the simulation methodology.

4.1 The Finite Elements Method

Physical phenomena are often described mathematically as systems of differential equations. These equations describe the relationships between the dependent and independent variables of this system and can be classified with regards to the number of independent variables: ordinary differential equations (ODE), when there is only a single independent variable; and as partial differential equations (PDE), when there are multiple independent variables. While ODE's can often be solved analytically, this is not always the case for PDE's. For these scenarios, numerical methods such as the finite elements method (FEM) can be employed to find approximate solutions to the physical problem [104]. In the following chapters, the FEM is used with the COMSOL Multiphysics® software to study the electromagnetic as well as thermal and mechanical behaviour of the hybrid-coated FCC beam screen in different conditions.

For the sake of simplicity, let us consider a dependent variable u that can be described as a function of the independent variables corresponding to a one-dimensional space, $u = f(x)$. While u may not be directly obtained by analytical calculations, it can be approximated by a function u_h composed of linear combinations of distinct basis functions ψ_i, as in

$$u(x) \approx u_h(x) = \sum_i u_i \psi_i(x)\,. \tag{4.1}$$

The goal of the FEM is therefore to find the coefficients u_i that approximate u within a given error tolerance.

First, the independent variables, in this case, x, are discretized so that the variable space is split into several nodes. The basis functions are then defined for all x values (the entire domain Ω). The simplest way to define the basis functions is by using piecewise linear functions so that each $\psi_i = 1$ in a single node and $\psi_i = 0$ everywhere else, as

shown in Figure 4.1. Here we see a uniform node distribution with linear basis functions, as well as an example of the analytical dependent variable u and its numerical approximation u_h.

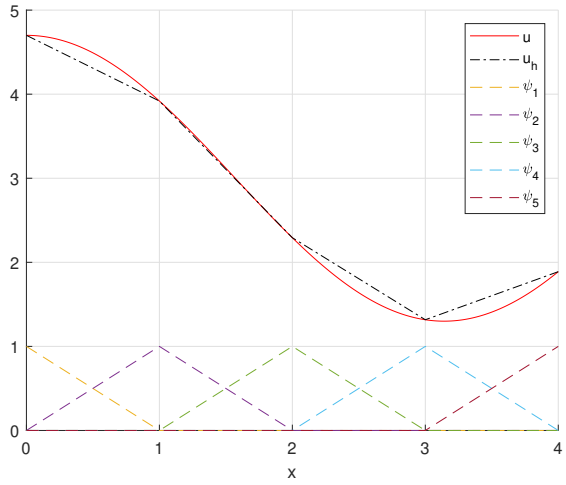


FIGURE 4.1: Dependent variable analytical function, numerical approximation and FEM linear basis functions in a uniformly distributed node space. Figure based on [104].

Now that we have defined the node distribution and the basis functions, the problem must be converted into its weak formulation. For that, let us consider an example defined by a simple PDE:

$$\nabla \cdot u = g(u,x)\,, \tag{4.2}$$

where $g(u,x)$ is a function of both the dependent and independent variables. Boundary conditions can restrict $g(u,x)$ or u in certain boundaries, and must be taken into account to solve the problem. The weak formulation for any ODE or PDE can be found by replacing u by its numerical approximation, multiplying both sides of the equation by a test function ϕ_j that belongs to Hilbert Spaces [105] and integrating over the domain Ω:

$$\int_\Omega \nabla \cdot u_h \phi_j dx = \int_\Omega g(u_h,x)\phi_j dx\,. \tag{4.3}$$

Therefore, the weak form relaxes the solution requirements when compared to its pointwise counterpart, because, while Equation 4.2 requires all the terms of the PDE to be well defined in all individual points of Ω, Equation 4.3 has to be true only for the domain as a whole, for all the test functions in the test functions space.

This results in a system of equations relating each coefficient u_i with the weak formulation coming from each ϕ_j, that can be summarised in matrix form by

$$AU_h = b\,, \tag{4.4}$$

where U_h is the dependent variable $1 \times n$ vector composed of u_i, b is a $1 \times n$ vector and A is the $n \times n$ system matrix. With the proper test functions, matrix A is sparse, resulting in a relatively fast solution. By solving this system, the coefficients u_i can be determined and the approximate solution u_h is found.

For time-dependent calculations, the u_i coefficients are functions of time, while ψ_i and ϕ_j are functions of the other independent variables. The coefficients are therefore recalculated for each time step by discretizing the time-domain independently. This can be done, for example, by approximating the derivative of the coefficients with respect to time

by its variation over the time step:

$$\frac{\partial u_i}{\partial t} \approx \frac{u_{i,t+\Delta t} - u_{i,t}}{\Delta t}. \tag{4.5}$$

4.2 Numerical Analysis Model

The simulations discussed throughout this chapter consist of FEM numerical analysis of different geometries of the hybrid REBCO-Cu coating under the dipole field produced by the bending magnets. To increase computation speed and facilitate that several geometries and field configurations are taken into account, the simulations will be developed in a 2D environment that corresponds to the cross section of the vacuum chamber (the $\hat{\boldsymbol{r}} \times \hat{\phi}$ plane of Figure 2.8).

In this section we will go through the formulation used to represent the electromagnetic phenomena related to the presence of HTS material in an external magnetic field, with an emphasis on how the resistivity of the superconductor is modelled. In addition, we will discuss how the coating geometry is described in terms of two parameters, and how the variation of these parameters affects the field quality in the vacuum chamber.

4.2.1 H-Formulation

As mentioned in Section 4.1, the FEM consists in finding approximate numerical solutions to the weak form of partial differential equations (PDE). The field quality inside the vacuum chamber emerges from the interaction between the materials of the beam screen and the external magnetic field generated by the bending magnets. This interaction can be described in terms of a few different dependent variables, using distinct PDE's. In this work, we use the H-formulation, which treats the magnetic field intensity H as the dependent variable, and is widely used as a means to study the behaviour of HTS in magnetic fields.

The H-formulation aims to numerically solve Faraday's equation,

$$\nabla \times \boldsymbol{E} = -\frac{\partial \boldsymbol{B}}{\partial t}. \tag{4.6}$$

To find this PDE as a function of a single state variable, namely H, three other relationships must be taken into account. Firstly, the materials present inside the vacuum chamber are non-magnetic, therefore their relative magnetic permeability μ_r can be considered equal to 1, which culminates in $B = \mu_0 H$ for all the simulation domains. Secondly, the electric resistivity of each material is different, and even presents a non-linar behaviour in the case of HTS. Therefore the relationship $\boldsymbol{E} = \rho \boldsymbol{J}$ will be individually described for each domain based on that material's resistivity. Finally, the current density is derived from the quasi-static approximation of Ampere's Law, $\nabla \times \boldsymbol{H} = \boldsymbol{J}$. Substituting these into Equation 4.6, we get

$$\nabla \times (\rho \nabla \times \boldsymbol{H}) = -\mu_0 \frac{\partial \boldsymbol{H}}{\partial t}. \tag{4.7}$$

In addition, Gauss's Law also has to be satisfied:

$$\nabla \cdot H = 0. \tag{4.8}$$

However, instead of being explicitly defined, this requirement is implicitly met for all time values by selecting initial conditions that satisfy it at $t = 0$. The initial conditions chosen for these simulations are $\boldsymbol{B} = 0$ and $\frac{\partial \boldsymbol{B}}{\partial t} = 0$ for all domains, at $t = 0$.

Since we are working in a 2D environment, these relationships can be further simplified by considering that the current and electric field only have longitudinal components ($\boldsymbol{E} = E_z \hat{\boldsymbol{z}}$, $\boldsymbol{J} = J_z \hat{\boldsymbol{z}}$), while the magnetic field is present

only in the cross-section plane ($\boldsymbol{H} = H_x\hat{\boldsymbol{x}} + H_y\hat{\boldsymbol{y}}$). The following system of equations can therefore be used to describe the entire set of relationships:

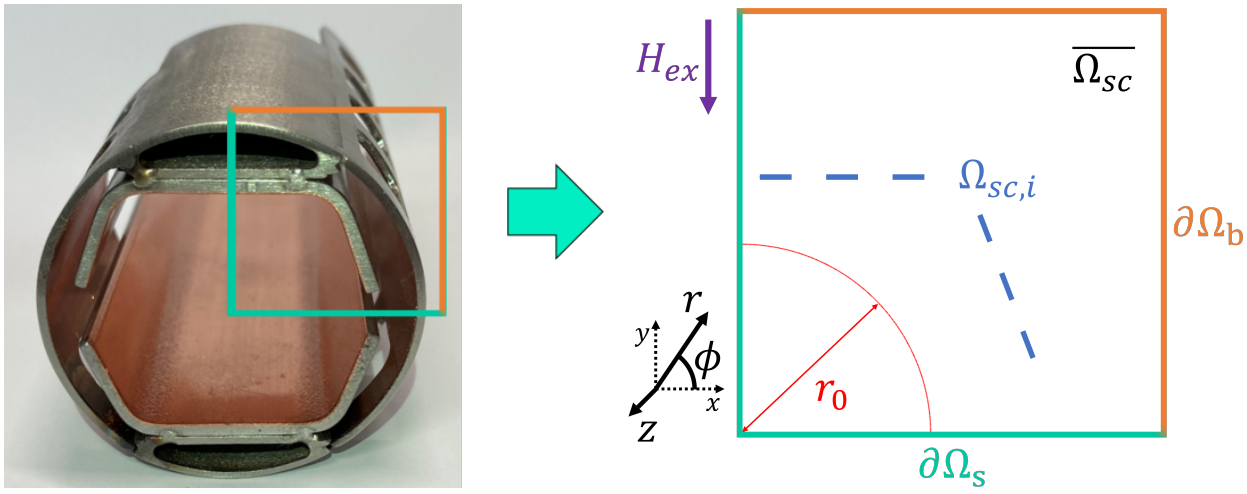
$$\mu_0 \frac{\partial H_x}{\partial t} = -\frac{\partial E_z}{\partial y} \tag{4.9}$$

$$\mu_0 \frac{\partial H_y}{\partial t} = \frac{\partial E_z}{\partial x} \tag{4.10}$$

$$E_z = \rho J_z \tag{4.11}$$

$$J_z = \frac{\partial H_y}{\partial x} - \frac{\partial H_x}{\partial y}. \tag{4.12}$$

Apart from this set of equations, it is also necessary to define a few constraints and boundary conditions. For that, we will refer to Figure 4.2, where a schematic of the simulation geometry is depicted. The superconducting segments of the hybrid coating are contained within the superconducting domains $\Omega_{sc,i}$. The other materials, that is, copper and steel, as well as the vacuum region are all part of a common domain, $\overline{\Omega_{sc}}$, where the material resistivity is defined as $\rho = 1\,\Omega$m. This specific value is commonly used in literature to represent materials with high resistivity and vacuum, where induced currents are expected to be negligible when compared to those flowing through the superconductor. Under the operating conditions of the beam screen, this is a reasonable assumption even for good conductors such as copper due to the low ramping rate of the magnetic fields. As we will see in Chapter 7, however, this assumption no longer holds for the high currents induced in the event of a quench of the main dipole magnets.



(a) (b)

FIGURE 4.2: Schematics of the simulation geometry. (a) Cross section of the beam screen, made of copper-coated stainless steel; and (b) simplified geometry of the first quadrant of the vacuum chamber. The simulation space is split into the superconducting domains $\Omega_{sc,i}$ and the $\overline{\Omega_{sc}}$ domain, which corresponds to all other materials and vacuum. The boundaries $\partial\Omega_b$ and $\partial\Omega_s$ represent the edges of the simulations space and the axes of symmetry, respectively. The reference radius r_0 marks the region where the magnetic field must be kept homogeneous.

The imposition of an external magnetic field is introduced by defining boundary conditions at the outer edges of the simulation space. At the $\partial\Omega_b$ boundaries, the magnetic field takes known values that vary over time. It is assumed that the distance from the HTS domains is large enough so that the field at these boundaries is the nominal magnetic

field coming from the magnets, according to

$$H_{b,x} = 0 \tag{4.13}$$

$$H_{b,y} = H_{ex} = \frac{t}{\mu_0}\frac{\partial B}{\partial t}, \tag{4.14}$$

where $\frac{\partial B}{\partial t}$ is the rate of change of the dipole field over time, which during field ramp up corresponds to $13.3\,\mathrm{mT/s}$.

Due to the symmetry of the beam screen and of the purely vertical external field, there is no need to consider the entire vacuum chamber in the simulation space. Instead, it can be limited to a single quadrant, provided the proper boundary conditions are used to enforce symmetry. The symmetry axes are defined in the $\partial\Omega_s$ boundaries, where the magnetic field values are constrained as follows:

$$H_{s,x} = 0\,. \tag{4.15}$$

This ensures that all the magnetic field lines are vertical when crossing the $\partial\Omega_s$ boundaries.

Finally, we assume throughout these simulations that the HTS segments are electronically insulated from each other, meaning that all currents are contained within each HTS domain, never crossing to another. This property depends on the techniques employed to produce the HTS coating, and may not be true for the methodology presented in the previous chapter. A deeper study analysing the flow of current between the layers of the coating is presented in Chapter 8, at which point the influence of other characteristics such as the contact resistance between the layers is taken into account. To ensure no current flows between different materials, a constraint is introduced by setting the total current of any given HTS domain $\Omega_{sc,i}$ to zero at all times. With this, all current loops will be contained within a single domain:

$$I_i = \int_{\Omega_{sc,i}} J_z dS = 0\,. \tag{4.16}$$

It is know that large aspect ratios, particularly those of the HTS domains, can be detrimental to the computation time of the simulations. To increase convergence speed, a homogenization method is used, based on which the thickness d of the $\Omega_{sc,i}$ domains is multiplied by a factor k_d [106]. To compensate for that with regards to its electromagnetic behaviour, the current density of the material is divided by the same factor, resulting in an unchanged sheet critical current density $J_c d$.

4.2.2 REBCO Resistivity

As discussed in Section 2.1, the resistivity of HTS materials is highly non-linear in the mixed state and depends on several factors. Since we are interested in the time-dependent behaviour of the beam screen, it is important that our model takes into account dynamic effects that may affect the current flow inside the superconducting material over time. To do this, the resistivity of the REBCO segments is given by

$$\rho_{sc} = \frac{E_c}{J_c}\left(\frac{J}{J_c}\right)^{N-1} + \mu_0 f d^2 \left[\frac{2H_{ac}}{J_c d} - \left(1 - \frac{J}{J_c}\right)\right]. \tag{4.17}$$

The fist term of Equation 4.17 comes from Anderson-Kim's theory, taking into account the flux creep that arises when the current density reaches values close to and above J_c. The second term comes from the wandering of vortices induced by the AC magnetic field produced by the particle beam (see Section 2.2). While said magnetic field is more resembling of a gaussian wave than a sinusoidal one, it can be considered as the latter in a first approximation. Likewise, the direction of the field is not perfectly perpendicular to the c-axis of the REBCO nor to the DC field, but

will be considered to be so, resulting in an AC field perceived by the HTS as $\boldsymbol{h}_{ac}(t) = H_{ac}\cos(\omega t)\hat{\boldsymbol{b}}$, where $\hat{\boldsymbol{b}}$ denotes the direction of the width of the delaminated CC.

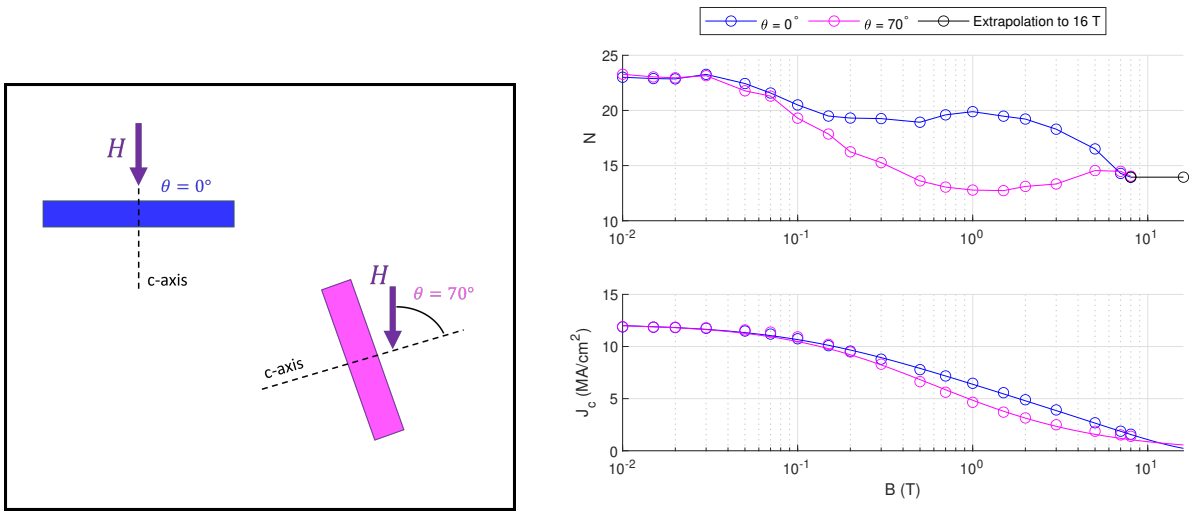
The dependence of J_c with the magnetic field is added in accordance to Equation 2.4, rewritten here in terms of the magnetic field intensity H:

$$J_c = J_c^{sf}\left(1+\frac{H}{H^*}\right)^{-\alpha}\left(1-\frac{H}{H_{irr}}\right)^2. \tag{4.18}$$

Note that, instead of scaling the magnetic field with the angle, as suggested in Section 2.1, the unscaled field value is used. To compensate for that and still account for HTS anisotropy, the coefficients of Equation 4.18 will be calculated separately for each HTS segment.

Under the external dipole field to which the beam screen is submitted, the HTS segments located on the top and bottom walls will be impinged by the magnetic field parallel to the c-axis, as shown in Figure 4.3a. On the other hand, the same magnetic field will form a $\approx 70°$ angle with the segments on the diagonal walls. Therefore, separate data sets for field angles of zero and 70° with the c-axis can be used to fit the measured curves to Equation 4.18. This assumes that the field disturbance produced around the HTS segments is small compared to the external field, which is a reasonable assumption when it comes to the J_c and N dependencies with field and angle.

The measured data used to calculate the coefficients for both field angles comes from measurements of SuperPower CC's at tilted angles [63] and is presented in Figure 4.3b, along with the fitted curves. Unlike J_c, the dependence of the transition index N with field intensity and angle is added by interpolating the measured data in the 0 to 8 T range and constantly extrapolating it from 8 to 16 T.



(a) (b)

FIGURE 4.3: J_c and N dependence with magnetic field angle and intensity for 0° and 70°. (a) Schematic representation of the field angle for the HTS segments in the beam screen; and (b) measurement data of N and its extrapolation to 16 T, and measurement data of J_c (points) and fitted curves (lines). Based on data of SuperPower coated conductors at 50 K from [63].

The coefficients obtained for Equation 4.18 are shown in Table 4.1. Note that any high enough value of H_{irr} would accurately describe the used data. Since H_{irr} must be smaller than H_{c2}, it has been limited to $\mu_0 H_{irr}$ =180 T, which is a reasonable $\mu_0 H_{c2}$ value for REBCO CC's when the applied magnetic field is parallel to the ab-plane.

TABLE 4.1: Coefficients obtained for Equation 4.18 from fitting *SuperPower Inc.* data from [63] at 50 K and field angles of 0º and 70º.

	$J_c^{sf}(MA/cm^2)$	$\mu_0 H^*(T)$	$\mu_0 H_{irr}(T)$	α
Top Wall	12.2	0.2	22	0.31
Diagonal Wall	12.2	0.5	180	0.83

4.2.3 Geometry Parametrization

As mentioned previously, one of the objectives of the FEM simulations of the coated beam screen is to find coating geometries that comply with both field quality and surface impedance criteria. To do that, it is convenient to describe the coating geometry as a function of a few parameters. These parameters can then be varied in order to evaluate their impact on the field homogeneity.

However, in order to reduce a complex geometry such as that of the hybrid coating to such a simple description, a set of rules must be defined to decrease the range of possible geometries that are considered. These rules were formulated with the intent of decreasing the computation effort demanded by the simulations as well as complying with physical requirements of the beam screen and are as following:

1. The coating is symmetric in the four quadrants of the vacuum chamber;
2. There are no HTS segments in the bent portion of the beam screen walls;
3. The number of HTS segments of each diagonal wall is equal to half that of the top (or bottom) wall; and
4. The segments located in either end of each wall must be HTS.

These restrictions allow us to summarise the coating geometry as a function of two parameters: the number of HTS segments per quadrant (n), and the ratio of HTS covering the flat portion of the walls (p). This pair of parameters was chosen not only because they can be used to easily describe the geometry, but also because they are conveniently correlated with the variables we want to evaluate. On one hand, the larger the HTS ratio p is, the lower the expected surface resistance is. On the other, the trapped field for a give ratio p is expected to decrease with the number of segments n, resulting in an increase in field quality. Note that n should always be an even integer in order to satisfy rule 3.

Figure 4.4 shows an example of a coating geometry, with $n = 6$ and $p = 50\%$. The dimensions of the alternated segments can be easily calculated from n and p. First, let us examine the top wall, the half-width of which is given by w_{top}. The HTS width w_{sct} and the copper gap width g_{top} are obtained by

$$w_{sct} = 2w_{top}\frac{p}{n} \tag{4.19}$$

$$g_{top} = 2w_{top}\frac{1-p}{n-1}. \tag{4.20}$$

The corresponding dimensions for the diagonal wall, with width w_{dia} and gap g_{dia}, are described by[1]

$$w_{scd} = 2w_{dia}\frac{p}{n} \tag{4.21}$$

$$g_{dia} = \begin{cases} 2w_{dia}\frac{1-p}{n-2} & n > 2 \\ 0 & n = 2 \end{cases}. \tag{4.22}$$

Knowing this, it is also straightforward to calculate the position of each HTS segment i along a given wall:

$$s_{sct,i} = \left(i - \frac{1}{2}\right)(w_{sct} + g_{top}) \tag{4.23}$$

$$s_{scd,i} = \left(i - \frac{1}{2}\right)(w_{scd} + g_{dia}) - \frac{g_{dia}}{2}. \tag{4.24}$$

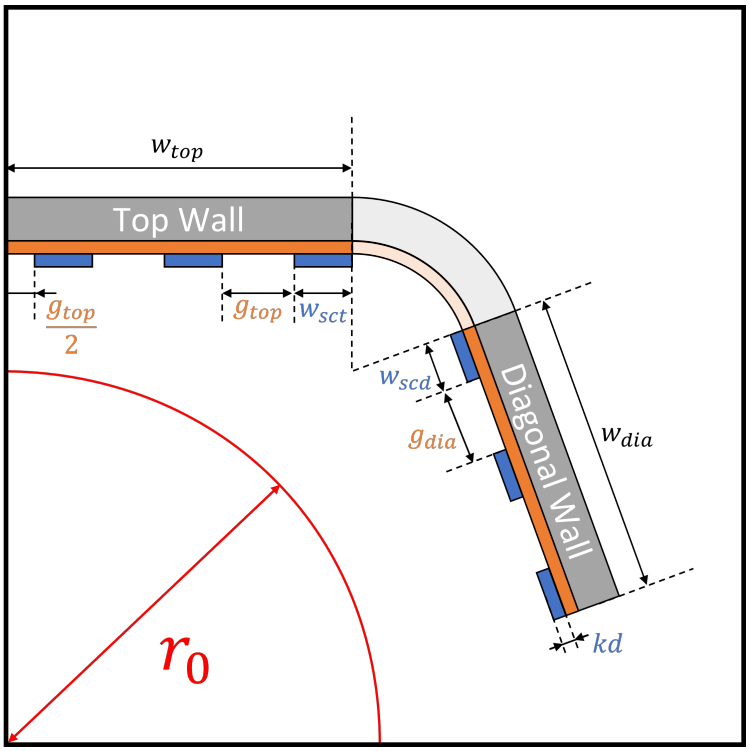


FIGURE 4.4: Schematic of the first quadrant of the inner walls of the FCC beam screen with a coating geometry of $n = 6$ and $p = 50\%$. The variables used to represent the dimensions of the HTS segments and the copper gaps are displayed, as well as the reference radius for field homogeneity.

The distribution of current induced in the superconductor segments, which in turn is affected by the geometry of the hybrid coating, will lead to distortions in the surrounding magnetic field. According to the field quality requirements imposed by CERN, the normalized field harmonics introduced by the coating within a reference radius r_0 from the center of the vacuum chamber must not surpass a few units of 1×10^{-4} (see Section 2.3 and Figure 4.4). This reference radius usually corresponds to $2/3$ of a magnet aperture, when referring to the quality of the field produced by a magnet. Applying the same criterion for the FCC beam screen, but considering an average of the distance between the inner walls of the beam screen and the center of the vacuum chamber, we obtain an $r_0 = 9\,\text{mm}$.

[1] Note that any geometry with two segments per quadrant contains only a single segment in each diagonal wall, meaning there are no copper gaps in the diagonal walls. This results in an HTS ratio that is larger than the value of p as a consequence of the specific case of $n = 2$ in Equation 4.22.

The field harmonics will be calculated according to Equations 2.62 and 2.63 at $r = r_0$. Due to the quadrant symmetry of the beam screen, the coating and the dipole field, the skew coefficients a_n vanish, as well as the even normal coefficients. Therefore, only the odd b_k coefficients must meet the field quality criterion.

By parametrizing the coating geometry, we aim to find the regions of the (n, p) combination space that satisfy the field homogeneity requirements, while still allowing for a relatively high HTS ratio p, so that the surface impedance can be significantly reduced when compared to a pure copper coating.

4.3 Field Quality Simulations

This section will present and discuss the results of the electromagnetic simulation of the hybrid REBCO-Cu coating of the beam screen during magnetic field ramp-up of the FCC bending magnets. The simulations were conducted with the COMSOL Multiphysics® software, using time-dependent studies of the general form PDE environment [107], which allows for the input of the coefficients of a generic PDE, as well as its boundary and initial conditions.

As the magnetic field increases from 0 to 16 T, the behaviour of the superconducting segments present in the beam screen coating will be studied, as well as the field harmonics produced at the reference radius r_0. We will see how the currents flowing through the HTS are affected by the demagnetizing effect induced by the AC field generated by the beam. In addition, measurements of magnetization and surface resistance of hybrid coating samples will be used to validate the simulation results and confirm whether the evaluated geometries show low surface resistance in conditions similar to those of the FCC.

4.3.1 Ramping up the Dipole Field

In particle accelerators such as the FCC, the bending magnets are first activated while there are no particles orbiting. The dipole magnetic field is then increases to H_{inj}, which is the magnetic field required for the particle bunches to be injected into the machine. After particle injection, the field is increased to H_{top}, the magnetic field at top energy, at which point the beams are ready for collision. In the case of the FCC, these values correspond to $\mu_0 H_{inj} = 1\,\mathrm{T}$ and $\mu_0 H_{top} = 16\,\mathrm{T}$, respectively, with a ramping rate of $13.3\,\mathrm{mT/s}$. In addition, to preserve the beam's orbit, field quality has to be maintained whenever there is a beam circulating in the vacuum chamber, that is, between injection and top energy. Therefore, the field quality within the vacuum chamber for field values below 1 T is not relevant for beam stability.

It is interesting to investigate how the superconducting segments of the hybrid coating react to the ramping dipole field introduced by the bending magnets. To do that, let us consider the numerical results obtained from the FEM simulation of an arbitrary coating geometry, with $n = 6$ and $p = 50\%$, henceforth referred to as "$(6, 50\%)$", without an oscilating field ($H_{ac} = 0$). In the top charts of Figure 4.5, we can see the current density and its corresponding J_c in an arbitrary point in the HTS domains. As expected, the J_c decreases as the field increases according to Equation 4.18. After a short transition interval, which happens below 1 T, the maximum current density J_{max} presents the same tendency to decrease with the magnetic field.

As a consequence, the trapped field in the HTS segments also decreases with the field, resulting in a decreasing distortion in the surrounding magnetic field. This is represented in a rather simplistic manner by the maximum relative field disturbance,

$$\eta(t) = \max_{r=r_0} \frac{|\boldsymbol{H}(r,\phi,t) - \boldsymbol{H}_{ex}(t)|}{|\boldsymbol{H}_{ex}(t)|} = \max_{r=r_0} \frac{\Delta H(r,\phi,t)}{H_{ex}(t)}\,, \tag{4.25}$$

evaluated at $r = r_0$ for each point in time, or in this case, for each value of applied field H_{ex}. The bottom chart in Figure 4.5 shows η, and we can see its descending tendency. The field harmonics are also presented, calculated from Equation 2.63, also decreasing with the applied field.

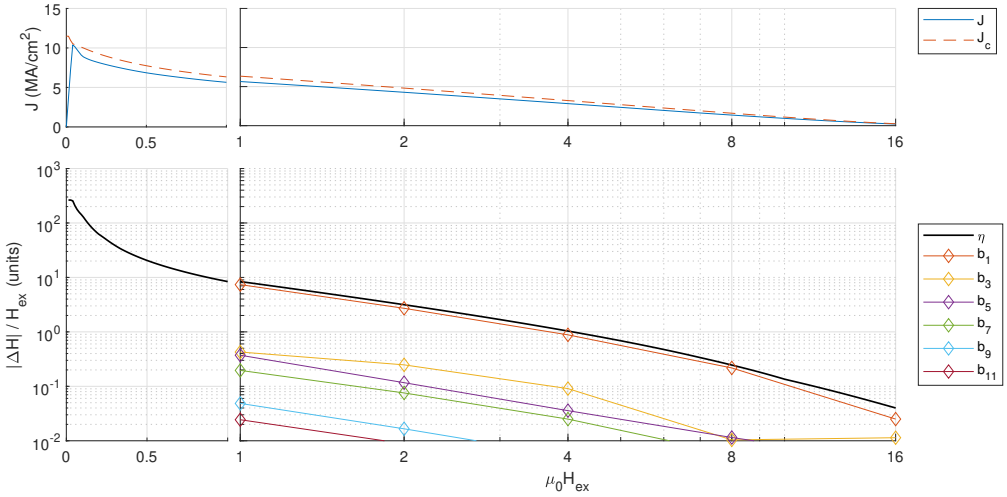
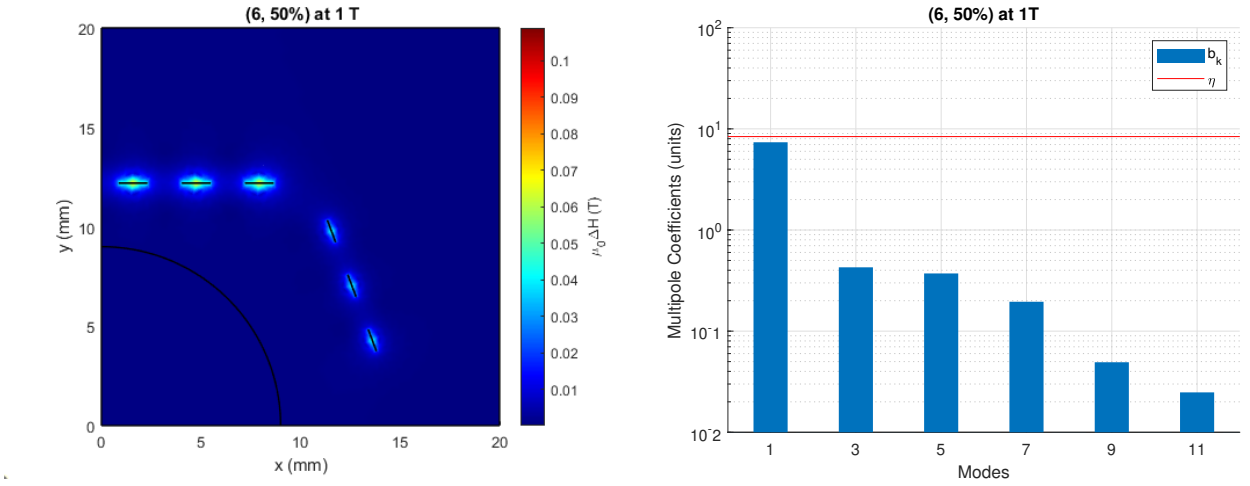


FIGURE 4.5: Simulation results of hybrid coating with $n = 6$ and $p = 50\%$. The dipole field increases from 0 to 16 T at a constant rate of 13.3 mT/s, which correspond to the conditions of the FCC bending magnets. The current density flowing through an arbitrary point inside the HTS domains and the corresponding J_c are shown on the top graphs; and the relative maximum field disturbance η (see Equation 4.25) and the field harmonics b_k calculated at $r = r_0$ are presented in the bottom graphs.

There are two main points to be derived from these results. First, that although η may not be the most precise way to quantify the field quality within the vacuum chamber, it is always larger than each individual field harmonic, which means that if η satisfies the field quality criterion, so too will the harmonics. Second, that due to the decreasing nature of J_c in an increasing dipole field, the largest field disturbance between injection and top energy, that is, between 1 and 16 T, happens at 1 T, which tells us that the moment of injection is the most critical in terms of field quality. These two points combined suggest that only a single variable has to be considered for each coating geometry to ensure it fulfills the field quality criterion: $\eta_{max} = \eta(\mu_0 H_{ex} = 1\,\mathrm{T})$. This will be the basis of the parametric evaluation of the coating geometries, which will be discussed later on this section.

Figure 4.6 presents the field disturbance in the vacuum chamber and the field harmonics at the reference radius at $\mu_0 H_{ex} = 1T$. Figure 4.6a shows that the distortion produced by the HTS segments reaches values as high as 10% in the proximity of the HTS domain, but decreases sharply as the distance from the coating increases. Figure 4.6b shows more clearly the first six odd normal field harmonics when the external field reaches 1 T. Here we see once again that all harmonics are below η and that the largest contribution to field distortion comes from the dipole coefficient, b_1. This is in agreement with the fact that the currents induced in the HTS tend to create a magnetic field that opposes the external field, creating a mainly dipole distortion in the opposite direction. It is worthy of notice that this geometry results in $b_k < 10$, which could be low enough to meet the field quality criterion. However, the relatively low HTS ratio, $p = 50\%$ would result in surface resistance values that can still be significantly improved.

In Figure 4.7, we see in more details the electric behaviour of the HTS segments during field ramp-up. After the short transition at very low fields, the electric field quickly reaches an equilibrium. Indeed, from Equations 4.9 and 4.10, the electric field should be proportional to the rate of change of the magnetic field. If we consider the HTS



(a) (b)

FIGURE 4.6: Field disturbance (a) in the vacuum chamber and (b) field harmonics at the reference radius at $\mu_0 H_{ex} = 1T$ for the $(6,50\%)$ geometry.

homogeneous along the c-axis, we obtain by integrating Equation 4.10 over x,

$$E = \mu_0 \frac{\partial H_y}{\partial t}(x - x_0) \approx \mu_0 \frac{\partial H_{ex}}{\partial t}\Delta x, \tag{4.26}$$

where x_0 is the point inside the HTS domain where $E = 0$, which corresponds to the center of the HTS segment if it is electronically insulated. By inputting the field rate of $13.3\,\mathrm{mT/s}$ and the distance between the data point and the center of the HTS segment $\Delta x = 0.69\,\mathrm{mm}$, we get $E/E_c \approx 0.1$, the equilibrium value reached in Figure 4.7. By rearranging the power law, we can obtain an approximation of J for all field values during ramp-up after the transient as

$$J = J_c \left(\frac{E}{E_c}\right)^{\frac{1}{N}} \approx J_c \left(\frac{\mu_0}{E_c}\frac{\partial H_{ex}}{\partial t}\Delta x\right)^{\frac{1}{N}}. \tag{4.27}$$

This is particularly useful as a quick estimation of the currents flowing in the HTS, that does not rely on the more complicated and time-consuming FEM solution. The obvious downside is not considering the transient behaviour of the HTS, at which point the electric field may assume very different values.

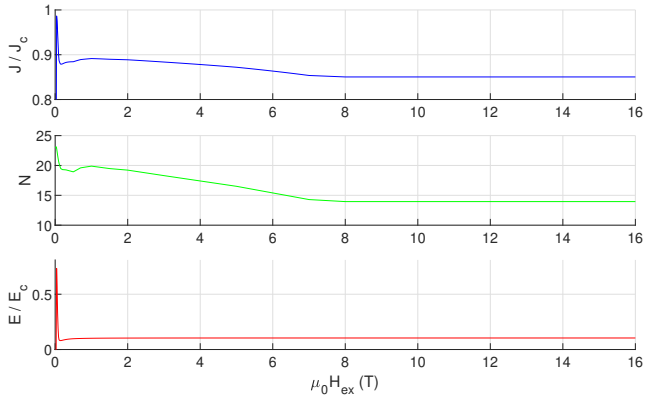


FIGURE 4.7: Current density J and electric field E normalized with respect to their critical values and transition index N in an arbitrary point inside the HTS domains of the top wall for the $(6,50\%)$ geometry while ramping the field from 0 to 16 T.

4.3.2 AC Demagnetization at High DC Fields

So far, the results shown have not considered the oscillating magnetic field produced by the beam. However, after beam injection, there may be an effect on the magnetization of the HTS segments due to their interaction with the AC field. This effect is already accounted for in the REBCO resistivity, given by the second term of Equation 4.17. We will now analyse the impact of different levels of H_{ac} in the currents flowing through the HTS.

Accodring to [74], the presence of an oscillating field perpendicular to both the DC field (the dipole field, in this case) and the c-axis of the superconductors induces the movement of vortices towards the center of the HTS, which in turn generates an electric field opposed to the current flow. This has the effect of demagnetizing the material, which can be understood as the permeation of vortices, decreasing the overall trapped field, as well as a decrease in the resulting current flow due to the dissipation of energy coming from the emergence of an opposing electric field. In any case, an equilibrium point is reached after a given number of cycles, at which point the vortex motion is interrupted and the induced electric field vanishes, leading to a current density value J_{eq} of

$$\frac{|J_{eq}|}{J_c} = \begin{cases} 1 - 2\frac{H_{ac}}{dJ_c}, & H_{ac} < \frac{d}{2}J_c \\ 0, & H_{ac} >= \frac{1}{2}dJ_c \end{cases}. \tag{4.28}$$

When superimposed to a ramping DC field, this equilibrium value will also change over time, along with J_c. However, since the timescales of the AC field are much shorter than those of the DC field, we can assume that the demagnetization effects happen instantaneously with regards to the ramping time of the DC field. This results in a $J(H_{ex})$ curve that is limited by J_{eq} on its upper side.

Simulation results of the HTS exposed to such conditions considering different H_{ac} are shown in Figure 4.8, where the equilibrium current density J_{eq} is plotted in dotted lines and the continuous lines of different colors correspond to the resulting current density due to the combined effect of both DC and AC fields. Note that whenever the current values without an AC field (black continuous line) are lower than the limiting J_{eq}, no demagnetizing effect is observed, which is the case for the entire $H_{ac} = 250\,\mathrm{A/m}$, the maximum AC field expected for the FCC beam screen. However, for higher H_{ac}, as H_{ex} increases and J_c decreases, so too does J_{eq}, even resulting in a complete demagnetization at 16 T for $H_{ac} >= 8 \times 250\,\mathrm{A/m}$.

In the case of partial demagnetization, the field harmonics will be affected by the decreasing currents, with an overall tendency of decreasing as well, resulting in an actual improvement in field quality. Most noteworthy, however, is the fact that only an AC field more than one order of magnitude higher than the one predicted for the FCC beam screen is strong enough to demagnetize the HTS segments at $\mu_0 H_{ex} = 1\,\mathrm{T}$.

At this point it is worth bringing into discussion the viability of this model when applied to the FCC beam screen. While the field produced by the particle beam presents high frequency components, it is very different from a sinusoidal wave in time. Because of this, the vortex displacement per cycle Δx will likely be smaller than the result of Equation 2.37, resulting in a lower demagnetizing effect and a larger J_{eq}.

These last two points combined tell us that, for the FCC conditions, we can assume that the most critical point in terms of field quality is still the moment of injection, at 1 T, allowing us to disregard the demagnetizing effect of the AC field, especially at low DC fields.

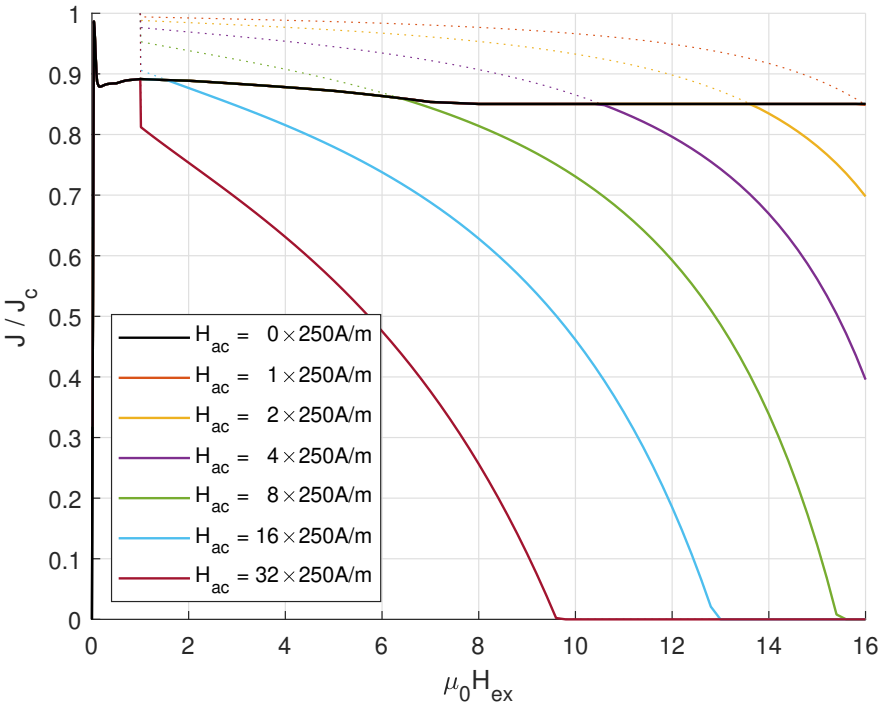


FIGURE 4.8: Normalized current density J (continuous lines) and equilibrium current densities J_{eq} (dotted lines) imposed by the presence of a perpendicular AC magnetic field with intensity H_{ac}. The electric field induced in the HTS by the AC fields limits the current density in the HTS so that $J <= J_{eq}$ [74]. The maximum expected AC field value at the beam screen is $H_{ac} \approx 250\,\mathrm{A/m}$.

4.3.3 High Field Quality Geometries

Now that we have established that the field homogeneity of the vacuum chamber will be at its worst during injection, we can use the maximum relative field disturbance η at 1 T (see Equation 4.25) as a means to evaluate several coating geometries with respect to their impact on the field quality. If the quality criterion is satisfied for $\eta(1\,\mathrm{T})$ it will also be for all field harmonics between injection and top energy.

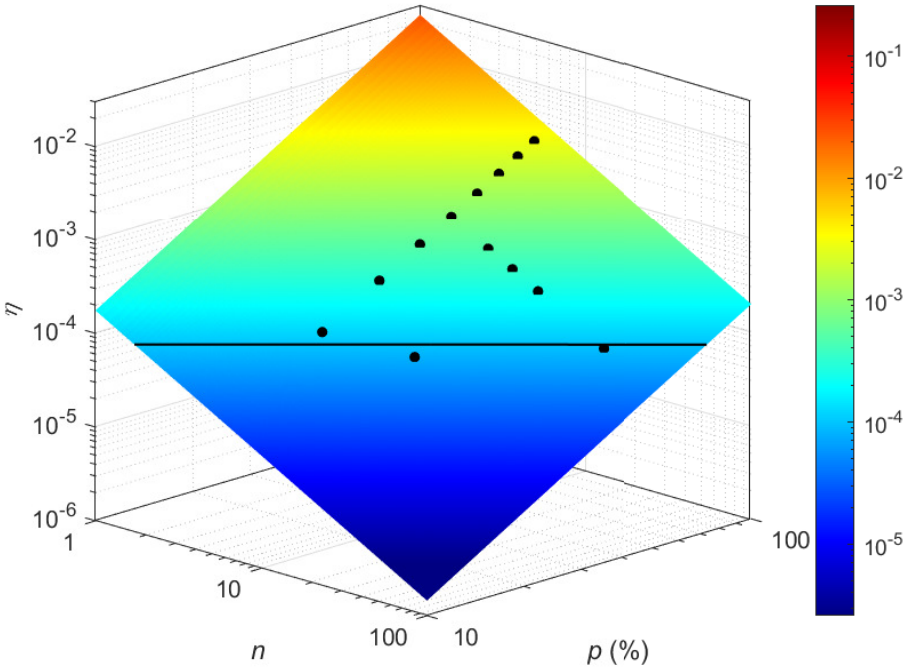
To do this, the same simulation procedure was repeated, only varying the geometric parameters, p and n. The results are shown in Figure 4.9. Each simulated coating geometry is represented by a point in the graph of Figure 4.9a with their corresponding harmonics shown in Figure 4.9b. With this, η can be obtained as a function of n and p according to

$$\eta = 240\frac{p^{2.1}}{n}\,[\text{units}]\,. \tag{4.29}$$

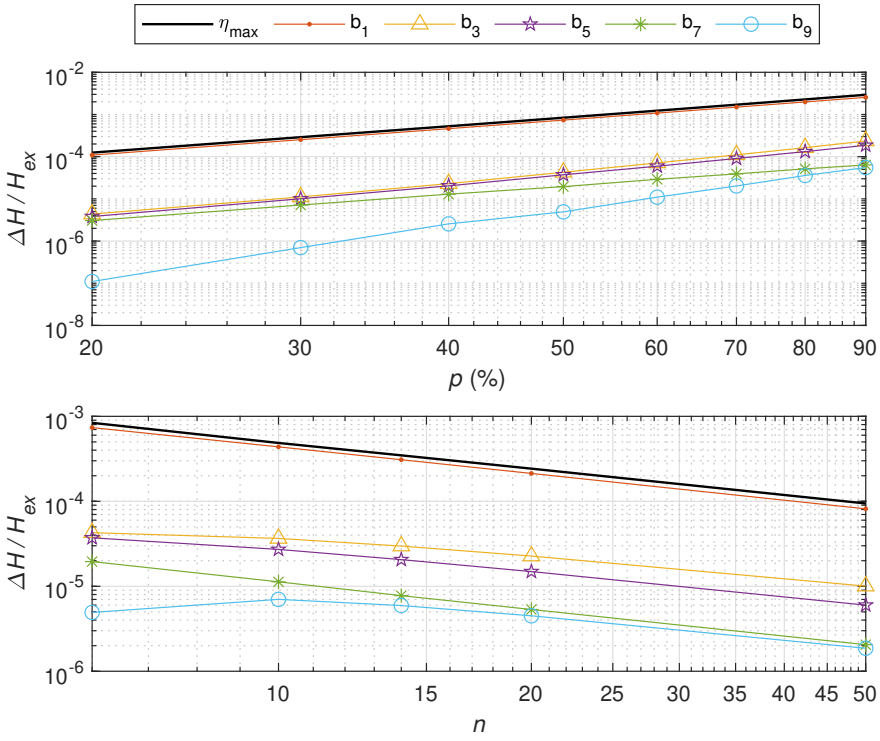
The surface described by this equation is the colored plane in Figure 4.9a, which can be used to extrapolate the simulation results. As expected from the behaviour of the trapped field in a HTS film (see Section 2.1), η is inversely proportional to n, but is directly related to p. The region below the black line corresponds to a relative field disturbance lower than one unit. Since the field quality criterion demands field harmonics of the order on one unit, the line actually represents a rather harsh limit, and even coating configurations that are above but close to it would still present acceptable field quality.

In order to achieve such low harmonics n and p must satisfy

$$n \gtrsim 240p^{2.1}\,, \tag{4.30}$$



(a)



(b)

FIGURE 4.9: Field homogeneity results for several coating geometries. (a) Maximum relative field disturbance η as a function of the HTS ratio p and number of segments n. Simulated data are shown in the dots, the colored surface represents the extrapolated relationship and the black line corresponds to $\eta = 1$ unit. (b) Field harmonics for $n = 6$ (above) and $p = 50\%$ (below).

which means that the number of segments n required to compensate for the HTS ratio p varies with, roughly, its square. To achieve low enough values of surface resistance, it might be necessary to increase p to values as close to 1 as possible, which in turn would require n to get ever closer to 240 segments per quadrant. Table 4.2 lists some possible geometries that would comply with the field quality criterion considering different ratios p. An increase in the number of segments would also require narrower HTS widths w and copper gaps g. Therefore, for different ranges of n, distinct striation technologies would be the most appropriate, such as mechanical scribing, ink-jet printing, two-level undercut profile substrate (2LUPS) and laser scribing. It is worth pointing out, though, that the coefficients in Equation 4.29 depend on the CC provider, and therefore so too will the combinations of n and p that fulfill the field quality criterion.

TABLE 4.2: Examples of geometries that comply with the field quality criterion and the technologies necessary to produce their striation pattern.

p	n	$w_{sct}(\mu\text{m})$	$w_{scd}(\mu\text{m})$	$g_{top}(\mu\text{m})$	$g_{dia}(\mu\text{m})$	η(units)	Technology
0.25	12	361	293	1180	1055	1.088	Mechanical scribing
0.50	48	180	147	184	153	1.166	Ink-jet printing
0.75	106	123	99	41	34	1.237	2LUPS
0.95	172	96	78	5	4	1.253	Laser scribing

4.3.4 Dipole Cancellation and Proposed Geometry

Although a good field quality is achievable simply by increasingly splitting the HTS into a large enough number of segments, another solution can be taken into account to further relax the field quality criterion and broaden the range of complying geometries. As shown in Figure 4.9b, the dipole component of the field harmonics b_1 is always the highest contribution to field inhomogeneity by a significant margin. However, the bending magnet itself produces a mainly dipole magnetic field. If this field is slightly over-tuned to compensate for the opposing effect of the HTS coating, the combined field harmonics will present a null dipole contribution ($b_1 = 0$). In this case, the field quality criterion has to be met only by the higher mode harmonics, (b_3, b_5, b_7, ...), which results in more geometries being acceptable in terms of field quality.

Figure 4.10 presents the field harmonics and maximum relative field disturbance of different coating geometries. The results for $(6, 50\%)$ are shown once again in Figure 4.10a, to serve as a reference, but we can see that already with this geometry the higher mode harmonics are below one unit. In terms of field quality, this would classify it as a complying geometry. However, the relatively low HTS ratio could still be an issue with regards to surface impedance. Figures 4.10b to 4.10d show the results of coating geometries with a higher ratio of $n = 95\%$, which is still a realistic value due to the required widths and gaps necessary to produce such narrow segments. As we can see, for both $n = 6$ and $n = 4$ the largest field harmonics (excluding b_1) are within a few units. This is not the case for $n = 2$ which surpasses 10 units in b_3, b_5 and b_7. With this we conclude that in order to keep such a large p, it is only necessary to striate the coating into four segments per quadrant, a easier prospect than the $n \approx 172$ necessary without the b_1 harmonic correction.

At this point it is worthwhile to make a closer examination of the dimensions of the $(4, 95\%)$ coating geometry. Table 4.3 lists the dimensions of the coating geometries analysed in Figure 4.10. Note that, for all the considered geometries, the widths of both diagonal and top wall segments are of the order of a few millimeters. We can thus tune the widths of the segments to match those commercially provided by the manufacturers, that is, 12, 4 and 2 mm, which would bypass the striation step of the coating production process, making it easier, faster and cheaper.

Based on this we can modify the widths of the $(4, 95\%)$ geometry so that $w_{sct} = 4$ mm and the two segments of each diagonal walls are 4 and 2 mm wide. By doing this, the number of segments is preserved, albeit now with distinct

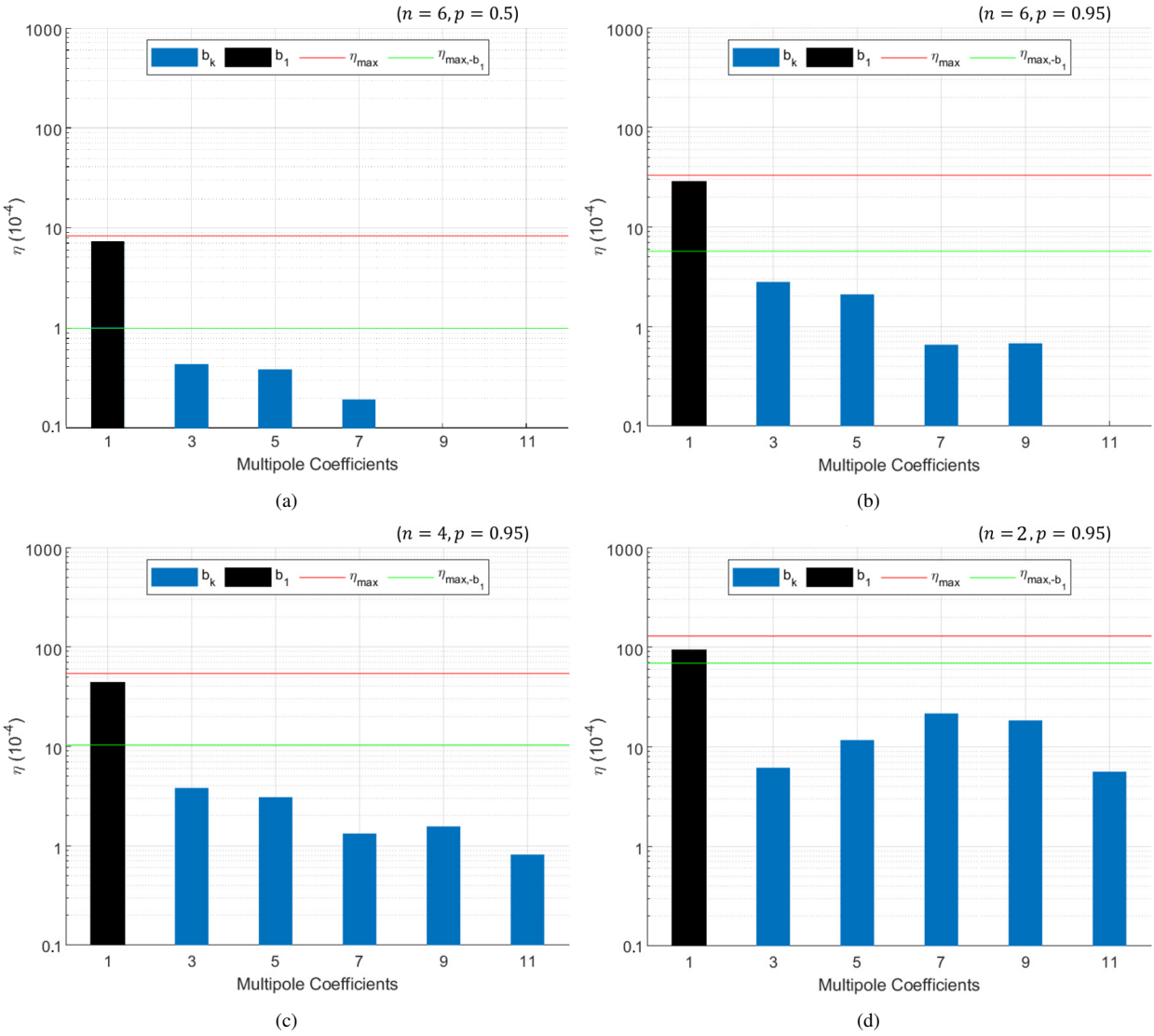


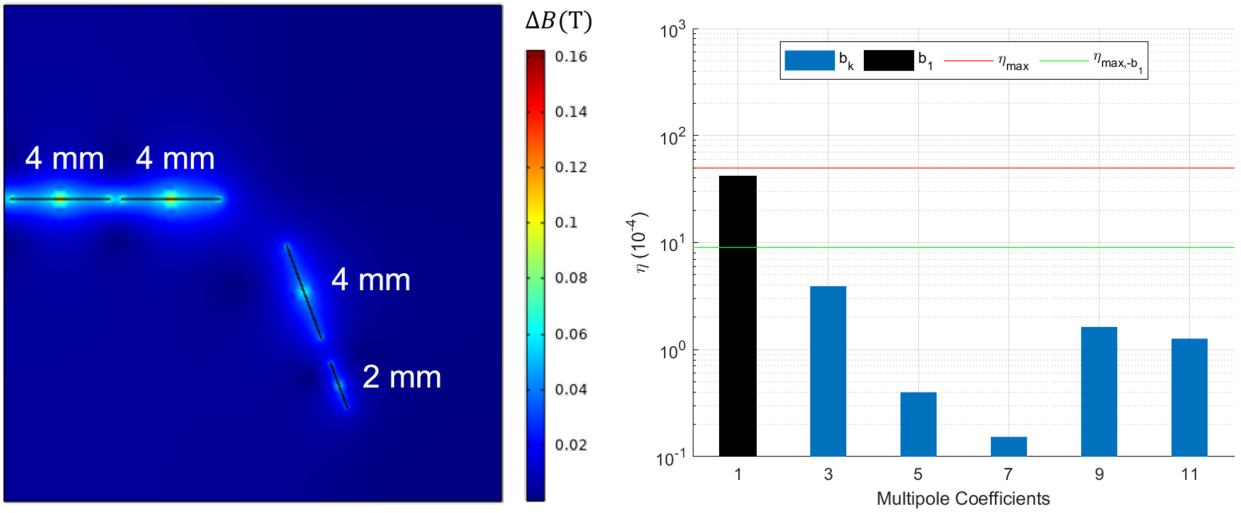
FIGURE 4.10: Field harmonics of four geometries and the maximum relative field disturbance η with (green line) and without (red line) cancellation of the dipole component. The geometries are (a) 6, 50%, (b) 6, 95%, (c) 4, 95%, and (d) 2, 95%.

TABLE 4.3: Dimensions of the geometries whose field quality results are shown in Figure 4.10.

p	n	w_{sct}(mm)	w_{scd}(mm)	g_{top}(mm)	g_{dia}(mm)
0.50	6	1.44	1.17	1.73	1.76
0.95	6	2.74	2.23	0.17	0.18
0.95	4	4.11	3.34	0.29	0.35
0.95	2	8.22	6.68	0.87	0

dimensions, but the HTS ratio decreases slightly to $p = 89\%$. The field disturbance and the field harmonics of this tailored geometry are shown in Figure 4.11. All non-dipole harmonics are below 4 units, which is still acceptable with respect to field quality. The ratio of 89% suggests a relatively low surface impedance compared with full copper, meaning that this geometry fulfills both criteria and offers the simplicity of not requiring any striation. For these reasons, we present this as the proposed geometry of the hybrid REBCO-Cu coating for the FCC BS.

It is important to note, however, that the impact of the surrounding structure on beam stability depends on the field



(a) (b)

FIGURE 4.11: Field quality results for the proposed geometry of the hybrid coating. (a) Field disturbance at $\mu_0 H_{ex} = 1\,\mathrm{T}$ and dimensions of each segment, and (b) Field harmonics and maximum relative field disturbance with and without correction of the dipole component.

homogeneity and on the beam coupling impedance, which in turn depends on the surface impedance of the constituent materials and on the geometry in which they are assembled. In other words, the ratio of HTS is not the sole factor to be taken into account, but also where it is placed, since regions of the coating that are closer to the beam present a larger impact to the beam. While the parametric study presented in this chapter aims to find a reasonable balance between field quality and surface resistance, it does not take into account the weighted contributions to the coupling impedance. A complementary study that receives as input the results of this thesis to further optimize the coating geometry in terms of the resulting beam coupling impedance is the subject of the doctoral thesis of Nikki Tagdulang at the ALBA Synchrotron and the Polytechnic University of Catalonia (UPC).

4.4 Magnetization and Surface Resistance Measurements

While the simulation results imply that field homogeneity can be achieved simultaneously with a high HTS ratio, which in turn suggests low surface impedance, it is important to validate the feasibility of the hybrid coating. To do this, samples of the hybrid coating in a simplified flat geometry with different striation patterns were produced to verify the impact of the two parameters in their trapped field and surface resistance.

To produce the striated patterns needed for our measurements, the REBCO content is removed in lines that follow the expected current path within the sample, revealing the copper layer beneath. Depending on the width of the copper gaps, the method employed to striate the coating may differ, going from mechanical scribing for larger gaps of around 1 mm, all the way down to laser scribing for thinner gaps in the micrometer range [108]. In this work the method used to produce the striated or hybrid coatings was chemically etching the REBCO layer after photolithography. This consists of producing a patterned mask covering the surface of the sample that protects it against chemical etching, ans subsequently submergin the sample in a bath of 1:20 H_3PO_4:H_2O solution, which etches away the REBCO only in the regions without the mask. The bath time and solution composition are carefully monitored to minimize excess of etching, which would make the gaps larger than desired.

The samples we prepared for our measurements can be split into two sets, as shown in Figure 4.12. For the magnetization measurements, three samples were produced from 12 mm × 30 mm coated conductors stripped off their stabilizing layers of copper and silver. Two of them were then striated into patterns with four and 16 segments, both with 75% HTS ratio, respectively named H1 and H2. One sample was not striated, maintaining a single segment with 100% HTS and named H0. For the surface resistance measurements, three pairs of samples were also produced by soldering and delaminating 12 mm × 12 mm CCs onto brass blocks. Likewise, two of them were striated to produce different patterns: sample pair R1, with 92% HTS and sample pair R2, with 42%. Sample pair R0 is not striated.

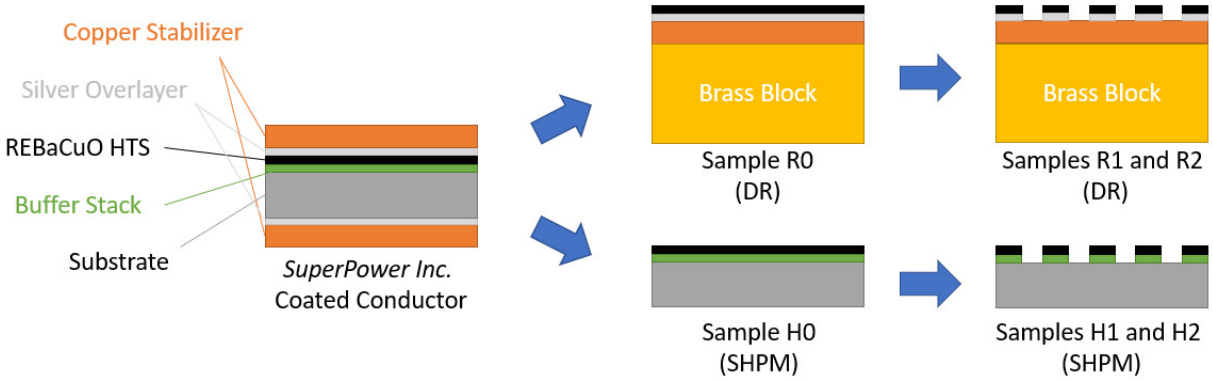
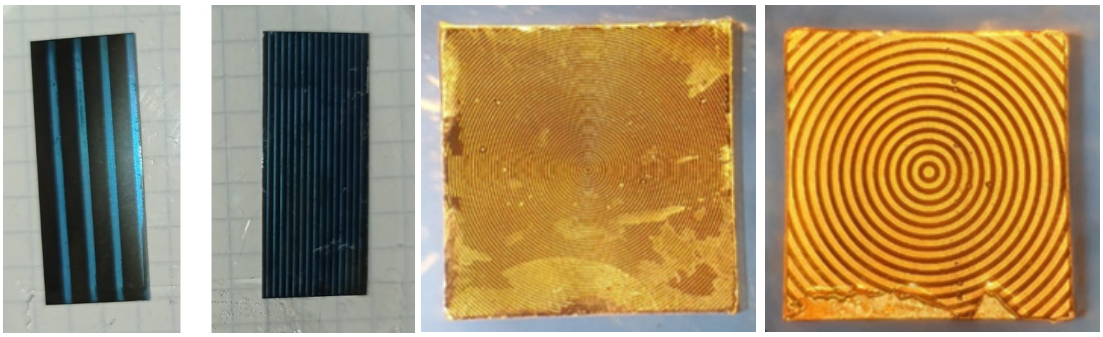


FIGURE 4.12: Schematic of the production process of the two sets of samples prepared for measurements. Samples H0, H1 and H2 for magnetization measurements via scanning Hall probe miscroscopy (SHPM) and samples R0, R1 and R2 for surface resistance measurements with a dielectric resonator (DR).

Unlike the samples prepared for the magnetization measurements, samples pairs R1 and R2 had their striation pattern produced in a circular fashion, so that each segment is a concentric ring. The reason for this is that the surface currents induced in these samples flow circularly. Therefore in order to avoid currents flowing through both copper and HTS, and consequently having the measured surface resistance affected by the contact resistance between these layers, the segments must present the same shape of the current flow: concentric rings. Note that although the segments are longitudinal in the FCC BS, the same concept applies, since there are no induced image currents that flow through different materials. Since the segments are ring-shaped in rectangular samples, the concept of number of segments does not translate directly to these samples. Figure 4.13 shows photographs of the samples, whose details are listed in Table 4.4. The dimensions for the sample pairs R1 and R2 were chosen to match those of simulated coating configurations that meet the field quality criterion without dipole cancellation.

Samples H0, H1 and H2 were then submitted to magnetization measurements via scanning hall probe microscopy (SHPM, see Chapter 3). The trapped field at 77 K measured from a distance of $400 \pm 100\,\mu$m from the surface of the samples in a transversal line at its center is shown in Figure 4.14a. The results show that as the number of segments increases, the maximum trapped field decreases. Compared to H0, samples H1 presents a decrease of 58% in its maximum trapped field. On top of that, the maximum trapped field of sample H2 decreases by 90% with respect to H1, in spite of the fact that both present the same HTS ratio. This confirms that even for the same amount of HTS material, it is possible to reduce the trapped field, and therefore increase field quality, by increasing the number of segments.

On the other hand, Figure 4.14b shows the simulation results replicating the same conditions of the experiment. In this case a very similar behaviour can be observed from the three samples, with a decrease in trapped field of 64% from H0 to H1 and of 87% from H1 to H2. The consistency between results from experimental measurements and



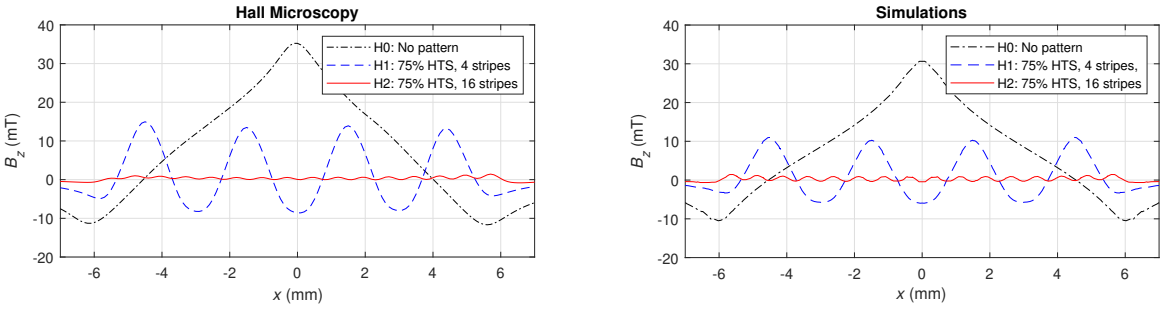
(a) (b) (c)

FIGURE 4.13: Samples produced for magnetization and surface resistance measurements. For magnetization measurements, (a) H1 and H2 with four and 16 segments and 75% HTS. For surface resistance measurements, (b) R1, with 92% HTS, and (c) R2, with 42%.

TABLE 4.4: Details of the samples produced for magnetization and RF measurements.

Sample	p	n	$w(\mu\text{m})$	$g(\mu\text{m})$	Pattern
H0	1.00	1			Rectangular
H1	0.75	4	2250	750.0	Rectangular
H2	0.75	16	560	187.5	Rectangular
R0	1.00				Circular
R1	0.92		121	10	Circular
R2	0.42		232	250	Circular

numerical analysis validates the model used for the simulations and sets the simulation methodology presented in this chapter as a prediction tool for the behaviour of different coating geometries based on coated conductors from distinct providers, with distinct material properties.



(a) (b)

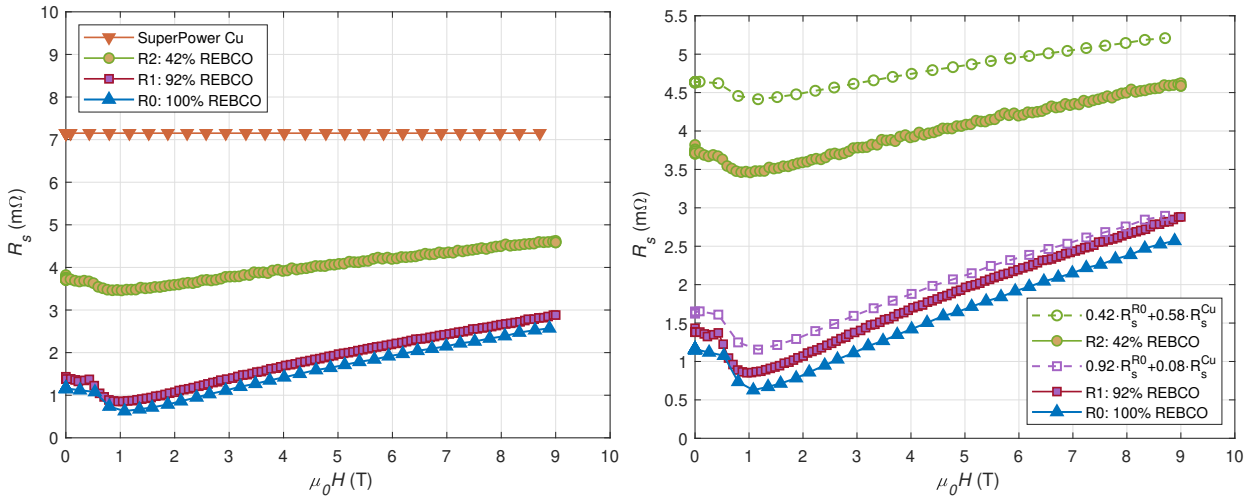
FIGURE 4.14: Trapped field in samples with different striation patterns. Comparison between (a) Experimental measurements via SHPM from a distance of $400 \pm 100\,\mu$m from the surface of the samples and (b) simulation results under similar conditions.

Following up on the magnetization measurements, sample pairs R0, R1 and R2 had their surface resistance measured as a function of the magnetic field at 50 K. The measurements results are depicted in Figure 4.15a and compared with the surface resistance of a pure copper sample consisting on the electroplated copper layer used as stabilizier in SuperPower samples. As expected, the surface impedance drops as the HTS ratio increases, reaching values very similar to pure REBCO for ratios close to 100%. Sample pairs R0 and R1 show very close curves, despite the fact that one is heavily segmented and the other is not. On the other hand, focusing on R2 shows us an intermediate behaviour, both in self field values as well as magnetic behavior.

Based on these results, the surface resistance as a function of the field of the hybrid samples can be approximated as [49]

$$R_s^{\text{hybrid}}(H) = p \cdot R_s^{\text{REBCO}}(H) + (1-p) \cdot R_s^{\text{Cu}}(H), \tag{4.31}$$

assuming that each material contributes linearly to the total surface resistance. This leads to the curves plotted in Figure 4.15b. As we can see, this simple model represents the data qualitatively well. On the other hand, the values predicted by the model are overestimated. This could have arisen from the fact that the current induced beneath the dielectric is not evenly distributed, which would result in a larger contribution coming from one of the materials. This effect would be enhanced for larger segment widths, which would explain the larger mismatch for sample pair R2. Alternatively, this incongruity could be caused by a preferential RF current flow in the HTS, resulting in lower total surface resistance. Although previous studies have shown small to no correlation between the induced currents and the material distribution in soldered copper pipes [109], it could be the case that the currents are more impacted by the large surface resistance difference between copper and HTS, as well as their different heights.



(a) (b)

FIGURE 4.15: surface resistance measurement results at 50 K and 8 GHz. Surface resistance of samples R0, R1 and R2 are shown (a) compared with a pure copper sample; and (b) compared with the linear approximation described by Equation 4.31.

In any case, it is clear that any non-zero HTS ratio represents an improvement in surface resistance with respect to pure copper, and that the larger improvements are obtained the closer to pure REBCO our coating is.

4.5 Chapter Summary and Conclusions

In this chapter, we showed the numerical analysis methodology used to simulate our hybrid REBCO-Cu coating for the FCC-hh beam screen. Our model consists on a H-formulation FEM solution of Faraday's law of induction coupled with the quasi-static approximation of Ampere's law. The resistivity of the superconducting material present in the coating is based on material properties of commercially available coated conductors and accounts for creep, AC field demanetization, superconductor anisotropy and dependence with field intensity and angle.

Simulations of the hybrid coating during field ramp-up of the bending magnets show that the most critical moment in terms of field quality is during injection, with an external applied diople field of $\mu_0 H_{ex} = 1\,\text{T}$. At this point, the field harmonics are the highest due to the decreasing dependence of J_c with $\boldsymbol{H}$ as well as the fact that the field harmonics are normalized with respect to the increasing external field. In addition, simulations considering HTS demagnetization

due to beam-induced perpendicular AC magnetic fields show that this effect is negligible for the predicted field values of the FCC. Only AC fields more than one order of magnitude higher than FCC's estimated $250\,\mathrm{A/m}$ would cause significant impact, potentially demagnetizing the coating at injection.

Based on these results, several coating geometries were simulated by varying HTS ratio p and number of HTS segments n. Simulation results show a broad range of possible geometries that comply with the field quality criterion, but that in many cases, and especially for high p, require a very large number of segments. To mitigate this, the possibility of cancelling the dipole harmonic contribution by applying an external dipole field slightly larger than nominal is evaluated, in which case the field quality criterion is relaxed, allowing for coating geometries with less segmentation. A coating geometry was proposed for the beam screen, which require segments as wide as commercially available coated conductors, bypassing the need to striate the delaminated coating, and making its production process easier, cheaper and faster while maintaining a high HTS ratio.

Finally, striated samples were submitted to magnetization and surface resistance measurements to validate the simulation results and confirm the effect of n and p on the trapped field and the surface resistance of the hybrid coating. The combined results from these measurements confirm that it is possible to simultaneously meet the field quality and surface resistance criteria, as long as the coating geometry is selected accordingly. Of course, when considering the more complex geometry of the beam screen, the contribution of each segment to both field quality and surface impedance will differ depending on its position inside the vacuum chamber and its distance from the beam, but the concept remains applicable.

In conclusion, the numerical analysis and experimental results presented throughout this chapter show that the field quality inside the vacuum chamber and the beam screen surface resistance, and therefore the beam coupling impedance, are highly dependent on the material distribution of the coating, but it can be tailored to outperform copper in terms of surface resistance and maintain high field quality while not requiring striation of the coated conductors used to produce the coating. These results set the CC-based hybrid REBCO-Cu coating as a strong candidate for the FCC-hh beam screen.

Chapter 5

Quadrupole, Beam Screen Misalignments and Other Field Configurations

As discussed in the previous chapter, the most critical moment in terms of field quality for the hybrid coating during dipole field ramping is the moment of injection ($\mu_0 H_{ex} = 1\,\mathrm{T}$), due to the high induced currents in the coating. Based on this, the maximum relative field disturbance η at 1 T was used to determine which coating geometries satisfy the field quality criterion. However, there are other relevant magnetic conditions under a dipole field to which the beam screen will be submitted during operation. In addition, while the sections of the FCC corresponding to the main dipole magnets equate to the majority of its length (65.7 km), it is important to consider the behavior of the coated beam screen under different magnetic arrangements such as the main quadrupole, the second most common magnet type in the FCC, which covers a total length of 5.4 km and plays an important role in the beam optics by focusing divergent particles into the ideal beam orbit (see Section 2.3) [9].

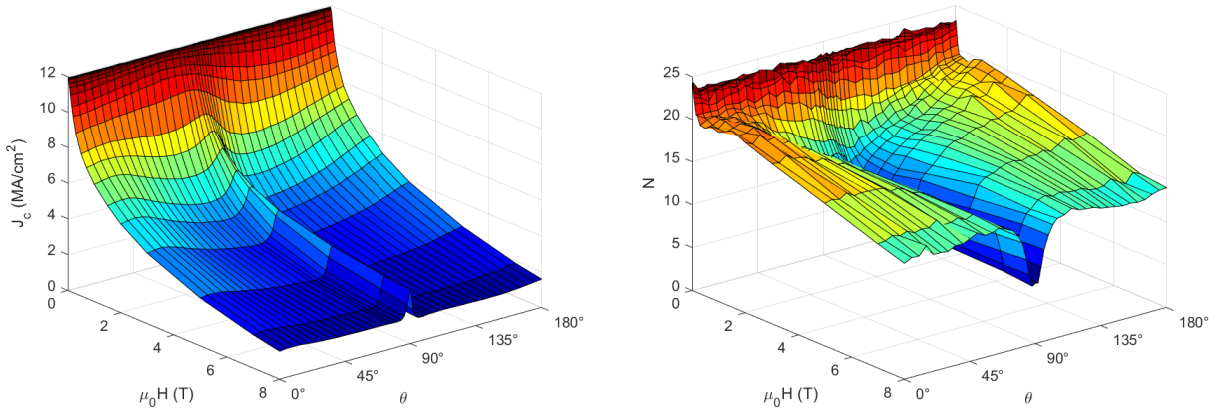
This chapter explores the behavior of the coating geometry proposed in Chapter 4 as a solution for field quality under dipole fields, when submitted to a varied set of magnetic conditions, including the quadrupole field of the focusing magnets and tilted magnetic fields produced by a potential misalignment of the beam screen with respect to the superconducting magnets that may arise during the assembly of the 91 km ring according to FCC tolerance. We will also analyse the behavior of the coating during injection, when the external magnetic field is held at 1 T, as well as what happens when the rate of change of the external field reverses, that is, when it ramps up, then down, or vice-versa. Finally, we discuss how the combined harmonics of the coating with the bending magnets could lead to an improvement in field quality with respect to their individual contributions.

5.1 Model Adaptations

To be able to consider an external field other than a dipole field, such as the quadrupole field produced by the focusing magnets, the simulation model has to be adapted to include new boundary conditions and a more complete dependence of the critical current density and the transition index N with the magnetic field.

Under a dipole field, the field angles with respect to the HTS segments are only two: one for the segments on the top walls and one for those on the diagonal walls. For this reason, we were able to model the J_c and N as functions of the field intensity for each of the field angles (see Figure 4.3). On the other hand, when the external field is a quadrupole field (see Figure 2.9), there will be a continuous range of impinging angles in both walls. To take that into account, we now define J_c and N as functions of both field angle and intensity, which includes all angles instead of only 0° and 70°. On top of that, instead of fitting J_c data into a curve, as done with Equation 4.18, we adopted the same method

employed with N previously, directly interpolating the measured data. This results in two 2D interpolation functions, $J_c(H,\theta)$ and $N(H,\theta)$, shown in Figure 5.1.



(a) (b)

FIGURE 5.1: Dependence of (a) critical current density J_c and (b) transition index N with field intensity H and angle θ employed for the adapted simulation model. Functions are interpolated between data points and extrapolated so that $J_c(\mu_0 H > 8\,\mathrm{T},\theta) = J_c(\mu_0 H = 8\,\mathrm{T},\theta)$ and $N(\mu_0 H > 8\,\mathrm{T},\theta) = N(\mu_0 H = 8\,\mathrm{T},\theta)$. Data from [63].

As previously seen in Equation 2.51, the magnitude and angle of an ideal $2k$-pole field depend respectively on the distance from the center and the angle with respect to the location of the poles. The equation can be rewritten in terms of the magnetic field intensity and angle, and taking the values at the magnet aperture ($H = H_{apt}$ and $r = r_{apt}$) as a reference. Nevertheless, we must recall that Equation 2.51 is written so that the argument of $\tilde{B}$ takes the direction of the vertical component as the reference and that the direction of angle increment is clockwise. In order to obtain the field angle in accordance to our coordinate system, the reference direction must be $\hat{\boldsymbol{x}}$, with the angle increasing in the counter-clockwise orientation:

$$H = H_{apt}\left(\frac{r}{r_{apt}}\right)^{k-1} \tag{5.1}$$

$$\theta_H = \frac{\pi}{2} - \phi(k-1)\,. \tag{5.2}$$

When it comes to its effect on J_c and N, a reasonable approximation is that the applied field fully permeates the HTS segments, as in a thin film behavior. As a consequence, the impinging magnetic field perceived by the material will be the nominal multipole field given in Equations 5.1 and 5.2. The angle θ between the HTS and the magnetic field is therefore given by

$$\theta = \theta_H - \theta_{HTS} = \frac{\pi}{2} - \phi(k-1) - \theta_{HTS}\,, \tag{5.3}$$

Based also on Equation 2.51, the x and y components of the magnetic field at any point within the magnet aperture can be calculated:

$$H_x = H\sin\theta_H = H_{apt}\left(\frac{r}{r_{apt}}\right)^{k-1}\sin(\phi(k-1)) \tag{5.4}$$

$$H_y = H\cos\theta_H = H_{apt}\left(\frac{r}{r_{apt}}\right)^{k-1}\cos(\phi(k-1))\,, \tag{5.5}$$

which leads us to our updated boundary conditions to account for field modes other than the dipole. The boundary of the simulated space is defined at the aperture, and therefore the magnetic field values at the boundary, depending on the mode are

$$H_{x,b} = H_{apt}\sin(\phi(k-1)) \tag{5.6}$$

$$H_{y,b} = H_{apt}\cos(\phi(k-1))\,. \tag{5.7}$$

This set of equations gives us the magnetic field distribution around a central point where $r = 0$. So far, we have considered a perfect alignment between the beam screen and the magnetic field, which results in both the field and the beam screen to be centered around the origin of our coordinate system, and both taking the same direction as the reference for the angle. Nevertheless, when the beam screen is assembled inside the magnet aperture, it may not be perfectly aligned with the magnets, whether by being tilted or displaced.

First, let us consider the case according to which the beam screen is displaced with regards to the center of the magnet alignment. To account for this, we can introduce a new coordinate system (r', ϕ', z) for the beam screen, while the magnetic field maintains its orientation according to (r, ϕ, z). The two coordinate systems are displaced from one another by Δx and Δy in the horizontal and vertical directions respectively, as shown in Figure 5.2.

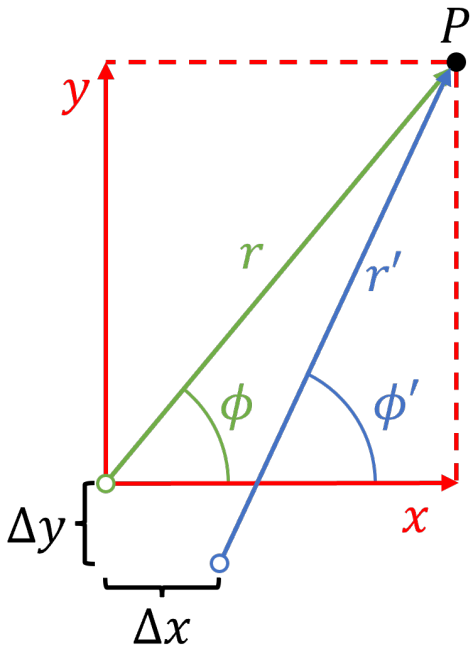


FIGURE 5.2: Coordinate systems used to account for a misalignment of the beam screen with respect to the surrounding superconducting magnets. The magnetic field is centered around (r, ϕ, z) while the beam screen is centered around (r', ϕ', z). A generic point P is shown represented in both coordinate systems.

On the other hand, to include a possible tilt of the beam screen, an offset angle has to be included in Equation 5.2. Rewriting Equation 5.3 with the added tilting angle ψ, we get the input angle for the field dependence of J_c and N:

$$\theta = \frac{\pi}{2} - \phi(k-1) - \theta_{HTS} - k\psi\,. \tag{5.8}$$

We can also find the boundary conditions for the misaligned beam screen. In this case, the boundaries of the simulation space still correspond to the magnet aperture, since they are aligned with the magnet coordinate system. However, Equations 5.6 and 5.7 must now be rewritten to include ψ:

$$H_{x,b} = H_{apt} \sin(\phi(k-1) + k\psi) \tag{5.9}$$

$$H_{y,b} = H_{apt} \cos(\phi(k-1) + k\psi)\,. \tag{5.10}$$

To conclude the model adaptations, the simulations may no longer present quadrant symmetry due to the misaligned multi-polar fields. In such cases, instead of simulating a single quadrant with the proper symmetry conditions, the simulations will now consider the entire vacuum chamber. After these changes, the model becomes much more versatile in terms of the magnetic field configurations it may analyse, using as input not only the number of pairs of poles k, but also the misalignment parameters, Δx, Δy and ψ.

5.2 Field Quality in a Quadrupole Field

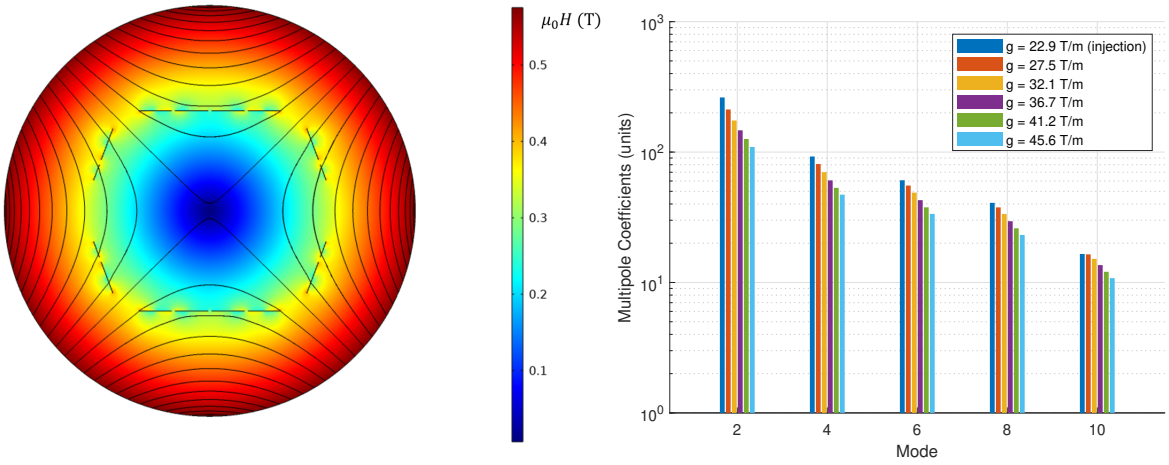
Unlike the dipole, the quadrupole field of the focusing magnets is defined by the field gradient inside the vacuum chamber. The field gradient should increase linearly along with the dipole field of the bending magnets, reaching $g_{top} = 367\,\mathrm{T/m}$ at top energy [9]. In a perfectly aligned quadrupole, this would result in a magnetic field ramping rate of $7.65\,\mathrm{mT/s}$ at the magnet aperture. Therefore, during the moment of injection, when the dipole field reaches 1 T, the quadrupole would reach 573 mT at the aperture and 206 mT at the reference radius, with a field gradient of $22.9\,\mathrm{T/m}$.

The simulation results carried out for the proposed geometry in a perfectly aligned normal quadrupole field are shown in Figure 5.3. In Figure 5.3a, we can see the characteristic magnetic field gradient of the quadrupole, albeit disturbed by presence of the HTS segments. Taking a closer look at the field harmonics produced by the hybrid coating, in Figure 5.3b, we notice once again the tendency of the field harmonics to decrease as the applied field increases, much like under a dipole field. On the other hand, the field harmonics that arise due to the interaction between the quadrupole field and the hybrid coating, this time, are the even normal coefficients, while the odd normal coefficients and the skew coefficients are comparably negligible.

Most notably, however, is that the field harmonics are orders of magnitude higher than those generated under a dipole field. This is caused partially because of the lower field values used to normalize the harmonics. At injection, for example, the nominal magnetic field at r_0 is only 206 mT, in contrast with the 1 T field that permeates the entirety of an ideal dipole field. The lower absolute values of the field itself also play a role through the field dependence of J_c. Since the critical current density is higher at lower fields, and therefore also the current flowing in the HTS, the field disturbance will also assume higher values.

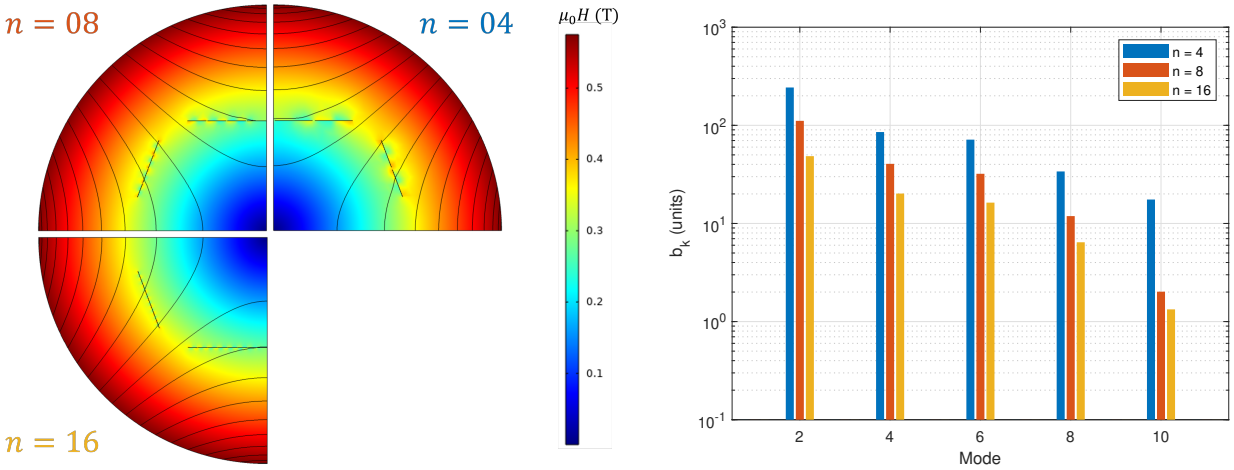
To mitigate the lower field qualty of the quadrupole, we can resort once more to the original strategy proposed for the hybrid coating and increase the number of HTS segments. The effect of the number of segments on the quadrupole field quality can be seen in Figure 5.4.

The clear tendency to decrease the impact on field quality as the number of segment increases is maintained for the quadrupole as well and the main contribution comes from the quadrupole component b_2, as expected. At this point, if we assume a behavior alike that of the relative field disturbance in the dipole, that is, an inverse dependence with n (see Equation 4.29), we can extrapolate the b_4 component, as shown in Figure 5.5.



(a) (b)

FIGURE 5.3: Simulation results of the proposed geometry of the hybrid coating under a perfectly aligned normal quadrupole field. (a) Magnetic field distribution and field lines at injection; and (b) field harmonics as the gradient increases from 22.9 T/m, which corresponds to the moment of injection, when the dipole field is 1 T, to twice that value.



(a) (b)

FIGURE 5.4: Simulation results of the coating geometries going from $n = 4$ to $n = 16$ and $p = 90\%$ under a perfectly aligned normal quadrupole field. (a) Magnetic field distribution and field lines; and (b) field harmonics at injection ($g = 22.9\,\mathrm{T/m}$).

The resulting relationship between $b4$ and n is given by

$$b_4 = 420 \cdot \frac{0.90^{2.1}}{n} [\text{units}], \tag{5.11}$$

which means that, if b_2 is corrected by a slightly larger applied field from the magnets, the largest remaining harmonic, b_4, will be below 10 units for $n > 64$. For instance, with $n = 172$, which still corresponds to reasonable copper gaps achieved via laser scribing (see Table 4.2), b_4 would be reduced to the much more acceptable value of 2 units.

In summary, the quadrupole is much more sensitive to the disturbance caused by the hybrid coating than its dipole counterpart, and the proposed geometry for the dipole, while suited for the sections of the beam screen submitted to the bending magnets, may not be the best solution for the sections within the focusing magnets. Even considering

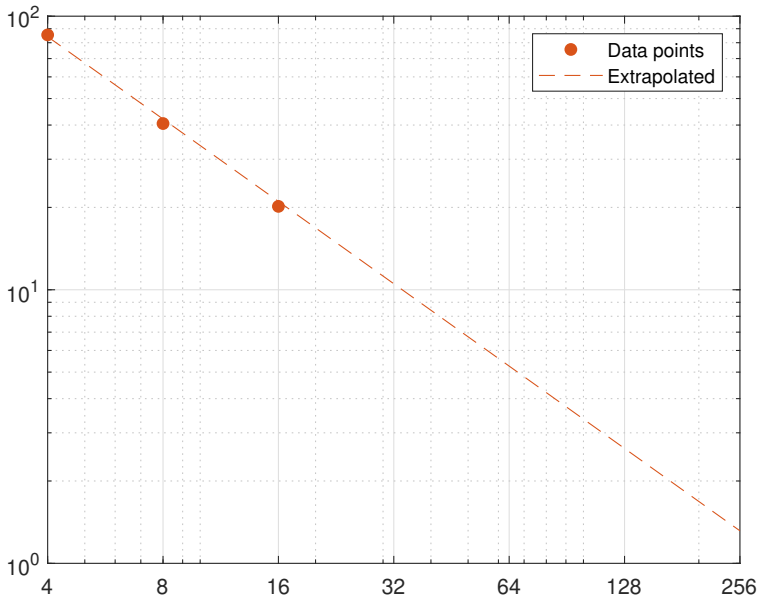


FIGURE 5.5: Octupole component of the field harmonics produced by coating geometries with $p = 90\%$ and n varying from 4 to 16. Data points are extrapolated according to Equation 5.11

correction of the quadrupole component of the field disturbance, these may require a more striated geometry, a smaller HTS ratio, or a combination of both.

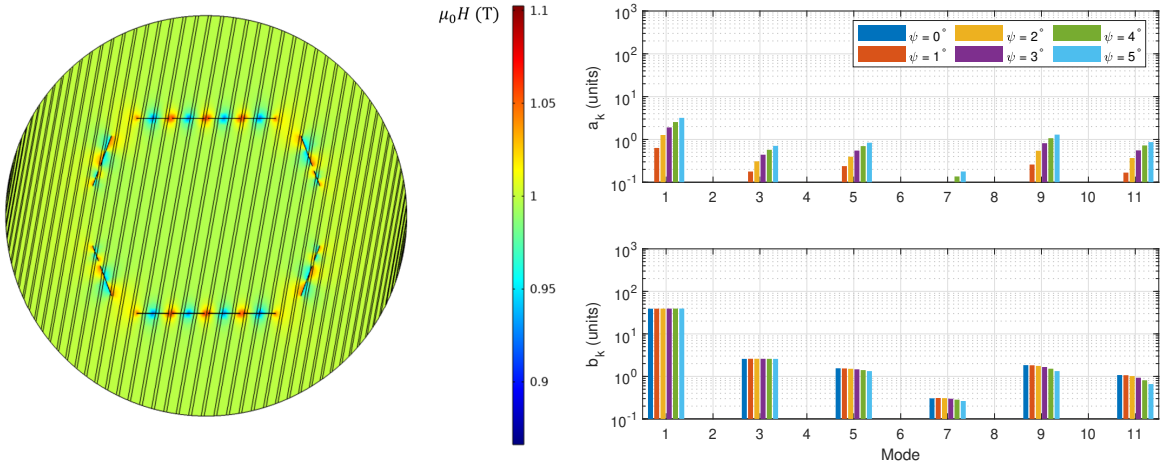
5.3 Misalignment Effects on the Field Quality

As mentioned previously, after assembly, it is possible that the beam screen is misaligned with regards to the magnetic field produced by the bending or focusing magnets. It is important to evaluate the impact of this misalignment in the field quality inside the beam screen. In this section we will analyse the field harmonics produced by the hybrid coating with the proposed geometry under tilted dipole and quadrupole fields.

Starting with the dipole configuration, whose results are presented in Figure 5.6, we can see the effect of having a tilted beam screen up to $\psi = 5°$. This time, it is important to consider also the even normal coefficients b_k as well as the skew coefficients a_k, since quadrant symmetry is broken. Nevertheless, for the tolerance predicted for the FCC, which is around 3°, all skew harmonics stay within the 1 unit mark, with the exception of the dipole component itself, which rises to 2 units.

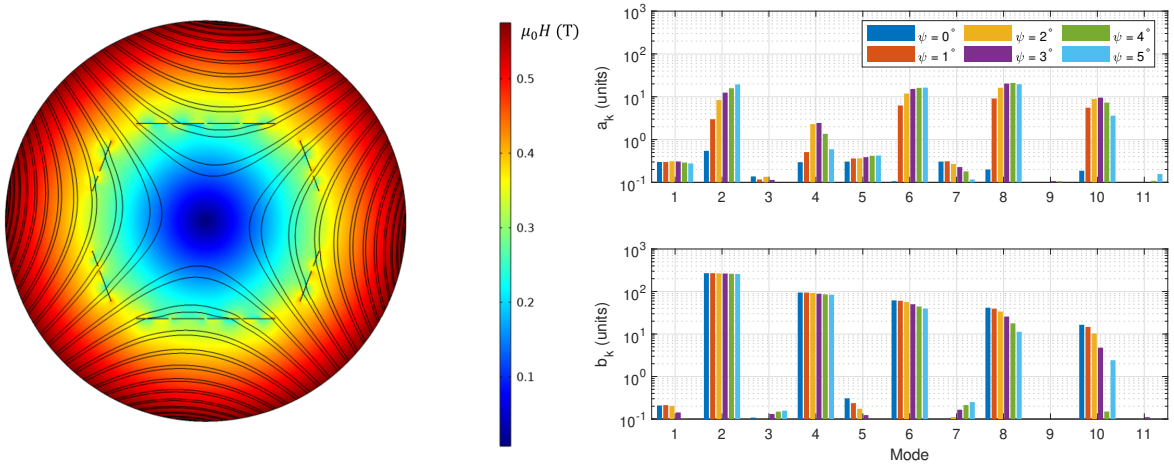
The quadrupole field, on the other hand, is susceptible not only to a tilted beam screen, but also to a displaced one, leading us to evaluate the effect of an increasing ψ, but also of Δx and Δy. Let us first consider the case according to which the quadrupole field is tilted, but still centered around the central point of the vacuum chamber ($\Delta x = 0$, $\Delta y = 0$, $\psi \geq 0$). The results for these field configurations are shown in Figure 5.7.

As we can see, the already high field harmonics produced under the quadrupole field are much more sensitive to the tilting angle. While the odd coefficients are mainly unchanged, we notice a transformation between the normal and skew coefficients. As the angle increases, the skew coefficients increase and the normal coefficients decrease. This is in agreement with the fact that an ideal skew quadrupole field corresponds to an ideal normal quadrupole field tilted by $\psi = 45°$. At the FCC tolerance of 3°, the skew coefficients are mostly around or below their normal counterparts, and are one order of magnitude lower than b_4, which would be the most contributing harmonic considering compensation of the normal quadrupole component b_2 by the quadrupole magnet.



(a) (b)

FIGURE 5.6: Simulation results of the proposed geometry under a tilted dipole field. (a) Magnetic field distribution and field lines with $\psi = 10°$; and (b) field harmonics at injection going from $\psi = 0°$ to $10°$.



(a) (b)

FIGURE 5.7: Simulation results of the proposed geometry under a tilted quadrupole field. (a) Magnetic field distribution and field lines with $\psi = 5°$; and (b) field harmonics at injection going from $\psi = 0°$ to $5°$.

When it comes to the displacement of the beam screen with respect to the focusing magnets, we see in Figure 5.8 that both for purely horizontal or purely vertical displacements, the even coefficients decrease slightly, with a more pronounced change in higher modes. In addition, the odd coefficients increase with the displacement: the normal coefficients during horizontal displacement; and the skew coefficients during vertical displacement. At the FCC tolerance of 0.4 mm, the altered coefficients in both cases never reach values quite as high as b_4, which is also in these configurations, still the limiting factor. It is worthwhile to notice, however, that the field quality of the quadrupole is more affected by a horizontal displacement than it is by a vertical displacement.

In all the cases considered in the simulations in which the quadrupole is tilted or displaced, there is a significant increase in a subset of the harmonics which were originally negligible, although they do not surpass the even normal harmonics produced by the perfectly aligned quadrupole field. For the tolerance of 0.4 mm and 3° estimated for the FCC, the altered coefficients are still low enough that, even considering a corrected quadrupole, they would still be of

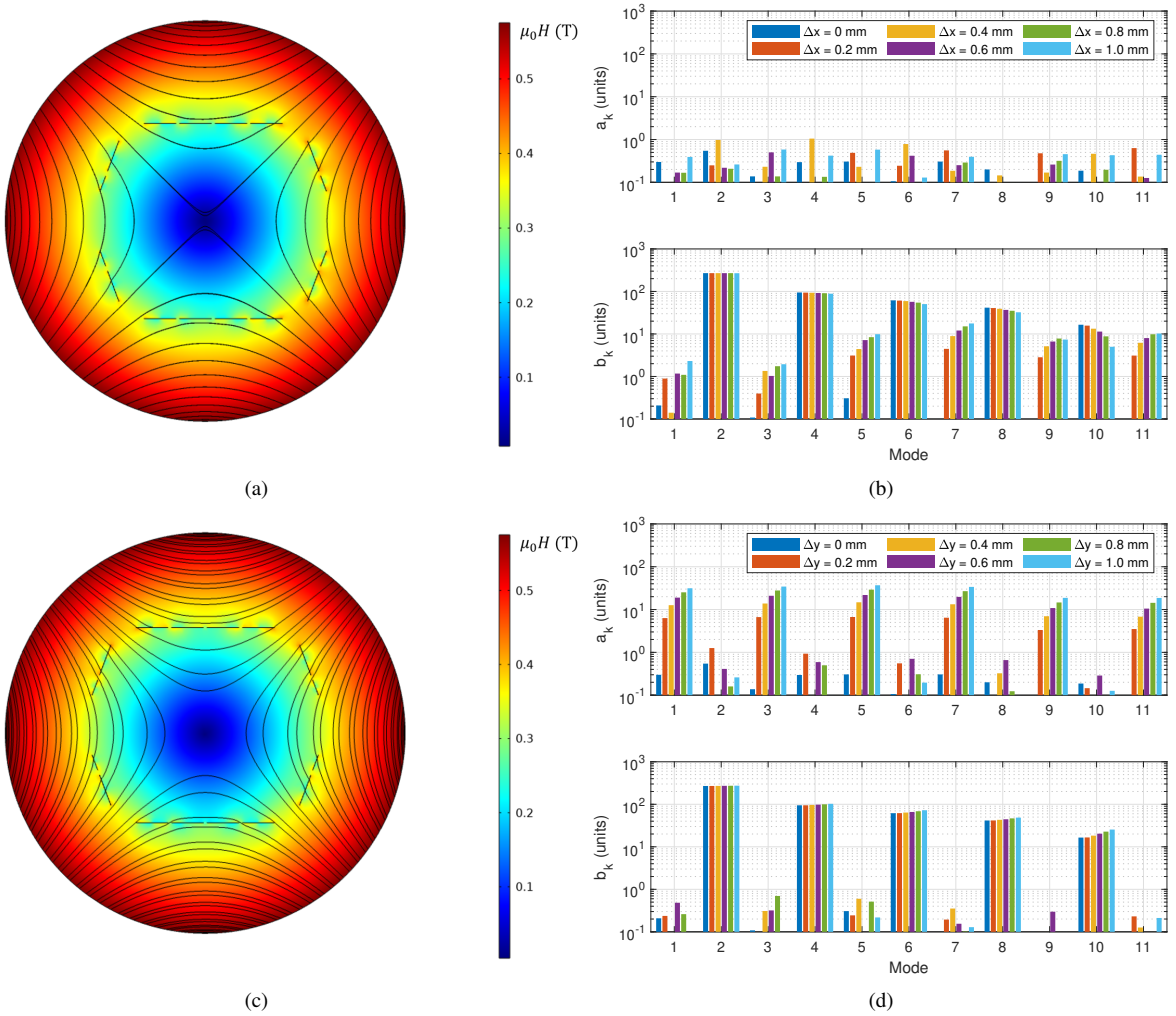


FIGURE 5.8: Simulation results of the proposed geometry under a displaced quadrupole field. Magnetic field distribution and field lines with (a) $\Delta x = 1$ mm and (c) $\Delta y = 1$ mm; and field harmonics at injection going from (b) $\Delta x = 0$ mm to 1 mm and (d) $\Delta y = 0$ mm to 1 mm.

the same order of the largest harmonic, b_4, or below. Unlike in the dipole field, however, these values are significant and may be meaningful to the overall field quality of the vacuum chamber. Nevertheless, the solution remains achievable by the means of a more striated geometry, which would result in higher field quality for the quadrupole in both the misaligned and the perfectly aligned scenarios.

5.4 Other Field Configurations

During operation of the FCC-hh, the beam screen will be submitted to field configurations other than a ramping external field. Although the expected critical moment in terms of field quality corresponds to the initial instants of injection, when the induced currents still have not been diminished by creep (see Section 2.1), it is valuable to understand what the behaviour of the coating and the field quality inside the vacuum chamber are in different situations.

Along this section we investigate the harmonic relaxation due to flux creep when the coated beam screen is exposed to the constant 1 T dipole field during injection, and how hysteretic effects impact on the field harmonics. In addition,

we discuss the combined effect of the coating and the dipole magnets on the overall field quality inside the vacuum chamber.

5.4.1 Harmonic Relaxation during Injection

After the external dipole field is brought up to 1 T, it is maintained at this value through the entire injection process, which took an average of around one hour in the LHC in 2017 [110]. Figure 5.9 shows the simulation results of the proposed geometry while the field is increased to and kept at 1 T over the course of one hour. While ramping up the external field, the behaviour is similar to those discussed in previous chapters (compare with Figure 4.7), but when the field ramping rate is brought to zero, the electric field and current density in the HTS immediately respond, quickly decreasing until negligible values of E are reached.

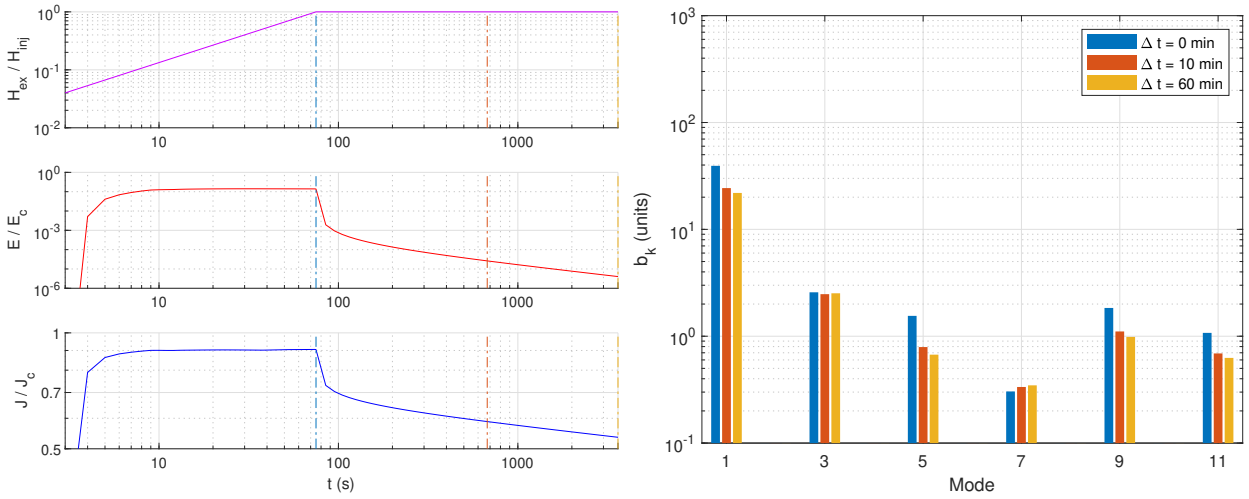


FIGURE 5.9: Simulation results of the proposed geometry before and during injection ($\mu_0 H_{ex} \leq \mu_0 H_{inj} = 1\,\mathrm{T}$) for one hour. (a) Magnetic field, current density and electric field at an arbitrary point inside the HTS domain normalized with respect to H_{inj}, J_c and E_c; and (b) field harmonics at $\Delta t = 0\,\mathrm{min}$, 10 min and 60 min from reaching the injection field ($t = 75\,\mathrm{s}$). Creep effect is responsible for decrease of the currents flowing in the HTS as well as an overall improvement in field quality.

The impact of this relaxation in the current flow can be seen in Figure 5.9b, where the field harmonics of three points in time are shown. As the current decreases over time, so to do most of the harmonics, with the exception of b_3, which remains constant within a small margin, and b_7, which, contrary to expectations, increases over time.

Figure 5.10 shows with more details the behavior of b_7 as the currents decrease. The simulated data points can be accurately fitted into a curve described by

$$b_7 = 0.37 - 0.17 t^{-0.24} [\text{units}] \tag{5.12}$$

which, in turn, results in a limit for the increase in b_7, given by $\lim_{t\to\infty} b_7 = 0.37$ units.

Therefore, as expected, the field quality tends to increase over time while the external field is kept at a constant value, and even the anomalous b_7 tends to a still acceptable value, lower than one unit. This result confirms the starting point of injection as the critical moment for the field quality in the vacuum chamber. It also opens the possibility of decreasing the field disturbance during injection by waiting a certain amount of time between reaching the injection field H_{inj} and starting the injection process, during which the field harmonics will decrease, especially in the first

few minutes. Nevertheless, it is important to point out that once the external fields start ramping again, the current levels will quickly rise to those achieved prior to the relaxation, resulting in field harmonics as high as the originally produced by the coating at 1 T.

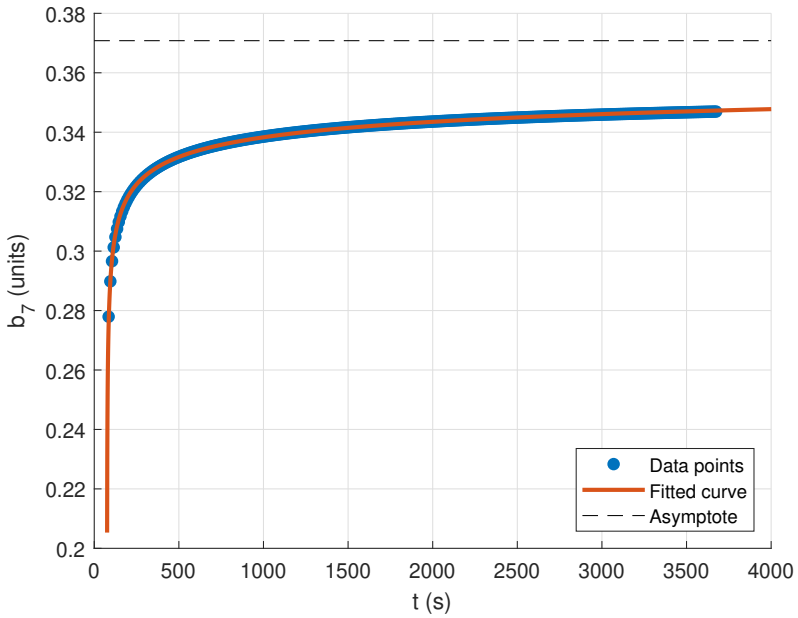


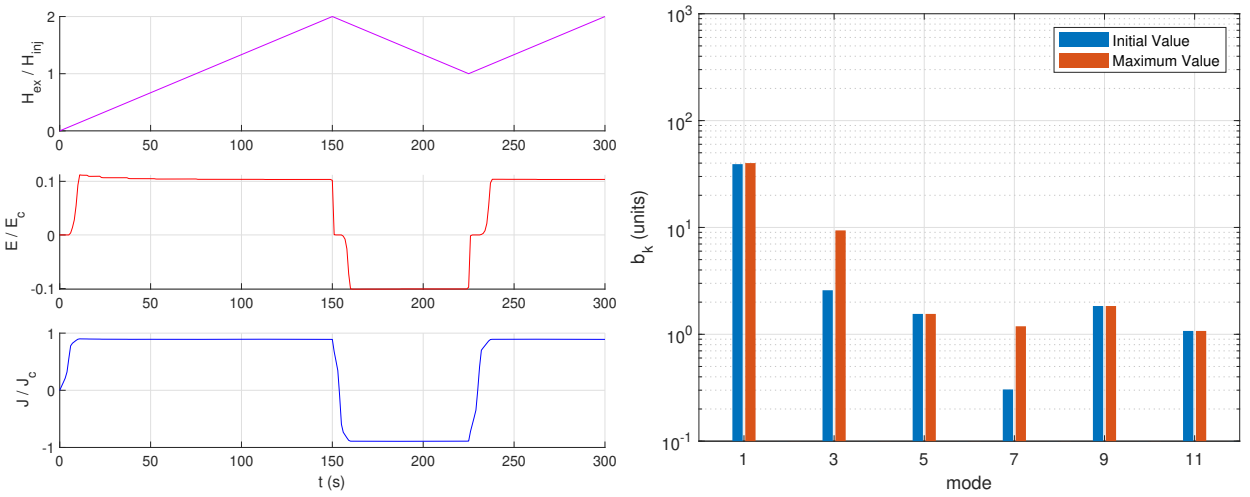
FIGURE 5.10: Component b_7 and fitted curve of the field harmonics produced by the proposed geometry of the hybrid coating over the course of one hour during injection, when the external field is maintained at 1 T.

5.4.2 Hysteresis Effects

After injection, the external field is increased up to its maximum value, which corresponds to 16 T in the case of the dipole. At this point the accelerator is operating at top energy and particle collisions can be performed. When the particle beam needs to be replenished, the dipole field is then brought back to 1 T, at which point the injection process is repeated. During operation of the LHC in 2017, this cycle was repeated around 2.5 times a day in average [110]. Although this magnetic cycle is limited by the injection field $\mu_0 H_{inj} = 1\,\mathrm{T}$ and the field at top energy $\mu_0 H_{top} = 16\,\mathrm{T}$, a conceptual understanding of the process can be achieved by analysing a simpler 1 to 2 T loop, whose results are depicted in Figure 5.11.

First, in Figure 5.11a, we notice that whenever the sign of the derivative of the field changes, both the electric field and current density also change directions after a transient interval of a few seconds. The field harmonics produced by the hybrid coating in subsequent cycles are impacted by this transient behavior, and some of them, namely b_3 and b_7, reach maximum values higher than those originally achieved at injection during the first cycle, as shown in Figure 5.11b.

To understand this, we take a closer look at the behavior of the harmonics during this magnetic field cycle, especially immediately after inverting the rate of change of the field. Figure 5.12 presents each field harmonic as a function of the applied dipole field. Here we see that all field harmonics present an hysteretic behavior, which is in agreement with the fact that the sign of each harmonic is directly linked to the sign of the rate of change of the external dipole field.



(a) (b)

FIGURE 5.11: Simulation results of the proposed geometry in a cycling external field from 1 to 2 T. (a) Magnetic field, current density and electric field at an arbitrary point inside the HTS domain normalized with respect to H_{inj}, J_c and E_c; and (b) field harmonics at 1 T during the first cycle and maximum field harmonics reached between 1 and 2 T during subsequent cycles.

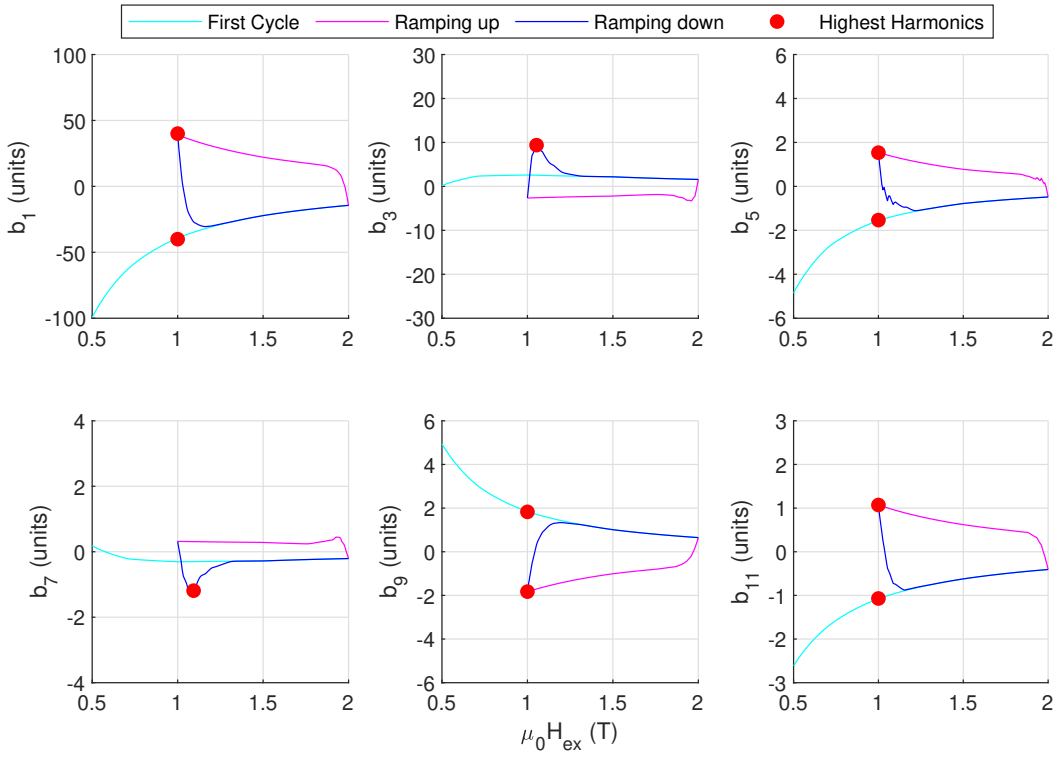


FIGURE 5.12: Odd normal field harmonics while cycling between 1 and 2 T. Highest values are achieved in different moments for b_3 and b_5, while the other harmonics maintain their maximum whenever $\mu_0 H_{ex} = 1$ T.

It is clearly noticeable, however, that b_3 and b_7 show a different behavior compared with the other harmonics. While b_1, b_5, b_9 and b_{11} have their maxima whenever the external field reaches H_{inj}, b_3 and b_7 present a peak immediately after changing directions which far surpasses the original values achieved when reaching H_{inj} for the first time, leading to the higher maxima in Figure 5.11b.

Having field harmonics exceeding those at injection means that injection is no longer the critical moment for field quality for any cycle after the first one, which comes from 0 T. Not only that, but also that each harmonic will be at its maximum in a different point in time. To remedy this, some sort of demagnetization cycle on the superconducting coating can be performed to reduce the impact of the harmonics in the field interval of relevance, that is, between 1 and 16 T. In the FCC, the particle beams are dumped after collision, which means there is no need to sustain high field quality when returning from top energy to injection. Therefore, the simplest way to ensure field quality is met throughout the entire relevant field range is to decrease the minimum field in a cycle so that the harmonic peak is moved out of the interval of interest.

To evaluate this, we have repeated the simulation, but this time with a magnetic cycle between 0.5 and 2 T, as shown in Figure 5.13. The behavior of the current density and electric field are very similar to the 1 to 2 T cycle, although displaced in time after ramping down from top energy. Once again, it is important to analyse the behavior of each harmonic individually, as presented in Figure 5.14. Here we see that simply by decreasing the lower limit of the field cycle, the peaks of b_3 and b_7 are moved out of the region of interest, making the injection point once more the critical moment in terms of field quality.

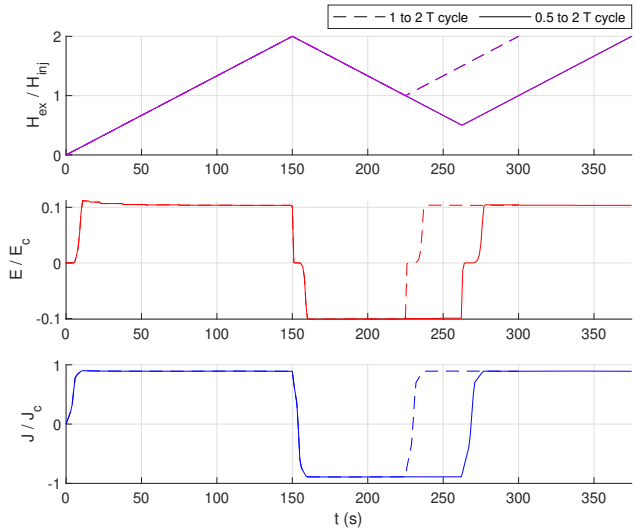


FIGURE 5.13: Magnetic field, current density and electric field at an arbitrary point inside the HTS domain normalized with respect to H_{inj}, J_c and E_c in a cycling external field from 0.5 to 2 T.

On another topic, it is interest to point out that in both situations we have considered so far in which there is a transient phase, the harmonics that present anomalous behavior with respect to the rest are b_3 and b_7. This stresses the sensibility these particular harmonics have to a change in the current distribution inside the HTS segments, which happens whenever $\partial H_{ex}/\partial t$ is modified. It may be the case that higher mode harmonics are also affected, but whatever solution deals with b_3 and b_7 will probably have a similar impact on higher modes as well.

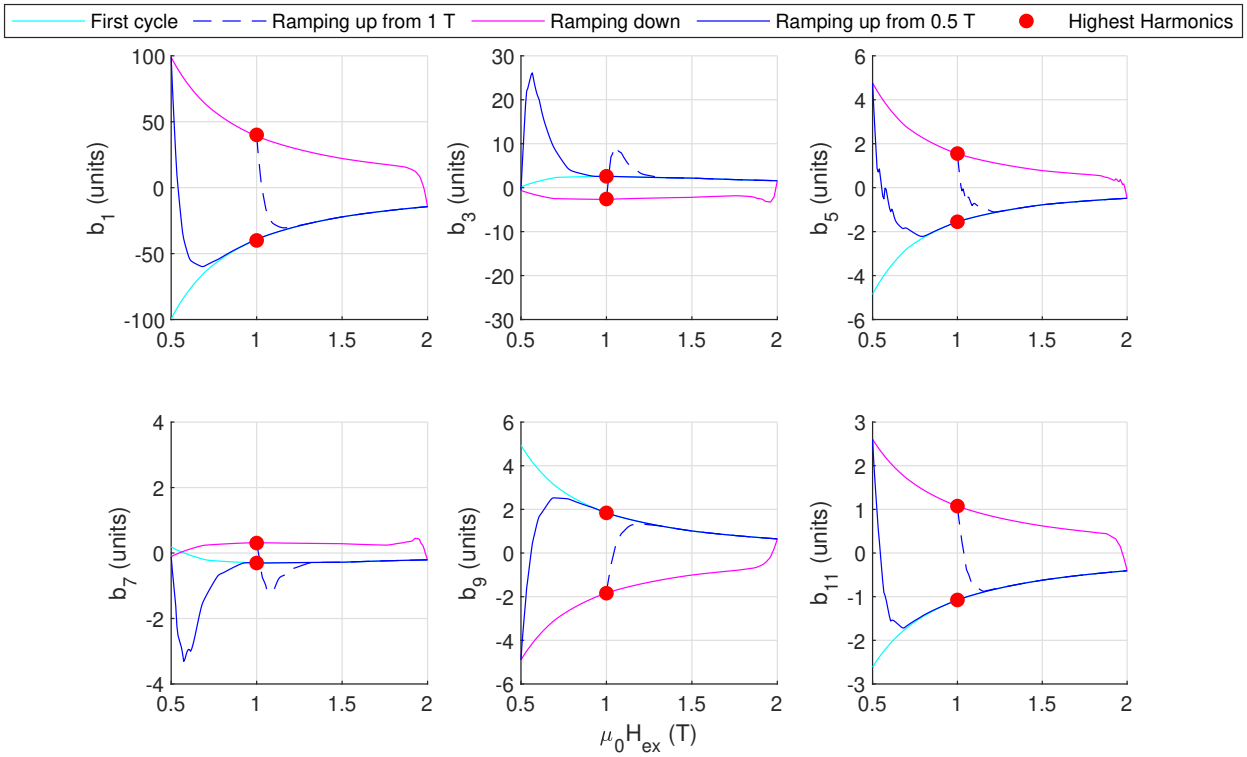


FIGURE 5.14: Odd normal field harmonics while cycling between 0.5 and 2 T. By reaching a minimum of 0.5 T, the highest values during ramp up within the relevant field range are reached at $\mu_0 H_{ex} = 1\,\mathrm{T}$ for all harmonics.

5.4.3 Combined Magnet-Coating Harmonics

Although we have considered an ideal dipole field as the external field to which the coated beam screen in submitted, in reality the field produced by the bending magnets will present harmonics of its own. The resulting magnetic field perceived at the reference radius will therefore be an addition of the contribution from the hybrid coating and the contribution from the main dipole magnets.

According to [9], the field harmonics produced by the magnets are given by table 5.1. However, they are calculated with respect to a reference radius of $2/3$ of the magnet aperture, that is, 17 mm. In order to obtain the magnet contribution in the same reference radius of the beam screen, we must scale the field harmonics to $r_0 = 9mm$. This is done by considering Equation 2.51. The scaled field harmonics are given by

$$b_k(9\,\mathrm{mm}) = \left(\frac{9}{17}\right)^{k-1} b_k(17\,\mathrm{mm})\,. \tag{5.13}$$

TABLE 5.1: Field harmonics off the FCC-hh main dipole magnets during injection.

b_2 (units)	b_3 (units)	b_4 (units)	b_5 (units)
5.6	-25	0.79	5.2

Figure 5.15 shows the contribution of both the main dipole magnet and the hybrid coating to the field harmonics at injection and at the reference radius of the beam screen. For this, we assume that the b_1 component coming from each source cancels each other, by applying a dipole field that is around 40 units larger than its nominal value. Comparing the values produced by each source, we can see that the contributions coming from the even components from the

coating are below one unit and far surpassed by the magnet harmonics. This is in agreement with the fact that the even coefficients should be negligible in a perfectly aligned external dipole field and only present non-zero values due to computational uncertainty.

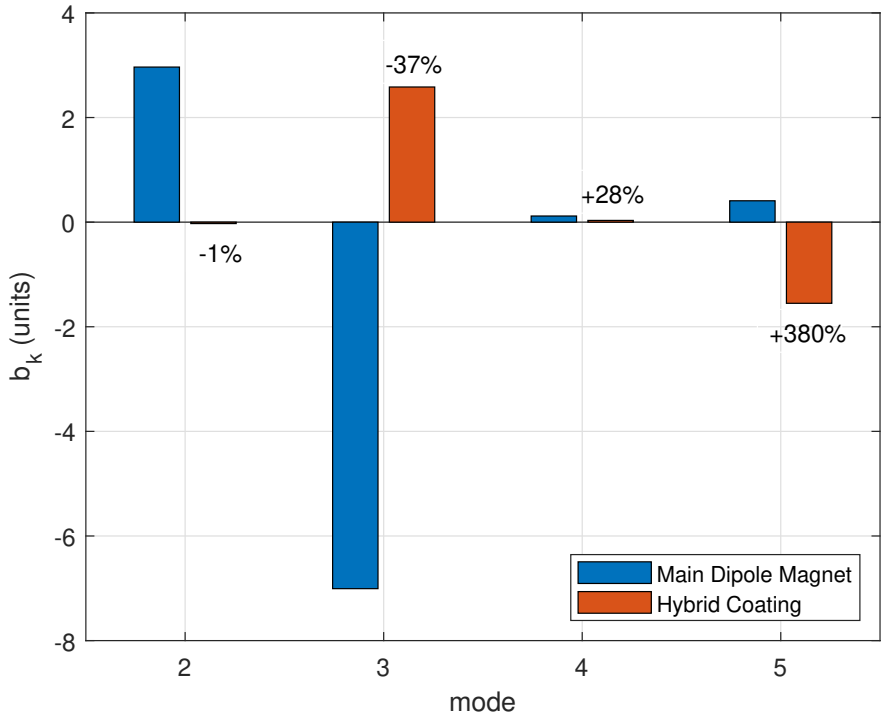


FIGURE 5.15: Contribution of the main dipole magnet and the hybrid coating to the field harmonics at injection. Percentage values represent the ratio between the contributions of the two sources.

The scenario changes when taking into account the odd coefficients. While the ratios between the magnet and coating harmonics for these modes sit under a factor 3, their signs are opposed, meaning that each source is partially compensated by the other. As a matter of fact, the greatest contributor to field harmonics, given a total compensation of the dipole component, is the magnet's b_3, which is partially corrected by the dipole counterpart, resulting in a decrease of 37% in the overall field disturbance with respect to the magnet on its own.

5.5 Chapter Summary and Conclusions

Throughout this chapter we have examined the behavior of the proposed geometry of the coated beam screen in other interesting field configurations apart from the ramping dipole field. To do that, the numerical model was adapted to account for external fields of higher modes that are tilted or displaced from the center of the beam screen. The dependence of J_c and N with the magnetic field was also developed to account for several impinging field angles onto the HTS segments.

The impact of a misaligned beam screen on the field harmonics produced inside the vacuum chamber is negligible within the tolerances estimated for the FCC-hh for the dipole magnets, but significant for the quadrupole. Although the altered field harmonics of the misaligned quadrupole are not high enough to surpass those originally produced by the perfectly aligned quadrupole, they must certainly be taken into account and the least possible misalignment is desirable.

Simulations of the hybrid coating under a constant dipole field after ramp-up revealed that the field harmonics tend to decrease over time as the current in the HTS segments goes down due to thermal creep. The exceptions are b_3 and b_7, which, in spite of not decreasing, do not reach dangerous values. On the other hand, when the hybrid coating was analysed under a cycling external field, the same harmonics reached their maxima in moments other than injection, threatening to shift the critical moment in terms of field quality. This can be mitigated, however, by employing a demagnetization cycle, shifting the peaks to outside of the 1 to 16 T relevant field range.

When considering the field harmonics produced by the main dipole magnet in combination with the contribution coming from the coating, we see that there is no dramatic change in the field quality. Furthermore, the fact that some contributions oppose one another suggests the possibility of fine tuning the coating geometry to counteract the magnet harmonics. This would convert the hybrid coating into a solution in terms of field quality, instead of a collateral effect from a surface impedance solution.

Finally, the simulation results discussed along this chapter present further evidence that the proposed geometry of the hybrid coating is a suitable coating for the dipole sections of the FCC-hh. On the other hand, they also make very clear that other geometries may be a better solution for other sections of the beam screen, particularly those under quadrupole fields, where more manageable harmonics would be achieved by highly striated coatings.

Chapter 6

Thermomechanical Behaviour of the Coated Beam Screen

While field quality and surface impedance are the main concerns regarding the use of HTS in the context of the FCC-hh beam screen, there are other requirements such as temperature and mechanical stress limits that must be satisfied. Therefore, it is important to evaluate the thermomechanical behaviour of the hybrid coating when operating under the dipole field produced by the bending magnets.

In this chapter we analyse the effects of the currents induced by the particle beam and by the external dipole field in the heat and force generation in the beam screen. We explain the numerical models adopted to do so as well as how the coupling between each of them works. Finally, we discuss the simulation results during ramp-up and injection, comparing with the pure copper coating of the beam screen.

6.1 Thermomechanical Model

To study the thermomechanical behaviour of the beam screen, we once again resort to FEM simulations. On the thermal side, we use the Heat Transfer on Solids interface from COMSOL Multiphysics®, and the PDE we are trying to solve is [111]

$$\rho_m C_p \frac{\partial T}{\partial t} - \nabla \cdot (\boldsymbol{k}_T \nabla T) = Q_V \,, \tag{6.1}$$

where ρ_m, C_p and k_T are material properties and stand for the material density, its specific heat and its thermal conductivity, and T and Q_V are the temperature and heat sources per unit volume, respectively. By inserting the heat sources arising from the current flow in the beam screen, we can use Equation 6.1 to find the temperature distribution across the entire structure.

On the mechanical side, the Solid Mechanics interface from COMSOL Multiphysics® is used, which solves the PDE system [112]

$$\rho_m \frac{\partial^2 \boldsymbol{u}}{\partial^2 t} = \nabla \boldsymbol{\sigma} + \boldsymbol{F}_V \tag{6.2}$$

$$\boldsymbol{\sigma} = \boldsymbol{C}\boldsymbol{\varepsilon} \tag{6.3}$$

$$\boldsymbol{\varepsilon} = \frac{1}{2}\left[(\nabla \boldsymbol{u})^T + \nabla \boldsymbol{u}\right] , \tag{6.4}$$

where $\boldsymbol{u}$, σ, ε and $\boldsymbol{F}_V$ are the displacement vector, the stress and strain tensors and the force vector per unit volume. $\boldsymbol{C}$ is the elasticity tensor, a fourth-order tensor that depends the Young's modulus E_y and Poisson's ratio ν_p of the material. Similarly to the heat sources in the Heat Transfer interface, $\boldsymbol{F}_V$ serves as the imput for the calculations, which allow us to find the deformation $\boldsymbol{u}$ as well as the strain and stress for all points of the beam screen.

This time, it is important to define domains for each different material, as the material properties will differ between the HTS segments, the steel and copper components of the beam screen, the silver and copper layers of the delaminated coated conductors, and the solder layers binding them to the beam screen. All materials are considered isotropic with the exception of the HTS segments, whose thermal conductivity assumes different values along the c-axis or the ab-plane [113–115].

The simulation space for both interfaces is comprised of only the beam screen structure, not including the surrounding vacuum chamber. There are two types of heat sources to be considered: the dipole-induced heat, coming from the current induced by the dipole magnetic field, and the beam-induced heat, coming from the image currents induced by the particle beam itself and the syncrhotron radiation it emmits. In addition, there is a negative heat source that represents the cooling channels that remove the heat from the beam screen. Likewise, the forces generated in the beam screen are Lorentz forces coming from the interaction of the dipole field with either the beam-induced or the dipole-induced currents. Figure 6.1 summarises the boundary conditions and sources in one half of the beam screen. For the purposes of these simulations, only the inner structure of the beam screen was considered, and all deformation is calculated with respect to the central point of the boundary between the cooling channel and the steel structure of the inner beam screen.

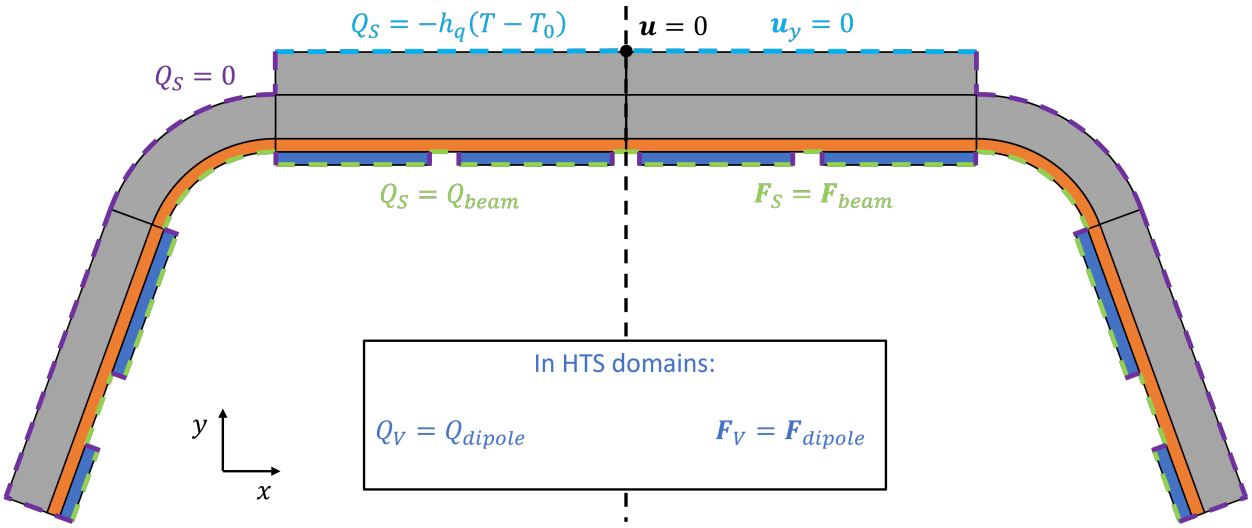


FIGURE 6.1: Boundaries and sources of the thermomechanical simulations. Q, $\boldsymbol{u}$ and $\boldsymbol{F}$ stand for heat, displacement and force. The contributions to force and heat coming from the dipole-induced currents are included by the means of heat and force sources per unit volume in all HTS domains, while those coming from the beam-induced currents, due to being only a superficial effect on the inner surface of the beam screen, are added as heat sources per unit area to the copper and HTS boundaries with vacuum. The cooling effect of the cooling channel is also accounted as heat per unit area on the boundary between the beam screen and the liquid helium channel.

The effects of the dipole field permeate the entire beam screen structure. However, the currents induced in the copper and steel during normal operation of the dipole magnets are negligible when compared to those in the HTS segments. The same can be said with regards to the heat and force loads produced by it, even considering the higher resistivities of the normal conductors. Therefore the heat and forces caused by dipole-induced currents are included

only in the HTS domains in the form of heat and force per unit volume, obtained via the electric field, the current density and the magnetic field resulting from the electromagnetic simulations of the beam screen coating under the dipole field:

$$\boldsymbol{F}_V = \boldsymbol{F}_{dipole} = \mu_0 J(\hat{z} \times \boldsymbol{H}) \tag{6.5}$$

$$Q_V = Q_{dipole} = JE\,. \tag{6.6}$$

The effects of the beam, on the other hand, are limited to the surface of the materials comprising the beam screen. At the main frequency of the beam, 1 GHz, the skin depth of the beam screen copper is below one micron, while that of the stainless steel sits around ten microns. In addition, the London penetration depth of the HTS amounts to only 170 nm [49]. With this in mind, it is reasonable to consider all materials as perfect electric conductors with respect to the image currents induced by the beam, which is then confined to their surface. This is done by adding boundary conditions to the surfaces of the beam screen. More details on how the beam effects are calculated will be discussed in Section 6.2. The cooling effect promoted by the helium channel is included also as a boundary condition according to which the heat is proportional to the difference between the temperature T of the structure and the temperature T_0 of the Helium, assumed to be constant at 50 K:

$$Q_{He} = -h_q(T - T_0)\,, \tag{6.7}$$

where $h_q = 5000\,\mathrm{W}/(\mathrm{m}^2\mathrm{K})$ stands for the heat transfer coefficient between the liquid helium and the surrounding steel structure [84]. We also assume that the boundary of the cooling channel does not move vertically to account for the mechanical resistance of the outer beam screen and the structure surrounding the cooling channel, which have not been included in the simulation.

At this point, it is important to consider how each physics interface is coupled with each other. On the one hand, the heats and forces in the beam screen arise due to the currents induced by the beam and the dipole, therefore there must be a connection of the electromagnetic simulations with the thermal and mechanical ones. This is done, as already explained, by adding the boundary conditions and sources. On the other hand, if the temperature shift or the mechanical strain caused by the induced currents is high enough, there may be an impact on the electromagnetic properties of the materials, most importantly the superconductor's J_c, which would require a two-way coupling. However, having this type of feedback between the different physics can significantly increase the computational effort. To avoid unnecessary increases in the computation time, we initially assume that whatever the thermomechanical effects caused by the induced currents are, they will be small enough not to impact in the material properties of the beam screen on the coating, which, as we will see further in this chapter, is a fair assumption.

6.2 Beam-Induced Effects in the Beam Screen

While the dipole-induced heat and force can be obtained directly from the dipole simulations, the beam-induced currents and their effects must be somehow accounted for. In this section we explore the numerical methods used to calculate the image currents induced by the beam on the inner surface of the beam screen, as well as the heat and forces arising from it.

6.2.1 Numerical Calculation of the Image Current Distribution

The particle beam travelling at the center of the vacuum chamber acts as an electric current I_{beam} that varies over time. It induces a time-dependent magnetic field on the surrounding region, which, in turn, induces image currents

in the beam screen, as discussed in Section 2.3. In a perfect infinite cylinder, the sheet current density is uniformly distributed along the circumference of its cross-section, and given by

$$J_S = \frac{I_{beam}}{2\pi r}. \tag{6.8}$$

The result of this equation is numerically identical to the magnetic field intensity component $H_{ac,||}$ that is tangential to the conductor's surface. Therefore, if the magnetic field distribution $\boldsymbol{H}_{ac}$ caused by the beam is found, so too are the image currents induced in the beam screen coating. Additionally, since the thermomechanical responses are much slower than the period of $\boldsymbol{H}_{ac}$, we can work with the average values over a period instead of the instantaneous ones.

To calculate the AC magnetic field distribution induced by the beam in the more complex geometry of the beam screen, a second simulation geometry was employed in addition to the influence of the dipole field presented in Chapter 4. Only two domains are considered in this simulation. The first one is the vacuum chamber itself, excluding the beam screen structure. The boundaries of this domain are defined as perfect conductors, an assumption that is in line with our first approximation that the image current is entirely contained on the surface of the material. The only electromagnetic source comes in the form of an electric current flowing through the second domain, defined by an arbitrarily small circle located in the very center of the vacuum chamber, with value equal to the average I_{beam}. The consequential $\boldsymbol{H}_{ac}$ in the surrounding region corresponds to the average induced magnetic field, which in turn yields $J_S = H_{ac,||}$ at the boundaries of the simulation space. Figure 6.2 illustrates the boundary conditions and current source for this simulation.

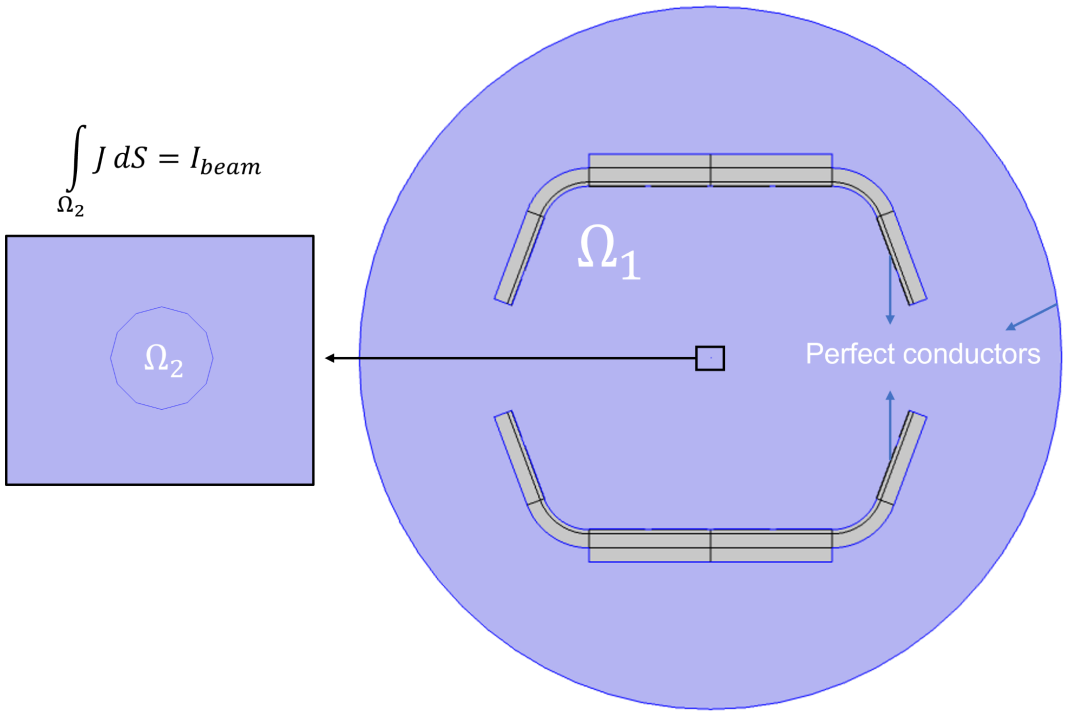


FIGURE 6.2: Boundaries and current source of the simulation to obtain the image current distribution in the beam screen coating. A total current equal to the average beam current I_{beam} is applied in the domain Ω_2, defined in an arbitrarily small circle in the center of the vacuum chamber. The boundaries of Ω_1, which correspond to the rest of the vacuum chamber, are defined as perfect conductors. The magnetic field distribution $\boldsymbol{H}_{ac}$ is calculated in Ω_1 and the image current is obtained from the tangential component of the field at the outer boundaries $\partial\Omega_1$.

While the beam intensity increases as the particles are accelerated, it is interesting to consider them to be constant and at the highest energy level throughout the entire ramping process. This allows the image currents to be calculated only once and replicated in time for the entire duration of the beam in the thermomechanical simulations, representing an upper limit for the heat and forces produced by the beam. Having this in mind, Figure 6.3 shows the sheet current density distribution along the surface width of the beam screen coating considering the approximated thickness of the delaminated coated conductors composing the hybrid coating to be zero.

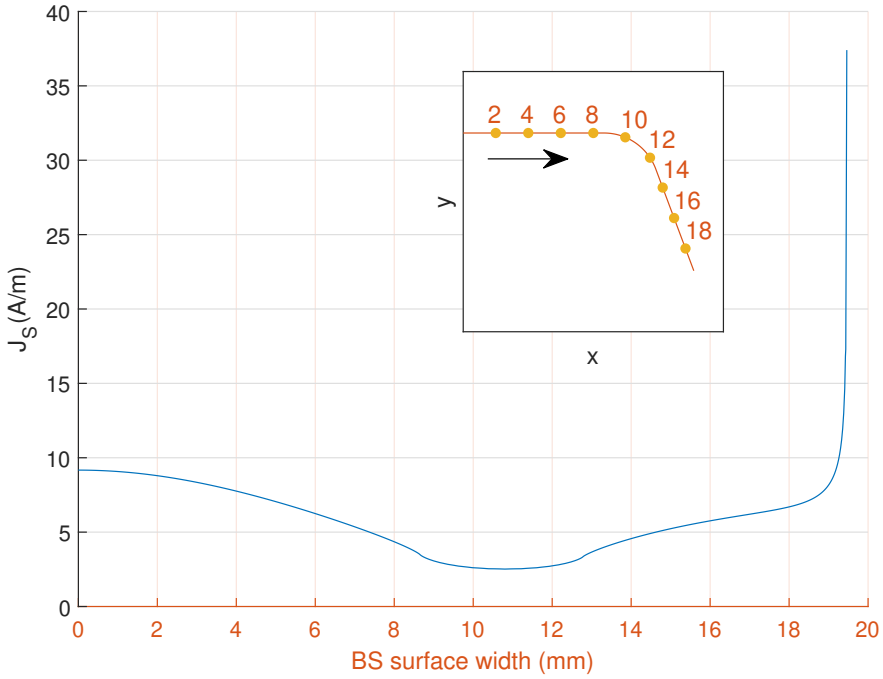


FIGURE 6.3: Average sheet current density calculated along the surface width of the beam screen coating, assuming all conductors behave as perfect conductors for an average beam current $I_{beam} = 0.5\,\text{A}$, as estimated for the FCC-hh beam. The BS surface width goes from 0 at the center of the beam screen ($x = 0$) to approximately 20 mm at the edge of the inner surface.

From these results, the dependence between J_S and the distance r from the center of the vacuum chamber is clear. Indeed, the largest values are achieved at the center of the beam screen, and close to the edges, where it is closest to the center of the vacuum chamber. In the opposite end of the spectrum, the curved parts of the surface, which are associated with the highest r, show the minimum values of J_S. Furthermore, it is interesting to note that at the edges, the J_S values are much higher than what could be explained solely by the decrease in the distance r. This increase may have arisen from edge effects due to the straight angle between the inner surface of the beam screen and the edge of the wall, which causes that currents induced to concentrate near the intersection of the two surfaces.

6.2.2 Resistive Wall Heating

Now that we have established what the image current distribution in the beam screen coating is, we can use it to calculate the heat sources that will be used as input for the heat transfer simulations. To do this we must first consider the resistive wall heating due to the beam-induced image currents in an infinite cylinder with radius r. The heating power per unit length is given by [116–118]

$$Q_L = \frac{I_{beam}^2 c^2}{2\pi^2 r M f_{rev}} \int_0^\infty \tilde{\lambda}^2(\omega) R_s(\omega) d\omega\,. \tag{6.9}$$

M, f_{rev} and R_s stand for the number of bunches, the revolution frequency in the accelerator and the longitudinal surface resistance of the cylinder walls. $\tilde{\lambda}$ is the power spectrum of the beam, which, like the surface resistance, is a function of the angular frequency ω. The power frequency can be approximated as a Gaussian curve given by

$$\tilde{\lambda}(\omega) = \frac{1}{c}\exp\left(-\frac{\sigma_z^2\omega^2}{2c^2}\right), \tag{6.10}$$

where σ_z is the RMS bunch length.

Equation 6.9 takes the form presented here due to the fact that in a cylinder, the image current distribution is uniform. To find a more general equation, that accounts for an irregular distribution such as the case of the FCC-hh beam screen, we must make a few adaptations, as following:

1. Replace the cylinder circumference $2\pi r$ by a generic perimeter l, which allows other shapes to be taken into account:
$$Q_L = \frac{I_{beam}^2 c^2}{\pi l M f_{rev}} \int_0^\infty \tilde{\lambda}^2(\omega) R_s(\omega) d\omega; \tag{6.11}$$

2. Differentiate both sides considering that the total image current, although still numerically equal to I_{beam}, will now come from differently weighted contributions depending on the distance from the center of the vacuum chamber:
$$dQ_L = \frac{(dI_{beam})^2}{dl} \frac{c^2}{\pi M f_{rev}} \int_0^\infty \tilde{\lambda}^2(\omega) R_s(\omega) d\omega; \tag{6.12}$$

3. Substitute $dI_{beam} = J_S dl$ and turn R_s into a function of both ω and l:
$$dQ_L = \frac{(J_S dl)^2}{dl} \frac{c^2}{\pi M f_{rev}} \int_0^\infty \tilde{\lambda}^2(\omega) R_s(\omega, l) d\omega; \tag{6.13}$$

4. Derivate both sides with respect to l to obtain the power per unit area as a function of l, since now it will differ depending on the material, which in turn depends on l:
$$Q_{beam}(l) = \frac{dQ_L}{dl} = \frac{c^2 J_S^2(l)}{\pi M f_{rev}} \int_0^\infty \tilde{\lambda}^2(\omega) R_s(\omega, l) d\omega. \tag{6.14}$$

Equation 6.14 corresponds to the heat per unit area used as boundary condition in the heat transfer simulations. Note that it depends on the sheet current density distribution $J_S(l)$, which is material independent, but also on the surface resistance distribution $R_s(\omega, l)$, which does depend on material distribution. Therefore, the total heat per unit length $P_L = \int_{l_{BS}} P_S(l) dl$ will also depend on the geometry of the hybrid coating.

The next step is to find the surface resistance as a function of l. Wherever l corresponds to an HTS segment, it will assume the value of the superconductor's $R_s^{HTS}(\omega)$. On the other hand, where l corresponds to a copper gap, it will assume the copper's surface resistance $R_s^{Cu}(\omega)$. These two must be distinguished with respect to their frequency behaviour. In fact, while $R_s^{Cu}(\omega)$ is proportional to $\sqrt{w}$ (see Equation 2.19), $R_s^{HTS}(\omega)$ scales with the square of the frequency at zero fields, a dependency which may vary when an external magnetic field is applied (see Equation 2.31). For the purposes of this work, we assume a square root dependence for copper and a square dependence for REBCO as theoretically predicted, although an exponent closer to 1 may be more accurate for in-field values[119]. This behavior is being investigated by Nikki Tagdulang and will be within the scope of her doctoral thesis. In any case,

both dependencies can be described as a single equation:

$$R_s(H,l) = K(H,l)\omega^{\nu(l)-1}\,, \tag{6.15}$$

where $K(H,l) = K_{Cu}$ and $\nu(l) = 3/2$ for copper, and $K(H,l) = K_{HTS}(H)$ and $\nu(l) = 3$ for HTS. Replacing these and Equation 6.10 into Equation 6.14, we get

$$Q_{beam}(H,l) = K(H,l)\frac{J_S^2(l)}{\pi M f_{rev}}\int_0^\infty \exp\left(-\frac{\sigma_z^2\omega^2}{c^2}\right)\omega^{\nu(l)-1}d\omega\,. \tag{6.16}$$

Fortunately, this can be simplified by exploiting a property of the gamma function[120], which results in

$$Q_{beam}(H,l) = K(H,l)\frac{J_S^2(l)}{2\pi M f_{rev}}\left(\frac{c}{\sigma_z}\right)^{\nu(l)}\Gamma\left(\frac{\nu(l)}{2}\right)\,. \tag{6.17}$$

We can determine K for both copper and HTS with the help of surface resistance measurements performed at 8 GHz and 50 K with a dielectric resonator[13]. For the beam screen copper, the measured surface resistance of $R_s^{Cu} = 7.5\,\mathrm{m\Omega}$ results in $K_{Cu} = 3.35\times10^{-8}\Omega\mathrm{s}^{-0.5}$. On the other hand, the surface resistance results and the obtained K_{HTS} for a *SuperPower inc.* coated conductors are shown in Figure 6.4. Here we see the dependence of R_s^{HTS} with the external magnetic field, which results in the fitting of K_{HTS} according to

$$K_{HTS}(H) \approx k_1\sqrt{\mu_0 H} + k_2\,, \tag{6.18}$$

with $k_1 = 5.3\times10^{-25}\Omega\mathrm{s}^2\mathrm{T}^{-0.5}$ and $k_2 = -4.5\times10^{-25}\Omega\mathrm{s}^2$. Combining this with the values of the gamma function at $\Gamma(3/2) = 0.886$ and $\Gamma(3/4) = 1.225$, we can extrapolate the surface resistance of both copper and HTS in terms of both frequency and magnetic field. Note, however, that a different frequency dependence could significantly change the estimated surface resistance values of the HTS when extrapolating down from 8 GHz, resulting in an increase on the beam-induced heat in the hybrid coating by up to 50 % with respect to our calculations, assuming a linear dependence instead.

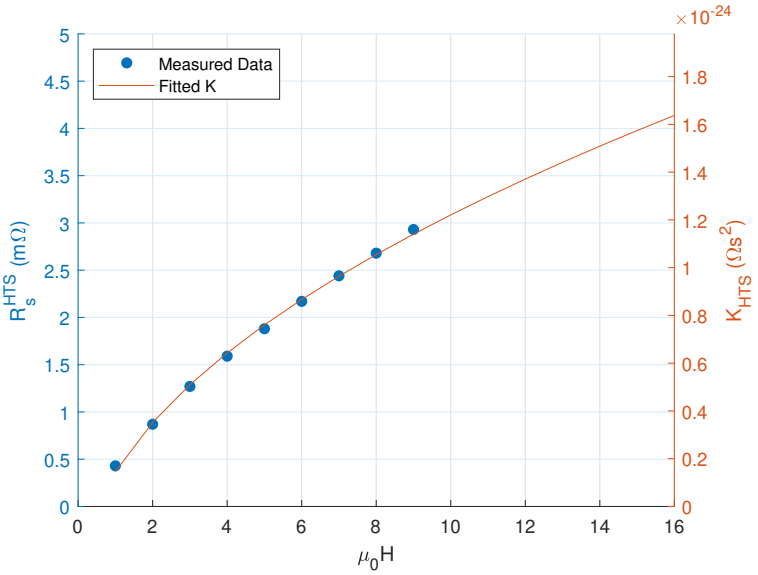
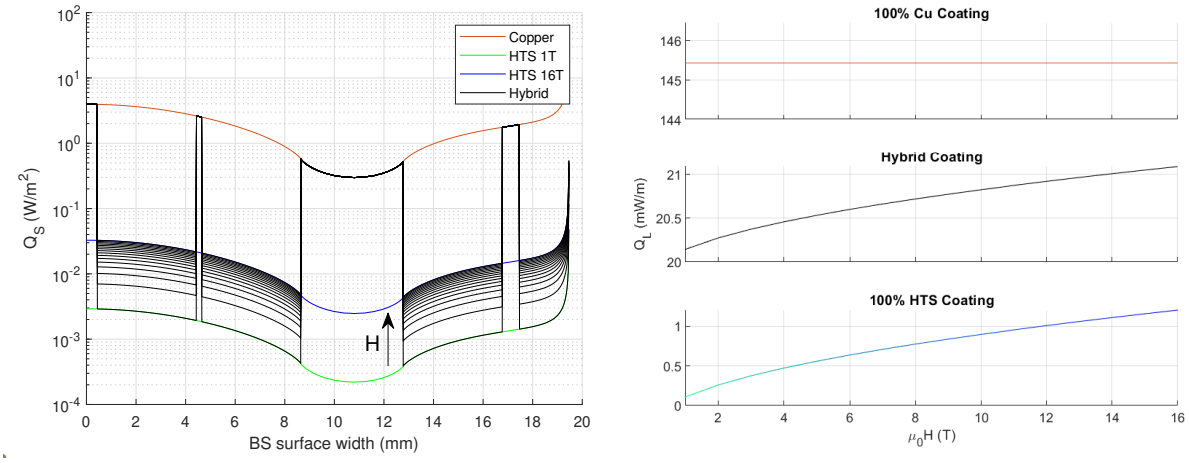


FIGURE 6.4: Surface Resistance measurements of *SuperPower Inc.* coated conductors above 1 T at 50 K and 8 GHz. K_{HTS} is obtained by fitting the data and dividing by the angular frequency squared.

Now that we have gathered all the necessary pieces, we can finally obtain the heat distribution caused by the induction of image currents in the beam screen coating. Figure 6.5 shows the heat per unit area generated along the surface width of the beam screen coating, as well as the total heat per unit length as a function of the external dipole field.



(a) (b)

FIGURE 6.5: Resistive wall heating due to the image currents induced by the particle beam in the beam screen coating. (a) Heat per unit area along the surface width (l) for different external dipole fields; and (b) total heat per unit length as a function of the external field for different types of coatings.

We can see that the heat as a function of the surface width preserves the shape of the induced sheet current density, as previously presented in Figure 6.3, for the pure copper and pure HTS coatings. On the other hand, the heat produced in the hybrid switches between the pure copper and pure HTS values, depending on the material distribution in the coating. As expected, the more copper is present the larger will be the heat generation due to the higher surface resistance values of the normal conductor.

This data also clarifies that, in terms of resistive wall heating, there are some key regions of the beam screen that play a more significant role in heat generation. Namely, the edges of the beam screen, pointed out previously, present the highest values of induced current. However, by ensuring that the region within 2 mm of the edge is coated with HTS, the heat per unit area generated there will be lower than the lowest contribution coming from the copper. On the other hand, since it is necessary to leave some regions with copper coating due to the necessity of preserving field quality, as discussed in Chapter 4, it is better that these parts are as far as possible from the beam. Particularly the bent region connecting the top wall to the diagonal wall, which is not coated with HTS due to the higher complexity of coating bent surfaces, shows a relatively low heat generation when compared to the other copper gaps, albeit still quite high when compared to the HTS.

While a pure HTS coating would be able to reduce the heat generation by two orders of magnitude when compared to pure copper, it is clear that it is not a viable option due to the field quality constraints. However, a hybrid coating such as the one proposed in Chapter 4 is able to decrease the heat by a factor 7, reaching only around 21 mW/m, even at high fields, while the pure copper coating would achieve 145 mW/m. It is worth noticing that even a small amount of exposed copper such as this (11% of the straight walls and 28% of the total surface), is enough to significantly impact on the heat generation, being responsible for around 95% of the total heat induced in the hybrid coating.

6.2.3 Beam-Induced Forces

On the mechanical side, the forces induced by the image currents can be obtained in a fairly simple manner, by multiplying the sheet current density by the external DC field:

$$F_{beam} = \mu_0 J_S(\hat{z} \times \boldsymbol{H}) . \tag{6.19}$$

Note that in a perfect dipole DC field, this results in a purely horizontal force distribution, with all contributors pointing towards the same direction. On one hand, this means that there is no quadrant symmetry for the force effects, even if the dipole and the beam screen are ideal and perfectly aligned. On the other hand, the fact that this is actually an oscillating force means that the beam may introduce vibrations to the system, whose consequences are not evaluated in this steady-state approximation.

At injection, the estimated average total force is approximately 0.23 N/m, reaching up to 3.64 N/m at top energy, distributed along the entire coating of the beam screen. However, the instantaneous beam current is expected to reach almost 50 times its average value, resulting in instantaneous forces of around 10 N/m at injection, up to 170 N/m at top energy. It is worthwhile to point out, though, that these induced forces will see little to no difference whether the coating is pure copper or the hybrid REBCO-Cu coating, since the current distribution in the surface of the beam screen is material independent[109] and the dipole field is only slightly deviated by the HTS trapped fields.

Figure 6.6 summarises in schematics the multiphysics couplings between all simulation interfaces. The outputs of the electromagnetic simulations of the beam screen under the dipole field are E, J and H, while the electromagnetic simulation of the average field produced by the beam yields J_S. The inputs for the heat transfer simulations are E and J, which are used to calculate the heat produced by the dipole-induced currents, and J_S and H, which are combined to find the beam-induced heat generated by the image currents. For the solid mechanics simulations, the inputs J and J_S are used in combination with H to obtain dipole- and beam-induced forces, respectively.

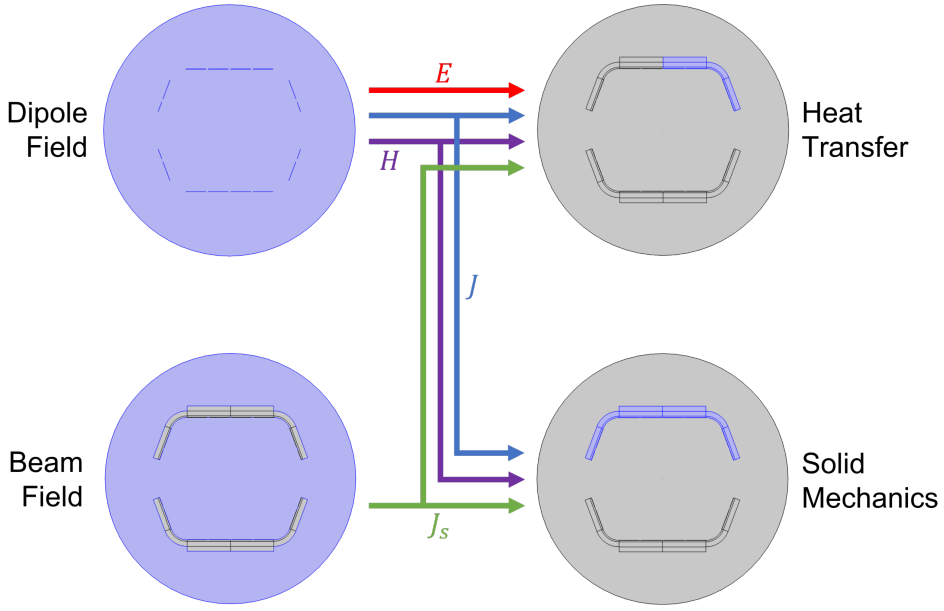
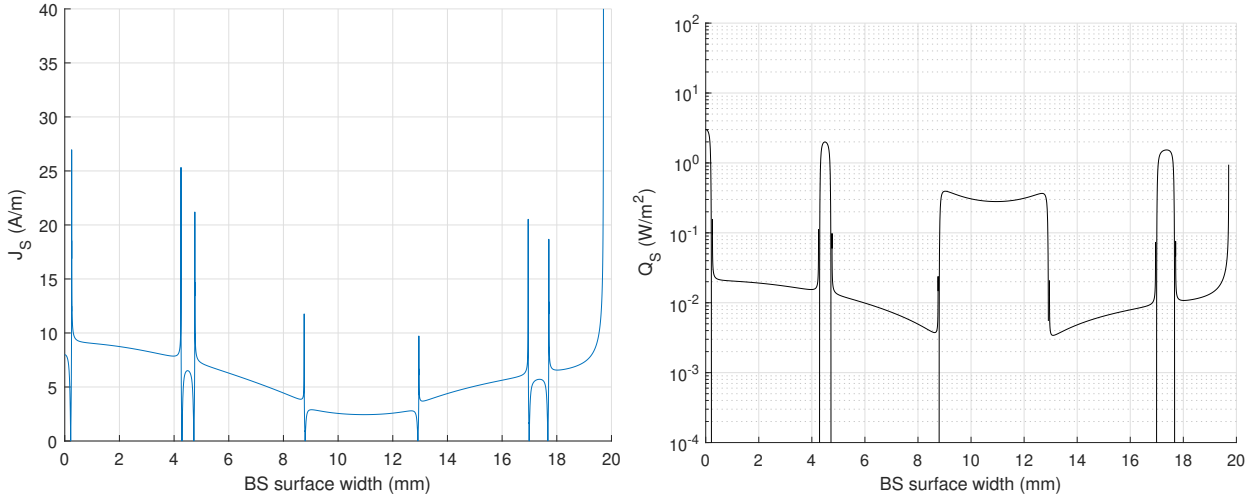


FIGURE 6.6: Schematic representation of the unilateral multiphysics coupling between the four physics interfaces. The outputs J, E and H from dipole simulations, and J_S from the beam simulations serve as input to calculate the force loads and heat sources for the heat transfer and solid mechanics simulations.

6.3 Thermomechanical Simulations

The thermomechanical simulations of the beam screen were performed with a ramping dipole field and during a one minute injection. The effects of the beam on the beam screen start acting when the dipole field reaches 1 T at $t = 75\,\mathrm{s}$, and last through the remaining simulation time. For simplicity, we have considered that the beam current is at its maximum throughout the entire magnetic field range. The sheet current density induced by the beam is shown in Figure 6.7, as well as the resulting heat generated in both the copper and the superconductor. It is worth noticing that, when comparing this data with Figures 6.3 and 6.5a, there are now discontinuities when transitioning from the copper regions to the HTS regions of the coating. This is due to the fact that the thickness of the CC layers are now being taken into account, which results in different heights in the coating, and therefore in steps in the current distribution. As a consequence, the resistive wall heating in the beam screen is lower than originally estimated, since the currents induced in the copper are slightly decreased.



(a) (b)

FIGURE 6.7: Beam-induced thermal effects in the beam screen coating considering its in-homogeneous thickness. (a) Beam-induced image currents; and (b) Beam-induced resistive wall heating. The discontinuities are due to the transition between the copper and HTS boundaries.

To account for the thermal effects of the syncrotron radiation, we have considered that a constant heat of $4\,\mathrm{W/m^2}$ is absorbed by the diagonal walls on the left side of the inner chamber of the beam screen after reaching the injection field. This value corresponds to the maximum heat density calculated in [10] for the inner chamber at top energy (16 T) and results in an overestimation of the total heat produced in the inner chamber by a factor 2. Nevertheless, as we will see this assumption plays only a minor role in the thermal response of the coated beam screen.

In Figure 6.8a, we can see the total heat generated as a function of time coming from both the dipole and the beam contributions. The resistive wall heating amounts to around $15\,\mathrm{mW/m}$ throughout its duration, running short of the previously predicted $21\,\mathrm{mW/m}$. Most worthwhile, however, is the fact that, throughout the entire duration, the total resistive heat, excluding the synchrotron contribution, is never larger than $65\,\mathrm{mW/m}$, meaning that the hybrid coating more than halves the resistive heat loads in the beam screen due to the lower surface resistance of its HTS portions. Furthermore, the dipole-induced heat load tends to decrease as the external dipole field increases due to the decreasing J_c and consequential progressive drop in the current flow, while the electric field is mostly maintained. Although the simulation was not extended beyond 8 T due to the inaccuracies that would arise from the extrapolation of the HTS properties, it is reasonable to assume that this trend will continue until higher field values.

With respect to the temperature response of the beam screen to these heat loads, we can see in Figure 6.8b its temperature profile at some key moments. First a global temperature maximum is reached at $t = 21\,\text{s}$, shortly after a peak in heat is generated and still at very low fields. This is due to the still high J_c of the HTS segments, which has not yet been reduced by the impinging magnetic field. As the field continues increasing, the temperature drops consistently, until reaching injection at 75 s. At this point, the dipole field is held constant at 1 T and the electric field, which arises from the slope in the magnetic field, drops immediately, as does the dipole-induced heat. For the next minute the heat sources in the beam screen are the image currents, which configure a considerably lower contribution, and the synchrotron radiation. After injection, the magnetic field once again starts increasing, leading to a local temperature maximum at 148 s, but as the field increases further and the heat load drops, so too does the temperature.

At all moments, the hottest point is the very edge of the beam screen coating, located at the end of the 2 mm wide HTS segment near the lateral gap of the beam screen. However, although the temperature behaviour is consistent with expectations, the shift in temperature is never larger than 5 mK. This means that the heat loads to which the beam screen is subjected are aptly handled by the cooling channels, resulting in negligible effects in the temperature, even when taking into account the exaggerated contribution from the synchrotron radiation. Furthermore, this tells us that the unilateral coupling adopted between the dipole field and the heat transfer interfaces is appropriate, since there is no need to introduce a dependence of J_c and N with the temperature during normal operation of the beam screen due to the relatively low electric fields.

When it comes to the solid mechanics analysis, the vectorial force loads imposed on the beam screen are not as simple to evaluate as their heat counterparts. The beam-induced forces are proportional to the magnetic field and therefore start at a constant value during injection to then increase at a constant rate over time during ramping. The dipole-induced forces however, are the result of two opposing dependencies. On one hand, the J_c, and therefore also the current density, decreases with H, on the other, H itself increases with the ramping dipole field. This results in force loads that initially tend to increase with the dipole field, only to have its behaviour reversed after reaching a given field value. The behaviours of the force loads are represented in Figure 6.9a via their instantaneous maxima as a function of time. It is interesting to note that, while the dipole-induced heat quickly vanishes at injection, as seen in Figure 6.8a, this is not the case for the dipole-induced force loads. This is due to the dependence of f_{dipole} with the magnetic field, which remains constant, while the dipole-induced heat is proportional to the electric field, which drops to zero at a constant magnetic field.

When comparing the maximum values achieved by each contribution we notice that the average forces produced by the beam are three orders of magnitude lower than those produced by the dipole field. Even if the instantaneous values of the beam-induced forces are considered, they would still be a factor 21 below the dipole contribution, which suggests that the impact of the beam regarding the mechanic behaviour of the beam screen is negligible compared to the dipole contribution.

Although the magnitude of the forces offers some hints towards the mechanic response of the beam screen, it is not enough to paint the whole picture. To complement this, Figure 6.9b presents the force load distribution along the hybrid coating coming from both contributions. After a short transition period at low fields before injection, both forces assume purely horizontal components. Due to the current distribution in the HTS segments, the force loads generated by the dipole field tend to stretch the segments of the top wall and to rotate the segments of the diagonal walls. The resulting torque tends to bend the diagonal walls inward. On the other hand, the beam-induced forces all point towards the same direction since the image currents flow in a single direction, breaking quadrant symmetry and having opposing effects on each side of the beam screen.

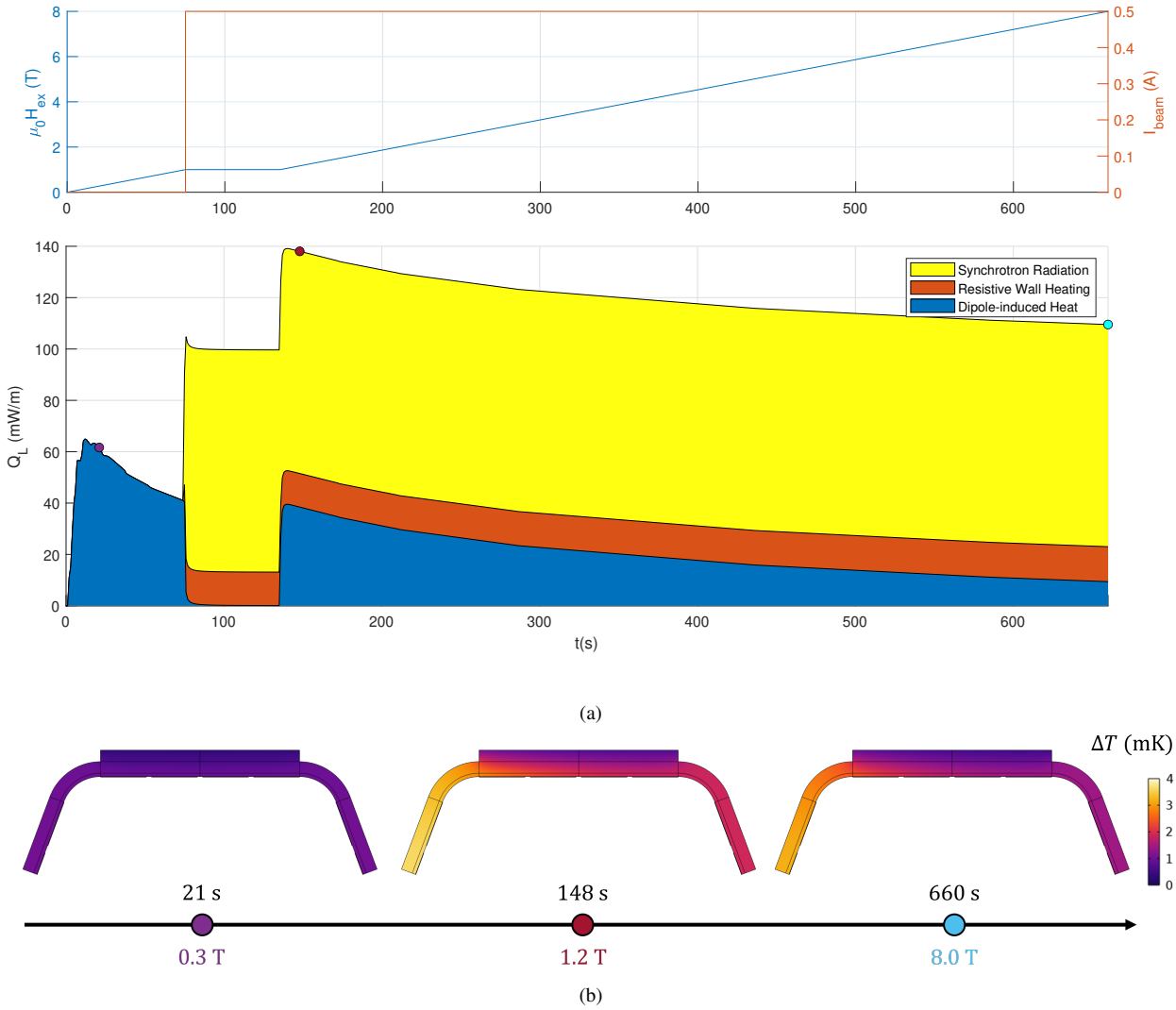


FIGURE 6.8: Simulation results for the thermal behaviour of the beam screen under a ramping dipole field and during injection, considering beam effects. (a) Heat sources generated as a response to the ramping dipole field, and the beam-induced image currents and synchrotron radiation as a function of time; and (b) Temperature profile of the beam screen at certain moments of interest. Local temperature maxima are achieved at $t = 21\,\text{s}$ and $t = 148\,\text{s}$, slightly after the dipole field starts increasing. As the dipole field increases, the temperature tends to fall due to the decreasing J_c. Nevertheless, the temperature shift along the entire range of operation is negligible at $\Delta T < 5\,\text{mK}$.

We can see the effects of the force loads on the beam screen in Figure 6.9c, where the stress profile and the deformation of the beam screen is shown at relevant moments, namely at injection, at the moment when maximum load is reached and at 8 T, which correspond respectively to $t = 75\,\text{s}$, 381 s and 660 s. Here the tendency of the dipole-induced forces to bend the diagonal walls becomes clear in all moments, which in turn induces relatively high stresses at the joint region connecting the top wall to the diagonal walls. The stress maxima at all moments correspond to this region and never surpass 3 MPa, a value that is well within the elastic regime for all metallic materials composing the beam screen.

It is interesting to note that even though quadrant symmetry is broken due to the beam-induced force loads, this asymmetry is not carried over to the stress response. In fact, the stress values in each quadrant are mirrored, within a

tolerance that is comparable to the error arising from the meshing itself, reinforcing the notion that the beam effects are negligible in the context of solid mechanics. We must not forget, though, that vibrations coming from the instantaneous force loads can still play a significant role, and should not be disregarded without further study. In any case, this effect will be only minimally impacted by the material distribution of the beam screen coating, and hence should not be held as argument against or in favor of adopting any type of coating, including the hybrid geometry proposed in this work.

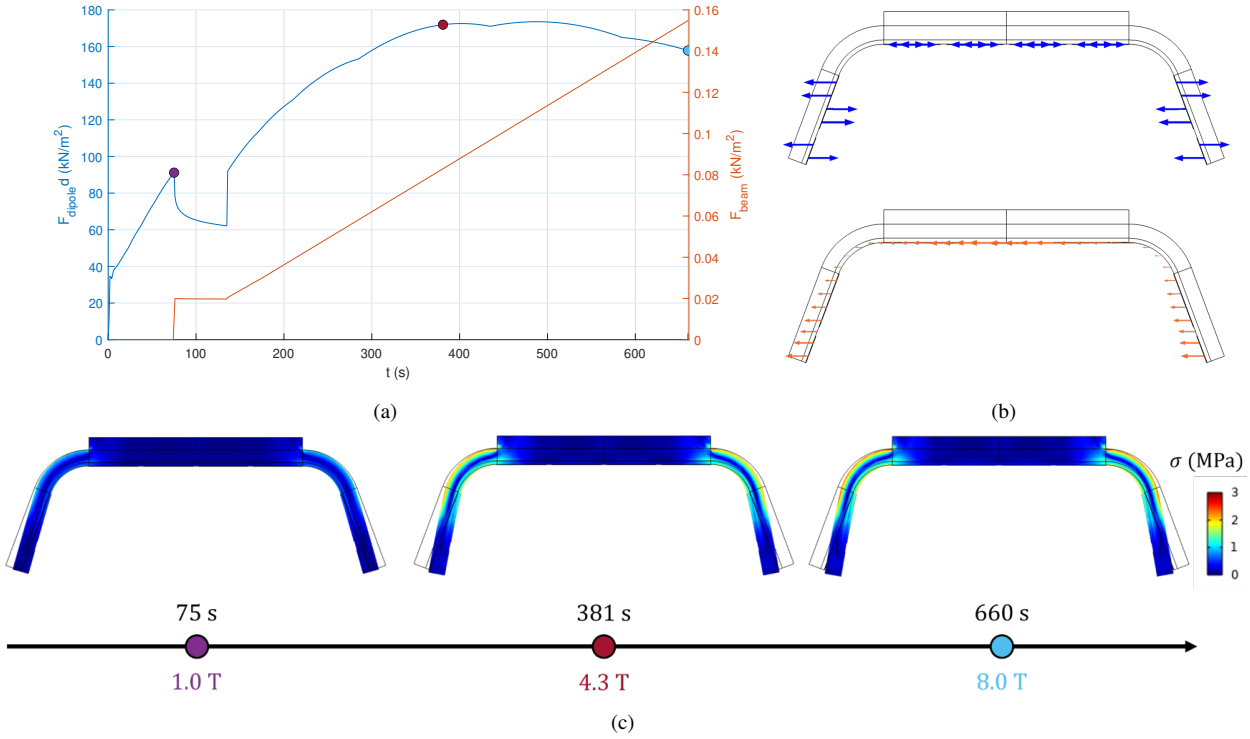


FIGURE 6.9: Force loads and deformation results due to ramping dipole field and beam-induced currents in the beam screen. (a) Maximum force per unit area produced by both the dipole- and beam-induced currents in the HTS segments, where h stands for the thickness of the HTS layer; (b) Force load induced by the dipole field (top) and by the beam (bottom) in the hybrid coating; and (c) Von Mises stress profile and deformation scaled by a factor 1000. The maximum value of stress is reached at $t = 381$ s due to the inverse dependence between J_c and H.

Regarding the effect on the HTS layers, the maximum stress reached is 2.2 MPa. Previous studies show that this is around two orders of magnitude below the necessary values to impact on the critical current of REBCO HTS [121, 122]. Therefore, once again we confirm the suitability of the unilateral coupling also for the solid mechanics interface when it comes to the regular operation of the beam screen under the dipole magnets.

The thermomechanical results of the hybrid coating during ramping and injection offer further evidence towards its viability as a low impedance coating for the FCC beam screen. At all fields below 8 T, there was no significant shift in temperature or inscrease in mechanical stresses. Although magnetic fields above 8 T have not been considered due to the inaccuracy of the extrapolation of HTS properties, the resulting behaviour of the beam screen with respect to both heat transfer and solid mechanics suggest that the beam screen response to the force and heat loads will only improve as the field increases. At top energy, the force loads are expected to maintain similar values than those achieved at 8 T, and the sole contribution to resistive wall heating will come from the beam-induced image currents, since the electric field generated by dipole-induced currents will vanish, similarly to what happens during injection.

6.4 Chapter Summary and Conclusions

In this chapter, the thermomechanical behaviour of the beam screen under a ramping dipole field and during injection was evaluated by the means of FEM numerical analysis. The adopted simulation model takes into account the synchrotron radiation and the image currents induced by the beam as well as those induced by the ramping dipole field, which in turn generate heat and force loads along the beam screen coating.

The simulation environment consists of four coupled physics interfaces. The dipole simulations developed in Chapter 4 and the particle beam simulations were used to calculate the current distribution inside the HTS segments and the surface currents induced by the beam in the hybrid coating respectively. Based on these outputs, the heat and force loads could be obtained for the heat transfer and solid mechanics interfaces respectively. To find the beam-induced heat loads, the formulae usually employed to calculate the resistive wall heating in perfect cylinders was adapted to consider the complex geometry of the beam screen, taking into account the different frequency dependencies of the surface resistance of copper and HTS.

Results show that the resistive heat produced in the beam screen can be significantly reduced by replacing the pure copper coating by the hybrid coating, resulting in negligible shifts in temperature. On the other hand, the forces induced in the hybrid coating do surpass those induced in a pure copper coating due to the dominating dipole field contribution. Nevertheless, the stresses induced by the Lorentz forces coming from both the beam and the dipole field are within the elastic regime for all beam screen materials.

The simulation results obtained along this chapter show the conformity of the hybrid coating with regards to its thermomechanical behaviour during normal operation of the beam screen. The results obtained at fields up to 8 T can be safely extrapolated to top energy, at which point the heat and force loads will be maintained or reduced. In combination to the results seen in Chapter 4, these show that the proposed geometry of the hybrid coating can achieve high field homogeneity under dipole fields and low surface impedance while not hindering the thermomechanical response of the beam screen.

Chapter 7

The Coated Beam Screen during a Dipole Magnet Quench

In the event of a magnet quench, the currents induced in the beam screen will surpass those flowing during regular operation of the accelerator, resulting in high Lorentz forces and heat loads. Therefore, it is interesting to analyse the behaviour of the beam screen also in this undesired situation, to verify whether it and its coating would survive the event. This chapter will go through the necessary adaptations to the model to account for the influence of a dipole magnet quench in the eletromagnetic and thermomechanical behaviour of the coated beam screen, how the different physics interfaces are coupled to handle the high temperatures and stresses that may arise, and the simulation results of the beam screen under a dipole quench. Additionally, we will investigate the tolerance of the HTS coating to the Lorentz forces that arise due to the rapidly changing magnetic field by the means of pull-off adhesion tests.

7.1 Model Adaptations

If the dipole magnet quenches while operating at top energy, it can go from 16 T to zero as fast as 300 ms, resulting in high induced currents not only in the HTS segments but also in the remaining conductors of the beam screen and its coating. The contribution coming from the normal conductors in terms of heat and force loads may now be high enough to play a significant role in the thermomechanical response of the beam screen. Hence, it is important that, in magnet quench simulations, the entire structure of the beam screen, as well as the metallic layers of the delaminated coated conductors, are taken into account. On the other hand, the particle beam will quickly escape from orbit once the dipole field starts dropping due to not being decelerated at the same pace, therefore we will not consider the heat and force load contributions coming from the beam-induced image currents.

In previous dipole simulations, we have obtained the current density distribution inside the HTS segments by solving the PDE system described by Equations 4.9 through 4.12, which account for the field distortion in the HTS segments and their vicinity. This was particularly important because the main goal of those simulations was to evaluate the field quality of the coating geometry in question. During a magnet quench, there is no necessity for this type of evaluation, since the preservation of the beam orbit is no longer a concern. The electromagnetic response of the beam screen will only serve as input for its thermomechanical behaviour. On the other hand, solving the previously adopted PDE system for the high field derivatives induced by the quench is very computationally demanding, especially when considering highly non-linear materials such as HTS. For these two reasons, we have opted to replace the numerical solution of the PDE system with an analytical approximation of the induced currents in the beam screen.

The main assumption for this approximation is the thin film behaviour of the HTS segments. According to it, it is reasonable to assume that the distortion in the magnetic field caused by the HTS segments is approximately zero compared to the external field, or, in the case of the dipole, that $\boldsymbol{H} \approx \boldsymbol{H}_{ex}$. While this approximation fails at very low fields, it will be quite accurate at higher fields, when the beam screen is exposed to the highest heat and force loads. In addition, we assume that the HTS is homogeneous along the c-axis. With this, we can obtain the electric field distribution inside the HTS segments (and any of the normal conductors) directly from the anti-derivative of Equation 4.10 with respect to x, which results in

$$E_z = \mu_0 \frac{\partial H_{ex}}{\partial t} x + C\,. \tag{7.1}$$

Since the time derivative of the applied magnetic field is constant in space, C can be replaced by a more convenient constant:

$$E_z = \mu_0 \frac{\partial H_{ex}}{\partial t} (x - x_0)\,, \tag{7.2}$$

where x_0 is the center of the combined structure formed by all electronically coupled conductors. The original assumption that the HTS segments are electronically insulated from the rest of the coated beam screen is maintained, therefore x_0 corresponds to the center of each HTS segment, when calculating the electric field inside that segment, and $x_0 = 0$ for all remaining conductors, which are considered to be connected.

Once we have determined the electric field induced by the time-varying dipole field, we can then obtain the current density across the whole beam screen. In both normal and superconductors, it is given by

$$J_z = \frac{E_z}{\rho}\,. \tag{7.3}$$

Now that J_z and E_z are known, as well as H_{ex}, we can calculate the force and heat loads for the heat transfer and solid mechanics interfaces:

$$F_{Vx} = -\mu_0 H_{ex} J_z \tag{7.4}$$

$$Q_V = J_z E_z\,. \tag{7.5}$$

Since the force loads are only due to the interaction between the dipole field and the beam screen, quadrant symmetry is restored, which allows us to consider only a single quadrant, with the proper symmetry conditions. For the solid mechanics interface, those are $u_x = 0$ at $x = 0$ and $u_y = 0$ at $y = 0$. This set of boundary conditions allows the beam screen to be deformed in place, but prevents it from displacing or rotating. For the heat transfer interface, the sole boundary heat source represents the cooling effect of the helium channel. The boundary conditions and heat and force sources are represented in Figure 7.1.

Unlike the normal operation of the accelerator, the shift in temperature may be significant, impacting in the resistivity of the materials of the beam screen and its coating. For the normal conductors, this relationship can be easily included by the means of a linear dependence between the resistivity and the temperature or by considering interpolation functions of measured data. For the HTS segments, however, a few extra steps must be performed.

When in the superconducting state, shifts in temperature influence the critical current density and the transition index of the material. To account for this, we once again resort to interpolation functions, this time correlating J_c and N with $\mu_0 H$ and T. Since we are neglecting the field disturbance caused by the HTS segments, there are only two angles between the REBCO and impinging fields: 0° for the top wall segments and $\approx 70^\circ$ for the diagonal ones. Therefore, we can apply two different interpolation functions for each property based on data of SuperPower inc.

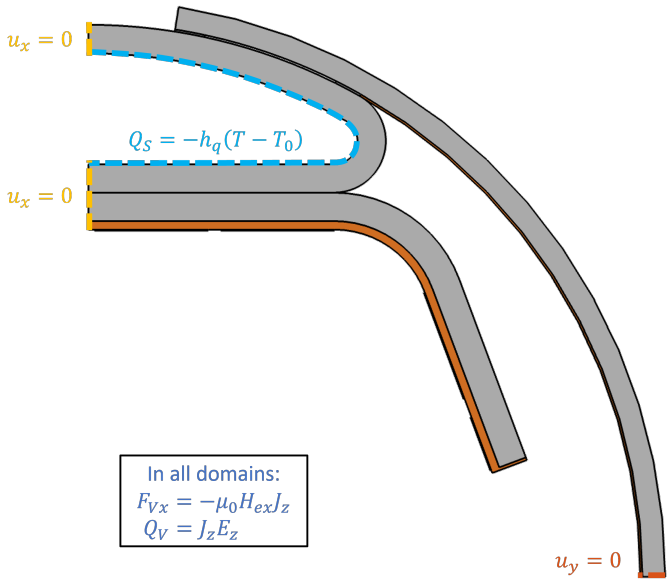


FIGURE 7.1: Boundary conditions and heat and force sources in the coated beam screen during a dipole magnet quench. The displacement boundary conditions are used to prevent rotation and displacement of the beam screen while preserving quadrant symmetry. All boundaries except for those of the helium channel are thermally insulated $Q_S = 0$, and the force and heat per unit volume produced by the dipole are defined in all domains.

coated conductors [63], as shown in Figure 7.2. Since the data does not cover the entire range of interest, reaching only a maximum temperature of 85 K and magnetic fields up to 8 T, we extrapolate it so that the N index is kept constant for values of H and T exceeding the data range and J_c is kept constant for higher values of field but drops to zero at $T_c = 92$ K.

However, this would result in an infinite resistivity at T_c, at which point the material should instead transition to its normal state, and therefore show its normal state resistivity. To account for this transition, an overcritical model should be adopted, as explained in Section 2.1, such as the overcritical adaptation of the power law. Hence, the resistivity of the HTS will be the parallel equivalent of the superconductor resistivity and its normal state counterpart, as shown in Equation 2.6, rewritten here for convenience:

$$\rho_{eq} = \rho_{pl} \parallel \rho_{ns} = \frac{\rho_{pl} \cdot \rho_{ns}}{\rho_{pl} + \rho_{ns}} .$$

The normal state resistivity, in turn, also scales linearly with the temperature, similarly to the other conductors in the beam screen, according to:

$$\rho_{ns}(T) = \rho_{Tc} + \alpha(T - T_c) . \tag{7.6}$$

The values employed for ρ_{Tc} and α are, respectively, $1 \times 10^{-6}\Omega$m and $4.7 \times 10^{-9}\Omega$m/K [66, 123]. With this, there will be a smooth transition from superconducting to normal state when approaching T_c from below.

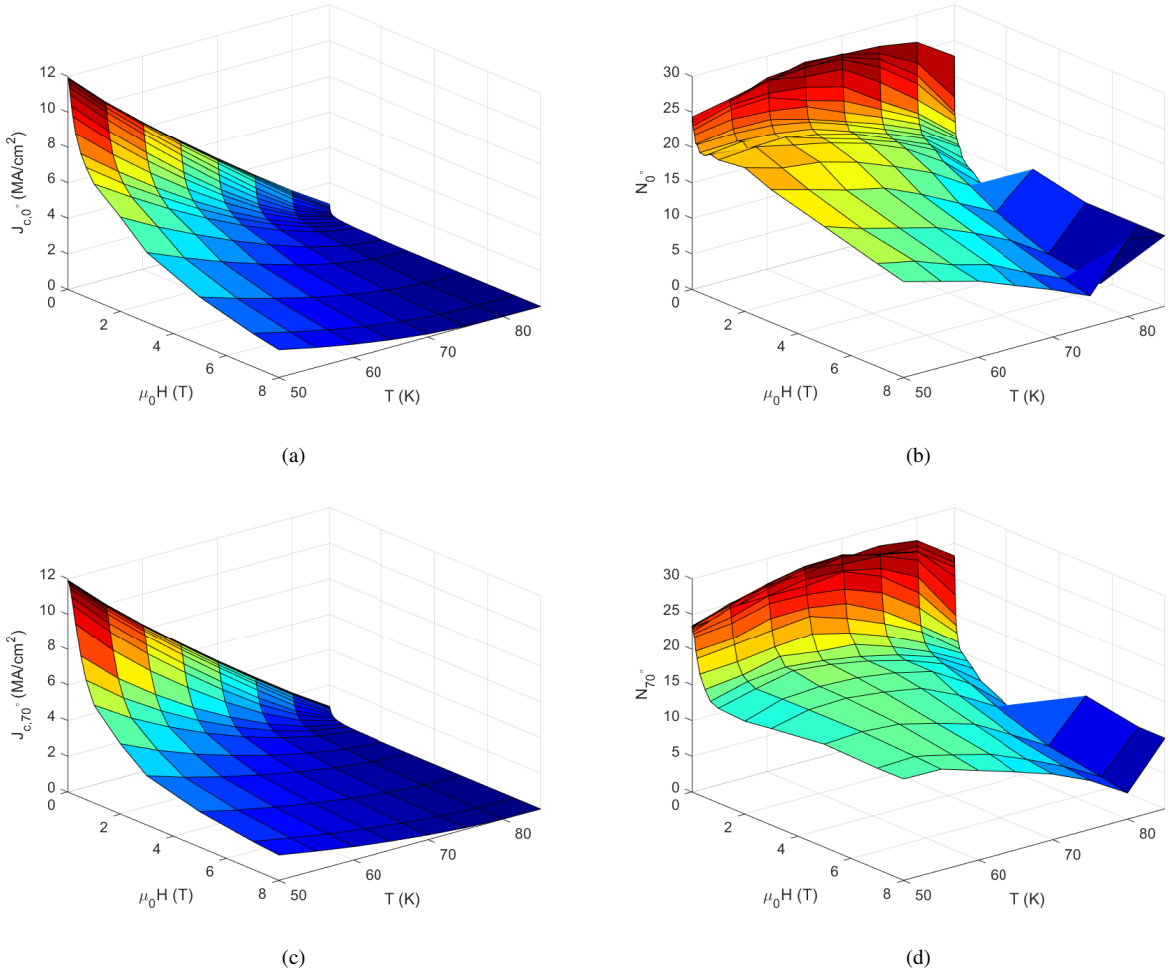


FIGURE 7.2: Dependence of critical current density J_c at (a) 0° and (c) 70°, and transition index N at (b) 0° and (d) 70° with temperature T and field intensity H employed for the adapted simulation model. Functions are interpolated between data points and extrapolated so that $J_c(T, \mu_0 H > 8\,\mathrm{T}) = J_c(T, \mu_0 H = 8\,\mathrm{T})$, $J_c(T \geq 92\,\mathrm{K}, \mu_0 H) = 0$, $N(T, \mu_0 H > 8\,\mathrm{T}) = N(T, \mu_0 H = 8\,\mathrm{T})$ and $N(T \geq 85\,\mathrm{K}, \mu_0 H) = N(85\,\mathrm{K}, \mu_0 H = 8\,\mathrm{T})$. Data from [63].

7.2 Thermomechanical Simulations during a Magnet Quench

The single input for the beam screen simulations under a dipole magnet quench is the external field $\mu_0 H_{ex}$, which starts at 16 T and quickly drops to zero over 300 ms, as shown in Figure 7.3. This assumption is based on the quench behavior of the NbTi magnets of the LHC, since the final design of the FCC main dipole magnets is still subject to change.

The resulting forces generated in the beam screen integrated over a quadrant rise to a maximum value of 84 kN/m, pointing outward horizontally with respect to the center of the beam screen ($x = x_0 = 0$). Figure 7.4 presents the distribution of force per unit volume in the coated beam screen. Likewise, the forces on the HTS segments also point outward, but in their case, with respect to the center of each individual segment. This change in behaviour with respect to normal conductors is due to the different neutral point x_0, which arises from the assumption that the HTS segments are electronically insulated from the other conductors. It must be pointed out, however, that depending on the coating method employed to attach the REBCO layer to the beam screen inner surface, this may not be the case, as we will discuss in the next chapter.

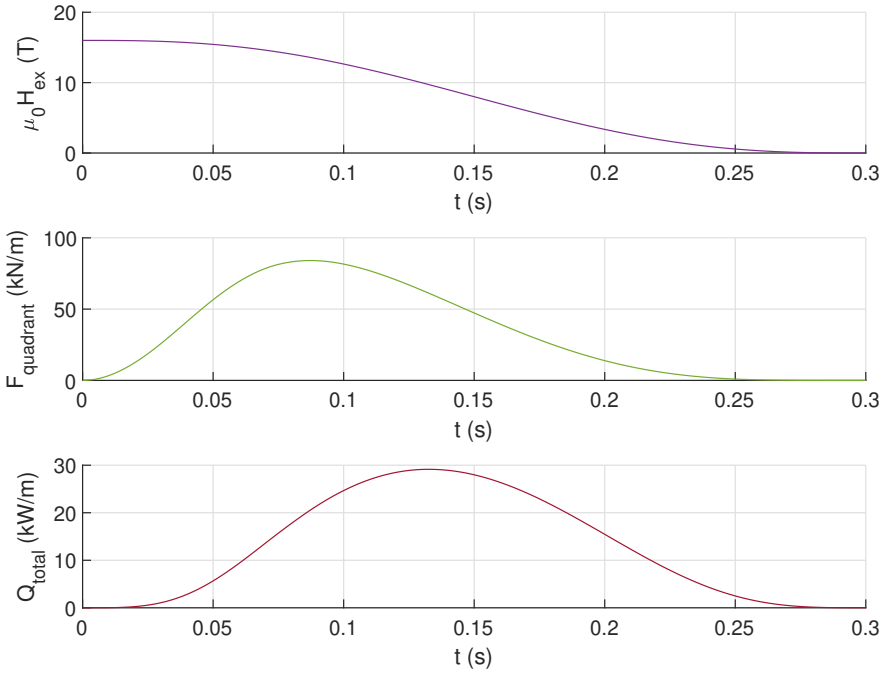


FIGURE 7.3: External applied field, resulting force load integrated over a quadrant and total heat generated in the beam screen during a 300 ms dipole magnet quench at top energy.

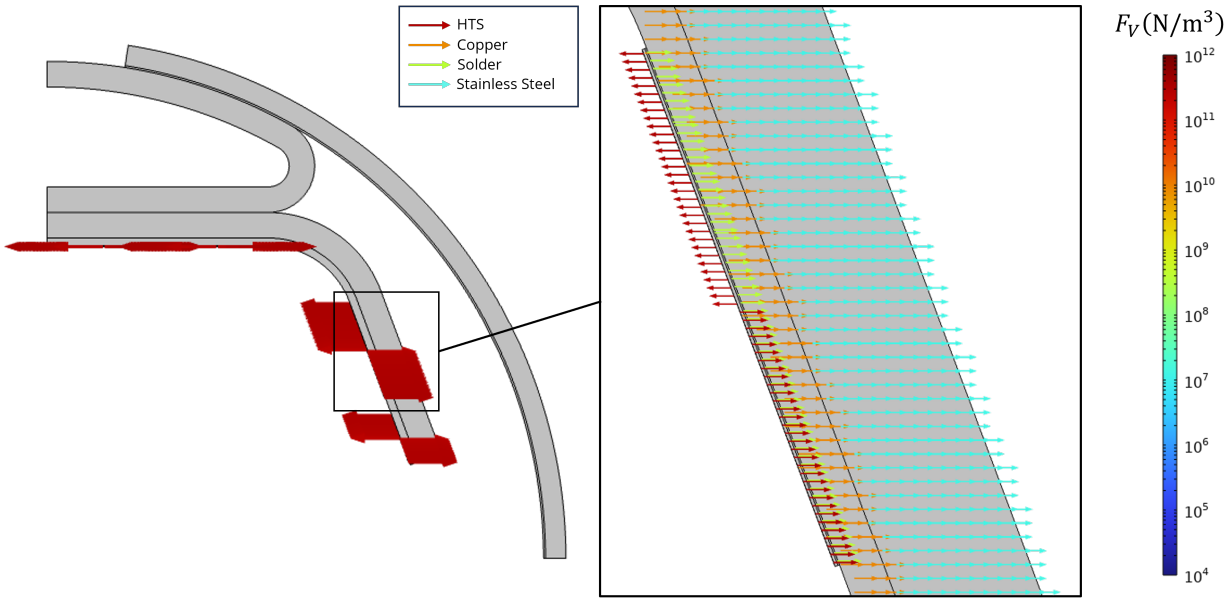


FIGURE 7.4: Force per unit volume distribution at the moment when the highest force loads are induced in the beam screen ($t = 86$ ms). The forces in all regular conductors point outward, while those induced in the HTS segments are split due to their different neutral point x_0. In spite of the higher forces in the HTS, the greatest contributors are the copper layers due to their much larger cross-section area.

It is worth noticing that the forces in each material differ orders of magnitude from one another due to their different resistivities. Although the forces per unit volume in the HTS highly surpass those in the metallic components of the beam screen, its average contribution amounts only to 8 % of the total forces due to their comparatively small thickness. In the other extreme, even though the cross-section area of the steel structure is large, its resistivity is too high to compete in terms of force. The strongest contributors are actually the copper layers, reaching 91 % of the total

forces, since they present a relatively large cross-section area and a still reasonably low resistivity.

Regarding its thermal behaviour, the heat generated amounts to a maximum of 28.4 kW/m, resulting in a total energy of 3.7 kJ/m transmitted to the beam screen along the entire duration of the quench. Once again, the highest contribution, over 97 %, comes from the copper layers, for the same reasons as the force loads. The total energy in the HTS segments is limited to less than 1 % due to the small cross-section area, in spite of the fact that the heat per unit volume is much higher in the HTS. This can be seen in Figure 7.5, where the heat distribution is shown, with a focus on the different layers. In addition, it is interesting to note that the HTS segments on the top wall play a larger role than those on the diagonal wall, due to their lower temperature, and therefore higher J_c.

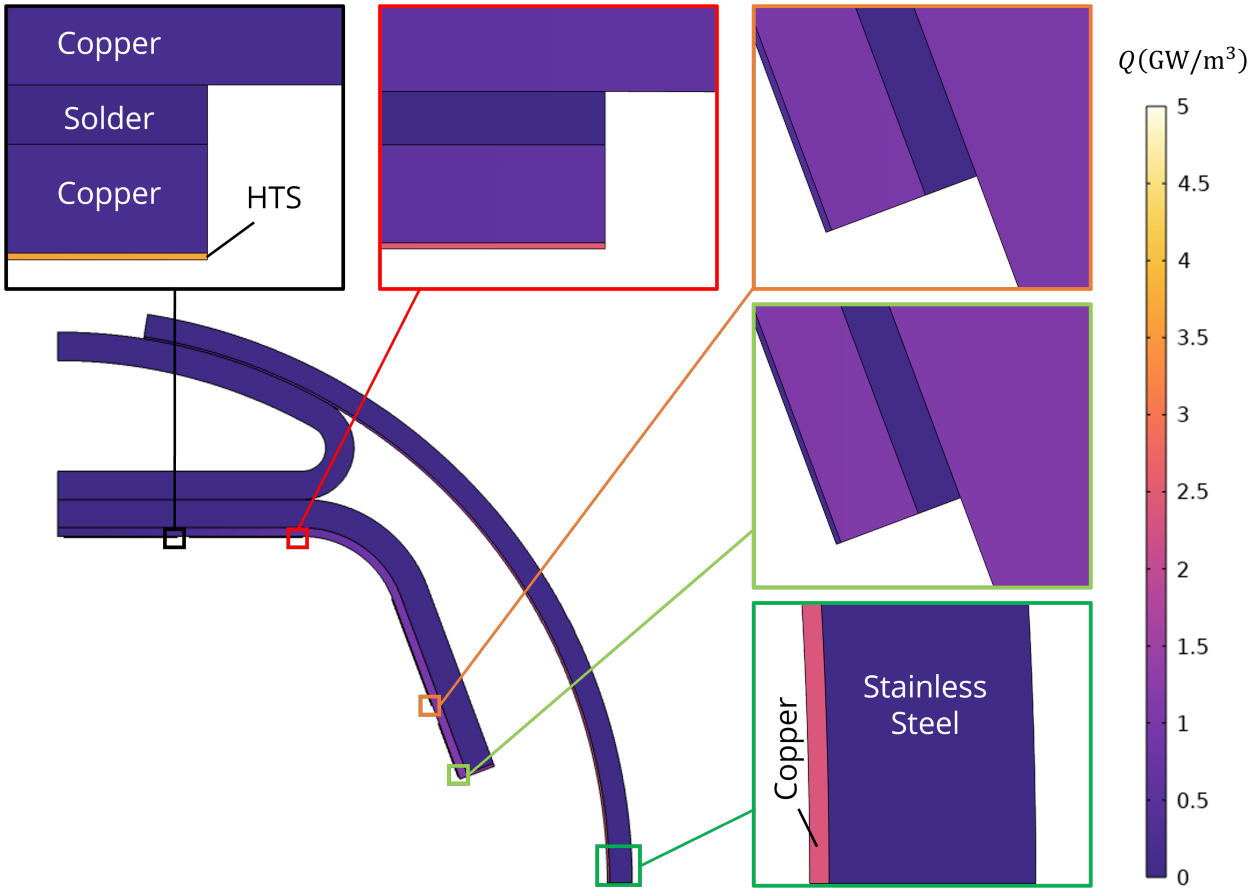
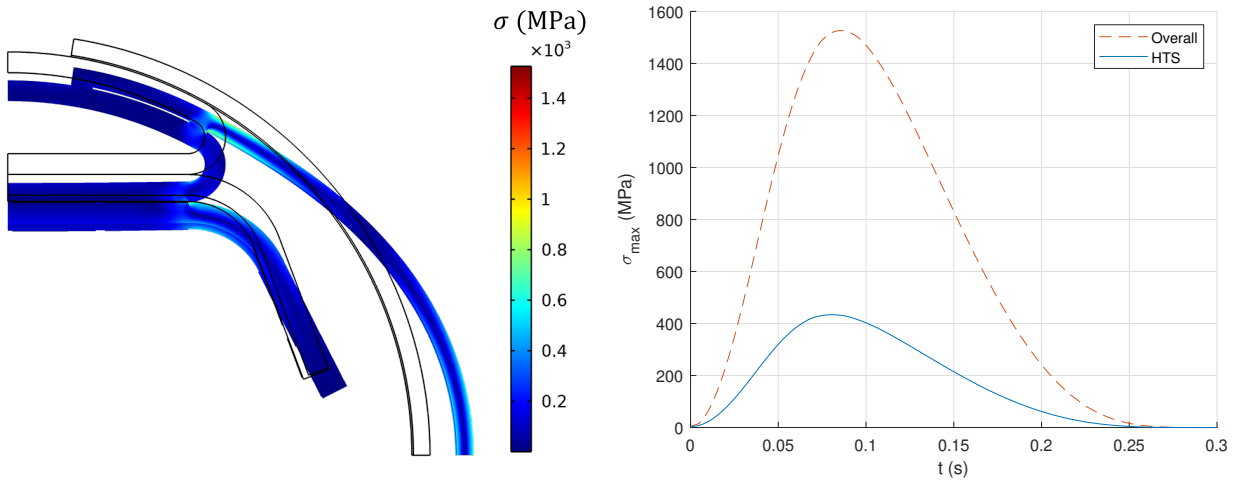


FIGURE 7.5: Heat distribution over in the coated beam screen during the moment of highest heat load ($t = 133$ ms). Although the heat per unit volume induced in the HTS segments is largest, the most significant contribution comes from the copper layers due to their much larger cross-section area.

As a consequence of the heat and force loads imposed on the coated beam screen due to a magnet quench, there is a significant effect in the mechanical stresses induced. Figure 7.6 summarises the mechanical response of the coated beam screen with the maximum values of stress and strain over time as well as the stress distribution and deformation at the moment of highest force load. As we can see, both stress and strain reach its maxima at the same time as the force loads, resulting in a general tendency of stretching the beam screen horizontally but compressing it vertically. The highest stresses achieved slightly surpass 1500 MPa in the welding connecting the outer wall to the cooling channel. However, this is a very local concentration of stresses in a small region that would most likely plasticize when submitted to such a load, relaxing the mechanical stresses due to slight deformations. By disregarding this outlier, the maximum values remain within the elastic limits of the stainless steel.

When compared to the beam screen with a pure copper coating under similar conditions [84], the results are very similar. Apart from the aforementioned very local stress maximum, the beam screen with both coatings shows stresses that do not surpass the yield stress of the P506 stainless steel, 1100 MPa. Likewise, both scenarios show similar displacements, reaching no more than 0.7 mm, less than the 1.5 mm gap between the beam screen and the cold bore. It is worthwhile to point out, though, that the analysis carried out along this chapter does not take into account pumping holes in the outer walls of the beam screen, which would result in asymmetries in the longitudinal direction and therefore could not be accurately considered in 2D simulations. Even so, the fact that both the copper coating and the hybrid coating show such similar results due to the low contribution to the force load coming from the HTS segments reinforces the small role of the added REBCO in the mechanical response of the beam screen to a magnet quench.



(a) (b)

FIGURE 7.6: Mechanical response of the coated beam screen to a 300 ms dipole magnet quench at top energy. (a) Stress distribution and deformation (scaled by a factor 3) at the moment of highest force load; and (b) Maximum values of stress reached.

Although the effect of the HTS in the stress distribution of the beam screen is relatively small, it is also important to evaluate how these stresses affect the electromagnetic properties of the HTS. The maximum mechanical stress in the HTS domains reaches a maximum of 430 MPa, corresponding to a strain of 0.3%, which is insufficient to cause lasting effects in the J_c. This means, on the one hand, that the HTS are not damaged by the mechanical effects of the quench and, on the other, that there is no need to consider any dependence between J_c and σ.

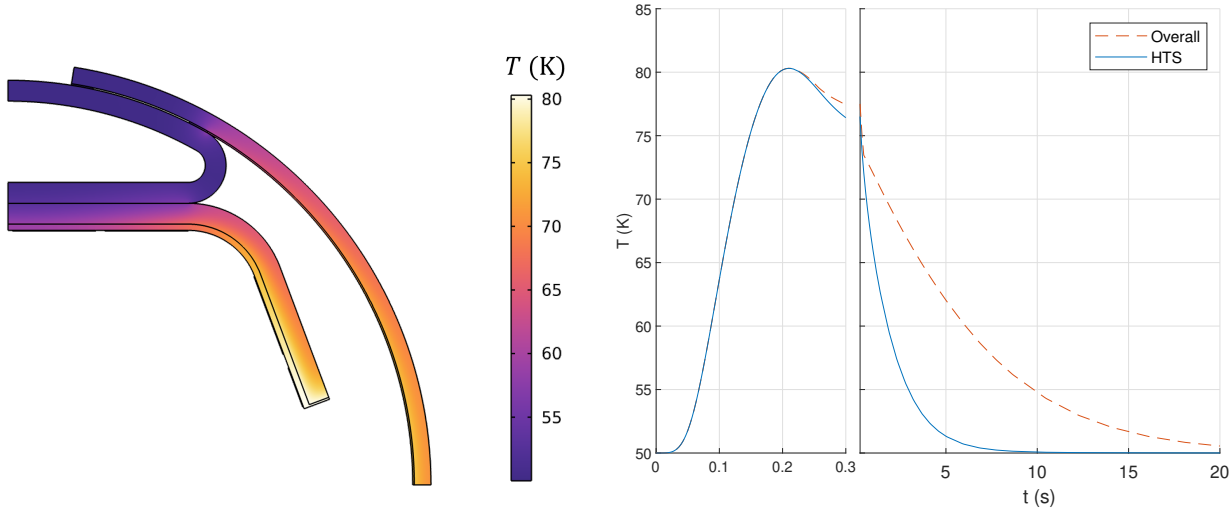
The copper layer covering the inner wall of the beam screen reaches stress values of up to 630 MPa at the bending connecting the top walls and the diagonal walls of the inner chamber, surpassing the elastic limit of the copper. These results are similar to those obtained during the design of the beam screen for the LHC, when maximum stresses of 690 MPa were calculated for the 1 mm thick copper layer. However, subsequent experiments with the LHC beam screen under a model magnet revealed no damage to the copper layer, and therefore the same can be expected from the FCC beam screen [124, 125].

The relatively high stresses produced in the copper can be partially transferred to the solder layer attaching the HTS segments to the beam screen, especially to those closer to the bending. There the stresses can reach values of up to 550 MPa, also exceeding the elastic limit of the material. Plastic deformation caused by this could on one hand accommodate the high mechanical strain before reaching the HTS layer, but on the other, lead to the detachment of the HTS coating. In particular, the segments coating the diagonal walls are exposed to normal forces pulling on the

HTS with up to 0.4 MPa of pressure applied over one half of the segment, which corresponds to a factor 2.5 larger than those achieved during regular operation, but still much below the adhesion strength typically found in copper-solder-copper joints, which stands in the range of tens of MPa [126, 127]. An investigation of our coating adhesion quality is presented in the next section of this chapter.

Let us now consider the thermal response of the beam screen to a magnet quench, presented in summary in Figure 7.7. During the quench, the temperature rises to a maximum of 80 K at 210 ms. Throughout the entire duration of the quench, the hottest point in the beam screen corresponds to the edge of the inner wall, which is the furthest away from the cooling channel. As soon as the quench ends, however, the maximum temperature quickly drops back to 50 K within the next 20 s.

Although this is a significant shift in temperature, it does not pose a threat to the structural integrity of the beam screen nor its coating. It is clear, however, that in order to accurately depict the behaviour of the superconductors, it is important to consider the dependence of J_c with the temperature, as has been done for this case. Even so, the overcritical model employed in this case proved to be unnecessary since the temperature range is still below T_c.



(a) (b)

FIGURE 7.7: Thermal response of the coated beam screen to a 300 ms dipole magnet quench at top energy. (a) Temperature distribution when the highest temperature is reached; and (b) maximum temperature over time during and a few seconds after the quench.

Even though the main purpose of this simulation is to evaluate the thermal behaviour of the coated beam screen considering perfect thermal contact between each of its constituent layers, it is interesting to also analyse what happens in the other extreme: if the HTS segments are thermally insulated. This allows us to consider a worst case scenario where, for any reason, the thermal contact between the HTS and the beam screen has been drastically decreased. In addition, it offers an insight on how the HTS react to a temperature shift that would bring it to its critical temperature.

In this case, all contact with the cooling channels responsible for removing the heat from the system has been severed and no other form of heat exchange is being considered apart from thermal conduction within each HTS segment, which means that any rise in temperature is now irreversible. Figure 7.8 shows the behaviour of several relevant quantities: the applied magnetic field, the induced electric field and current density, the HTS resistivity and the temperature, all corresponding to a single arbitrary point inside the HTS. Figure 7.8a presents the results considering the same J_c that was used in the previous simulations discussed in this chapter (case A), while Figure 7.8b shows the same results with J_c multiplied by a factor 10 to artificially rise the temperature to T_c (case B).

In both cases, as an electric field is induced by the time-varying magnetic field, the current density in the HTS starts increasing. As the temperature rises, approaching T_c, the J_c progressively decreases, limiting J, which then decreases as well. At 230 ms, the two scenarios diverge. In case A, it remains below T_c, and the current density, although small, is still present. In case B, however, T finally reaches T_c, when the superconductor transitions to its normal state. At this point, the resistivity immediately rises to its normal state value. In the normal state, the current flowing in the HTS is negligible, meaning that the heat being generated is also zero, which in turn prevents the temperature from rising above T_c.

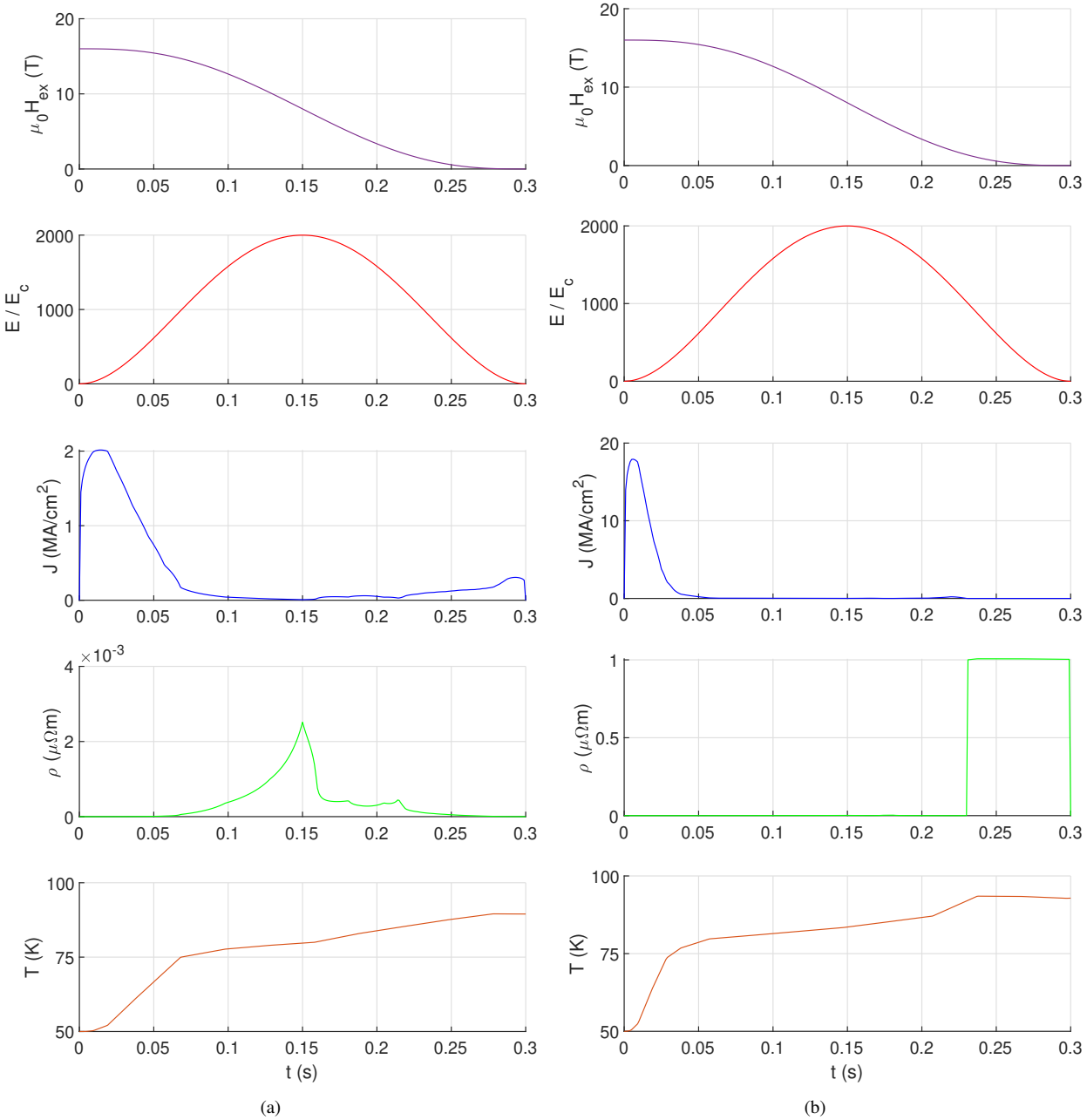


FIGURE 7.8: Behaviour of several quantities in an arbitrary point inside the HTS during a magnet quench with J_c multiplied by factors (a) 1 and (b) 10. In both scenarios, the current flow is limited by the increase in temperature. However, if T reaches T_c, which is the case in (b) at 0.23 s, the resistivity quickly rises to its normal state value, effectively ceasing all current flow.

This reveals the self-limiting nature of HTS when exposed to an external time-varying field. Since the electric field is determined only by the magnetic field, any increase in its resistivity causes a decrease in the generated heat. If this heat is enough to bring it to T_c, the heat generation will always be limited by its normal state resistivity, according to

$$Q = \frac{E^2}{\rho}, \tag{7.7}$$

where E is an imposed electric field. This means that, although contact with hotter materials could still bring the HTS to higher temperatures, the heat generated in the HTS itself will not increase its temperature above T_c unless the time derivative of the magnetic field is extremely high, even when compared to those achieved during a magnet quench at top energy. This is in direct opposition to what happens with HTS when submitted to an imposed current, as is the case in critical current transport measurements, for instance, where any increase in the resistivity causes an increase in the heat generation, according to

$$Q = \rho J^2, \tag{7.8}$$

where J is an imposed current density, ultimately resulting in the emergence of hot spots and a quench in the HTS. In the context of the FCC-hh beam screen, this is a very beneficial property, which protects the HTS segments from thermal damage during regular operation, a magnet quench or even if the HTS is thermally insulated.

7.3 Pull-off Adhesion Testing

To ensure the HTS coating can withstand the pulling pressures induced by the Lorentz forces generated in the beam screen, it is important to understand what its tolerance is to normally applied pulling forces. One way to find this is to perform pull-off adhesion tests, which consist in gluing a metallic dolly to a portion of the coating and subsequently pulling it normally until failure.

The experimental setup of the adhesion test is shown in Figure 7.9. To improve adhesion between the sample and the dolly, their surfaces are usually sanded prior to applying the adhesive, and the tested region is usually cut off from the remaining coating to ensure no tangential forces are produced.

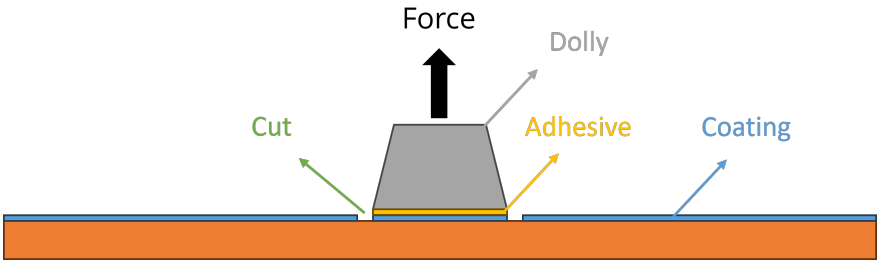
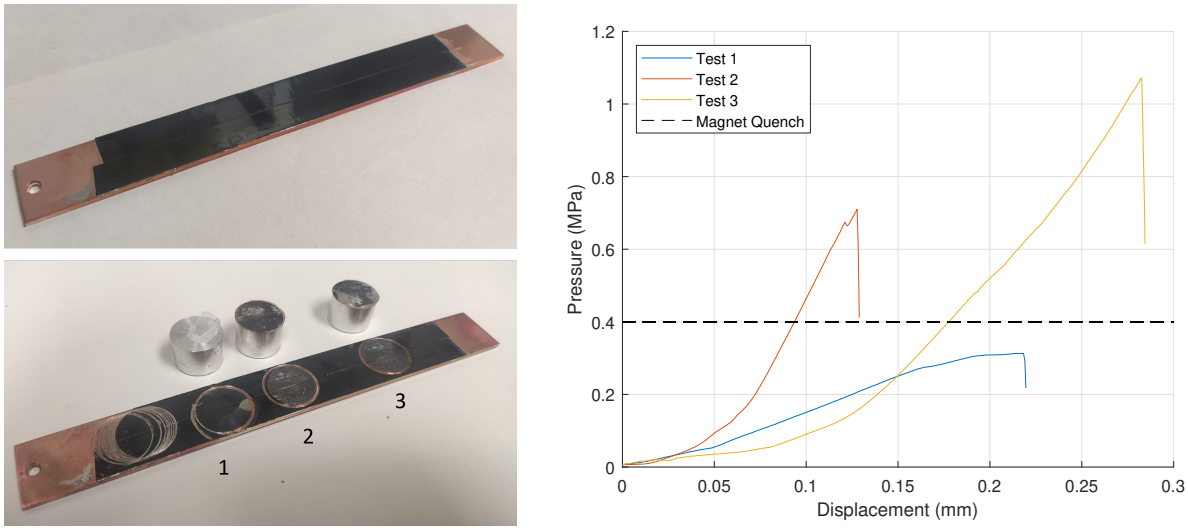


FIGURE 7.9: Schematic of the experimental setup during an adhesion pull-off test. A metallic dolly is glued to a region of the coating sample which is cut-off from the remaining surface. The dolly is then pulled normally to the surface and the force during failure is registered.

The sample prepared for testing was prepared according to the methodology presented in Chapter 3. Figure 7.10 shows the coating sample before and after testing. The coating consists of two parallel coated conductors delaminated and soldered to a copper coated steel plate. The sample was divided into three regions for testing, evidenced in Figure 7.10a by the numbers 1, 2 and 3. These correspond to the pressure curves obtained during testing, shown in continuous lines in Figure 7.10b with the same enumeration. The dashed line corresponds to the maximum pulling pressure expected during a magnet quench according to the simulations presented in this chapter.



(a) (b)

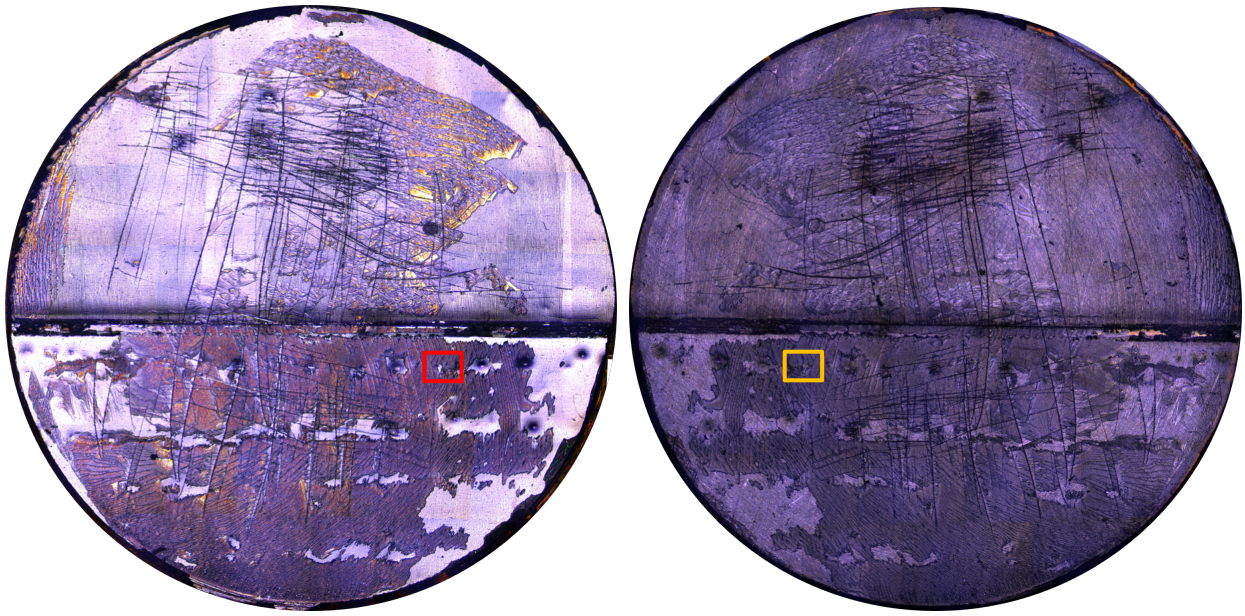
FIGURE 7.10: Pull-off adhesion test results. (a) Sample of HTS coating soldered to copper coated stainless steel plates before (top) and after (bottom) testing with numbered regions corresponding to Tests 1, 2 and 3, and (b) pressure curve as a function of displacement obtained during testing the three regions.

Each tested region showed a different response to the pull-off test. Firstly, we can see that Test 1 failed before reaching the estimated pulling pressure for a magnet quench. However, when inspecting the dolly and the sample after testing, it became clear that it was a glue failure, that is, no coating was detached from the sample, which is in agreement with the fact that Region 1 was not sanded as to improve the adhesion with the dolly and was glued to it with a relatively weak epoxi adhesive, Araldite® Rapid Resine. As a means to increase adhesion, Regions 2 and 3 were sanded with a P400 sandpaper before application of a stronger, hot curing epoxi matrix system based on Araldite® LY 556, Aradur 917 and Accelerator DY 070. With a proper adhesion between the coating and the dolly, Regions 2 and 3 achieved pulling pressures of 0.71 and 1.07 MPa at failure, surpassing the expected values during a magnet quench, 0.4 MPa, by a significant margin. Subsequent analysis of the sample and dollies revealed that the coating was indeed detached from the sample.

Although the maximum pressure values offer evidence to the tolerance of the HTS coating to the forces induced during a magnet quench, it is still surprising that the adhesion of the coating is at least one order of magnitude weaker than the bond usually achieved in a copper-solder-copper joint, as mentioned in the previous section. To further investigate this, we examined Region 3 of the sample and the corresponding dolly under an optical microscope.

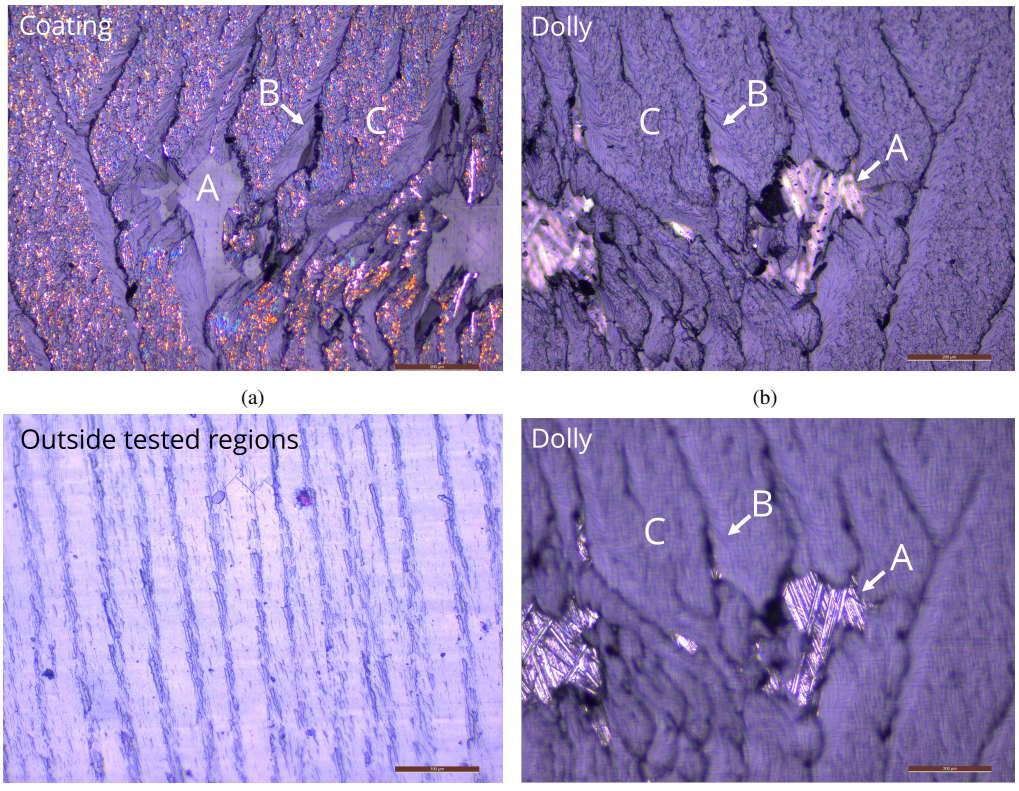
Figure 7.11 consists in the optical images of the sample and the dolly. Here the deep scratches from sanding the coating are clearly noticeable, as well as a very inhomogeneous color distribution. The colored rectangles mark points that are representative of the entire Region 3 in terms of hue and texture, and therefore we recorded magnified images of this area, which are shown in Figure 7.12. At this point, we can employ the image analysis techniques discussed in Chapter 3 to achieve a better understanding of the breaking patterns produced during the pull-off test.

In Figure 7.12a, we can see the magnified surface of the coating sample, which can be further divided into three distinct regions by applying the same concepts employed in Chapter 3. Firstly, region A corresponds to a smooth gray surface. From the color and texture, this suggests that here the fracture happened between the REBCO layer and the glue, which would be characterized as a glue failure. Region B corresponds to gray, inhomogeneous ridges, which is evidence for partial excavation of REBCO and corresponds to a cohesive fracture in the REBCO layer. Finally,



(a) (b)

FIGURE 7.11: Optical images of (a) Region 3 of the coating and (b) corresponding dolly after pull-off test. The rectangles correspond to the magnified optical images shown in Figure 7.12.



(a) (b)

(c) (d)

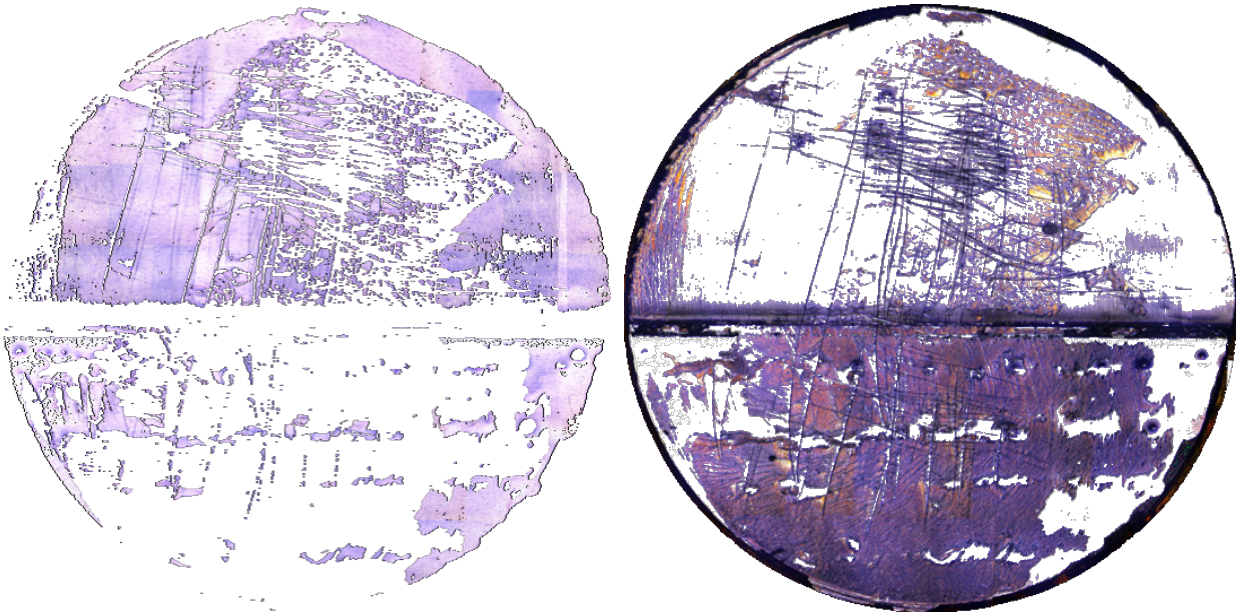
FIGURE 7.12: Optical images of Region 3 of (a) the coating sample and (b and d) of the corresponding dolly with different focusing lengths. An image of a region of the coating (c) outside any tested region is shown for comparison.

Region C shows an uneven surface composed of a mixture of shiny, reflective areas and small gray ridges. This reflectiveness is characteristic of metals, which implies adhesive fracture between the REBCO layer and the metallic layers underneath. Once again, the gray ridges, like in Region B, correspond to cohesive fracture in the REBCO layer.

To corroborate with this interpretation, we can take into account Figures 7.12b and 7.12d, showing the corresponding regions in the dolly with two different focusing lengths. Here we see the characteristic gray of the REBCO layer permeating the majority of the image (Regions B and C), with two main islands where, once more, a shiny surface is seen (Region A). By altering the focusing length it becomes clear that these islands are deeper than the surrounding REBCO, and therefore are the exposed surface of the dolly, seen through the added layer of adhesive. This is in agreement with the aforementioned interpretation of the three regions.

Finally, Figure 7.12c depicts an optical of the coating outside any of the tested regions, revealing the exposed surface of the REBCO layer after delamination, and undamaged by the pull-off tests. Its similarities with Region A of Figure 7.12a are evident, with a much smoother and more homogeneous surface than any of the surrounding regions.

Having analysed and interpreted the different fracture patterns throughout the surface of the coating, we were then able to use the filtering methods presented in Chapter 3 to split the entirety of Region 3 into its damaged (cohesive and adhesive fractures) and undamaged (glue failure) portions, which are presented in Figure 7.13.



(a) (b)

FIGURE 7.13: Optical images of Region 3 of the coating split into (a) undamaged areas and (b) excavated REBCO by color filtering as discussed in Chapter 3.

Most interesting, though, is the fact that no fractures occurred in or around the soldering layer, which is further confirmed by the absence of excavated metals on the surface of the dolly. However, it is not clear how the roughness of the sandpaper used to sand the sample affects these results, since it is possible that the damage caused by sanding weakens the integrity of the REBCO layer. In addition, there is a fundamental difference between the lorentz forces generated in the REBCO and the forces applied to the coating in these experiments. In the former, the forces are constitute a body load, and are distributed along the thickness of the material. This results in a linear increase of

the stresses from the top surface of the REBCO layer, reaching maximum at the bottom. In the latter, the entire force is applied directly to the surface of the layer, which, in terms of stress, translates to a more homogeneous but more strenuous distribution, since the same maximum stress is achieved directly on the top surface as is maintained throughout the whole thickness. In any case, while more measurements would be interesting to investigate this further, it is clear that, even in these demanding conditions, the coating is still strong enough to endure the relatively large forces induced during a magnet quench.

7.4 Chapter Summary and Conclusions

This chapter brought into discussion the behaviour of the coated beam screen in the event of a dipole magnet quench. To do this, the model used for the FEM simulations was adapted. On one hand, it was simplified to consider the thin film behaviour of the HTS segments, allowing for a faster estimation of the current density and electric field distribution inside them. On the other, a J_c dependence with the temperature was added to account for a temperature range starting at 50 K and reaching values above T_c by including an overcritical formulation of the HTS resistivity.

The simulation results showed only a diminutive impact of the coating in the mechanical stresses and temperature of the beam screen during a magnet quench. Apart from a very local effect, the maximum stresses are within the elastic regime of the stainless steel and those reached in the HTS layers are not enough to impact on its electromagnetic properties, much less to damage the material. Similarly, although there is a significant rise in temperature, it is not nearly enough to offer any danger to the beam screen structural integrity or to damage the HTS.

In addition, we have also explored a worst case scenario according to which the beam screen is thermally insulated from the cooling channels and the surrounding environment. Even in these pessimistic conditions, the temperature does not surpass T_c, demonstrating the very beneficial capability of these materials to protect themselves when under highly variable external magnetic fields, effectively limiting their maximum temperature at T_c unless in contact with a hotter material.

Finally, the adhesion tests performed with a sample of the HTS coating demonstrated its resilience, even when taking into account the high Lorentz forces emerging during a magnet quench.

These positive results show not only that HTS play a minor role on the force and heat loads of the beam screen during a magnet quench, but also that they can survive such extreme events with no expected deterioration in performance.

Chapter 8

Transversal Current Flow in the Hybrid Coating

Throughout literature, whenever HTS Coated Conductors are evaluated be the means of FEM numerical analysis, it is a standard assumption to consider them electronically insulated from the surrounding conductors. This applies in general for HTS due their very high conductivity compared with normal conductors, and in particular for CC's due to the presence of buffer layers, which act as electronic insulators between the REBCO layer and other conductors. The consequence of having an electronically insulated HTS domain is portrayed in Equation 4.16, reproduced here for convenience:

$$I_i = \int_{\Omega_{sc,i}} J_z dS = 0\,.$$

This equation basically defines the total current I_i flowing in a given cross-section domain $\Omega_{sc,i}$ of the HTS as zero, as the current flowing in one direction ($J_z > 0$) has no other path to close the circuit other than bending backwards and flowing back through the same cross-section ($J_z < 0$). Although we have considered this common premise in the previous chapters of this thesis, it is interesting to investigate some conditions under which this will not necessarily hold true, such as when coated conductors are soldered directly to a common conductor, as described in Chapter 3.

In this chapter we will develop an analytic evaluation of HTS segments that are electronically connected to a common copper layer, and make a comparison with the results of corresponding FEM analysis. With this, we aim to answer the question of whether such conditions could play a role in the current distribution in the beam screen coating and consequently affect the field quality inside the vacuum chamber of the FCC.

8.1 Electronically Coupled HTS Segments

In order to analyse the effect of electronically coupled segments in the beam screen coating, let us first consider a simplified configuration composed of three electronically connected slabs with perfect electric contact and same thickness. This set of slabs is exposed to an external time-varying normal magnetic field, so as to generate planar currents flowing through the slabs. Depending on the resistivity of the materials involved the shape of the current paths will be different, as shown in Figure 8.1. If the middle slab has a similar resistivity to that of the two lateral slabs, there will be no significant distinction between the materials, meaning the current densities will be similar throughout the entire set and the current loop will intercept all the slabs (Figure 8.1a). On the other extreme, if the resistivity of the middle slab is infinite, there cannot be any current flowing through it, which results in the current loops closing inside each of the lateral slabs (Figure 8.1c). The intermediate state in which the resistivity of the middle

segment is still finite but much larger than that of the lateral segments causes most of the current loops to close inside each lateral segment, while some of them intercept the middle segment (Figure 8.1b).

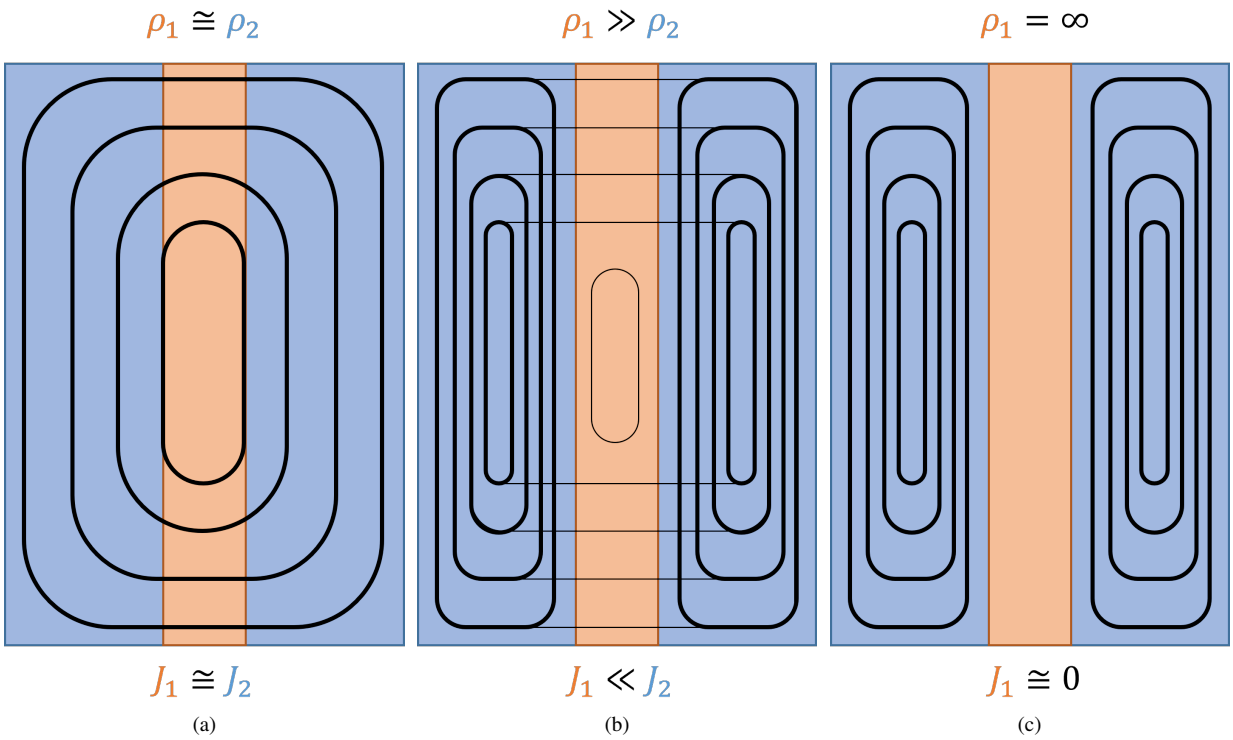


FIGURE 8.1: Schematics of the current distribution in electronically connected slabs of different materials under a normal varying magnetic field. (a) The materials have similar electric resistivity, resulting in current densities of the same order of magnitude; (b) the intermediate slab has much larger resistivity, resulting in decreased currents flowing through it, which in turn causes most of the current loops to be contained inside each of the edge slabs; and (c) The intermediate slab has infinite resistivity, which causes the two edge slabs to be electronically insulated from one another.

Now let us assume that the two lateral slabs are HTS in the superconducting state and the middle slab is made of copper. This situation is akin to that of the FCC beam screen. Furthermore, based on the methodology to produce the hybrid coating, discussed in Chapter 4, there are no buffer layers insulating the HTS from the surrounding conductors, which we will also consider here. While operating around or below J_c, the resistivity of the HTS is either zero or, at most, much lower than that of copper, which satisfies the conditions shown in Figure 8.1b. However, since the currents flowing through the copper due to the ramping magnetic field are much lower than those in the HTS, it is usually a reasonable premise to assume that there are no currents flowing in the copper, and thus the situation is simplified by considering that the HTS segments are electronically insulated and that the copper segments play no role in the current distribution, which corresponds to Figure 8.1c.

However, although the current densities in the copper are indeed much lower than their HTS counterparts, this may not be the case for the total current flowing transversely through the copper if the dimensions of the copper are much larger than those of the superconductors. This situation is illustrated by the means of an equivalent electric circuit in Figure 8.2. For simplicity, we assume that the current density in the HTS segments is equal to J_c, as described by the Bean model. In addition, the external magnetic field induces a voltage $V \propto \partial B/\partial t$ in the copper, which in turn generates a transversal current $I_1 = V/R$. On one hand, if the HTS segments are insulated, $I_1 = 0$ and the currents in the HTS flowing in each direction $aI_c = (1-a)I_c = 0.5I_c$ are the same. On the other hand, if the transversal resistance of the copper is low enough to allow for a significant current flow (I_1 of the same order of I_c), there will be

a non-negligible imbalance ΔI in the HTS currents:

$$\Delta I = I_1 = aI_c - (1-a)I_c = (2a-1)I_c\,. \tag{8.1}$$

It is straightforward to note that the current in the copper, and therefore the current imbalance in the HTS, depends not only on the resistivity of the copper segment, but also on its dimensions. Applying the same concept to the beam screen, with its 16 m long sections, the resulting transversal resistance might be small enough so that the effect of the copper segment on the current distribution could not be neglected, impacting on the field quality inside the vacuum chamber.

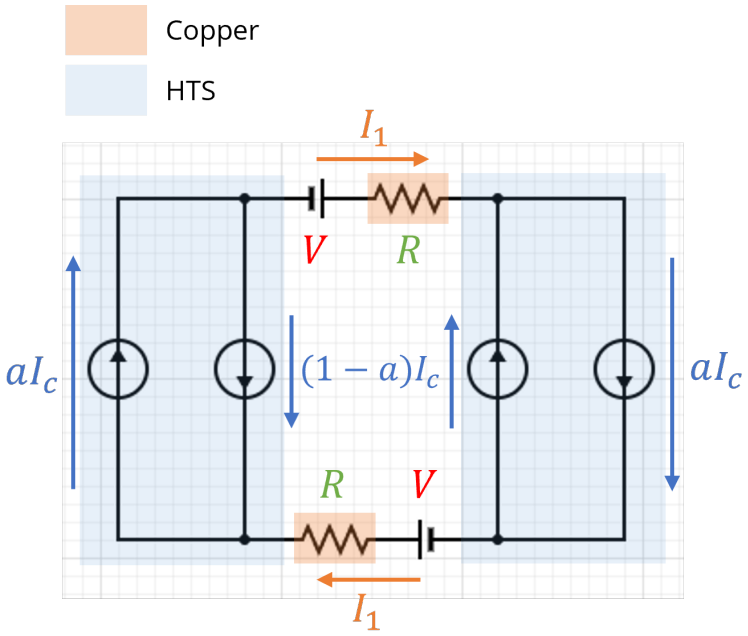


FIGURE 8.2: Equivalent electric circuit of two HTS segments electronically connected to a common copper segment. Depending on the total resistance of the copper segment in the transversal direction R, there may be a significant amount of current flow through the copper from one HTS segment to the other, resulting in an imbalance of current inside the HTS, represented by the constant a. The voltage induced by the external varying field is $V \propto \partial B/\partial t$. In the insulated case, R tends to infinity and $I_1 = V/R$ vanishes, making $a = 1-a = 0.5$ so that the current loop closes entirely through the HTS.

To find the current imbalance as a function of the length of the slab, we must first evaluate the current density distribution at the central longitudinal axis of the slab set. In other words, we must find the transverse current density J_x at $z = 0$, as shown in Figure 8.3a. To do this, it is useful to note that the superconductors will act as short-circuits with respect to the current flowing transversely through the copper, which causes the longitudinal current flow to be concentrated on the HTS slabs, and therefore we can assume that the current in the copper has no longitudinal component, reducing Faraday's equation to

$$\frac{\partial J_x}{\partial z} = \frac{1}{\rho_{Cu}}\frac{\partial B_y}{\partial t}\,. \tag{8.2}$$

By integrating both sides with respect to z and taking into account that J_x is zero at $z = 0$, the expression for J_x is obtained:

$$J_x = \frac{z}{\rho_{Cu}}\frac{\partial B_y}{\partial t}\,, \tag{8.3}$$

as shown in the top graph of Figure 8.3b, where J_{max} refers to the maximum value of J_x, at $z = l/2$ with l corresponding to the length of the slabs.

Now that we know the current distribution at the center of the slab set ($x = 0$), it is possible to make use of Kirchoff's circuital law to find the current imbalance ΔI. Without losing generality, let us consider the closed region depicted by the red dashed line in Figure 8.3a, defined as $x \geq 0$ and $z' \leq z \leq l/2$. As it is a closed boundary, Kirchoff's law states that all currents flowing inward must be equal to those flowing outward. Since we assume there are no longitudinal currents in the copper and that the current density distribution is homogeneous along the normal direction, this reduces to

$$\Delta I = I_x = d_{Cu} \int_{z'}^{l/2} J_x dz, \tag{8.4}$$

where d_{Cu} is the thickness of the copper slab. By replacing J_x from Equation 8.3 and changing the variable, we get

$$\Delta I = \frac{d_{Cu}}{2\rho_{Cu}} \frac{\partial B_y}{\partial t} \left[\left(\frac{l}{2} \right)^2 - z^2 \right], \tag{8.5}$$

the graph of which is shown at the bottom of Figure 8.3b.

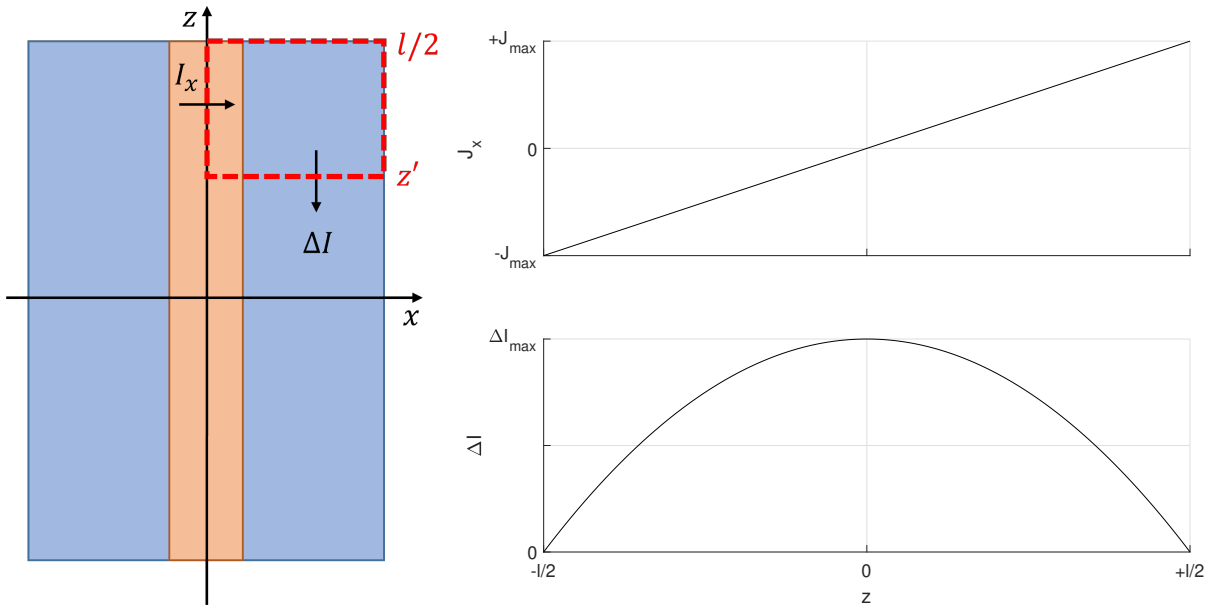


FIGURE 8.3: Evaluation of the transverse current density distribution in the copper and current imbalance in the HTS. (a) Schematic of the slabs with the redborder sub-region where Kirchoff's Circuital Law is applied; and (b) Current density J_x at $x = 0$ and current imbalance ΔI as a function of z.

This means that the current distribution in the HTS segments depends on z, resulting in the breaking of the longitudinal symmetry. By applying this to the beam screen, it opens the possibility that the transversal flow of currents through the copper would result in field geometric harmonics that are no longer constant along the z-axis, making purely bi-dimensional simulations of the beam screen not enough to fully represent this scenario. In addition, at the center of the segments ($z = 0$), Equation 8.5 reduces to

$$\Delta I_0 = \Delta I(z = 0) = \frac{d_{Cu} l^2}{8\rho_{Cu}} \frac{\partial B_y}{\partial t}, \tag{8.6}$$

showing that the problem would scale quadratically with the total length of the device. It is important to note, however, that these equations are derived from approximating the behaviour of the HTS to that of a short circuit, which is not the case when approaching or exceeding its critical current. In fact, when these conditions are met, the current flowing

through the HTS and therefore also the transverse current in the copper will be limited by the electric field generated inside the superconductor. In this perspective, ΔI and ΔI_0 act as upper limits, and whenever they are above I_c, we can conclude that the HTS segments are fully coupled via their connection to the copper slab, as depicted in Figure 8.1a. On the other hand, if $\Delta I_0 < I_c$, at least some of the current loops are closing inside the HTS, never flowing through the copper.

8.2 Numerical Analysis for Transverse Currents Simulation

To evaluate the behaviour of electronically coupled HTS segments in conditions similar to those of the FCC beam screen, it is necessary to employ a three-dimensional simulation model. To achieve this, we used a multi-physics coupling between the Magnetic Field Formulation (mfh) and the Magnetic Field, no Currents (mfnc) physics in COMSOL Multiphysics®. The former solves Maxwell equations for electromagnetism, not unlike the model developed in Chapter 4, but this time for all three dimensions and contains the domains that represent the metallic conductors. The latter assumes zero current flow and contains the surrounding vacuum domain, reducing to [128]

$$\boldsymbol{H} = -\nabla V_m \tag{8.7}$$

$$\nabla \cdot \boldsymbol{B} = 0\,. \tag{8.8}$$

The external boundary of the vacuum domain is defined as the external applied field $\boldsymbol{B} = B_{ex}\hat{\boldsymbol{y}}$, and the common boundary of the two physics is such that both magnetic fields are the same: $\boldsymbol{B} = \boldsymbol{B}_{mfnc} = \boldsymbol{B}_{mfh}$. Figure 8.4 shows a schematic summary of the model, represented in two dimensions by the central cross-section of the simulated domains for simplicity, although all relationships hold in three dimensions.

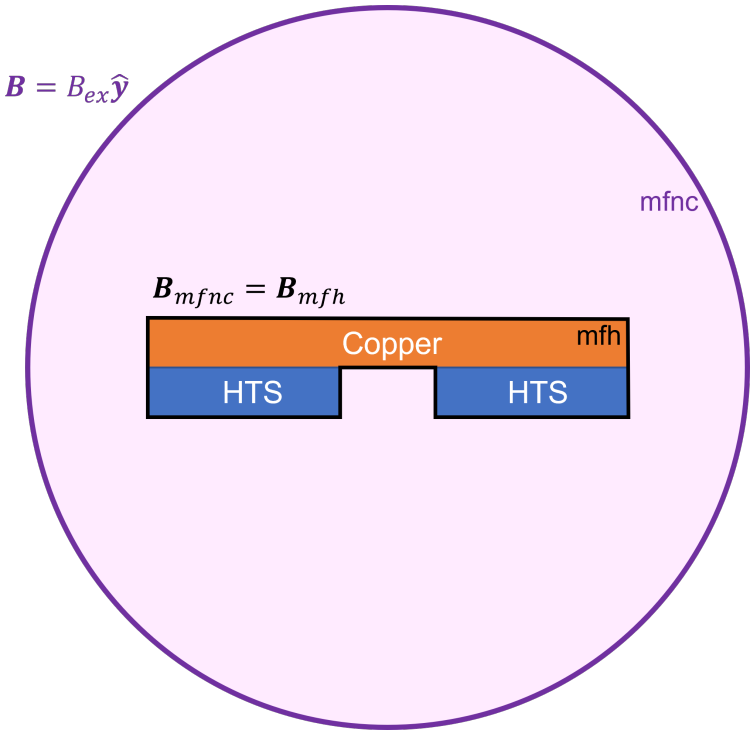
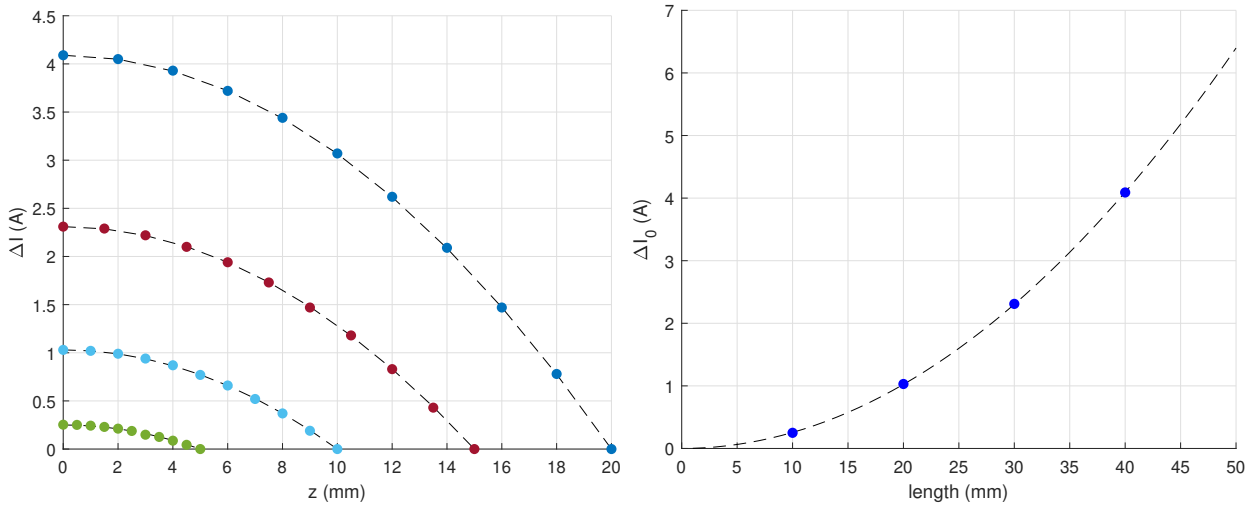


FIGURE 8.4: Schematic of the multi-physics model used for the three-dimensional simulations of electronically coupled HTS segments. Material domains are shown, as well as the appropriate boundary conditions.

In the simulations presented in this section, we analyse a simplified geometry composed only of two 4 mm wide HTS segments connected to a 10 mm wide copper slab with perfect electric contact to verify how the current distribution in the HTS segment is affected by currents flowing transversely through the copper. The resistivity of copper is assumed to be constant and equal to $\rho_{Cu} = 5 \times 10^{-10} \mu\Omega$m, while that of the HTS is once again represented by a power law (Equation 4.17), with constant $J_c = 10\,\mathrm{MA/cm^2}$ and $N = 21$. Due to the extreme aspect ratios of coated conductors, the computational effort required to simulate these structures is very high, often resulting in divergence or requiring a very long time to converge. Nevertheless, the behaviour predicted in Figure 8.3b should be noticeable even in shorter samples.

In Figure 8.5, we can see the simulations results of the current imbalance for different lengths. In these results we notice once again the hyperbolic trend of the current imbalance. On the other hand, Figure 8.5b shows the current imbalance at the center, ΔI_0, and we can see, as predicted by Equation 8.6, the dependence with the square of the length.



(a) (b)

FIGURE 8.5: Simulation results of the current imbalance (a) as a function of z for different lengths and (b) at $z = 0$ as a function of the total length.

The simulation results can than be extrapolated to the actual length of the beam screen sections, which are 16 m long. This extrapolation is shown in Figure 8.6, where we can see that the estimated value of ΔI_0 far exceeds I_c. In reality, as the current density surpasses J_c, the electric circuit shown in Figure 8.2 no longer describes accurately the behaviour of the connected slabs, since it does not take into account the resistive component that arises in the superconductors in such scenario. The emergence of the non-linear resistivity of the HTS would limit the current flowing through them to values close to I_c, allowing more and more current to flow longitudinally through the copper as ΔI_0 rises. Despite the limitations of our model, the fact that ΔI_0 surpasses I_c tells us that the HTS segments are fully coupled. In this situation, the transverse current flow through the copper concentrates near its ends, at $z \approx \pm l/2$, and the current distribution inside a given HTS segment is unidirectional and constant along most of its length and especially around the center ($z = 0$).

Under this assumption, we can repeat the field quality simulations discussed in Section 4.2 without the constraint that enforces the total current in each HTS segment to be zero (see Equation 8). With this, the current will flow in a single direction in the segments located at the right-hand side of the beam screen and in the opposite direction in the segments located at the left-hand side, closing the loop through the copper connecting them. In other words, the neutral line given by x_0 in Equation 7.2, which corresponds to the center of the HTS segment in the insulated case, will

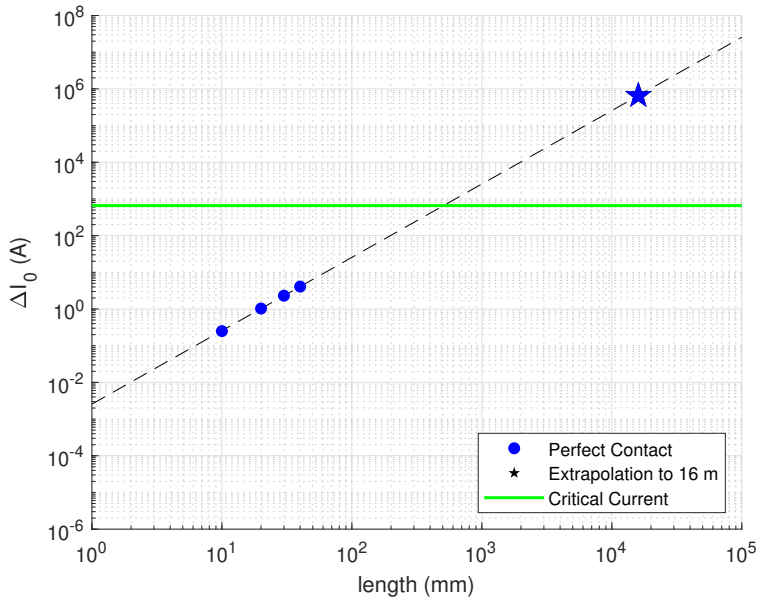
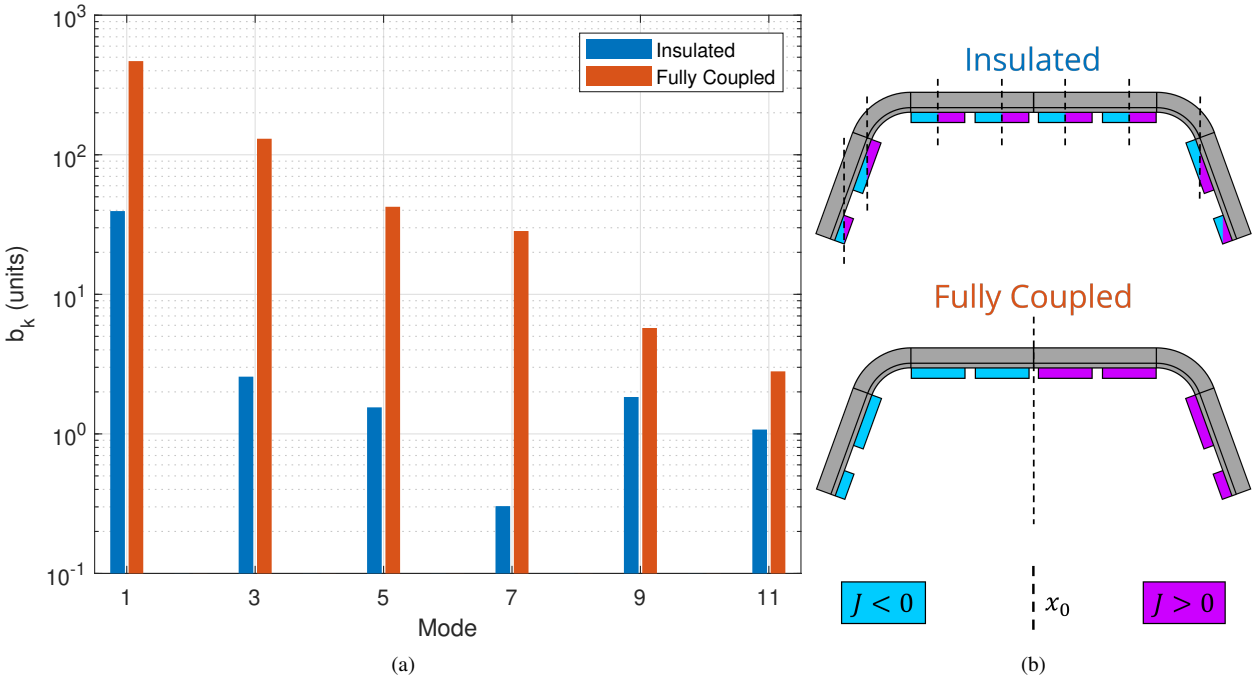


FIGURE 8.6: Extrapolation of the simulated ΔI_0 with respect to length and comparison with I_c.

instead be at $x_0 = 0$. The consequence is a much higher set of field harmonics, reaching even hundreds of units in some cases, as it can be seen in Figure 8.7. This is explained by the fact that most of the reduction in the harmonics caused by HTS striation is now being bypassed, since electronically coupled segments work as a single albeit discontinuous segment.



(a) (b)

FIGURE 8.7: Effects of insulated and fully coupled HTS segments on (a) field harmonics and (b) longitudinal current distribution (schematic representation).

It becomes clear that the influence of transverse currents can lead to a strong current imbalance in the HTS segments, ultimately resulting in excessive field harmonics during field ramp-up and defeating the purpose of adopting the hybrid

coating as initially designed. Therefore, to achieve a similar field quality to that calculated in Chapter 4, it is important that the HTS segments are loosely coupled or entirely decoupled.

8.3 The Effect of Contact Resistance in Transverse Current Flow

In order to decouple the HTS segments, it is necessary to somehow decrease the transverse current flowing through the copper. Several strategies can be employed to achieve this goal, such as introducing an insulating layer or increasing the contact resistance between the copper and HTS. In the this section, we will explore how the current imbalance is impacted by an increase in the contact resistance.

In reality, the electrical contact between the HTS segments and the copper of the beam screen, as good as it may be, will not be perfect and may play a role in diminishing the transverse current flow through the copper segments. Furthermore, it can be intentionally increased to do so. State of the art soldering of coated conductors achieves a contact resistance of $R_c = 40\,\mathrm{n\Omega cm^2}$ [129]. Therefore, to evaluate the impact of the contact resistance on the transverse currents, we have estimated a contact resistance around 100 times worse, at $R_c = 4.2\,\mu\Omega\mathrm{cm}^2$, and repeated the simulations described in the previous section with this value.

The current imbalance resulting from these simulations with the influence of the contact resistance are shown in Figure 8.8. Unsurprisingly, we notice the quadratic trend once more, but the intensity of the current is two orders of magnitude lower than that achieved with a perfect contact (compare with Figure 8.5), showing how effective the contact resistance can be as a means to decrease the transverse currents.

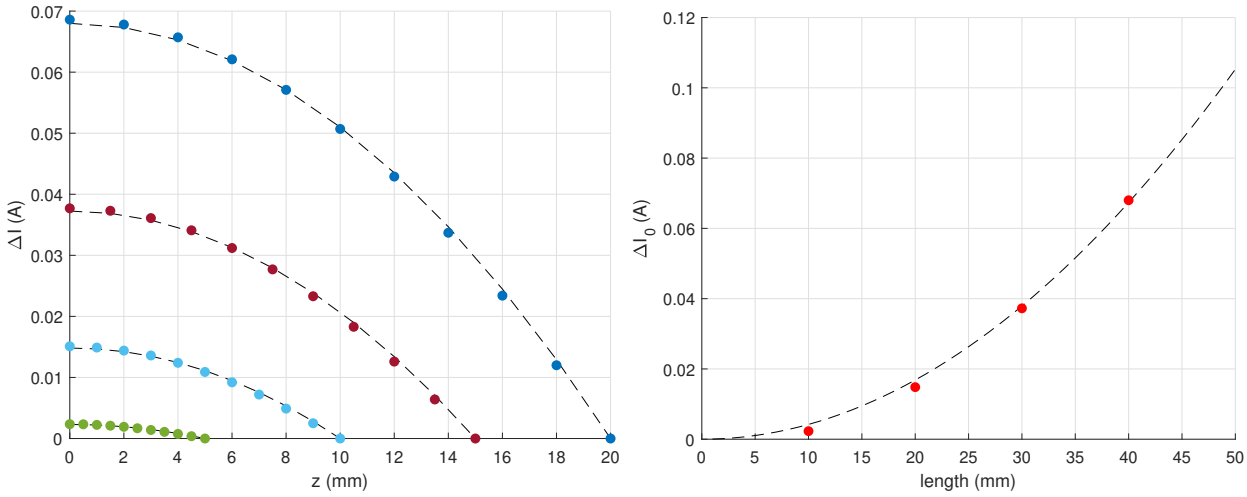


FIGURE 8.8: Current imbalance (a) as a function of z for different lengths and (b) at $z = 0$ as a function of the total length with a contact resistance $R_c = 4.2\,\mu\Omega\mathrm{cm}^2$.

In figure 8.9a we extrapolate these results to the 16 m length of the beam screen, where we can see that, despite the drop in orders of magnitude, the current imbalance is still above I_c, and therefore the HTS segments are still coupled, even with such a relatively high contact resistance. To find the threshold above which the HTS segments would be decoupled, we repeated the simulations with different contact resistance values and extrapolated their results to 16 m, as represented by the colored dots in Figure 8.9b. For the contact resistance values employed, we can see an evident decrease in the estimated current imbalance, but not enough to bring it below I_c. On the other hand, simulating the three-dimensional effects caused by transverse current flow with higher contact resistance values demands increasing computational efforts, ultimately resulting in divergent solutions. To still be able to evaluate how a higher contact

resistance may limit the current imbalance, we extrapolated these results also with respect to the contact resistance, assuming contributions in series coming from the resistance of the copper and the contact resistance:

$$\Delta I \propto (R_{Cu} + R_c)^{-1}, \tag{8.9}$$

which is represented by the dashed line in Figure 8.9b. It is worthwhile to point out, though, that the data used for extrapolation is very far from the target conditions with respect to both length and contact resistance, meaning that the extrapolated values presented throughout this chapter may be significantly inaccurate. In any case, it is clear that the contact resistance plays a major role in determining the current imbalance in the HTS segments.

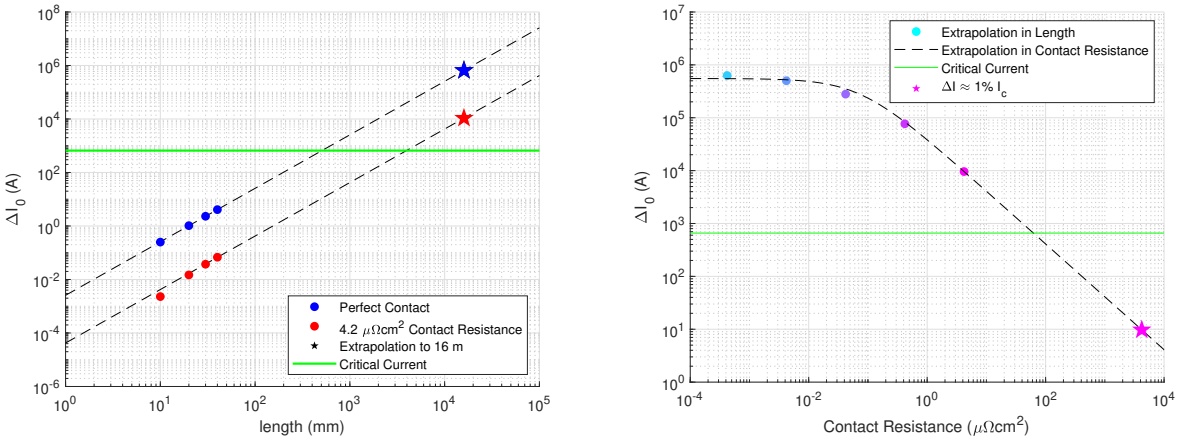


FIGURE 8.9: Extrapolation of the simulated ΔI_0 (a) with respect to length, with a contact resistance of zero and $4.2\,\mu\Omega\text{cm}^2$, and (b) with respect to both length and contact resistance, at a length of 16 m.

To investigate where our soldering technique stands with regards to this topic, we measured the contact resistance of one of our coatings at 77 K by the means of the Transfer Length Method (TLM), which consists in measuring the resistance between several soldered pads at different distances and extrapolating the results to a distance of zero, which would correspond to double the total resistance of the contact. This value is then multiplied by the effective contact area, which is reduced due to current crowding, to obtain the contact resistance [130, 131]. In other words, if the resistance vs. distance curve can be fit into a linear dependence of the form $y = ax + b$, then the contact resistance will be given by

$$R_c = \frac{w_p b^2}{4a}, \tag{8.10}$$

where w_p is the width of the contact pads. To produce the pads, small pieces of $4 \times 1 mm^2$ of coated conductor were soldered to a copper plate and delaminated, after which their REBCO layer was chemically etched to uncover the silver layer below to facilitate the soldering of the wires for measurement. The contact resistance between the silver layer and the REBCO layer is assumed to be negligible in comparison to the total contact resistance. The measured data is shown in Figure 8.10 and resulted in a value of $82.4\,\mu\Omega\text{cm}^2$, which, from Figure 8.9b, is enough to bring the current imbalance to values close to I_c, but not much below it. This tells us that, in order to preserve field quality during ramp-up, it may be necessary to not rely only on the contact resistance between the HTS segments and copper as is, but instead to actively pursue a solution, that being an intentional increase in the contact resistance or a different approach.

Based on the results presented in Figure 8.9b, we can obtain a rough estimation of the necessary contact resistance to reduce the transverse current to only 1% of I_c: $R_{c,1\%} \approx 4\,\text{m}\Omega\text{cm}^2$, as represented by the pink star in the same figure.

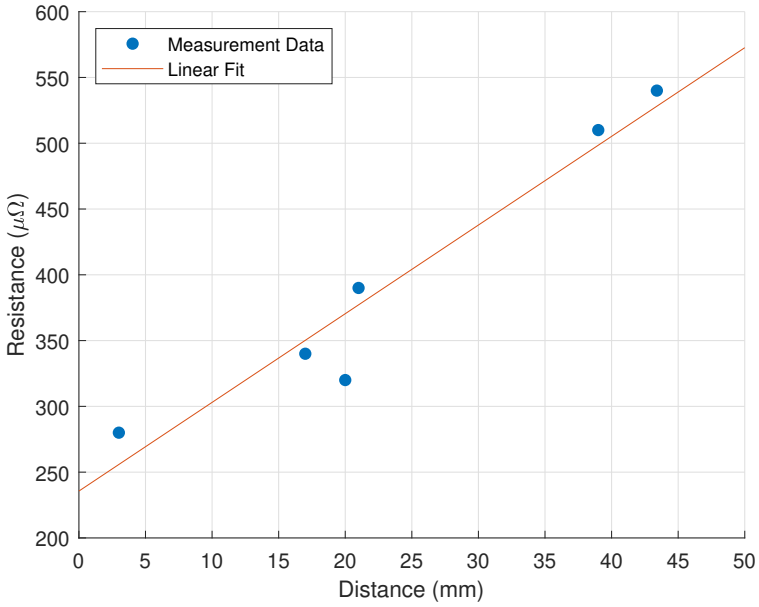


FIGURE 8.10: Transfer Length Method (TLM) data for measurement of the contact resistance between the HTS and copper of the hybrid coating. The fit coefficients are $a = 6.74\,\mu\Omega/\text{mm}$ and $b = 235.62\,\mu\Omega$, and the width of the contact pads is $w_p = 4\,\text{mm}$, resulting in a contact resistance of $82.4\,\mu\Omega\text{cm}^2$, according to Equation 8.10.

This would be enough to decrease the impact on the field quality to negligible values. To intentionally increase the electrical contact resistance between the HTS segments and the beam screen, a 20 to $100\,\mu$m thick pyrolitic graphite sheet (PGS) could be added as an intermediate layer. This could be achieved by electroplating the PGS with a thin layer of copper on both its surfaces [132] so that it can be soldered onto the beam screen on one side, and onto the CC on the other. The remaining coating process would be as described in Chapter 3. Studies show a transverse resistivity for PGS of around 0.06 to $0.3\,\Omega$cm, resulting in a contact resistance of up to $0.6\,\text{m}\Omega\text{cm}^2$ [133]. This, in turn, would translate to an estimated reduction of the transverse current flow to only around 10% of I_c in the simplified geometry analysed in this chapter, significantly decreasing the coupling between the HTS segments.

Apart from actively increasing the contact resistance, other strategies may be considered that would have an obvious impact on the coupling between HTS segments:

- **Replacing solder with a non-conductive adhesive** would allow for a complete decoupling of the HTS segments with the cost of increasing the thermal resistance between layers. To evaluate the feasibility of this soulution, more thermomechanical simulations are needed. In addition, the adhesive material should be compatible with high-vacuum;
- **Shortening the beam screen sections** would decrease the transverse currents by a factor squared with its length but could aggravate other issues such as interference caused by wake fields and surface impedance due to the more constant interruption of the longitudinal distribution of HTS and the higher amount of other more resistive materials;
- **Decreasing the field rate of the main dipole magnets** would decrease the transverse currents by the same factor but would result in more time being required to cycle the machine;
- **Increasing the resistivity of the beam screen copper** would also decrease the transverse currents, but might lead to an increase in surface resistance which would lead to an increase of the beam impedance and of the heat

generation. Other hybrid coating geometries with a higher HTS ratio would need to be investigated; and

- **Striating the beam screen copper at an angle** would decrease the transverse currents by forcing them to flow through the stainless steel below, which has a much higher resistivity, while minimizing the effect on the surface impedance by keeping the exposed steel out of direct line of sight of the beam.

In the end, it may be necessary that a combination of these or other methods is used, so that an optimal balance between the benefits and harms is achieved.

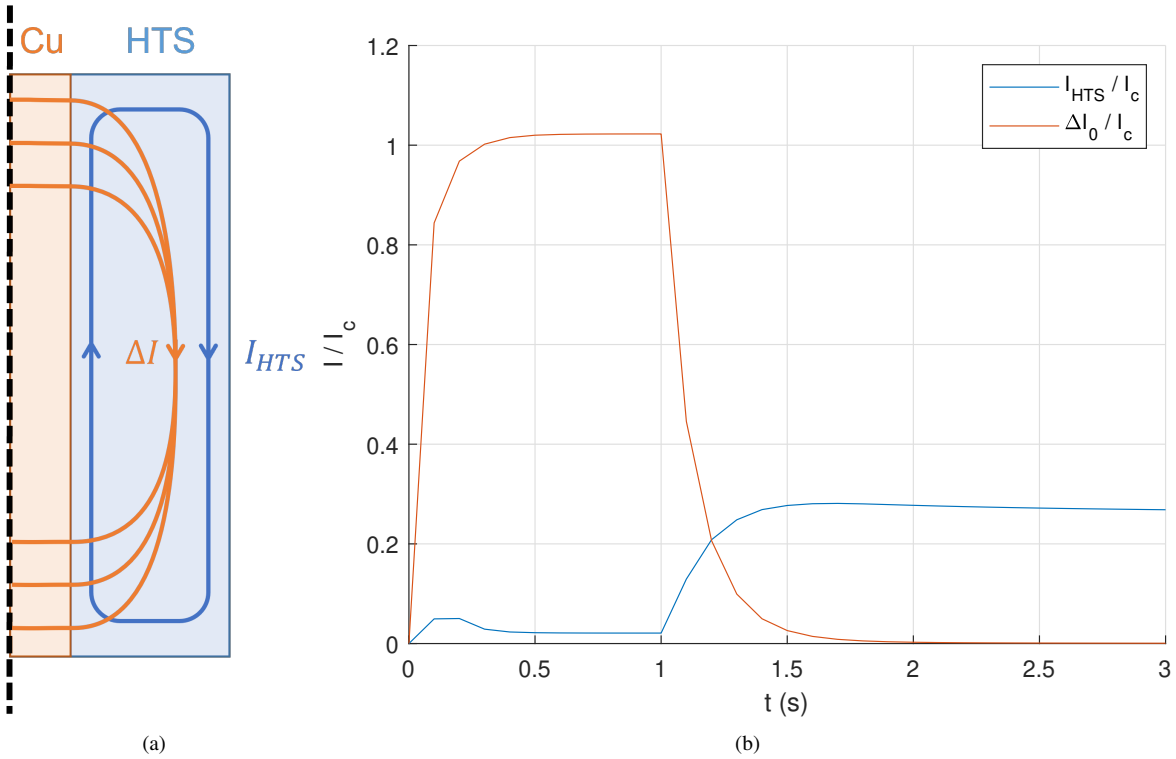
8.4 Coupled HTS Segments in a Constant Field

When reaching a constant magnetic field, such as during injection or at top energy, the main agent with respect to the currents being induced in the beam screen will no longer be in play, resulting in a very different scenario from the one presented so far. Therefore, it is important to evaluate also how the transverse current flow is affected when a field plateau is reached. However, the difficulties imposed by the extreme aspect ratios of the hybrid coating remain. To bypass this issue while still considering the high transverse current values expected to emerge in the operational conditions of the beam screen (see Figure 8.6), we can artificially inflate the ratio $\frac{\Delta I_0}{I_c}$ by arbitrarily increasing the magnetic field rate of the dipole magnets or decreasing the values of the material properties of the coating, ρ_{Cu} and I_c (see Equation 8.6). Doing so will allow us to evaluate the behaviour of the current imbalance in fully coupled HTS segments without the need to take into account their true aspect ratios.

Let us consider the current imbalance generated by a field rate forty times higher than that of the FCC dipole magnets, $32\,\mathrm{T/min}$, on HTS segments with an I_c of $270\,\mathrm{A}$. This values were chosen so that $\frac{\Delta I_0}{I_c} \approx 1$ without severely increasing the required computation time. Although the results obtained in this manner do not correspond to the specific operating conditions of the FCC, the two cases are similar in the sense that the HTS segments are fully coupled, and therefore the flow of current should be similar when reaching a field plateau. The main difference is that the high value of $\frac{\Delta I_0}{I_c}$ is reached not due to the length of the beam screen, but instead because of the increased field rate and reduced I_c.

The currents over time in the aforementioned conditions are shown in Figure 8.11. The external dipole field is increased at a constant rate until $t = 1\,\mathrm{s}$, after which it is kept at a constant value. During ramp-up we notice, as expected, very high values of current imbalance ΔI_0 slightly surpassing I_c. At this point, the current imbalance predicted by Equations 8.5 and 8.6 is attenuated by the increasing resistivity arising in the HTS segments. This happens because the electric field induced in the tape cannot be neglected, and the HTS no longer operates as a short circuit, which was one of the assumptions for arriving in these equations. As a consequence, any current flowing exclusively through the HTS segment I_{HTS} has its value reduced from $\approx I_c/2$ at no coupling to zero at full coupling. For these conditions, almost full coupling is achieved with $I_{HTS} = 0.02 I_c$ at $t = 1\,\mathrm{s}$.

When the field plateau is reached, the situation is quickly changed. The current imbalance, which flows through the copper, decays to zero over the course of a second due to the dissipative nature of the regular conductor. On the other hand, and perhaps counterintuitively, the current flowing exclusively through the HTS segment increases over the same period, resulting in $I_{HTS} = 0.25 I_c$ at the end of the three seconds of simulation. This tells us that some of the current that was originally flowing through the copper changes direction at the 1 s mark, closing the loop through the superconductor, while some of it, forced to remain flowing through the copper, decays over time until vanishing. Therefore, after a quick transient interval, the HTS segments are once again decoupled, with a persistent current larger than I_{HTS} during ramp-up, but smaller than that which would be observed in insulated segments, which is around $0.9 I_c$ depending on the N index value and the rate of change of the magnetic field.



(a) (b)

FIGURE 8.11: Current behaviour during ($t < 1\,\mathrm{s}$) and after ($t > 1\,\mathrm{s}$) magnetic field ramp-up with fully coupled HTS segments. (a) shows a schematic representation of the distribution of current flowing transversely through the copper (ΔI_0) and closing the loop through the HTS segment (I_{HTS}), and (b) presents their evolution over time.

In Figure 8.12 we take a closer look at the current imbalance and the HTS-exclusive current as a function of the z coordinate during and after ramping the magnetic field. The dots show the simulations results while the dashed lines are a guide for the eye. While the field is increased, ΔI shows a similar behaviour to that observed previously, reaching its maximum at the center and decreasing to zero when reaching the end of the device. However, unlike its previous iterations, the curve formed by the simulated data points is now better described by

$$\Delta I = \Delta I_0 \left[\left(\frac{l}{2} \right)^{2.24} - z^{2.24} \right], \tag{8.11}$$

with an exponent slightly larger than 2. A distortion like this is not unexpected, since the proximity to I_c causes higher electric fields to be induced in some parts of the tape, resulting in an heterogeneous suppression of the total current. This behaviour, of course, only persists during ramp-up, and ΔI quickly drops to zero after the 1 s mark, as shown by ΔI_0 in Figure 8.11b.

When observing the current confined to the HTS, some insight is obtained on the reason why I_{HTS} increases after reaching the field plateau. Comparing its values during and after ramp-up, we notice that although the curve increases as a whole, the amount by which it increases is not uniform. During ramp-up, while the current imbalance was close to I_c, there is not much room for I_{HTS} to flow without locally increasing J, and subsequently leading to a higher electric field E. As a consequence, I_{HTS} is close to zero when $\Delta I \approx I_c$, but increases with z since the current imbalance is smaller near the ends of the HTS segment. When the current imbalance vanishes due to the constant magnetic field, the electric field induced in the HTS drops, allowing for more current to flow in a closed loop inside of it, especially near its center.

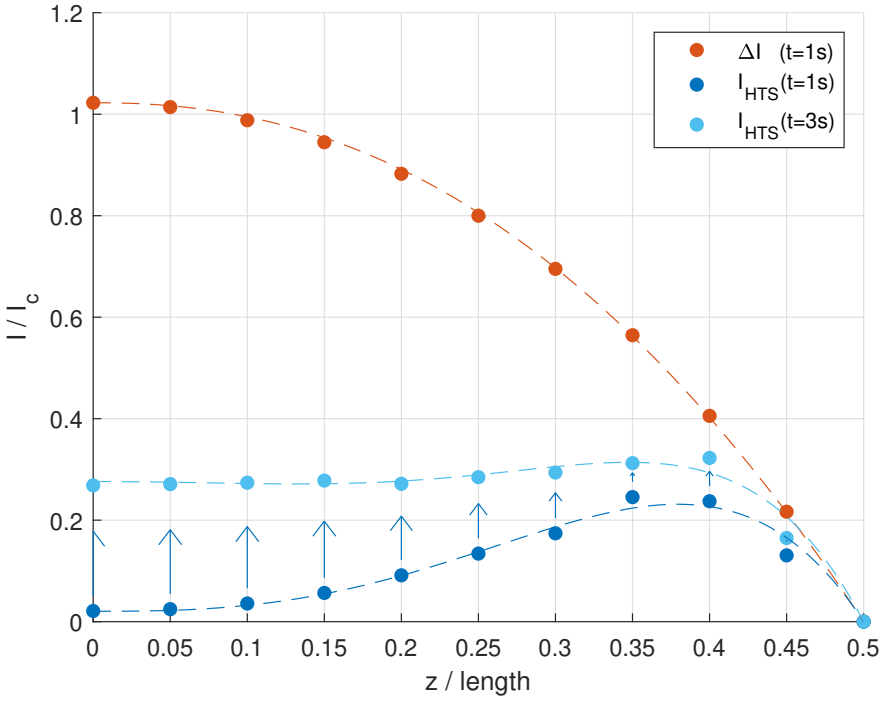


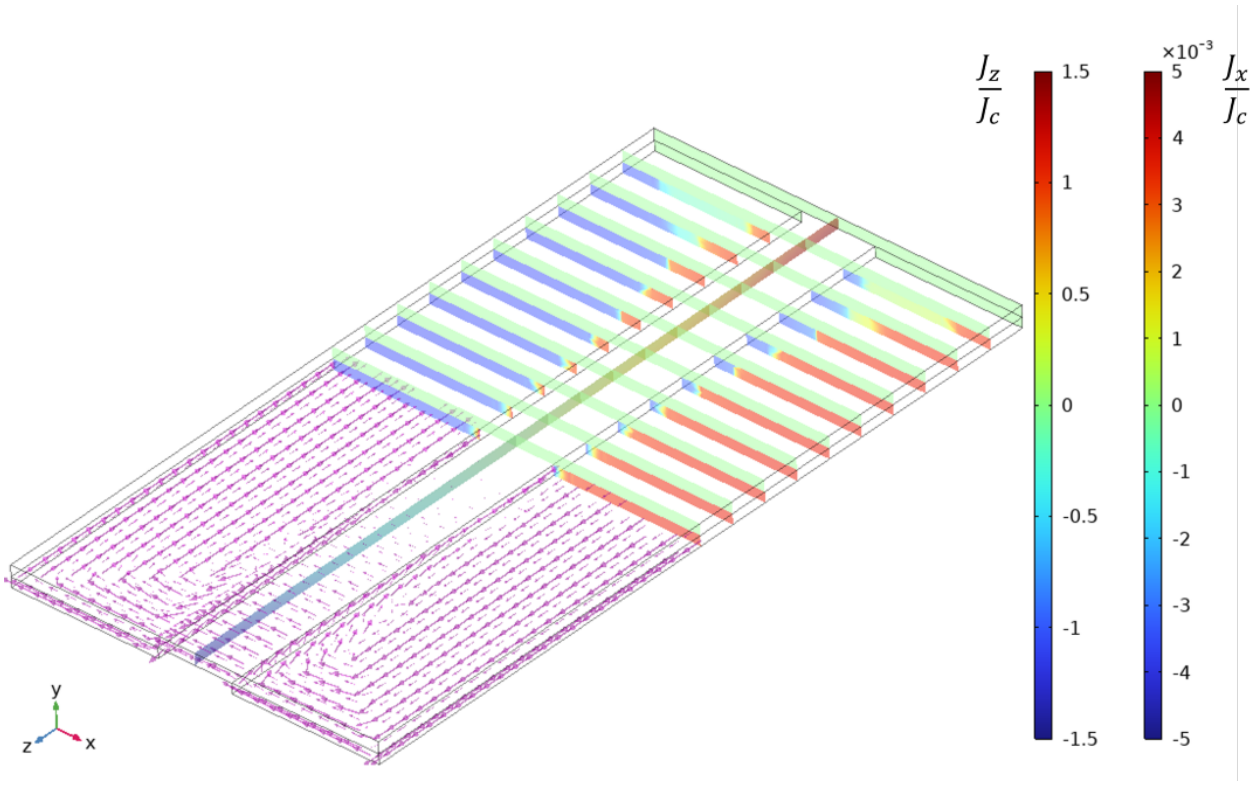
FIGURE 8.12: Current flow in coupled HTS segments during ($t = 1\,\mathrm{s}$) and after ($t = 3\,\mathrm{s}$) magnetic field ramp-up.

Now that we have a better understanding of the mechanisms that dictate the current flow in the HTS segments during and after magnetic field ramp-up, Figure 8.13 offers further evidence of how the behaviour of the HTS segments complies with expectations based on the analytic developments presented in the previous sections. Here we evaluate the path and intensity of the current density flowing both through the HTS and the copper. Figure 8.13a shows the expected behaviour of the coupled HTS segments, with most of the current flowing through the copper and connecting both HTS segments. Meanwhile, a small fraction of the current changes directions instead of crossing to the copper. The transverse current density in the copper increases from the center to the edges.

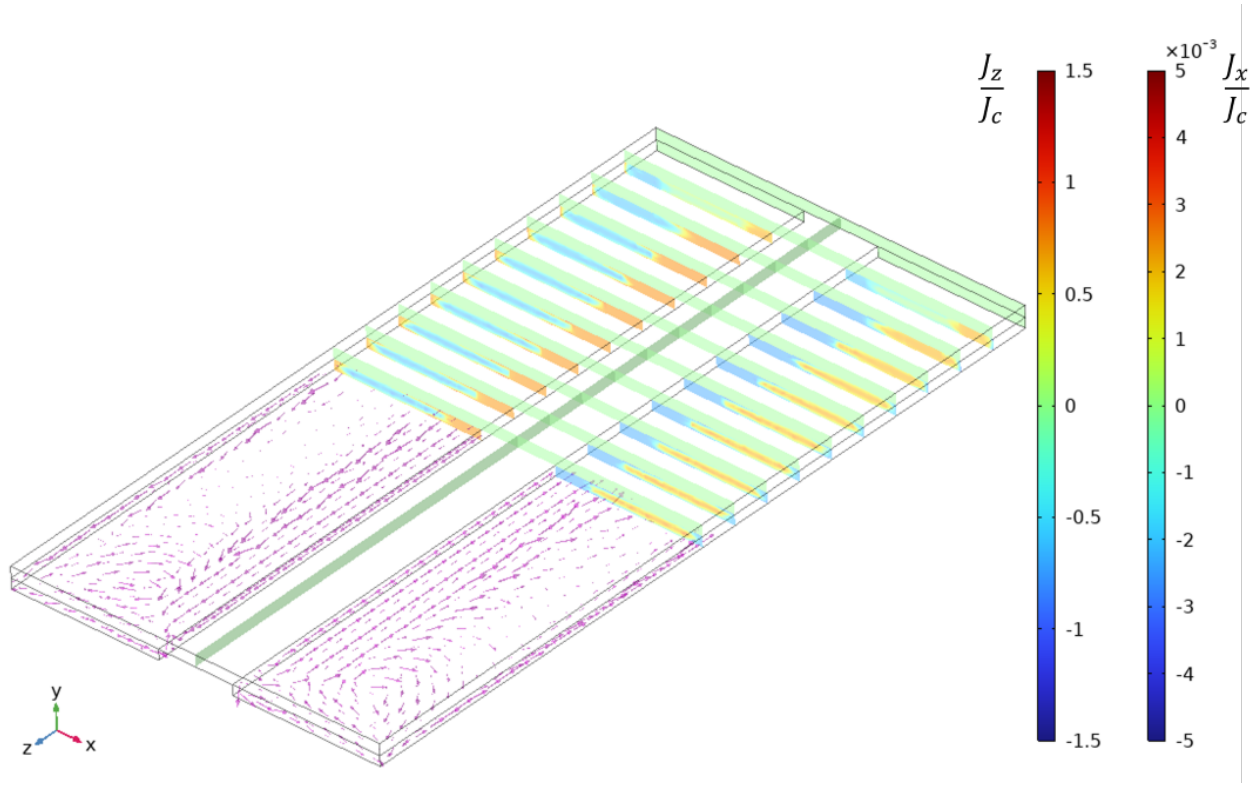
When the field plateau is reached, in Figure 8.13b, the transverse current in the copper vanishes, leading to a closed current path inside each of the HTS segments. It is interesting to note, however, that there is a significant amount of transverse current flowing inside the HTS segments, even far from the edges. In addition, the clearly non-uniform current distribution along the z-axis means that the field quality will also not be homogeneous for different values of z.

Although a precise calculation of the field harmonics after magnetic field ramp-up would require a more accurate computation of the current distribution in the real geometry of the beam screen, it is possible to provide a rough estimation of the field quality by considering a few approximations:

- The current density is uniform along the z direction: $J(z) \approx J(z = 0)$;
- The transverse current flow is zero;
- The sheet current density used to calculate the field distortion is the integral along the c-axis of current density; and
- Each HTS segments in a quadrant of the hybrid coating has the same current distribution, normalized to its width.



(a)



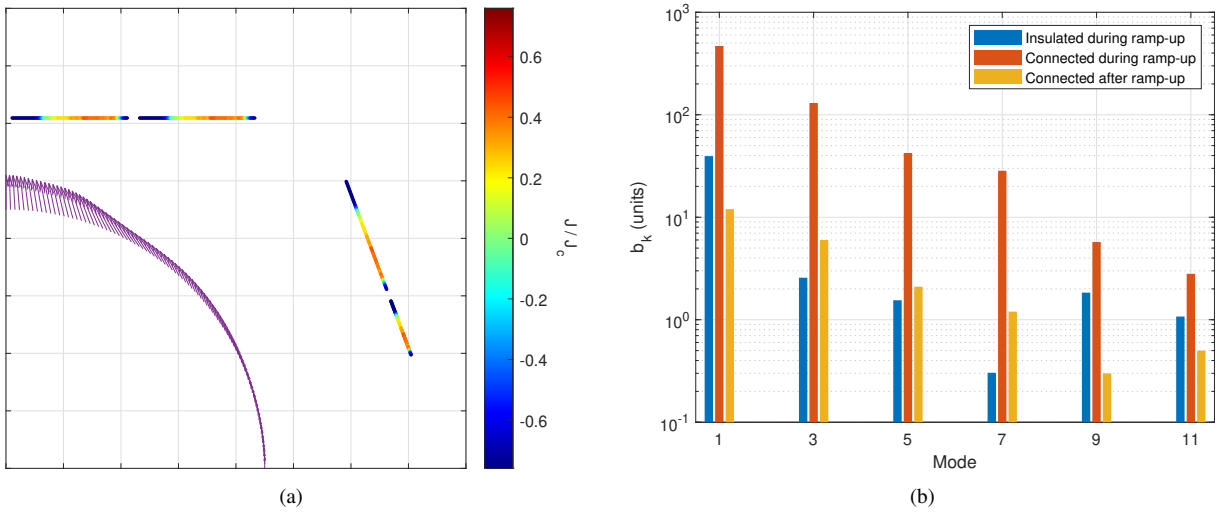
(b)

FIGURE 8.13: Current density distribution and current vector map in coupled HTS segments (a) during ($t = 1\,\mathrm{s}$) and (b) after ($t = 3\,\mathrm{s}$) magnetic field ramp-up. Dimensions are re-scaled to facilitate convergence and visualization.

With this, the field distortion at the reference radius can be calculated from a variation of the magnetic field produced by an infinitely long wire derived from Biot-Savart law considering the sheet current density $\boldsymbol{J}_s$:

$$\Delta B = \frac{\mu_0}{2\pi} \int_{\partial\Omega_{sc}} \boldsymbol{J}_s \times \frac{\boldsymbol{r'}}{|\boldsymbol{r'}|^2} dw, \tag{8.12}$$

where dw represents an infinitesimal increment along of the width of the HTS segment, $\partial\Omega_{sc}$, and r' is the vector distance from the current source to the point where the field is calculated. With it, the approximated field harmonics can be obtained, as shown in Figure 8.14.



(a) (b)

FIGURE 8.14: Field quality estimated from the current density distribution at $z = 0$ after magnetic field ramp-up. (a) shows the sheet current density in each HTS segment and the field distortion created by it, and (b) shows a comparison of the field harmonics produced by coupled segments during ramp-up, coupled segments at a field plateau, and insulated segments during ramp-up.

The first thing to note is that the field harmonic values obtained with this approximation are much lower than those estimated for the coupled HTS segments during field ramp-up even being surpassed by the insulated case during ramp-up for some modes. Not only are the currents densities circulating in the HTS lower after ramp-up, but they are also confined within each HTS segment, which decreases their contributions to the field disturbance. Since these two aspects are also true for the beam screen geometry, we expect that this first approximation, although perhaps lacking in precision, can at least offer an assessment of the orders of magnitude involved.

8.5 Chapter Summary and Conclusions

Throughout this chapter we have evaluated the impact of transverse current flow through the copper of the beam screen on the longitudinal current distribution inside the HTS segments and in the field quality of the vacuum chamber when the HTS segments are electrically connected to the copper sheet. We have employed analytic approximations as well as numerical analysis to investigate which operational conditions result in electronically coupled HTS segments.

The simulation results, corroborated by the analytic development presented, reveal a square dependence between the transverse current flow and the length of the device under investigation. Depending on the material properties and operational conditions, the transverse current, numerically equal to the current imbalance in the HTS segments, can vary from 0 (uncoupled) to $\approx I_c$ (fully coupled). While fully coupled segments may have a massive impact on the field harmonics, reversing the benefits brought by the segmentation of the HTS material, it is clear that these negative

effects are only present during magnetic field ramp-up, after which the currents quickly decay and rearrange, resulting in much higher field quality, close to the values expected for insulated segments.

We have investigated how the transverse current flow is affected by the electric contact resistance between the HTS segments and the copper layer coating the beam screen's stainless steel. Even though the contact resistance resulting from our soldering technique is not expected to fully decouple the coating, results show a strong dependence between the contact resistance and the current imbalance in the HTS, and actively increasing the contact resistance via means such as an added layer of thin pyrolytic graphite sheet is a promising solution to achieve the acceptable levels of coupling.

Finally, alternatives such as altering the field rate of the dipole fields, shortening the beam screen sections or striating the beam screen copper can be adopted by themselves or in combination with an increased contact resistance to decrease transverse current flow if it proves to be an issue in the operating conditions of the beam screen.

Chapter 9

HTS Coated Beam Screen Prototypes and Radio-Frequency Cavities

Throughout the previous chapters, we have employed FEM analysis as a powerful tool to investigate the electromagnetic and thermomechanical performance of the coated beam screen in the operational conditions of the FCC-hh. In addition, Chapters 3 and 4 showed high performing samples resulting from the hybrid coating techniques proposed in this work. However, it is important to evaluate how the hybrid coating performs with regards to these and other aspects by performing experimental measurements with proof-of-concept devices. As of the writing of this thesis, proof-of-concept devices are in different stages of development, employing the same coating techniques introduced in Chapter 3.

In spite of the fact that the coating methods employed in this work were designed with the specific purpose of coating the FCC beam screen, they could prove to be useful to other applications that require low surface impedance materials, such as radio-frequency resonating cavities. In this chapter, the prototypes of the coated beam screen will be presented, as well as other devices where a hybrid or full HTS coating was adopted.

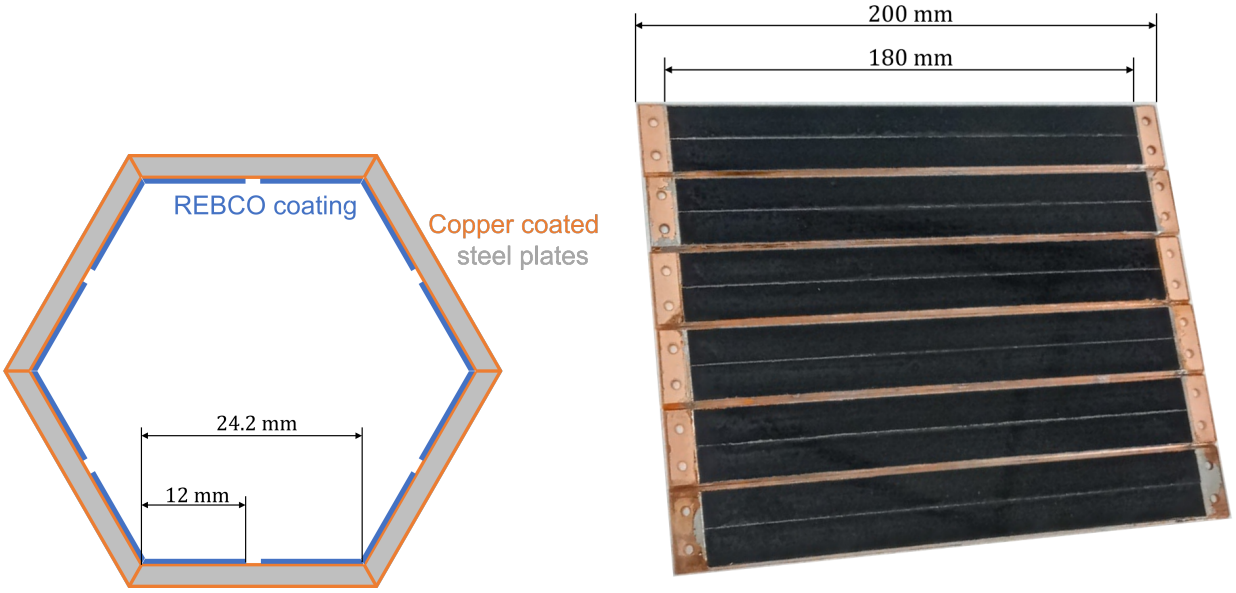
9.1 HTS Coated Beam Screen Prototypes

The proof-of-concept devices presented in this section have the purpose of evaluating the behaviour of the coated beam screen with respect to different aspects, namely surface impedance, photodesorption and field homogeneity.

Surface Impedance Measurements

The first coated beam screen prototype consists of six 200 mm long copper coated steel plates arranged in a hexagonal assembly as shown in Figure 9.1. Each of the plates is then coated with exposed REBCO HTS produced from two soldered and delaminated 12 mm wide and 180 mm long coated conductors with a 0.2 mm gap in-between. When assembled together with lids on both ends, the six coated plates form a resonating cavity that can be used as a proof of concept to evaluate the coating's effect on coupling impedance under the FCC-hh beam screen conditions at CERN's installations.

The simpler, flat geometry of this proof-of-concept device sacrifices fidelity to the beam screen design to facilitate production and measurements. On one hand, the coating method is simpler when applied to flat surfaces and when employing 12 mm wide HTS segments instead of the 4 and 2 mm widths needed for the hybrid coating. On the other, measurements such as those performed via Hall Scan Prove Microscopy or other methods can benefit from the simpler geometry as well. The HTS coated conductors selected for this prototype were provided by Fujikura with added

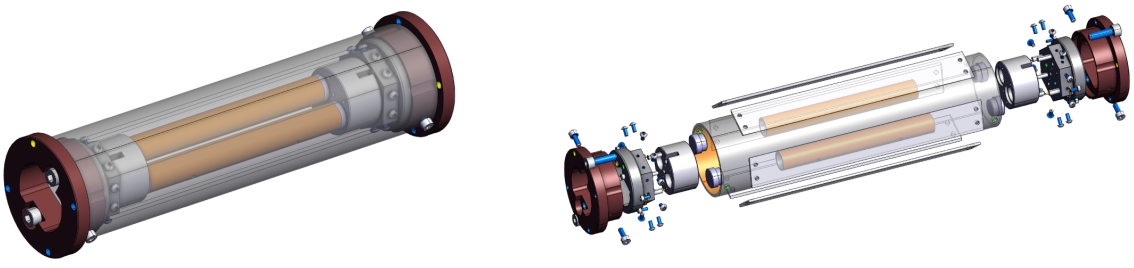


(a) (b)

FIGURE 9.1: The hexagonal proof-of-concept device for the coated FCC beam screen to evaluate surface impedance. (a) shows a schematic of its cross-section while (b) presents a photograph of the six coated plates that compose it.

artificial pinning centers due to their high performance in terms of surface impedance throughout the entire magnetic field range of interest.

A resonator system has been developed at CERN to measure the surface impedance of the prototype. The two-rods resonating cavity enclosed by the hexagonal prototype is shown in Figure 9.2. Although the results from such a measurement are expected to be impacted by the distinguished geometry of the device with respect to the beam screen design, they can provide an estimate of the positive impact of the HTS coating on its radio-frequency performance. A first measurement has been performed revealing that the resonator system as originally designed was not sensitive enough to accurately measure the coating's low surface impedance. The resonator system is currently being redesigned to account for the low expected impedance values.



(a) (b)

FIGURE 9.2: Two rods resonating system enclosed by the hexagonal prototype. (a) shows a schematic representation of the system and (b), its exploded view. Images created and provided by Dr. Patrick Krkotić.

Photodesorption Measurements

As of the writing of this thesis another device is currently being developed to investigate the photodesorption of the coated beam screen when exposed to synchrotron light. The prototype consists of a copper pipe with a inner cavity with the shape of a decagon. To allow for the coating process, which cannot be performed in closed cavities, the device has to be split into more than one piece. Although several separate pieces would facilitate coating, a two-piece system was chosen to minimize vacuum losses, as shown in Figure 9.3. Each of the faces of the inner decagon has a 12.35 mm width and will be coated with a 12 mm wide delaminated and soldered coated conductor.

The photodesorption measurements will be conducted in one of the beamlines at the High Energy Accelerator Research Organization (KEK) in Japan. One of the ends of the devices will be closed by a HTS coated lid, while the other will be connected to the beamline to receive synchrotron radiation. The synchrotron light will impinge on one of the decagon faces and the photodesorption rate will be measured. This experimental routine will be repeated for the same coated cavity before and after addition of a amorphous carbon coating, which will be performed at CERN, and will be compared with copper cavities without HTS, before and after amorphous carbon coating as well.

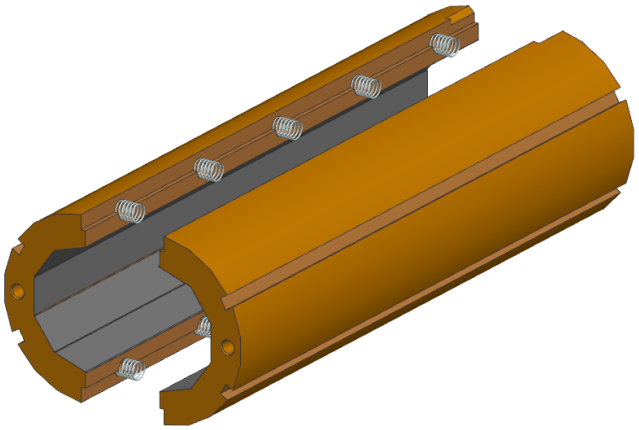


FIGURE 9.3: Schematics of the decagonal proof-of-concept device for the coated FCC beam screen to evaluate photodesortpion. Image created and provided by Oriol Traver.

Field Quality Measurements

Since field homogeneity requires a coating geometry matching that of the beam screen design, another prototype is being implemented with the real geometry of the beam screen and its coating. The 20 cm long beam screen has already been produced at CERN and sent to ICMAB for coating. Once this second prototype is coated, it will be submitted to field quality measurements at CERN.

The magnetic field inside the beam screen chamber will be measured by rotating coils both during ramp-up and at constant dipole field, which can then be used to calculate the field harmonics. Although this prototype is relatively short and this is not the goal of this measurement, the experiment could shed light into the effect of the coupling of HTS segments as described in 8. If a transverse current flow is present in the beam screen prototype, it is possible that its effects are observed in the magnetic field distribution, which would then become evident by comparing the experimental results with the simulations.

9.2 REBCO-Coated Cavities for Axion Dark Matter Search

Observation of the movement of galaxies in our universe show spinning velocities that exceed those expected from the gravitational pull of their observable matter. The extra mass needed for such motion is attributed to dark matter, which, unlike regular matter, does not interact with the electromagnetic force. Although it is estimated to outweigh visible matter by a factor six, the fact that is does not emit, reflect or absorb light makes its detection very difficult [134, 135].

Theories suggesting physics beyond the standard model often propose candidates for dark matter. Among these, the axion is a theoretical particle that, in spite of not interacting directly with the electromagnetic force, is believed to convert into a photon in the presence of a strong external magnetic field, a property that can be exploited as a means for its detection [136]. The Relic Axion Detector Exploratory Setup (RADES) at CERN is an axion haloscope experiment that employs a resonating cavity under a strong dipole field in an attempt to detect axions from the Milky Way's dark matter halo passing through the cavity or, otherwise, to establish limits to their possible mass range [137].

Each cavity can detect a certain axion mass m_A based on its resonating frequency, which in turn depends on its volume V. However, the cavity's volume is also tied to the sensitivity of the experiment. The pursuit of higher mass axions demands small cavities with higher resonating frequencies, which result in lower sensitivity. Therefore, it is important to fine-tune other parameters as well as the volume in order to maximize the capabilities of detecting the elusive particle.

The figure of merit F of the experiment for the axion detection experiment is given by

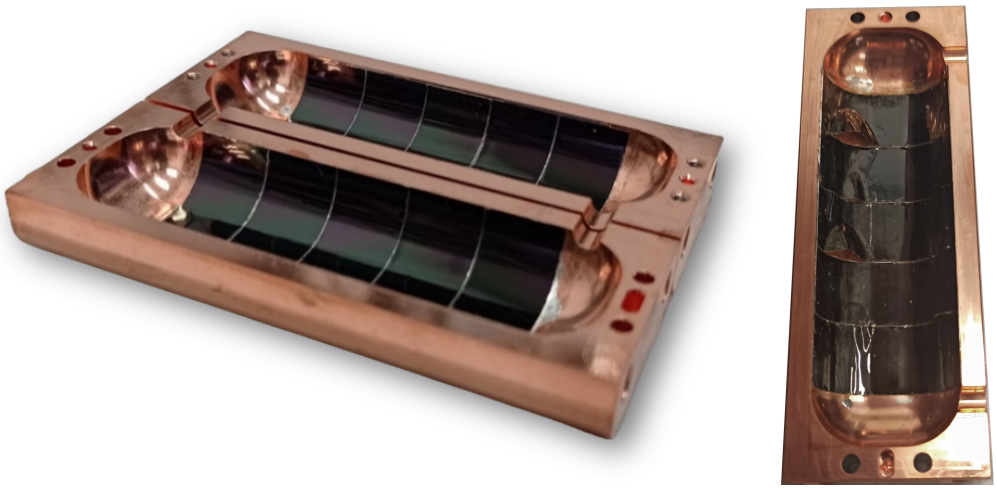
$$F \propto g_{\alpha\gamma}^2 m_A^2 B^4 V^2 T_{sys}^{-2} G^4 Q\,, \tag{9.1}$$

where $g_{\alpha\gamma}$, B, T_{sys}, G and Q are, respectively, the axion coupling to two photons, the external magnetic field, the detection noise temperature, the geometrical factor of the cavity and its quality factor. Materials such as REBCO HTS are promising candidates for coatings of this type of haloscopes, since they offer surface impedance values lower than those of copper, and therefore higher Q, even under strong magnetic fields and at high resonant frequencies due to their high upper critical magnetic fields and pinning forces.

With the goal of increasing the experiment's sensibility by improving the cavity's quality factor, we have coated two RADES's cavities with our HTS coating technique [138], as described in Chapter 3. The two halves of the first coated cavity are shown in Figure 9.4a. The direction of the HTS tapes is such that no current is expected to flow across tape boundaries, which might otherwise decrease the quality factor. Five segments of 12 mm wide REBCO coated conductors were soldered onto each half and delaminated. The selected provider for the first cavity was THEVA, since their product shows a very smooth delamination interface in general, but especially when the CC is attached to curved surfaces. The rounded corners of the cavities were left uncoated since their quarter sphere-like geometry makes it difficult to coat and the exposed copper would result only in an 8 % expected degradation in quality factor.

The REBCO-coated cavity was submitted to a dipole magnetic field of up to 11 T at 4.2 K and had its quality factor measured while simultaneously hunting for axion particles with a resonating frequency of 9 GHz. Results show a quality factor between 60,000 and 80,000 for the REBCO-coated cavity throughout the magnetic field range, outperforming a pure Cu-coated cavity by a factor 1.5 to 2. Although this shows the potential for HTS in such applications, a factor 5 was expected based on the surface impedance of REBCO when compared to copper. This discrepancy was attributed to the bending of the HTS segments during the coating procedure.

To mitigate the issue, a second cavity was coated, this time with HTS tapes provided by Fujikura, due to their high performance at high fields and smaller critical bending radius. However, when put to the test, the coating proved not to have been soldered appropriately, partially detaching from the cavity due to the Lorentz forced induced at high fields, as presented in Figure 9.4b. Analysis of the cavity after testing suggests that the pressure applied during soldering might not have been applied homogeneously, leading to low adhesion in certain regions of the coating. Before failure, the coating presented a quality factor above 200,000 at zero field, showing a significant improvement with respect to its predecessor. An extensive study of how the bending radius impacts on the quality of the HTS coating and how to improve the coating technique for these conditions is undergoing as part of Neil Lamas's doctorate thesis.



(a) (b)

FIGURE 9.4: Cavities coated with our REBCO coating technique for axion dark matter detection. (a) Two halves of the first RADES's REBCO-coated axion detection cavity, coated with THEVA coated conductors. (b) One half of the second RADES's REBCO-coated axion detection cavity, coated with Fujikura coated conductors. The HTS coating suffered a catastrophic failure when exposed to the dipole magnetic field, partially detaching from the cavity. Figure (b) was created from a photograph provided by Dr. Jessica Golm.

The results of the axion detection experiment performed with the first REBCO-coated cavity have been used to rule out a portion of the possible axion mass range and are the subject of an upcoming publication. For future experiments with REBCO-coated cavities, a new cavity design will be implemented at RADES, consisting of six faces with flat central areas and round corners, as shown in Figure 9.5. The new shape of the corners allows for the coating of the entire surface. In addition, the central area, where the currents are highest, will not require bent tapes. With these combined changes, we hope to further increase the cavity's quality factor.

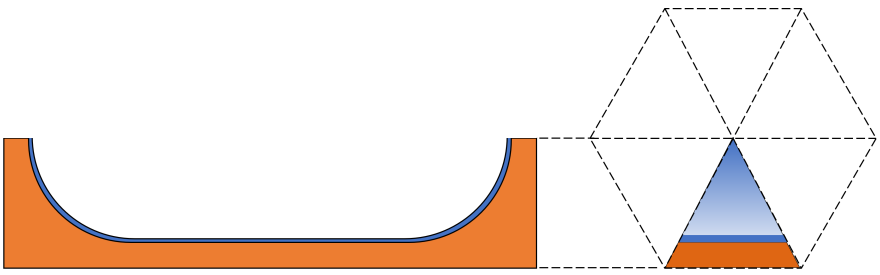


FIGURE 9.5: Schematic representation of the new axion detection cavity design with a flat central area. On the left, its frontal view; and on the right, its central cross-section view.

9.3 REBCO-Coated Disc for RF Testing

High gradient particle accelerators count with the high electric fields generated inside accelerating cavities to quickly raise the velocity of charged particles. The main candidate material for high gradient acceleration are normal conducting accelerating structures, due to the higher surface fields that can be sustained in comparison with LTS. However, the high peak electric and magnetic fields at the surface of the material cause vacuum arcs that lead to RF breakdowns, which in turn, can perturb acceleration. As a means to mitigate this, one of the adopted strategies is to decrease the operating temperature to cryogenic levels, reducing the breakdown rates due to the increased hardness of the material, in addition to increasing the cavity's quality factor, and therefore increasing its efficiency.

The investigation of the performance of these cavities under cryogenic temperatures has brought forth the interest in evaluating how HTS structures would perform under similar conditions. In an effort to accomplish this, the research team at the Stanford Linear Accelerator Center (SLAC) National Accelerator Laboratory have designed and implemented an X-band cryogenic RF material testing system to measure the quenching RF magnetic field and the surface resistance of material samples in a disc shape of up to 50 mm in diameter [139].

The main component of the RF system is a hemispherical copper cavity, as shown in Figure 9.6a, operating with a resonating frequency of approximately 11.4 GHz in a TE_{013} like mode. The surface resistance of the sample is obtained in the temperature range from 3 to 300 K directly from the quality factor:

$$R_{s,sample} = G_{sample}\left(\frac{1}{Q_0} - \frac{R_{s,body}}{G_{body}}\right), \tag{9.2}$$

where

$$R_{s,body} = \left[\left(\frac{1}{G_{body}} + \frac{1}{G_{sample}}\right) Q_{0,ref}\right]^{-1} \tag{9.3}$$

and G, Q_0 and R_s refer to the geometric factors, the unloaded quality factor and the surface resistance, respectively. The quenching RF field, on the other hand, is determined by measuring the quality factor at different power levels.

In a collaboration with SLAC, we have prepared for measurement in their RF system a REBCO-coated disc sample composed of four REBCO Fujikura coated conductors soldered onto a copper disc and delaminated according to the techniques presented in Chapter 3. Due to the rectangular shape of the HTS segments, an additional step was necessary in this case. The soldered REBCO pieces exceeded the area of the discs and their protruding portions were removed after the regular coating procedure. The resulting sample can be seen in Figure 9.6b.

Preliminary quality factor results from experiments where the RF power was ramped from 100 to 1600 W at each temperature, show that our REBCO-coated sample outperforms pure copper by a factor 19 at 80 K and 100 at 4 K. It is worth pointing out, though, that the TE_{013} like mode induces currents that are forced to cross the boundaries between HTS segments, resulting in a high contribution to surface resistance coming from the copper and the solder alloy, resulting in an overall quality factor lower than that expected for currents contained within the HTS. Nevertheless, these results show the potencial of REBCO coatings for other RF applications such as the accelerating cavities in particle accelerators. A more detailed analysis of these results is the is part of the scope of Neil Lamas's doctoral thesis.

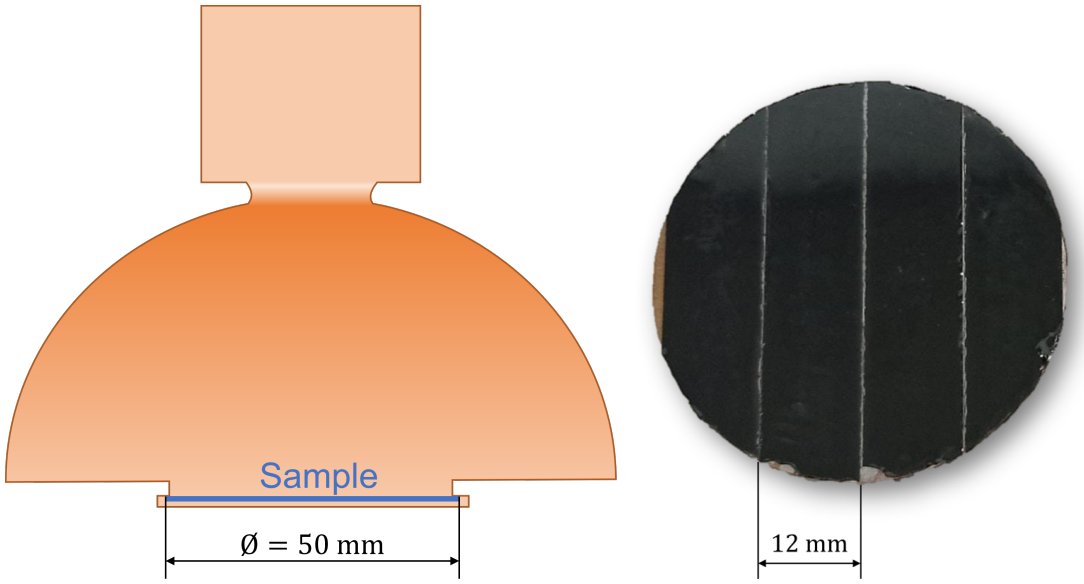


FIGURE 9.6: SLAC's experimental setup for measuring the quality factor of normal and superconducting samples. (a) presents a schematic of the hemispherical resonating cavity and (b) shows the REBCO-coated disc analysed with the system.

9.4 Chapter Summary and Conclusions

In this chapter we have briefly presented devices and collaborations in which our coating technique was employed to produce REBCO-coated radio-frequency cavities.

Firstly, three prototypes of the coated beam screen are in different stages of development. The Hexagonal cavity for coupling impedance measurements has been produced and coated, but still waits for a measuring system sensitive enough for the low impedance values of the hybrid coating. The decagonal cavity for photodesorption measurements has been designed and is under production, after which it will be coated and sent for testing at KEK in Japan. Finally, a prototype with the exact geometry of the beam screen will be used to evaluate the field quality under a ramping and constant dipole field. The beam screen has been produced by CERN and will be coated at ICMAB to subsequently be sent back to CERN for measurement.

With the increasing interest in our coating technique and its suitability for RF applications, we have coated a resonating cavity for use at the RADES experiment for axion dark matter detection at CERN. On one hand, preliminary results show a quality factor higher than copper by a factor 1.5 at 11 T, 4.2 K and 9 GHz. On the other, as it has been demonstrated by the Center for Axion and Precision Physics Research (CAPP), where a haloscope coated with REBCO using delaminated coated conductors has shown a quality factor of 13×10^6 at 5.4 GHz, 100 mK and 8 T, it is clear that there is still a lot of room for improvement by taking measures to mitigate issues arising from bending the coated conductors during the coating procedure. By selecting the appropriate CC provider, increasing the bending radius or adapting the cavity's geometry to remove curved areas, we expect to achieve even higher quality factors, coalescing the REBCO coating as a strong suitor for such low impedance applications.

Finally, we have collaborated with SLAC to produce a REBCO-coated disc for measurement in their high RF power testing system. Measuremets at 11.4 GHz in temperatures ranging from 4 to 80 K and up to RF powers of 1.6 kW show a significant increase in performance with respect to copper, even when considering the crossing of HTS boundaries by the currents induced in the TE_{013} like mode.

From the results of our REBCO-coated samples, there is increasing evidence of their suitability for RF applications other than the coating of the FCC beam screen. In the specific case of the RADES experiment, employing our REBCO coated has already yielded results with a better sensitivity than that which would otherwise be available simply with a pure copper coating. Furthermore, ongoing work aims to ensure that, as the interest for such technology increases, the coating methods can be adapted to account for the needs of each specific application.

Chapter 10

General Conclusions

In the context of the FCC-study, it is important that the beam screen, responsible for shielding the superconducting steering magnets from the synchrotron radiation emitted by the particle beam, presents low surface impedance and high magnetic field quality. In this work, finite elements method (FEM) numerical analysis was used as a means to investigate the behaviour of the FCC beam screen when coated with a hybrid REBCO-Cu coating, aiming to reduce its surface resistance while maintaining magnetic field disturbance within the acceptable levels. We have also developed techniques to coat devices such as, but not limited to, the FCC beam screen with a REBCO layer, resulting in high-performing coatings for radio-frequency (RF) and strong magnetic field applications. These techniques were employed to produce laboratory samples of the hybrid coating to validate our simulation results and for the coating of RF devices.

The methodology developed for the production of REBCO coatings consists of soldering REBCO coated conductors (CC) onto a given surface and subsequently delaminating them, so that the REBCO layer is exposed to the cavity. This method is particularly interesting for applications with high-frequency excitations, which require a low surface impedance surface to be exposed inside the cavity. For the case of the FCC-hh or other applications in which the trapped field in the superconducting layer is relevant, we have investigated the striation of the REBCO layer, resulting in a hybrid coating consisting of alternated segments made of REBCO and a normal conductor, usually copper.

Once a coating is complete, it is important to be able to evaluate its electromagnetic performance. To that end, we have used the combined tools from scanning electron microscopy (SEM), energy dispersive spectroscopy (EDX) and scanning hall probe microscopy (SHPM) to correlate the critical current density (J_c) distribution in the coating with the different layers where the delamination happened. With the data from SEM and EDX, we are able to identify the delamination interface for different providers, while SHPM provides the J_c distribution in the coating. By merging these, we have observed that whenever the delamination interface happens inside the REBCO layer, by causing the removal of a significant portion of the REBCO from the coating, J_c vanishes locally, effectively destroying superconductivity locally in that region. However, if the delamination interface occurs between buffer layers or between a buffer layer and the REBCO layer, there is essentially no damage. With this in mind, the coating techniques proposed in this work are optimized to decrease REBCO excavation as much as possible, and thus ensure minimum damage to the superconducting coating's electromagnetic properties.

By combining the aforementioned microscopy tools with optical microscopy, we were able to associate the different delamination interfaces, and especially regions with excavated REBCO, to the colors reflected in the resulting coating. This correlation enabled us to develop a quick method to assess the quality of the coatings after production based on optical obseravtion, providing an estimation of how the coatings will perform without the need of submitting it to the longer and more complicated processes of SEM, EDX and HSPM. Based on this, we were able to achieve an

area ratio of preserved REBCO above 95%, with the vast majority of this damage being confined to the edges of the coating.

The field disturbance generated by the trapped field in the hybrid coating is heavily affected by the size of the REBCO segments and by how they are arranged. We have employed FEM simulations and H-formulation to calculate the magnetic field along a reference radius around the center of the vacuum chamber when submitted to an external dipole field of up to 16 T distorted by the hybrid coating. By varying the geometric parameters, namely the ratio p and number of REBCO segments n, we were able to establish how the hybrid coating geometry impacts the magnetic field geometric harmonics. To accomplish this, the heavily non-linear resistivity of the superconducting material was accounted for by the means of Anderson-Kim's power law, with a J_c and transition index N that vary with the intensity and angle of the magnetic field with respect to the REBCO segments according to experimental data of commercially available coated conductors. This allows us to consider not only the anisotropy of these materials, but also flux-creep effect due to energy dissipation for current values near J_c.

The simulation results showed that the most critical moment in terms of field quality is during injection, when the dipole field reaches 1 T, which occurs several times a day during the operation of the accelerator. By analysing several simulations with distinct geometries, we were able to extrapolate the results and condense the relationship between n, p and the maximum relative field disturbance η_{max} into a single equation. It became clear that, while a high REBCO ratio is necessary to ensure low surface impedance, the field disturbance is significantly decreased by raising the number of REBCO segments. Therefore, a compromise between these two situations was needed. These observations were confirmed by experimental measurements of surface resistance and trapped field of hybrid coating laboratory samples prepared with our coating technique, showing that the hybrid coating could indeed be used as a means to decrease surface impedance while simultaneously achieving high field quality.

We have demonstrated that a broad range of coating geometries attends these criteria, but the width of their REBCO segments would have to be of only a few micrometers in order to achieve the high number of segments required. Although possible, this would make the production process of the coating more complex, time-consuming and expensive. In an attempt to find a better solution, we considered the possibility of using the dipole magnets themselves to compensate the main component of the field harmonics produced by the hybrid coating, namely the dipole component, by applying a dipole field slightly larger than nominal. By doing this we were able to relax the field quality criterion and propose a geometry that would fulfill it with only four segments per quadrant, and using commercially available widths of 2 and 4 mm.

In this same simulation setup, we had the opportunity to also verify how the current distribution in the REBCO segments is affected by the alternated magnetic field generated by the particle beam. We saw that a possibly beneficial effect arises when the dipole field rises above certain values, but for the FCC it was only meaningful above 11 T. Since this does not change the results during injection, it remains being the critical moment and the n and p requirements are unaffected. However, it is interesting that such an effect may have positive consequences during regular operation of the machine, at top energy.

While a geometry had been proposed for the dipole sections of the beam screen, the behaviour of the hybrid coating under other magnetic field configurations is still of great interest. Our numerical model was adapted to be able to account for a quadrupole magnetic field, as well as misalignment of the beam screen with respect to the superconducting magnets. This showed that our proposed geometry might not be suited for the quadrupole sections, since the field harmonics produced by the coating were much higher in this case. Furthermore, the coating under quadrupole field is much more affected by a misalignment in the beam screen than when under a dipole field, which must be taken into account when the quadrupole geometry is defined. However, it is noteworthy that alike its dipole counterpart,

the field harmonics under an external quadrupole field can be decreased by employing an increased number of narrower segments, meaning that the same methods originally proposed for the dipole can be used for the quadrupole as well.

Exploring other field configurations, we analyzed how the field harmonics decrease over time during injection due to creep, implying that any delay in injection would further increase field quality. In addition, considering a non-ideal dipole field revealed that in some situations the combined contributions from the magnet and the coating can partialy cancel each other, leading to a lower harmonic contribution overall. Finally, we studied the hysteresis effects that can occur while ramping the magnetic field down and up and we observed that it can lead to spikes in some harmonics. We demonstrated that this effect, however, can be mitigated by reaching a decreasing the magnetic field below 1 T, to ensure that, when reaching the injection field, the harmonics are again within the acceptable levels.

Beyond the magnetic field quality simulations of the coated beam screen, it is also of relevance to explore its thermomechanical behaviour both during regular operation and in the event of a magnet quench. In the former case, the heat and force loads come not only from the dipole-induced currents in the coating, but also from those induced by the particle beam. These currents were calculated by considering all materials in the beam screen as perfect conductors and by driving a constant current through the very center of the vacuum chamber, whose value is the average beam current, 0.5 A. Thus, the image sheet current densities in the beam screen were obtained. They can then be used to calculate the heat and force loads in the coating. To do this, we have adapted the resistive wall heating formula to consider the irregular geometry of the beam screen and extrapolated the experimentally measured surface resistance of REBCO samples to match the conditions of the FCC.

Once the contributions coming from the beam and from the dipole field were calculated, they could be used as inputs for our thermomechanical simulations, through which the temperature and mechanical stress distribution were determined. The results coming from this analysis show negligible increase in both temperature and stress during the regular operation of the beam screen, reinforcing that the thermomechanical integrity of the structure and its coating is not hindered by the adoption of superconductors.

When it comes to a dipole magnet quench, the high rate of change of the magnetic field generates elevated electric fields and currents, resulting in high thermal and force loads. Due to the expected increase in temperature and stress, it becomes necessary to consider the dependence of J_c with these two variables. The bilateral coupling to do so, on the other hand, requires a much larger computational effort. To bypass this, we adapted the numerical model to calculate an approximation of the dipole-induced current distribution in the coated beam screen, assuming that there is no field distortion in the surrounding region of the coating. The results obtained from these simulations showed a much larger effect in both thermal and mechanical aspects when compared to the beam screen during regular operation. The temperature increases from 50 to 80 K, and the mechanical stresses reach several hundreds of MPa. It is particularly interesting, though, that although this situation is much more strenuous on the coated beam screen, neither the temperature nor the stresses are high enough to inflict any expected damage to the REBCO segments, since not only the maximum mechanical stress is below the irreversibility level, but the maximum temperature does not even surpass the critical temperature T_c. As a matter of fact, it becomes clear that, due to the inductive nature of the currents flowing through the REBCO, it is highly unlikely that any temperature shift coming from these currents exceed T_c. In addition, the forces calculated from the simulations were compared to the results of pull-off adhesion tests, which showed that the coating is capable of enduring the forces induced during a magnet quench.

As regards to the numerical analysis of high temperature superconductors (HTS), it is a common practice to consider each HTS domain to be electronically insulated from the others, confining the electric current to flow in a closed path inside of it. This is a reasonable premise, in particular when the oxide buffer layers of the CC act as insulators between

the different REBCO layers of, for instance, stacked coated conductors. However, in the case of our hybrid coating, this might not be the case due to the absence of insulating layers between the REBCO segments and the metallic structure of the beam screen, and the length of superconducting segments employed in the application. We used analytic calculations and FEM numerical analysis to confirm that the extreme aspect ratio of the beam screen and its coating leads to transverse current flow between REBCO segments through the commonly connected copper layer, which will likely cause an imbalance of current inside each HTS domain and, consequently, have an negative impact in the field harmonics generated inside the vacuum chamber. This effect is controlled by several aspects, such as the resistivity and thickness of the copper layer, the critical current of the REBCO, the rate of change of the magnetic field during ramping and, especially, the length of the beam screen section.

Although the extrapolation of our simulation results led to an estimated full coupling between the REBCO segments, it is also clear that the contact resistance between the copper and the HTS can be used as a tool to mitigate this effect, if it proves to be an issue. By itself, a significant increase in contact resistance by means of an added intermediate layer such as Pyrolytic Graphite Sheet (PGS) could be enough to decrease transverse current flow all by itself . Otherwise, it could be used in combination with other solutions such as shortening the beam screen sections or striating the copper layer of the beam screen to accomplish this feat. In any case, we also established that this current imbalance only occurs while the magnetic field is being ramped, and that the transverse current flow quickly vanishes when reaching a constant dipole field. This implies that the field harmonics are restored to reasonable values both during injection and top energy.

Finally, our coating technique was employed for the production of a REBCO-coated beam screen prototype consisting of a simplified hexagonal geometry to be used for several experiments including surface resistance measurements and vacuum compatibility tests planned for the near future. In addition, RF resonating cavities for axion dark matter search in the Relic Axion Dark-Matter Exploratory Setup (RADES) experiment were coated with REBCO using our methodology, showing improvements with respect to pure copper at fields of up to 11 T. The measurements performed with one of these REBCO-coated cavities contributed to the delimitation of possible mass range of the axion particle. We have also prepared a coated disc sample for surface resistance measurements in a collaboration with the Stanford Linear Accelerator Center (SLAC) National Accelerator Laboratory to evaluate whether the coating is suitable for high-gradient accelerating cavities. Results at high RF powers show that it also outperforming copper both at 4 and 80 K.

In summary, the results obtained throughout this thesis reinforced the suitability of the hybrid Cu-HTS coating as a solution for low surface impedance and high field quality for high energy circular particle accelerators' beam screens. Electromagnetically, these two requirements can be achieved simultaneously by having a large REBCO ratio and a large enough number of segments, respectively, although the latter can be significantly reduced by considering a compensation of the dipole field harmonc by the main dipole magnets. Thermomechanically, the coating integrity is preserved both during regular operation and in the event of a magnet quench, likely the most extreme scenario to which the device may be exposed. Although some concern is warranted due to possible transverse current flow and its impact on field quality, it is also clear that there are many solutions that can be employed without hindering the other benefits brought by the hybrid coating. All in all, the hybrid REBCO-Cu coating sets itself as a promising candidate for the FCC beam screen, and we expect that future measurements with the beam screen prototypes will offer further evidence in this regard.

Appendix A

Simulation Details

The numerical analysis discussed throughout this thesis was performed via COMSOL Multiphysics® simulations with several different geometries, physics and magnetic field configurations. In this appendix, we will list the most important aspects of each simulation file, which can be accessed in [140].

A.1 Parametric Study and other Dipole Simulations

The simulations used to evaluate the impact of the parameters p and n in the field quality are identical in terms of physics and material properties, but consist of different coating geometries defined by the parameters under study. COMSOL LiveLink™ for MATLAB® was used to allow for a more versatile construction of the different hybrid coating geometries under analysis [100, 141]. Most of the simulation files created throughout this work were slightly adapted from or at least partially based on the files generated in this procedure.

The following is a version of the code written in MATLAB to generate, run and extract results from the COMSOL simulations developed for the parametric study of n and p. The material properties of the HTS domains are based on data from [63]. An earlier version of this code was also used to generate the results published at [142], and slightly modified versions of the generated COMSOL files were used to generate the simulation of proposed geometry for the dipole sections of the beam screen as well as to compare with the HSPM results.

```
% FCC_BS_Hybrid_Coating - COMSOL numerical analysis of the hyrbid REBCO-Cu
% coating for the FCC beam screen: geometry parameter evaluation
%
% Inputs:
%    pt - Ratio of flat walls with CC
%    N  - Number of CC per quadrant
%
% Outputs:
%    Several variables, plots and files from the COMSOL results
%
% Other m-files required: none
% Subfunctions: none
% MAT-files required: none
%
% Author: Guilherme Theophilo Telles
```

```
% Institut de Ciencia de Materials de Barcelona (ICMAB - CSIC)
% email: gtelles@icmab.es
% April 2022; Last revision: 25-July-2023

%% MODEL

model = ModelUtil.create('Model');

%% LAUNCH COMSOL

mphlaunch(model,500);
%ModelUtil.showProgress(true);


%% SIMULATION PARAMETERS

pt = 0.95;                  % Ratio of flat walls with CC
N = 2;                      % Number of CC per quadrant
                            % (must be even and larger than 2)
k = 7;                      % Coated Conductor Homogenization Factor
Nmt1 = 8;                   % Horizonal mesh divisions for top wall
Nmt2 = 1;                   % Vertical mesh divisions for top wall
nsct = round(N/2);          % Number of CC on top wall
nscd = round(N/2-0.25);     % Number of CC on diagonal wall
pd = pt;                    % Ratio of flat diagonal area with CC
Nmd1 = Nmt1;                % 'Horizonal' mesh divisions for top wall
Nmd2 = Nmt2;                % 'Vertical' mesh divisions for top wall

mu0 = pi*4e-7;              % Vacuum permeability

%Beam Screen parameters (SI units)

hcu = 0.322e-3;             % Copper thickness
hsc = 1.35e-6;              % REBCO thickness
hbs = 12.520e-3;            % Top wall height
wbs = 14.113e-3;            % Diagonal wall edge horizontal distance
er = 3.2e-3;                % Beam screen corner radius
hg = 3.8551e-3;             % Beam screen gap height
theta = 69.5;               % Diagonal wall tilting angle (in degrees
thetarad = theta*pi/180;    % ... and in radians)
r0 = 9e-3;                  % Reference radius for field quality

% REBCO Properties

int_fields = [0 0.010 0.015 ...
```

```
    0.02 0.03 0.05 0.07 0.1 ...
    0.15 0.20 0.3 0.5 0.7 1 ...
    1.5 2 3 5 7 8 16];          % Magnetic field (T)

int1_N = [22.91 23.01 22.89 ...
    22.86 23.27 22.44 21.58 ...
    20.50 19.49 19.31 19.26 ...
    18.93 19.60 19.89 19.48 ...
    19.22 18.30 16.51 14.29 ...
    13.95 13.95];               % Power law's N index (top wall)

int2_N = [23.3 23.28 23.040 ...
    22.96 23.15 21.78 21.30 ...
    19.30 17.86 16.25 15.27 ...
    13.61 13.05 12.78 12.73 ...
    13.11 13.33 14.55 14.48 ...
    14.04 14.04];               % Power law's N index (diagonal wall)

% int3_Jc = 1e2/hsc*[1606.560 ...
%     1603.61 1599.21 1594.88 ...
%     1585.79 1550.61 1510.73 ...
%     1450.31 1360.91 1290.46 ...
%     1186.19 1050.73 968.870 ...
%     873.710 751.910 660.490 ...
%     528.53 362.2 253 214.27];   % Critical current density (top wall)

% int4_Jc = 1e2/hsc*[1609.160 ...
%     1607.14 1603.41 1599.91 ...
%     1592.56 1564.94 1536.41 ...
%     1474.70 1378.42 1279.49 ...
%     1120.94 894.990 758.260 ...
%     627.430 500.290 425.130 ...
%     336.71 252.98 205.59 187.33]; % Critical current density (top wall)

% Jc values are fitted into a curve.
% The data used (above) could be used in an interpolation function instead.

%Effective widths
wtop = wbs - (hbs-hg)/tan(thetarad) - er*(1-cos(thetarad))/sin(thetarad);
wdia = (hbs-hg-er*(1-cos(thetarad)))/sin(thetarad);

%Superconductor width
wsct = 2*wtop*(pt/N)
wscd = wdia*(pd/nscd)

```

```
%Reset component and study
if exist('comp1','var') == 1
    model.component.remove('comp1');
    clear comp1
end
if exist('std1','var') == 1
    model.study.remove('std1');
    clear std1
end

%COMPONENT
comp1 = model.component.create('comp1',true);
geom1 = comp1.geom.create('geom1', 2);
phys1 = comp1.physics.create('g', 'GeneralFormPDE', {'Hx' 'Hy'});
mesh1 = comp1.mesh().create("mesh1");

%PHYSICS
phys1.field('dimensionless').field('H');
phys1.prop('ShapeProperty').set('shapeFunctionType', 'shcurl');
phys1.feature('gfeq1').setIndex('Ga', {'0' '-uy'}, 0);
phys1.feature('gfeq1').setIndex('Ga', {'0' 'E'}, 0);
phys1.feature('gfeq1').setIndex('Ga', {'-E' '-H2y'}, 1);
phys1.feature('gfeq1').setIndex('Ga', {'-E' '0'}, 1);
phys1.feature('gfeq1').setIndex('f', 0, 0);
phys1.feature('gfeq1').setIndex('f', 0, 1);
phys1.feature('gfeq1').setIndex('da', 'mu0', 0);
phys1.feature('gfeq1').setIndex('da', 'mu0', 3);

%DEFINITIONS

% Interpolation for N and Jc Field Dependency

int1 = model.component("comp1").func().create("int1", "Interpolation");
int2 = model.component("comp1").func().create("int2", "Interpolation");
%int3 = model.component("comp1").func().create("int3", "Interpolation");
%int4 = model.component("comp1").func().create("int4", "Interpolation");

for i = 1:length(int1_N)
    int1.setIndex('table', int_fields(i), i-1, 0);
    int1.setIndex('table', int1_N(i), i-1, 1);
    int2.setIndex('table', int_fields(i), i-1, 0);
    int2.setIndex('table', int2_N(i), i-1, 1);
    %int3.setIndex('table', int_fields(i), i-1, 0);
    %int3.setIndex('table', int3_Jc(i), i-1, 1);
    %int4.setIndex('table', int_fields(i), i-1, 0);
```

```
    %int4.setIndex('table', int4_Jc(i), i-1, 1);
end
int1.set('extrap', 'linear');
int2.set('extrap', 'linear');
%int3.set('extrap', 'linear');
%int4.set('extrap', 'linear');

%Waveform for External Dipole Field
wv1 = model.component('comp1').func.create('wv1', 'Wave');
wv1.set('type', 'triangle');
wv1.set('smoothactive', false);
wv1.set('freq', 'pi/2/(20*60)');

% Global Variables
var1 = comp1.variable.create('var1');
var1.label('Global');
var1.set('r0', num2str(r0));
var1.set('mu0', num2str(mu0));
var1.set('k', num2str(k));
var1.set('Hmax', '16/mu0');
var1.set('Happ', 'Hmax*wv1(t[1/s])');
var1.set('J', 'Hyx-Hxy');
var1.set('H', 'sqrt((Hx+eps)^2+(Hy+eps)^2)');

% Top wall superconductor variables
var2 = comp1.variable.create('var2');
var2.label('Superconductor');
var2.set('rhosc', '(1e-4/Jc)*(abs(J/Jc))^(N-1)');
var2.set('N', 'int1(mu0*Happ)');
%var2.set('Jc', 'int3(mu0*H)/k');
var2.set('Jc','12.15e10/k*(1+mu0*H/0.2011)^(-0.3058)*(1-mu0*H/22.16)^2');
var2.set('E', 'rhosc*J');
var2.set('mur', '1');
var2.selection.geom('geom1', 2);

% Vacuum variables
var3 = comp1.variable.create('var3');
var3.label('Air');
var3.set('rhoair', '1');
var3.set('E', 'rhoair*J');
var3.set('mur', '1');
var3.selection.geom('geom1', 2);

% Diagonal wall superconductor variables
var4 = comp1.variable.create('var4');
```

```
var4.label('SuperconductorTilted');
var4.set('rhosc', '(1e-4/Jc)*(abs(J/Jc))^(N-1)');
var4.set('N', 'int2(mu0*Happ)');
%var4.set('Jc', 'int4(mu0*H)/k');
var4.set('Jc','12.34e10/k*(1+mu0*H/0.4881)^(-0.8264)*(1-mu0*H/1.361e9)^2');
var4.set('E', 'rhosc*J');
var4.set('mur', '1');
var4.selection.geom('geom1', 2);

%GEOMETRY

%Vacuum Square
sq1 = geom1.feature.create('sq1','Square');
sq1.set('size',20e-3);
sq1.set('base','corner');

%Copper gaps on top and diagonal
if nsct > 1
    gtop = max(0,2*wtop*(1-pt)/(N-1));
else
    gtop = 0;
end
if nscd > 1
    gdia = max(0,wdia*(1-pd)/(nscd-1));
else
    gdia = 0;
end

%Top HTS rectangles
if nsct > 0
    if mod(N,2)
        r(1) = geom1.feature.create('r1','Rectangle');
        r(1).set('size',[wsct/2 k*hsc]);
        r(1).set('pos',[0 hbs-hsc/2-hcu]);
    end

    for i = (1+mod(N,2)):(N-nsct+mod(N,2))
        name = strcat('r',num2str(i));
        r(i) = geom1.feature.create(name,'Rectangle');
        r(i).set('base','center');
        r(i).set('size',[wsct k*hsc]);
        r(i).set('pos',...
            [-wtop+wsct/2+(i+nsct-1-mod(N,2))*(gtop+wsct) hbs-hsc/2-hcu]);
    end
end
```

```
241
242 %Diagonal HTS rectangles
243 if nscd > 0
244
245     for i = (nsct+1):(nsct+nscd)
246         pause(0.1)
247         name = strcat('r',num2str(i));
248         r(i) = geom1.feature.create(name, 'Rectangle');
249         r(i).set('base','center');
250         r(i).set('size',[wscd, k*hsc]);
251         r(i).set('pos',[wtop+wscd/2+(wscd+gdia)*((i-nsct)-1) ...
252             hbs-hsc/2-hcu]);
253         rotlist{i-nsct} = name;
254     end
255
256     rot1 = geom1.feature.create('rot1', 'Rotate');
257     rot1.set('pos',[wtop hbs-er]);
258     rot1.set('rot',-theta);
259     rot1.selection('input').add(rotlist);
260     clear rotlist
261 end
262
263 %Builds the geometry
264 geom1.run;
265 pause(1)
266 %mphplot(model);
267
268
269 %BOUNDARIES, CONSTRAINTS & DOMAINS
270
271 %Boundaries
272 Nbou = geom1.getNBoundaries;
273 dir1 = phys1.create('dir1', 'DirichletBoundary', 1);
274 dir1.setIndex('useDirichletCondition', 1, 1);
275 dir1.setIndex('r', 'Happ', 1);
276 dir1.selection.set([3+4*mod(N,2) Nbou]);
277 dir2 = phys1.create('dir2', 'DirichletBoundary', 1);
278 dir2.setIndex('useDirichletCondition', 0, 1);
279 dir2.selection.set([1 2]);
280
281 % Constraints
282 Ndom = geom1.getNDomains;
283 for i = 1:(Ndom-1-mod(N,2))
284     pause(0.1)
285     name = strcat('intop',num2str(i));
```

```
    intop(i) = comp1.cpl().create(name, 'Integration');
    intop(i).selection.set(i+1+mod(N,2));
    nome = strcat('constr',num2str(i));
    constr(i) = phys1.create(nome, 'PointwiseConstraint', 2);
    constr(i).selection.set(i+1+mod(N,2));
    constr(i).set('constraintExpression', strcat(name,'(J)'));
end

% Superconductor and Vacuum Domains
var2.selection.set([2:round(1+(Ndom-1)/2)]);
var3.selection.set([1]);
var4.selection.set([round((Ndom-1)/2)+2:Ndom]);

% MESH
map1 = mesh1.create("map1", "Map");
map1.selection.set([2:Ndom]);

% Diagonal wall mesh
dis1 = map1.create('dis1', 'Distribution');
dis1.selection.set([Nbou-2-(nscd-1)*4:4:Nbou-2]);
dis1.selection.add([Nbou-3-(nscd-1)*4:4:Nbou-3]);
dis1.set('numelem', Nmd1);
dis2 = map1.create('dis2', 'Distribution');
dis2.selection.set([Nbou-4-(nscd-1)*4:4:Nbou-4]);
dis2.selection.add([Nbou-1-(nscd-1)*4:4:Nbou-1]);
dis2.set('numelem', Nmd2);

% Top wall mesh
dis3 = map1.create('dis3', 'Distribution');
dis3.selection.set([Nbou-2-(nscd+nsct-1-mod(N,2))*4:4:Nbou-2-nscd*4]);
dis3.selection.add([Nbou-3-(nscd+nsct-1-mod(N,2))*4:4:Nbou-3-nscd*4]);
dis3.set('numelem', Nmt1);
dis4 = map1.create('dis4', 'Distribution');
dis4.selection.set([Nbou-4-(nscd+nsct-1-mod(N,2))*4:4:Nbou-4-nscd*4]);
dis4.selection.add([Nbou-1-(nscd+nsct-1-mod(N,2))*4:4:Nbou-1-nscd*4]);
dis4.set('numelem', Nmt2);

% Top-Center Mesh

if mod(N,2)
    dis5 = map1.create('dis5', 'Distribution');
    dis5.selection.set([4 6]);
    dis5.set('numelem', round(Nmt1/2));
    dis6 = map1.create('dis6', 'Distribution');
    dis6.selection.set([3 8]);
```

```
    dis6.set('numelem', Nmt2);
end

% Vacuum Mesh
ftri1 = mesh1.create('ftri1', 'FreeTri');

% Build Mesh
mesh1.run;

%% STUDY

std1 = model.study.create('std1');
time = std1.create("time", "Transient");
time.activate('g', true);
time.set('tlist', '(20*60/8)*range(0,0.05,1)');

%% Run Simulation

std1.run

%% Results Extraction

% Reference Circle for Field Quality
pc1 = model.result.dataset.create('pc1', 'ParCurve2D');
pc1.set('exprx', 'r0*cos(s)');
pc1.set('parmax1', 'pi/2');
pc1.set('expry', 'r0*sin(s)');
model.result('pg1').run;

tr = mphinterp(model,{'t'},'dataset','pc1');
Hxr = mphinterp(model,{'Hx'},'dataset','pc1');
Hyr = mphinterp(model,{'Hy'},'dataset','pc1');
Happr = mphinterp(model,{'Happ'},'dataset','pc1');
sr = mphinterp(model,{'s'},'dataset','pc1');

%% Save model

rootpath = ...
    'G:\Meu Drive\ICMAB Guilherme\MATLAB COMSOL\Geometries\Auto Sims\';
savename = sprintf('SPRP_%03d_%03d_%03d_%03d_%03d',k,N,100*pt,Nmt1,Nmt2);
savepath = [rootpath,savename,'\']

if ~exist(savepath, 'dir')
   mkdir(savepath)
end
```

```
376
377 model.save([savepath,savename,'.mph']);
378
379 %% Multipole Expansion
380
381 Bappr = transpose(mu0*Happr);
382 Bxr = transpose(mu0*Hxr);
383 Byr = transpose(mu0*Hyr);
384 phir = transpose(sr);
385
386 Bex = Bappr(1,:);
387
388 Bmr = sqrt(Bxr.^2+(Byr-Bappr).^2)./Bappr;
389 Brmax = max(Bmr);
390
391
392 Brr = (Bxr.*cos(phir)+(Byr-Bappr).*sin(phir))./Bappr;
393
394 phir = [phir;pi-flip(phir(1:end-1,:))];
395 Brr = [Brr;flip(Brr(1:end-1,:))];
396 phir = [phir;2*pi-flip(phir(1:end-1,:))];
397 Brr = [Brr;-flip(Brr(1:end-1,:))];
398
399 Nf = length(phir);
400
401 H = [1:120];
402 p = fft(Brr);
403 P2 = abs(p/Nf);
404 P1 = P2(1:Nf/2+1,:);
405 P1(2:end-1,:) = 2*P1(2:end-1,:);
406 f = (0:(Nf/2));
407 Pt = transpose(P1);
408
409 figure
410 hold on
411 bar(f,P1)
412 xlim([0 12])
413 xticks([1:2:11])
414 grid on
415 xlabel ('Modes')
416 ylabel('Multipole Coefficients')
417 title(sprintf('Disturbance Multipole Expansion: n = %01d, p = %01d%%', ...
418     N,100*pt))
419
420 figure
```

```
hold on
bar(f,P1(:,find(Bex>=1,1,'first')))
plot([min(f) max(f)],[1e-4 1e-4],'g')
plot([min(f) max(f)],Brmax(find(Bex>=1,1,'first')).*[1 1],'r')
xlim([0 12])
ylim([1e-6 1e-2])
set(gca,'Yscale','log')
xticks([1:2:11])
legend('B_{ex} = 1 T','Field Quality Criterion', ...
    'Maximum Field Disturbance')
grid on
xlabel ('Modes')
ylabel('Multipole Coefficients')
title(sprintf('Disturbance Multipole Expansion: n = %01d, p = %01d%%', ...
    N,100*pt))

%savefig([savepath,savename,'_Multipole1T.fig']);
%saveas(gcf,[savepath,savename,'_Multipole1T.png']);

%% Extract entire data:

data = mpheval(model, ...
    {'t','J','mu0*Happ','mu0*Hx','mu0*(Hy-Happ)','mu0*Hy'});

t = data.d1;
J = data.d2;
B = data.d3;
dBx = data.d4;
dBy = data.d5;
By = data.d6;
x = repmat(data.p(1,:),length(t(:,1)),1);
y = repmat(data.p(2,:),length(t(:,1)),1);
dB = sqrt(dBx.^2+dBy.^2);
r = sqrt(x.^2+y.^2);

tr = t(r<=r0);
dBr = dB(r<=r0)./B(r<=r0);
tr = reshape(tr,length(tr)/sum(B(r<=r0)==1),sum(B(r<=r0)==1));
dBr = reshape(dBr,length(dBr)/sum(B(r<=r0)==1),sum(B(r<=r0)==1));
dBrmax = max(abs(transpose(dBr)));
tex = tr(:,1);

iB=(find(Bex>=1,1,'first'));

model.result('pg1').feature('surf1').set('expr', ...
```

```
    'sqrt(Hx^2+(Hy-Happ)^2)/Happ');
model.result('pg1').setIndex('looplevel', iB, 0);
model.result('pg1').run;

solplot = mphplot(model,'pg1','rangenum',1);
title('|B_{ext}| = 1 T');
xlabel('x (m)')
ylabel('y (m)')

savefig([savepath,savename,'_dB1T.fig']);
saveas(gcf,[savepath,savename,'_dB1T.png']);

save([savepath,savename]);

Time = tex;
MaxField = transpose(Brmax);
ExtField = transpose(Bex);
MpCoeff = transpose(P1(1:11,:));

FieldQuality = [Time,ExtField,MaxField,MpCoeff];

save([savepath,savename]);
save([savepath,savename,'_FieldQuality.txt'], 'FieldQuality', '-ASCII');
save([savepath,savename,'_FieldQuality.mat'], 'FieldQuality');
```

A.2 Simulation of AC Field Demagnetization

The effect of a perpendicular AC field in the dipole-induced current distribution in HTS segments was studied by considering a second component to the resistivity of the HTS domains, derived from Equations 2.37 and 2.47:

$$\rho_{sc} = \rho_{sc1} + \rho_{sc2} \tag{A.1}$$

$$\rho_{sc1} = \frac{E_c}{J_c}\left|\frac{J}{J_c}\right|^{N-1} \tag{A.2}$$

$$\rho_{sc2} = 2\mu_0 f d^2 \Delta h \tag{A.3}$$

$$\Delta h = \begin{cases} \frac{H_x - H_p}{dJ_c}, & (H_x > H_p) \wedge (t > t_{inj}) \\ 0, & (H_x \leq H_p) \vee (t \leq t_{inj}) \end{cases} \tag{A.4}$$

$$H_p = \frac{1}{2}(dJ_c - |J_s|), \tag{A.5}$$

where $t_{inj} = 75\,\mathrm{s}$ stands for the starting moment of injection, when a dipole field of 1 T is reached, and the conditions defining Δh are enforced by multiplying $\frac{H_x - H_p}{dJ_c}$ by a step function of time centered at $t = 75\,\mathrm{s}$ and a ramp function of $H_x - H_p$ centered around zero.

A.3 Quadrupole and Other Field Configurations

In Chapter 5, most of the simulations discussed require a magnetic field angle with respect to the HTS segments that is different than those originally considered in the dipole field simulations. This is included by the means of two variations to the model:

1. A new coordinate system is added so that the external magnetic field and the beam screen can be centered around two distinct points in space;
2. The boundary conditions of the vacuum chamber must allow for magnetic fields with any number of poles $2n_p$ and tilted by an angle ψ; and
3. The REBCO electromagnetic properties must reflect the effect of multiple simultaneous field angles $\Delta\theta$.

The first modification is achieved by creating two cylindrical coordinate systems around which the magnetic field and the beam screen are centered, respectively named *sys2* and *sys3*. Any displacement of the beam screen (and of *sys3*) with respect to the origin of *sys2* is included by changing the origin of *sys3* and moving the beam screen accordingly. The position of the HTS segments is calculated with respect to *sys3* while calculations with the magnetic field use *sys2* as the reference.

The vacuum chamber remains aligned with *sys2*. The external magnetic field imposed at its boundaries is therefore given by Equations 5.9 and 5.10, rewritten here for convenience, where ϕ is the angle with respect to *sys2*:

$$H_{x,b} = H_{apt}\sin(\phi(n_p-1)+n_p\psi)$$
$$H_{y,b} = H_{apt}\cos(\phi(n_p-1)+n_p\psi)\,.$$

To preserve symmetry in ideal multipole fields and account for the fact that COMSOL uses angles in the interval $[-\pi,\pi]$ instead of $[0,2\pi]$, we calculate the angle between the magnetic field and the HTS segments by adapting Equation 5.8:

$$\theta = \text{remainder}\left[\frac{\pi}{2}-\phi_2(n_p-1)-n_p\psi,\,\pi\right]-\theta_{HTS}\,, \tag{A.6}$$

where ϕ_2 stands for the angular position in *sys2*. The angles of the HTS segments θ_{HTS} are stored in a piecewise function that correlates them with their angular position in *sys3*, shown in Figure A.1. Similarly, θ_{HTS} is given by

$$\theta_{HTS} = \text{pw1}(\text{remainder}[\phi_3+2\pi,\pi])\,. \tag{A.7}$$

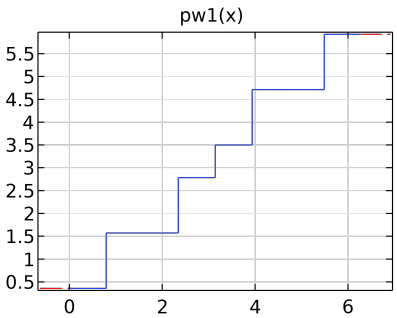


FIGURE A.1: Piecewise function *pw1* that correlates the angles of the HTS segments (y-axis) with their angular position in *sys3* (x-axis).

A.4 Thermomechanical Simulations

The thermomechanical simulations are comprised of two components, each with its own geometry, material properties and physics. The first component, *comp1*, is very similar to those presented in the previous sections of this appendix, whose purpose is to calculate the effects induced in the beam screen by the magnetic field produced by the superconducting magnets. Its geometry considers only the HTS segments and vacuum surrounding it, neglecting any currents induced in the other materials of the beam screen. The second component, *comp2*, on the other hand, considers not only the HTS segments, but also the metallic structure of the beam screen and the different layers of the delaminated coated conductors themselves, which will be relevant when computing the temperature and stress distribution across the beam screen and its coating.

The distributions of current density, electric field and magnetic field calculated via *comp1* are then used as inputs for *comp2*, which contains the physics for the computation of the thermomechanical behaviour as well as the effects induced by the beam. Communication between the two components is attained by the means of linear extrusion functions, which correlate the variables in the HTS domains of *comp1* to the HTS domains in *comp2*. It is worth noting that while an homogenizing factor k is used in the HTS segments of *comp1* to facilitate computation, it is not necessary for *comp2*, leading to different thicknesses. The current density values must therefore be corrected by the same factor k when moving between components.

The simulation of the beam effects has as a goal the determination of the image current distribution along the inner surface of the beam screen. It was originally designed as a magnetic field simulation, with a current imposed at the very center of the vacuum chamber corresponding to the average beam current. By considering all the beam screen materials to be perfect conductors, we could then obtain an approximated average of the surface current density distribution. Nevertheless, during development we noticed that the same results could be achieved with a much shorter computation time by considering an analogous electrostatic situation instead.

To explore this analogy, let us consider the two scenarios in question:

1. The beam current induces a magnetic field distribution in the vacuum chamber, which in turn induces surface currents in the beam screen; and
2. A static charge density replaces the beam current, inducing an electric field in the vacuum chamber, which in turn induces surface charges in the beam screen.

The first step to prove the analogy is to consider a shift in the reference frame. If we consider the first scenario but change the reference frame to be that of the moving particles, they will generate only an electric field, since they are now static, resulting in the second scenario. This can be further corroborated by considering the Lorentz transformations of the electric and magnetic fields [143]:

$$\boldsymbol{E}'_{\parallel} = \boldsymbol{E}_{\parallel} \tag{A.8}$$

$$\boldsymbol{B}'_{\parallel} = \boldsymbol{B}_{\parallel} \tag{A.9}$$

$$\boldsymbol{E}'_{\perp} = \gamma(\boldsymbol{E}_{\perp} + \boldsymbol{v} \times \boldsymbol{B}) \tag{A.10}$$

$$\boldsymbol{B}'_{\perp} = \gamma\left(\boldsymbol{B}_{\perp} + \frac{1}{c^2}\boldsymbol{v} \times \boldsymbol{E}\right), \tag{A.11}$$

where $\gamma = [1-(v/c)^2]^{-0.5}$ and the indices $\parallel$ and $\perp$ refer to components parallel and perpendicular to the relative velocity between the reference frames. If we consider the primed variables to be those of scenario 1 and the unprimed to be those of scenario 2, all the fields parallel to the movement vanish and we can use Equation A.11 to obtain the

relationship between the magnetic field in the reference frame 1 with the electric field in reference frame 2:

$$\boldsymbol{B}_1 = \frac{\gamma}{c^2}\boldsymbol{v} \times \boldsymbol{E}_2 \,. \tag{A.12}$$

Using the constitutive relations $\boldsymbol{D} = \varepsilon_0 \boldsymbol{E}$, $\boldsymbol{B} = \mu_0 \boldsymbol{H}$, and $\varepsilon_0 \mu_0 = c^{-2}$, we get

$$\boldsymbol{H}_1 = \gamma \boldsymbol{v} \times \boldsymbol{D}_2 \,, \tag{A.13}$$

and finally, by considering that all materials are perfect conductors, the magnetic intensity $\boldsymbol{H}$ and the electric displacement D have their magnitudes equal to the sheet current density J_s and the electric charge surface density ρ_s, respectively, at the material boundaries. Since all fields are perpendicular to $\boldsymbol{v}$, this results in

$$J_{s,1} = \gamma v \rho_{s,2} \,, \tag{A.14}$$

confirming that these two distributions are analogous. This means that a linear charge density of $1\,\mathrm{C/m}$ will induce a surface charge density that is numerically equal to the sheet current density induced by a 1 A current. After comparing simulations of both scnearios and obtaining numerically identical results, we have decided to employ the electrostatic analogy to decrease simulation time, by the means of COMSOL's Electrostatics Interface [144]. The magnitude of $\boldsymbol{D}$ at the beam screen boundaries calculated in such a manner is then converted to its equivalent sheet current density by multiplying it by $1\,\mathrm{m/s}$, and used as input for the heat and force sources of the thermomechanical interfaces.

It is worth noting, though, that all these calculations consider only the average beam current, and therefore neglect dynamic effects which could play a relevant part, especially in the solid mechanics simulations due to beam-induced vibrations in the beam screen structure.

The material properties used for the thermomechanical interfaces in *comp2* are given by Table A.1. All the materials were considered to be in their elastic regimes and the silver layer of the CC was merged with the copper layer due to its very thin thickness.

TABLE A.1: Material properties for the thermomechanical simulations. Values are based on data from [87, 145–148] and COMSOL's standard values.

	Stainless Steel	Copper	Solder Alloy	REBCO
Density ($\mathrm{kg/m^3}$)	7850	8960	9000	6300
Heat Capacity ($\mathrm{J/kg/K}$)	95	100	50	79
Thermal Conductivity ($\mathrm{W/m/K}$)	5.8	1016.69	50	27 (*ab*-plane); 4 (*c*-axis)
Young's Modulus (GPa)	200	110	60	150
Poisson's Ratio	0.3	0.35	0.4	0.2

A.5 Magnet Quench Simulations

The simulations of the coated beam screen under a magnet quench are mostly based on the thermomechanical simulations during normal operation. The main differences consist in the removal of the beam-induced effects and the replacement of the general form PDE physics by an approximated analytic calculation of the electric field and the current induced by the variation of the dipole field in the beam screen.

Firstly, for the purpose of obtaining the electric field, the magnetic field is assumed to be unaffected by the induced currents. From this, we then get E from 7.1. Once the electric field is determined, the current density can then be calculated from the overcritical resistivity of the REBCO, given by Equation 2.6, and from the resistivity of the other materials. The material properties used for this simulation setup are based on [87, 145–148] and COMSOL's standard values. The electric resistivity of the steel and of the solder alloy is given by

$$\rho_{ss} = 480 + 0.8T \quad [\text{n}\Omega\text{m}] \tag{A.15}$$

$$\rho_{solder} = 11.25 + 0.075T \quad [\text{n}\Omega\text{m}]\,, \tag{A.16}$$

and the thermomechanical properties of the solder alloy and of the REBCO segments are considered constant for the relevant temperarture range due to its relatively small thickness. The employed heat capacity, thermal conductivity and electric resistivity of copper and stainless steel are presented in Table A.2.

TABLE A.2: Material properties included as interpolation functions for the magnet quench simulations. Data from [145–147].

Temperature (K)	Heat Capacity (J/kg/K)		Thermal Conductivity (W/m/K)		Electric Resistivity (nΩm)
	Copper	Stainless Steel	Copper	Stainless Steel	Copper
50	100	95	1016.69	5.8	0.668
55			863.41		0.861
60	128	135	749.43	6.8	1.08
65			665.27		1.34
70	167	170	603.13	7.6	1.62
75			557.09		1.93
77	188	195		8.07	
80	197	205	522.79	8.26	2.26
85			497.08		2.60
90	230	230	477.68	8.86	2.96
95			462.95		3.32
100	250	251	451.68	9.4	3.69

To avoid convergence issues due to having N dependent on T, which itself is calculated using N, this feedback loop between the variables is broken by using the *nojac* operator in COMSOL, which excludes a given mathematical expression from the Jacobian solver [149]. This solution is only necessary for N and not for J_c since the former is an exponent and therefore presents higher non-linearity.

A.6 Transverse Current Simulations

As mentioned in Chapter 8, the transverse current simulations employ the Magnetic Field Formulation and the Magnetic Field, No Currents interfaces from COMSOL to calculate the current distribution in electronically coupled HTS segments through a copper slab. These simulations question whether the HTS segments can be considered insulated in long devices, that is, whether the total currents flowing longitudinally through the HTS segments are always zero. The simulations files were adapted from [150, 151].

While the resistivity of the superconductor is still described by the power law, both J_c and N are considered constant for all field values to decrease simulation time. For the same purpose, the HTS segments are homogenized by a large factor k so that the resulting equivalent thickness is similar to that of the copper slab, that is, around $300\,\mu$m. In a similar manner, when non-zero contact resistance is considered, an intermediate layer is added between the REBCO and the copper, with a similar thickness and with a resistivity ρ_c given by

$$\rho_c = \frac{R_c}{d_c}\,, \tag{A.17}$$

where R_c and d_c are the contact resistance and the thickness of the added layer.

The applied dipole field is increased at a constant pace until the HTS has reached full penetration, at which point the induced currents in the structure remain nearly constant and the behaviour discussed in Chapter 8 can be observed.

Bibliography

[1] CERN. *The Standard Model*. 2022. URL: https://home.web.cern.ch/science/physics/standard-model (visited on 01/18/2023).

[2] CERN. *The Large Hadron Collider*. 2022. URL: https://home.cern/science/accelerators/large-hadron-collider (visited on 01/18/2023).

[3] S. Myers. "The large hadron collider 2008–2013". In: *International Journal of Modern Physics A* 28.25 (2013), p. 1330035.

[4] G. Aad et al. "Observation of a new particle in the search for the Standard Model Higgs boson with the ATLAS detector at the LHC". In: *Physics Letters B* 716.1 (2012), pp. 1–29.

[5] L. M. Lederman and D. Teresi. *The God particle: If the universe is the answer, what is the question?* Houghton Mifflin Harcourt, 2006.

[6] *The Nobel Prize in Physics 2013*. 2013. URL: https://www.nobelprize.org/prizes/physics/2013/summary/ (visited on 01/18/2023).

[7] CERN. *Future Circular Collider Study Kickoff Meeting, University of Geneva*. 2014. URL: http://indico.cern.ch/e/fcc-kickoff (visited on 01/18/2023).

[8] FCC collaboration et al. "FCC Physics Opportunities: Future Circular Collider Conceptual Design Report Volume 1". In: *European Physical Journal C* 79.6 (2019), p. 474.

[9] FCC collaboration et al. "FCC-hh: The Hadron Collider: Future Circular Collider Conceptual Design Report Volume 3". In: *European Physical Journal: Special Topics* 228.4 (2019), pp. 755–1107.

[10] I. Bellafont. "Study of the beam induced vacuum effects in the cryogenic beam vacuum chamber of the future Circular Hadron Collider". PhD thesis. Universitat Politècnica de Catalunya, 2020.

[11] S. Calatroni. "HTS coatings for impedance reduction in particle accelerators: case study for the FCC at CERN". In: *IEEE Transactions on Applied Superconductivity* 26.3 (2016), pp. 1–4.

[12] T. Puig et al. "Coated conductor technology for the beamscreen chamber of future high energy circular colliders". In: *Superconductor Science and Technology* 32.9 (2019), p. 094006.

[13] A. Romanov et al. "High frequency response of thick REBCO coated conductors in the framework of the FCC study". In: *Scientific reports* 10.1 (2020), pp. 1–12.

[14] D. Van Delft and P. Kes. "The discovery of superconductivity". In: *Physics Today* 63.9 (2010), pp. 38–43.

[15] K. I. Wysokinski. *Remarks on the first hundred years of superconductivity*. 2011. DOI: 10.48550/ARXIV.1111.5318. URL: https://arxiv.org/abs/1111.5318.

[16] *The Nobel Prize in Physics 1913*. 2022. URL: https://www.nobelprize.org/prizes/physics/1913/summary/ (visited on 01/18/2023).

[17] W. Meissner and R. Ochsenfeld. "Ein neuer effekt bei eintritt der supraleitfähigkeit". In: *Naturwissenschaften* 21.44 (1933), pp. 787–788.

[18] A. M. Forrest. “Meissner and Ochsenfeld revisited”. In: *European Journal of Physics* 4.2 (1983), p. 117.

[19] C. J. Gorter and H. Casimir. “The thermodynamics of the superconducting state”. In: *Z. tech. Phys* 15 (1934), pp. 539–42.

[20] F. London and H. London. “The electromagnetic equations of the supraconductor”. In: *Proceedings of the Royal Society of London. Series A-Mathematical and Physical Sciences* 149.866 (1935), pp. 71–88.

[21] F. London and H. London. “Supraleitung und diamagnetismus”. In: *Physica* 2.1-12 (1935), pp. 341–354.

[22] C. A. Reynolds et al. “Superconductivity of Isotopes of Mercury”. In: *Phys. Rev.* 78 (4 May 1950), pp. 487–487. DOI: 10.1103/PhysRev.78.487. URL: https://link.aps.org/doi/10.1103/PhysRev.78.487.

[23] E. Maxwell. “Isotope Effect in the Superconductivity of Mercury”. In: *Phys. Rev.* 78 (4 May 1950), pp. 477–477. DOI: 10.1103/PhysRev.78.477. URL: https://link.aps.org/doi/10.1103/PhysRev.78.477.

[24] H. Fröhlich. “Theory of the Superconducting State. I. The Ground State at the Absolute Zero of Temperature”. In: *Phys. Rev.* 79 (5 Sept. 1950), pp. 845–856. DOI: 10.1103/PhysRev.79.845. URL: https://link.aps.org/doi/10.1103/PhysRev.79.845.

[25] V. L. Ginzburg and L. D. Landau. “On the theory of superconductivity”. In: *On superconductivity and superfluidity*. Springer, 2009, pp. 113–137.

[26] J. Bardeen and M. J. Stephen. “Theory of the motion of vortices in superconductors”. In: *Physical Review* 140.4A (1965), A1197.

[27] *Nobel Prize in Physics 1972*. 2022. URL: https://www.nobelprize.org/prizes/physics/1972/summary/ (visited on 01/18/2023).

[28] J. G. Bednorz and K. A. Müller. “Possible high T_c superconductivity in the Ba-La-Cu-O system”. In: *Zeitschrift für Physik B Condensed Matter* 64.2 (1986), pp. 189–193.

[29] A. A. Abrikosov. “On the magnetic properties of superconductors of the second group”. In: *Sov. Phys. JETP* 5 (1957), pp. 1174–1182.

[30] J. Banchewski. “Transient Liquid Assisted Growth of YBCO Superconducting Films: Growth Kinetics, Physical Properties and Vortex Pinning”. PhD thesis. Universitat Autònoma de Barcelona, 2020.

[31] U. Essmann and H. Träuble. “The direct observation of individual flux lines in type II superconductors”. In: *Physics letters A* 24.10 (1967), pp. 526–527.

[32] A. M. Campbell and J. E. Evetts. “Flux vortices and transport currents in type II superconductors”. In: *Advances in Physics* 21.90 (1972), pp. 199–428.

[33] D. A. Cardwell and D. S. Ginley. *Handbook of superconducting materials*. Vol. 1. CRC Press, 2003.

[34] A. Berenov et al. “Microstructural characterization of $YBa_2Cu_3O_{7-\delta}$ thick films grown at very high rates and high temperatures by pulsed laser deposition”. In: *Journal of materials research* 18.4 (2003), pp. 956–964.

[35] M. Hawley et al. “Growth mechanism of sputtered films of $YBa_2Cu_3O_7$ studied by scanning tunneling microscopy”. In: *Science* 251.5001 (1991), pp. 1587–1589.

[36] J. L. MacManus-Driscoll et al. “Strongly enhanced current densities in superconducting coated conductors of $YBa_2Cu_3O_{7-x}$+ $BaZrO_3$”. In: *Nature materials* 3.7 (2004), p. 439.

[37] M. K. Wu et al. “Superconductivity at 93 K in a new mixed-phase Y-Ba-Cu-O compound system at ambient pressure”. In: *Phys. Rev. Lett.* 58 (9 Mar. 1987), pp. 908–910. DOI: 10.1103/PhysRevLett.58.908. URL: https://link.aps.org/doi/10.1103/PhysRevLett.58.908.

[38] M. Tinkham. *Introduction to superconductivity*. Courier Corporation, 2004.

[39] T. H. Johansen et al. "Measurements and model calculations of forces betpeen a magnet and granular high-Tc superconductor". In: *Applied Superconductivity* 2.7 (1994), pp. 535–548. ISSN: 0964-1807. DOI: https://doi.org/10.1016/0964-1807(94)90043-4. URL: https://www.sciencedirect.com/science/article/pii/0964180794900434.

[40] J. G. Ossandon et al. "Influence of oxygen deficiency on the superconductive properties of grain-aligned $YBa_2Cu_3O_{7-\delta}$". In: *Phys. Rev. B* 45 (21 June 1992), pp. 12534–12547. DOI: 10.1103/PhysRevB.45.12534. URL: https://link.aps.org/doi/10.1103/PhysRevB.45.12534.

[41] Y. Iijima et al. "In-plane aligned YBa2Cu3O7-x thin films deposited on polycrystalline metallic substrates". In: *Applied Physics Letters* 60 (1992), pp. 769–771.

[42] A. Goyal, M. Parans Paranthaman, and U. Schoop. "The RABiTS Approach: Using Rolling-Assisted Biaxially Textured Substrates for High-Performance YBCO Superconductors". In: *MRS Bulletin* 29.8 (2004), 552–561. DOI: 10.1557/mrs2004.161.

[43] K. Kakimoto et al. "High-speed deposition of high-quality RE123 films by a PLD system with hot-wall heating". In: *Superconductor Science and Technology* 23.1 (Dec. 2009), p. 014016. DOI: 10.1088/0953-2048/23/1/014016. URL: https://dx.doi.org/10.1088/0953-2048/23/1/014016.

[44] V. Selvamanickam et al. "MOCVD-Based YBCO-Coated Conductors". In: *MRS Bulletin* 29.8 (2004), 579–582. DOI: 10.1557/mrs2004.164.

[45] V. Matias et al. "YBCO films grown by reactive co-evaporation on simplified IBAD-MgO coated conductor templates". In: *Superconductor Science and Technology* 23 (Dec. 2009), p. 014018. DOI: 10.1088/0953-2048/23/1/014018.

[46] A. Molodyk et al. "Development and large volume production of extremely high current density $YBa_2Cu_3O_7$ superconducting wires for fusion". In: *Scientific reports* 11.1 (2021), pp. 1–11.

[47] X. Li et al. "The development of second generation HTS wire at American Superconductor". In: *IEEE transactions on applied superconductivity* 19.3 (2009), pp. 3231–3235.

[48] X. Obradors and T. Puig. "Coated conductors for power applications: materials challenges". In: *Superconductor Science and Technology* 27.4 (2014), p. 044003.

[49] A. Romanov. "Superconducting $REBa_2Cu_3O_7$ Coated Conductors for proton beam screens in high field particle accelerators". PhD thesis. Universitat Autònoma de Barcelona, 2022.

[50] P. Krkotić. "Evaluation of the Surface Impedance of ReBCO Coated Conductors and Requirements for Their Use as Beam Screen Materials for the FCC-hh". PhD thesis. Universitat Politècnica de Catalunya, 2022.

[51] P. Krkotić, U. Niedermayer, and O. Boine-Frankenheim. "High-temperature superconductor coating for coupling impedance reduction in the FCC-hh beam screen". In: *Nuclear Instruments and Methods in Physics Research Section A: Accelerators, Spectrometers, Detectors and Associated Equipment* 895 (2018), pp. 56–61.

[52] P. Krkotic et al. "RF Characterisation of HTS-CC Tapes as Alternative Coating for the FCC-hh Beam Screen". FCC week 2019. 2019. URL: https://indico.cern.ch/event/727555/contributions/3461230/.

[53] P. Krkotić et al. "Evaluation of the nonlinear surface resistance of REBCO coated conductors for their use in the FCC-hh beam screen". In: *Superconductor Science and Technology* (2021).

[54] P. Krkotic et al. "RF Characterisation of HTS-CC Tapes as Alternative Coating for the FCC-hh Beam Screen". FCC Week 2019. 2019. URL: https://indi.to/TVwS8.

[55] P. Krkotić et al. *HTS REBaCuO coated conductors for the FCC-hh beam screen: Performance under photon irradiation at the ALBA Synchrotron Light Source*. 2019. URL: https://indico.cern.ch/event/727555/contributions/3430768/attachments/1875329/3088389/POSTER_FCC19-SR_Irradiation_V7.pdf.

[56] C. P. Bean. "Magnetization of hard superconductors". In: *Physical review letters* 8.6 (1962), p. 250.

[57] J. Gutierrez et al. "Strong isotropic flux pinning in solution-derived $YBa_2Cu_3O_{7-x}$ nanocomposite superconductor films". In: *Nature materials* 6.5 (2007), pp. 367–373.

[58] P. W. Anderson. "Theory of Flux Creep in Hard Superconductors". In: *Phys. Rev. Lett.* 9 (7 Oct. 1962), pp. 309–311. DOI: 10.1103/PhysRevLett.9.309. URL: https://link.aps.org/doi/10.1103/PhysRevLett.9.309.

[59] Y. B. Kim, C. F. Hempstead, and A. R. Strnad. "Flux Creep in Hard Superconductors". In: *Phys. Rev.* 131 (6 Sept. 1963), pp. 2486–2495. DOI: 10.1103/PhysRev.131.2486. URL: https://link.aps.org/doi/10.1103/PhysRev.131.2486.

[60] H. T. Coffey. "Modified London Model for Type-II Superconductors". In: *Phys. Rev.* 166 (2 Feb. 1968), pp. 447–456. DOI: 10.1103/PhysRev.166.447. URL: https://link.aps.org/doi/10.1103/PhysRev.166.447.

[61] L. Civale et al. "Scaling of the hysteretic magnetic behavior in $YBa_2Cu_3O_7$ single crystals". In: *Phys. Rev. B* 43 (16 June 1991), pp. 13732–13735. DOI: 10.1103/PhysRevB.43.13732. URL: https://link.aps.org/doi/10.1103/PhysRevB.43.13732.

[62] G. Blatter, V. B. Geshkenbein, and A. I. Larkin. "From isotropic to anisotropic superconductors: A scaling approach". In: *Phys. Rev. Lett.* 68 (6 Feb. 1992), pp. 875–878. DOI: 10.1103/PhysRevLett.68.875. URL: https://link.aps.org/doi/10.1103/PhysRevLett.68.875.

[63] S. Wimbush, N. Strickland, and A. Pantoja. "Critical current characterisation of SuperPower Advanced Pinning 2G HTS superconducting wire". In: (Mar. 2021). DOI: 10.6084/m9.figshare.4256624.v3. URL: https://figshare.com/articles/dataset/Critical_current_characterisation_of_SuperPower_Advanced_Pinning_2G_HTS_superconducting_wire/4256624.

[64] W. Paul et al. "Fault current limiter based on high temperature superconductors – different concepts, test results, simulations, applications". In: *Physica C: Superconductivity* 354.1 (2001), pp. 27–33. ISSN: 0921-4534. DOI: https://doi.org/10.1016/S0921-4534(01)00018-1. URL: https://www.sciencedirect.com/science/article/pii/S0921453401000181.

[65] J. Duron et al. "Modelling the E-J relation of high-Tc superconductors in an arbitrary current range". In: *Physica C Superconductivity* 401 (Jan. 2004). DOI: 10.1016/j.physc.2003.09.044.

[66] N. Riva et al. "A wide range E-J constitutive law for simulating REBCO tapes above their critical current". In: *Superconductor Science and Technology* 34 (Sept. 2021). DOI: 10.1088/1361-6668/ac2883.

[67] S. V. Yuferev and N. Ida. *Surface impedance boundary conditions: a comprehensive approach*. CRC press, 2018.

[68] A. Alimenti. "Advanced microwave resonant measurement techniques for the characterization and study of dielectrics, conductors and superconductors". PhD thesis. University Roma Tre, 2020.

[69] S. Remillard. *Two-Fluid Model Surface Impedance: A Tutorial for Work in the Hope College Microwave Group*. July 2017.

[70] S. Revenaz et al. "Frequency dependence of the surface impedance of $YBa_2Cu_3O_{7-\delta}$ thin films in a dc magnetic field: Investigation of vortex dynamics". In: *Phys. Rev. B* 50 (2 July 1994), pp. 1178–1189. DOI: 10.1103/PhysRevB.50.1178. URL: https://link.aps.org/doi/10.1103/PhysRevB.50.1178.

[71] S. Calatroni and R. Vaglio. "Surface Resistance of Superconductors in the Presence of a DC Magnetic Field: Frequency and Field Intensity Limits". In: *IEEE Transactions on Applied Superconductivity* 27.5 (2017), pp. 1–6. DOI: 10.1109/TASC.2017.2691604.

[72] N. Sakamoto, F. Irie, and K. Yamafuji. "The Flux Flow Voltage in a Type II Superconducting Foil in the Presence of a Superposed Perpendicular AC Field". In: *Journal of the Physical Society of Japan* 41.1 (1976), pp. 32–38. DOI: 10.1143/JPSJ.41.32. URL: https://doi.org/10.1143/JPSJ.41.32.

[73] E. H. Brandt. "Thin superconductors in a perpendicular magnetic ac field: General formulation and strip geometry". In: *Phys. Rev. B* 49 (13 Apr. 1994), pp. 9024–9040. DOI: 10.1103/PhysRevB.49.9024. URL: https://link.aps.org/doi/10.1103/PhysRevB.49.9024.

[74] E. Brandt and G. Mikitik. "Why an ac Magnetic Field Shifts the Irreversibility Line in Type-II Superconductors". In: *Physical review letters* 89 (Aug. 2002), p. 027002. DOI: 10.1103/PhysRevLett.89.027002.

[75] J. Rossbach and P. Schmüser. "Basic course on accelerator optics". In: (1994). DOI: 10.5170/CERN-1994-001.17. URL: https://cds.cern.ch/record/247501.

[76] B. J. Holzer. *Beam optics and lattice design for particle accelerators*. en. 2013. DOI: 10.5170/CERN-2013-001.171. URL: http://cds.cern.ch/record/1533020.

[77] S. Russenschuck. In: *Field Computation for Accelerator Magnets*. John Wiley & Sons, Ltd, 2010, pp. 237–268. ISBN: 9783527635467. DOI: https://doi.org/10.1002/9783527635467.ch6.

[78] S. Calatroni. private communication. Jan. 2021.

[79] R. P. Walker. "Synchrotron radiation". In: (1994). DOI: 10.5170/CERN-1994-001.437. URL: http://cds.cern.ch/record/398429.

[80] G. Arduini et al. *Electron Cloud Effects in the CERN SPS and LHC*. Tech. rep. 2000.

[81] R. L. Gluckstern. "Analytic methods for calculating coupling impedances". In: (Nov. 2000). DOI: 10.5170/CERN-2000-011.

[82] L. Hänichen. "Numerical calculation of beam Coupling Impedances in Synchrotron Accelerators". en. PhD thesis. Darmstadt: Technische Universität Darmstadt, 2016. URL: http://tuprints.ulb.tu-darmstadt.de/5367/.

[83] A. Chao. "Beam Dynamics of Collective Instabilities in High Energy Accelerators". In: (July 2017). DOI: 10.23730/CYRSP-2017-003.43.

[84] I. Bellafont et al. "Design of the future circular hadron collider beam vacuum chamber". In: *Phys. Rev. Accel. Beams* 23 (3 Mar. 2020), p. 033201. DOI: 10.1103/PhysRevAccelBeams.23.033201. URL: https://link.aps.org/doi/10.1103/PhysRevAccelBeams.23.033201.

[85] van Bugteren, J. and others. "Numerical Analysis on the Application of a ReBCO Superconducting Coating on the Beam Screen". In: (2017).

[86] A. Preuss et al. "Critical Current Degradation of Coated Conductors Under Soldering Conditions". In: *IEEE Transactions on Applied Superconductivity* 28.4 (2018), pp. 1–5. DOI: 10.1109/TASC.2018.2804094.

[87] J. Ekin and G. Zimmerman. "Experimental Techniques for Low-Temperature Measurements: Cryostat Design, Material Properties, and Superconductor Critical-Current Testing". In: *Physics Today - PHYS TODAY* 60 (May 2007), pp. 321,333,547–611. DOI: 10.1063/1.2743130.

[88] B. W. Hakki and Paul D. Coleman. “A dielectric resonator method of measuring inductive capacities in the millimeter range”. In: *IRE Transactions on Microwave theory and techniques* 8.4 (1960), pp. 402–410.

[89] P. Krkotić, A. Aguasca, and J. O’Callaghan. “Small footprint evaluation of metal coatings for additive manufacturing”. In: *2018 48th European Microwave Conference (EuMC)*. IEEE. 2018, pp. 882–885.

[90] L. F. Chen et al. *Microwave electronics: measurement and materials characterization*. John Wiley & Sons, 2004.

[91] S. Calatroni and R. Vaglio. “High-Temperature Superconductor Coatings for Beam Impedance Reduction in Particle Colliders: Nonlinear Effects”. In: *IEEE Transactions on Applied Superconductivity* 31.3 (2021), pp. 1–8.

[92] R. E. Collin. *Foundations for microwave engineering*. John Wiley & Sons, 2007.

[93] A. Alimenti et al. “Challenging microwave resonant measurement techniques for conducting material characterization”. In: *Measurement Science and Technology* 30.6 (2019), p. 065601.

[94] N. Klein et al. “Dielectric properties of rutile and its use in high temperature superconducting resonators”. In: *Journal of applied physics* 78.11 (1995), pp. 6683–6686.

[95] N. Pompeo, K. Torokhtii, and E. Silva. “Dielectric resonators for the measurements of the surface impedance of superconducting films”. In: *Measurement Science Review* 14.3 (2014), pp. 164–170. ISSN: 13358871. DOI: 10.2478/msr-2014-0022.

[96] Keysight Technologies. *Data Sheet: FieldFox Handheld Analyzers 4/6.5/9/14/18/26.5/32/44/50 GHz*. 2020.

[97] Rohde & Schwarz. *R&S ZNB/ZNBT Vector Network Analyzers User Manual, 1173.9163.02 , Version 60*. 2021.

[98] P. Krkotić, G. T. Telles, and B. Bozzo. *Drohms: Dielectric Resonator Surface Impedance Measurement System Version 1.0*. 2019.

[99] Terrabits. *Rohde & Schwarz python instrument control toolbox by Terrabits*. 2021. URL: https://github.com/Terrabits/rohdeschwarz (visited on 12/27/2021).

[100] The MathWorks Inc. *MATLAB version: 9.10.0 (R2021a)*. Natick, Massachusetts, United States, 2021. URL: https://www.mathworks.com.

[101] The MathWorks Inc. *Color Thresholder - MATLAB*. 2023. URL: https://es.mathworks.com/help/images/ref/colorthresholder-app.html (visited on 07/24/2023).

[102] M. Abd Mutalib et al. “Chapter 9 - Scanning Electron Microscopy (SEM) and Energy-Dispersive X-Ray (EDX) Spectroscopy”. In: *Membrane Characterization*. Ed. by Nidal Hilal et al. Elsevier, 2017, pp. 161–179. ISBN: 978-0-444-63776-5. DOI: https://doi.org/10.1016/B978-0-444-63776-5.00009-7. URL: https://www.sciencedirect.com/science/article/pii/B9780444637765000097.

[103] X. Granados et al. “Magnetic Mapping - A Way to Test and Understand Current Flows in Thin and Bulk Superconductors”. In: *Advances in Science and Technology* 47 (Oct. 2006), pp. 1–6. DOI: 10.4028/www.scientific.net/AST.47.1.

[104] COMSOL AB. *Detailed Explanation of the Finite Element Method (FEM)*. 2017. URL: https://www.comsol.com/multiphysics/finite-element-method (visited on 07/24/2023).

[105] M. Loaiza. “A Short Introduction to Hilbert Space Theory”. In: *Journal of Physics: Conference Series* 839.1 (May 2017), p. 012002. DOI: 10.1088/1742-6596/839/1/012002. URL: https://dx.doi.org/10.1088/1742-6596/839/1/012002.

[106] V. Zermeno et al. “Calculation of AC losses in stacks and coils made of second generation high temperature superconducting tapes for large scale applications”. In: *Journal of Applied Physics* 114 (Aug. 2013). DOI: 10.1063/1.4827375.

[107] COMSOL Multiphysics® v. 5.5. COMSOL AB. “COMSOL Multiphysics® Reference Manual”. In: Stockholm, Sweden, 2019, p. 992.

[108] A. C. Wulff, A. B. Abrahamsen, and A. R. Insinga. “Multifilamentary coated conductors for ultra-high magnetic field applications”. In: *Superconductor Science and Technology* 34.5 (Apr. 2021), p. 053003. DOI: 10.1088/1361-6668/abee2b. URL: https://dx.doi.org/10.1088/1361-6668/abee2b.

[109] F. Caspers et al. “Image currents in azimuthally inhomogeneous metallic beam pipes”. In: *Conf. Proc. C* 0106181 (2001). Ed. by Peter W. Lucas and Sara Webber, pp. 1835–1837.

[110] Georges-Henry Hemelsoet. “Time Spent at Injection”. In: (2019), pp. 129–132. URL: https://cds.cern.ch/record/2813520.

[111] COMSOL Multiphysics® v. 6.0. COMSOL AB. “Heat Transfer Module User’s Guide”. In: Stockholm, Sweden, 2021, p. 176.

[112] COMSOL Multiphysics® v. 6.0. COMSOL AB. “Structural Mechanics Module User’s Guide”. In: Stockholm, Sweden, 2021, pp. 361–400.

[113] M. Sutherland et al. “Thermal conductivity across the phase diagram of cuprates: Low-energy quasiparticles and doping dependence of the superconducting gap”. In: *Phys. Rev. B* 67 (17 May 2003), p. 174520. DOI: 10.1103/PhysRevB.67.174520. URL: https://link.aps.org/doi/10.1103/PhysRevB.67.174520.

[114] M. Bonura and C. Senatore. “Transverse Thermal Conductivity of REBCO Coated Conductors”. In: *IEEE Transactions on Applied Superconductivity* 25.3 (2015), pp. 1–4. DOI: 10.1109/TASC.2014.2367163.

[115] N. Bagrets et al. “Thermal properties of 2G coated conductor cable materials”. In: *Cryogenics* 61 (2014), pp. 8–14. ISSN: 0011-2275. DOI: https://doi.org/10.1016/j.cryogenics.2014.01.015. URL: https://www.sciencedirect.com/science/article/pii/S0011227514000241.

[116] W. Chou and F. Ruggiero. *Anomalous Skin Effect and Resistive Wall Heating*. Tech. rep. Geneva: CERN, 1995. URL: https://cds.cern.ch/record/691905.

[117] F. Caspers, M. Morvillo, and F. Ruggiero. “Surface Resistance Measurements for the LHC Beam Screen”. In: (1998). URL: https://cds.cern.ch/record/328007.

[118] E. Métral. *Beam screen issues*. 2011. arXiv: 1108.1643 [physics.acc-ph].

[119] N. Belk et al. “Linear and nonlinear microwave dynamics of vortices in $YBa_2Cu_3O_{7-\delta}$ thin films”. In: *Phys. Rev. B* 56 (18 Nov. 1997), pp. 11966–11978. DOI: 10.1103/PhysRevB.56.11966. URL: https://link.aps.org/doi/10.1103/PhysRevB.56.11966.

[120] I. S. Gradshteyn and I. M. Ryzhik. *Table of Integrals, Series, and Products*. Academic Press, 1980.

[121] H. S. Shin et al. “The strain effect on critical current in YBCO coated conductors with different stabilizing layers”. In: *Superconductor Science and Technology* 18.12 (Nov. 2005), S364. DOI: 10.1088/0953-2048/18/12/023. URL: https://dx.doi.org/10.1088/0953-2048/18/12/023.

[122] K. Konstantopoulou. “Mechanical behavior of 2G REBCO HTS at 77 and 300 K”. PhD thesis. Universidad Politécnica de Madrid, 2015.

[123] F. Dias. “Magnetic Irreversibility and Resistive Transition in YBaCuO Superconductors: Interpretations and Possible Correlations”. In: Apr. 2012. ISBN: 978-953-51-0545-9. DOI: 10.5772/38401.

[124] R. Maleyran and R. Valbuena. *Calculation results of Eddy current effects on the LHC dipole screen*. Tech. rep. Geneva: CERN, 1993. URL: https://cds.cern.ch/record/1970415.

[125] B. Angerth et al. "The LHC beam screen: specification and design". In: (Jan. 1994).

[126] Olayide R. Adetunji et al. "Tensile, hardness and microstructural properties of Sn-Pb solder alloys". In: *Materials Today: Proceedings* 44 (2021). International Conference on Materials, Processing & Characterization, pp. 321–325. ISSN: 2214-7853. DOI: https://doi.org/10.1016/j.matpr.2020.09.656. URL: https://www.sciencedirect.com/science/article/pii/S2214785320373818.

[127] Olayide R. Adetunji et al. "Tensile behavior of pb-sn solder/cu joints". In: *J. Electron. Mater* 16 (1987), pp. 203–208. DOI: https://doi.org/10.1007/BF02655488.

[128] COMSOL Multiphysics® v. 6.0. COMSOL AB. "AC/DC Module User's Guide". In: Stockholm, Sweden, 2021, pp. 80–92.

[129] M. Drienovsky et al. "Induction Soldering of Coated Conductor High-Temperature Superconducting Tapes With Lead-Free Solder Alloys". In: *IEEE Transactions on Applied Superconductivity* 28.4 (2018), pp. 1–5. DOI: 10.1109/TASC.2018.2805102.

[130] H. Murrmann and D. Widmann. "Current crowding on metal contacts to planar devices". In: *IEEE Transactions on Electron Devices* 16.12 (1969), pp. 1022–1024. DOI: 10.1109/T-ED.1969.16904.

[131] H. H. Berger. "Models for contacts to planar devices". In: *Solid-State Electronics* 15.2 (1972), pp. 145–158. ISSN: 0038-1101. DOI: https://doi.org/10.1016/0038-1101(72)90048-2. URL: https://www.sciencedirect.com/science/article/pii/0038110172900482.

[132] H. Liu et al. "Size-selective electrodeposition of meso-scale metal particles: a general method". In: *Electrochimica Acta* 47.5 (2001), pp. 671–677. ISSN: 0013-4686. DOI: https://doi.org/10.1016/S0013-4686(01)00747-2. URL: https://www.sciencedirect.com/science/article/pii/S0013468601007472.

[133] S. Nakamura et al. "Low temperature transport properties of pyrolytic graphite sheet". In: *Cryogenics* 86 (2017), pp. 118–122. ISSN: 0011-2275. DOI: https://doi.org/10.1016/j.cryogenics.2017.08.004. URL: https://www.sciencedirect.com/science/article/pii/S0011227517301212.

[134] CERN. *Dark Matter*. 2023. URL: https://home.cern/science/physics/dark-matter (visited on 07/13/2023).

[135] NASA. *Dark Energy, Dark Matter*. 2023. URL: https://science.nasa.gov/astrophysics/focus-areas/what-is-dark-energy (visited on 07/13/2023).

[136] C. B. Adams et al. *Axion Dark Matter*. 2023. arXiv: 2203.14923 [hep-ex].

[137] A. Melcón et al. "First results of the CAST-RADES haloscope search for axions at 34.67 μeV". In: *Journal of High Energy Physics* 2021.10 (Oct. 2021). DOI: 10.1007/jhep10(2021)075. URL: https://doi.org/10.1007%2Fjhep10%282021%29075.

[138] J. Golm et al. "Thin Film (High Temperature) Superconducting Radiofrequency Cavities for the Search of Axion Dark Matter". In: *IEEE Transactions on Applied Superconductivity* 32.4 (June 2022), pp. 1–5. DOI: 10.1109/tasc.2022.3147741. URL: https://doi.org/10.1109%2Ftasc.2022.3147741.

[139] D. W. Martin et al. "Cryogenic RF Material Testing at SLAC". In: *Conf. Proc. C* 110328 (2011). Ed. by Todd Satogata and Kevin Brown, pp. 1030–1032.

[140] G. T. Telles. *Numerical Analysis of Hybrid REBCO-Cu Coatings for the Future Circular Collider Beam Screen*. 2024. DOI: 10.5281/zenodo.11394250. URL: https://doi.org/10.5281/zenodo.11394250.

[141] COMSOL Multiphysics® v. 5.4. COMSOL AB. "LiveLink™ for MATLAB® User's Guide". In: Stockholm, Sweden, 2018.

[142] G. T. Telles et al. "Field quality and surface resistance studies of a superconducting REBa2Cu3O—Cu hybrid coating for the FCC beam screen". In: *Superconductor Science and Technology* 36.4 (Feb. 2023), p. 045001. DOI: 10.1088/1361-6668/ac97c9. URL: https://dx.doi.org/10.1088/1361-6668/ac97c9.

[143] T. L. Chow. *Introduction to Electromagnetic Theory: A Modern Perspective*. Jones and Bartlett Publishers, 2006. ISBN: 9780763738273. URL: https://books.google.es/books?id=dpnpMhw1zo8C.

[144] COMSOL Multiphysics® v. 6.0. COMSOL AB. "AC/DC Module User's Guide". In: Stockholm, Sweden, 2021, pp. 55–73.

[145] P. Duthil. *Material Properties at Low Temperature*. en. 2014. DOI: 10.5170/CERN-2014-005.77. URL: http://cds.cern.ch/record/1973682.

[146] N. Simon, E. Drexler, and R. Reed. "Properties of Copper and Copper Alloys at Cryogenic Temperatures". In: *NIST Monograph* 177 (Jan. 1992).

[147] M. Morrone. Personal Communications. 2022.

[148] M. Rahim et al. "Reliability of flip chip assemblies subjected to extreme low temperatures". In: vol. 2006. July 2006, pp. 1379–1389. DOI: 10.1109/ITHERM.2006.1645506.

[149] W. Frei. *Accelerating Model Convergence with Symbolic Differentiation*. 2020. URL: https://www.comsol.com/blogs/accelerating-model-convergence-with-symbolic-differentiation/ (visited on 12/14/2023).

[150] A. Arsenault, F. Sirois, and F. Grilli. "Implementation of the H-ϕ Formulation in COMSOL Multiphysics for Simulating the Magnetization of Bulk Superconductors and Comparison With the H-Formulation". In: *IEEE Transactions on Applied Superconductivity* 31.2 (2021), pp. 1–11. DOI: 10.1109/TASC.2020.3033998.

[151] A. Arsenault, F. Sirois, and F. Grilli. *H-ϕ Formulation in COMSOL Multiphysics for Simulating the Magnetization of Bulk Superconductors and Comparison With the H-Formulation*. 2020. URL: https://www.htsmodelling.com/?wpdmpro=h-%cf%95-formulation-in-comsol5_5 (visited on 08/18/2023).